A Review of the Gas-Puff *Z*-Pinch as an X-Ray and Neutron Source

John L. Giuliani, *Member, IEEE*, and Robert J. Commisso, *Fellow, IEEE*

***Abstract*— Fisher and collaborators at the University of California, Irvine, invented the gas puff *Z*-pinch in the late 1970s using a 200-kA generator. The implementation of gas puffs as a copious source of X-rays has encountered major challenges, such as disruptive instabilities and the quest for long implosion times. During nearly four decades of experimental and theoretical efforts, those challenges have been successfully met to a great extent. This success is a result of the efforts of a large number of researchers. Today, the gas-puff *Z*-pinch has evolved into a powerful source of X-rays and neutrons, and is fielded on multi-Mega-Ampere generators. The basic force imploding a pinch is straightforward, but the operation of a gas puff requires specialized hardware and a thorough understanding of the radiation physics involves magnetohydrodynamics coupled with nonequilibrium ionization kinetics. The goal of this review is to document the experiments and theory that have led to the success of the gas puff as a K-shell X-ray and neutron source. Consequently, this review takes a historical approach to the covered material, but also provides a broad introduction to relevant scientific concepts.**

***Index Terms*— Gas puff, magnetohydrodynamics, plasma neutron sources, plasma radiation sources, *Z*-pinch.**

Manuscript received February 5, 2015; revised June 17, 2015; accepted June 25, 2015. Date of current version August 7, 2015. The work of J. L. Giuliani was supported by the Department of Energy/National Nuclear Security Administration under Grant DE-NA0001564. The work of R. J. Commisso was supported by the U.S. Naval Research Laboratory, Washington, DC, USA, through the Basic and Applied Research Programs.

The authors are with the Plasma Physics Division, U.S. Naval Research Laboratory, Washington, DC 20375 USA (e-mail: john.giuliani@nrl.navy.mil; robert.commisso@nrl.navy.mil).

Color versions of one or more of the figures in this paper are available online at http://ieeexplore.ieee.org.

Digital Object Identifier 10.1109/TPS.2015.2451157

I. Introduction

Z-PINCHES use the electrical current from a pulsed power generator to transform a material load into a plasma and then magnetically compress it onto the axis aligned with the current flow. There are a variety of load configurations for a *Z*-pinch, including among others: 1) single wires [I-1]; 2) fibers [I-2]; 3) cylindrical wire arrays [I-3]; 4) planar wire arrays [I-4]; 5) liners [I-5]; 6) dynamic hohlraums [I-6]; 7) foams [I-7]; 8) magnetized inertial fusion targets [I-8]; and 9) gas puffs. In the case of the gas puff load, the originally nonconducting gas must undergo a phase change to a plasma, usually as a result of a breakdown process, to carry the generator current. Applications necessitate that a hot dense plasma be formed and persist for sufficient time to produce the desired output. This generally occurs by the interaction of the current and the magnetic field associated with the current (known as the self-magnetic field), leading to the plasma compressing upon itself, or pinch.

There have been many reviews of dense *Z*-pinches because the field has rapidly evolved. Two early reviews were by Haines [I-9] and Dangor [I-10]. The Haines review stressed the dense plasma focus (DPF) and looked at the *Z*-pinch as a close relative of the DPF. Both reviews noted the advent of high-power, high-current, low-impedance, and water-line generators as opening up possibilities for fusion applications of *Z*-pinches. The configurations studied featured a uniform static fill through which current was passed, rather than a gas puff.

The first comprehensive review that focused on *Z*-pinches (wire arrays and gas puffs) was by Pereira and Davis [I-11] and it concentrated on radiation production. Reviews of the general physics of the *Z*-pinch physics can be found in [I-12] and [I-13]. The latter is practically a book and has more than 700 references. Reference [I-14] is a book on *Z*-pinches that emphasizes dynamics and stability. Spielman and De Groot [I-15] present a historical review

of Z-pinches up to 2001. Reviews of work by specific institutions include: 1) Coleman *et al*. [I-16] on pinch experiments at Maxwell Physics International (MPI); 2) Coverdale *et al*. [I-17] on radiation output from the Z and refurbished Z (ZR) generators at Sandia National Laboratories (SNL); 3) Cuneo *et al*. [I-18] on magnetically driven implosions for inertial confinement fusion at SNL; and 4) Giuliani *et al*. [I-19] on pinch research at U.S. universities. Other reviews of interest to gas puffs will be cited later in appropriate sections.

This review is focused on the successful development of gas-puff Z-pinches as a plasma radiation and neutron source. Since the turn of the century, there has been tremendous progress in developing gas-puff configurations that can stably implode from large radii, at high current, and achieve significant K-shell X-rays from noble gases or neutrons from D_2 puffs. (In the precise definition, K-shell radiation are photons emitted from bound-bound, including inner shell, and free-bound transitions to the 1s atomic state. In practice, however, measurements of K-shell power or yield generally refer to photons greater than some energy E_γ, where E_γ is less than but close to the He-α transition of the He-like ion. This can include free-bound recombination to levels of principal quantum number >1 and free-free emission.) Driven by these achievements, there have also been improvements in multidimensional, magnetohydrodynamic (MHD) simulations that include the physics of nonlocal thermodynamic equilibrium (non-LTE) ionization. These developments could not have been covered by most of the previous reviews because of their early date [I-11], [I-12], [I-14]–[I-16], or because of their focus on wire arrays [I-18], [I-19]. There is admittedly some overlap here with topics covered in [I-13] and [I-17]. The present review aims to tell a more complete story of the physics, technology, and progress made in utilizing gas-puff Z-pinches to produce X-rays and neutrons. There is a strong historical flavor in our writing with many references included, as many scientists from several institutions have made important contributions to propel this research forward. For scientists new to the field, there is also an attempt to provide both a firm basis from which to carry out experiments or modeling as well as to give an overview of how the physics understanding and radiation output of gas-puff Z-pinches evolved. For such new researchers, it is important to note that the mission driver for over three decades has been the development of Ar radiation sources for photons above $\sim$3 keV by the Defense Threat Reduction Agency (formerly Defense Nuclear Agency, and later the Defense Special Weapons Agency) and the Department of Energy/National Nuclear Security Administration (NNSA).

Not covered by this review are: 1) the DPF (there are some similarities between the DPF and gas-puff Z-pinch and a review of DPFs was recently completed in [I-20]); 2) Z-pinch-driven lasers; 3) capillary discharges; 4) embedded pinches with insulating walls; 5) pinches for particle transport and focusing; 6) low-density gas puffs (here by Z-pinch we mean a dense Z-pinch with a compressed central density of $\gg 10^{16}$ cm^{-3}); and 7) the development of diagnostic instruments.

An outline was presented at the beginning of this section to enable a bird's eye view of the article. The early history of gas puffs is covered in the following section. Section III provides some theoretical background to Z-pinches. We have found it useful to put such material near the beginning so that subsequent discussions have the terms and concepts readily available. The following three sections are organized according to the evolution of a gas-puff Z-pinch: 1) initial conditions; 2) implosion; and 3) stagnation. Most of the technology review is in Section IV on initial conditions. Section V on implosion clarifies the motivation and challenges that Z-pinches faced in going to large-radius and long-time implosion. Section VI on stagnation covers the heart of the matter: experiments and theory on K-shell and neutron plasma sources. The penultimate section collects together and describes many simple and complex variations on the standard gas puff. Section VIII looks to the future.

To orient a reader unfamiliar with gas-puff Z-pinches, we present in Fig. I-1 a drawing of the basic components in a gas-puff Z-pinch with the current and self-magnetic field forming the radially inward $\mathbf{J} \times \mathbf{B}$ pinch force. Below the drawing are successive visible images from [I-21] of a neon gas puff moving from ionization, through implosion, and finally to stagnation on the z-axis.

There are advantages and disadvantages of gas puffs for Z-pinches relative to wire arrays. One advantage of gas puffs is that the initial density distribution is axisymmetric; at least they are designed to be so. Wire arrays have an inherent azimuthal variation due to the finite number of wires. Second, on small current generators ($\sim$1 MA), successive experiments for simple gas puffs can be performed without breaking vacuum. This engenders a high shot rate per day with much data. Nozzles for gas puffs can be designed to produce tailored distributed density profiles. This feature has been especially important in developing advanced radiation sources. A major disadvantage of gas puffs is that there are a limited number of species to use in a nozzle with plenums. Wire arrays are limited by the available thickness of wires, which impacts on the number of wires in an array, but there are many material choices and alloys. The large range of wire materials allows one to create high-temperature broadband radiation as with tungsten [I-18]. Another disadvantage of gas puffs is that the initial density distribution must be measured as opposed to wire arrays where the initial conditions are precisely known.

Gas-puff Z-pinches have been fielded on many generators. Section VI-A has a table listing generators and load conditions for particular shots. For the same generator, the nozzle configuration, and/or current, and/or implosion time, can be widely different. So, throughout this paper whenever the radiation or neutron output from a generator is discussed, we include parenthetically the typical current and implosion time for the experiments. There are also two tables in the Appendix presented for ease in cross-referencing throughout this paper. The first contains a list of acronyms and their meanings. The second table is a list of important mathematical symbols, with a short description and the equation or figure where they are first used.

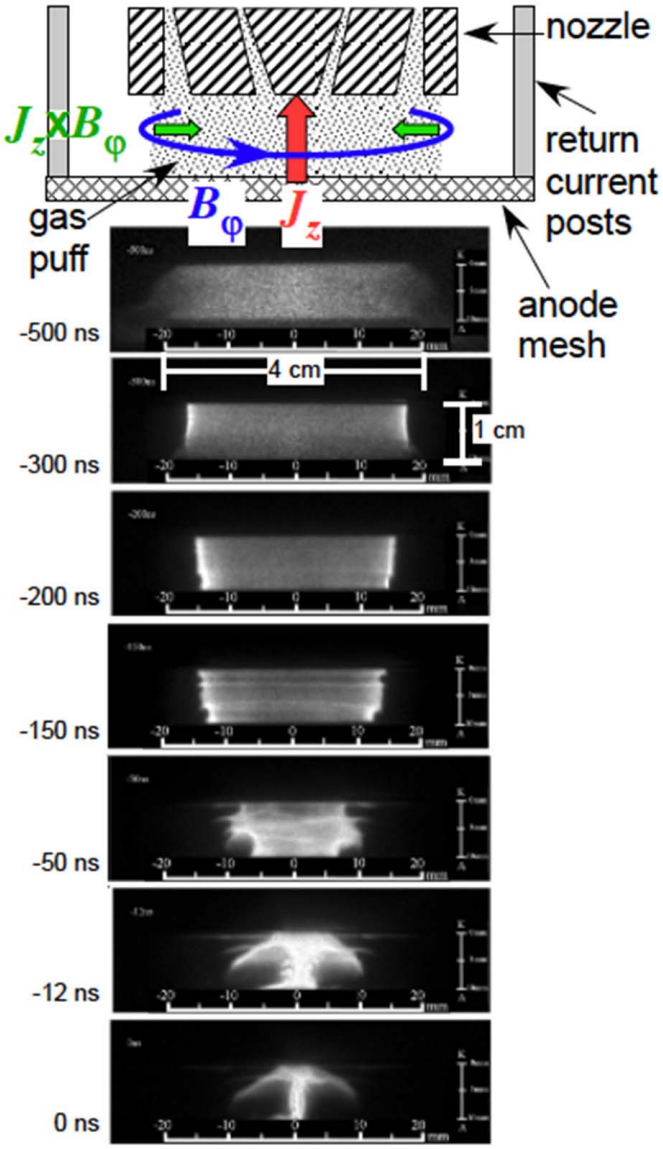

Fig. I-1. Top: schematic of a gas puff Z-pinch showing the basic hardware and electromagnetic components. Bottom: successive visible images of neon gas puff initiation, implosion, and stagnation. The time of peak radiative emission is 0 ns. Images are adapted from [I-21].

For our ground rule on references, we have mostly avoided citing abstracts of presentations at meetings. The content of the presentations associated with such abstracts is not accessible to future researchers. Published documentation in Conference proceedings and laboratory reports that can be obtained will be referenced.

II. Early History

A team led by Amnon Fisher at the University of California, Irvine (UCI), published the first gas puff linear Z-pinch experiments in the late 1970s. The motivation for gas puffs, as expressed in [II-1], was that vacuum spark gaps were irreproducible for pinch loads and an exploding wire could not reach high temperatures without a large current for the resistive heating needed to make the solid-wire change phase. The system at UCI could produce ~200 kA in ~600 ns.

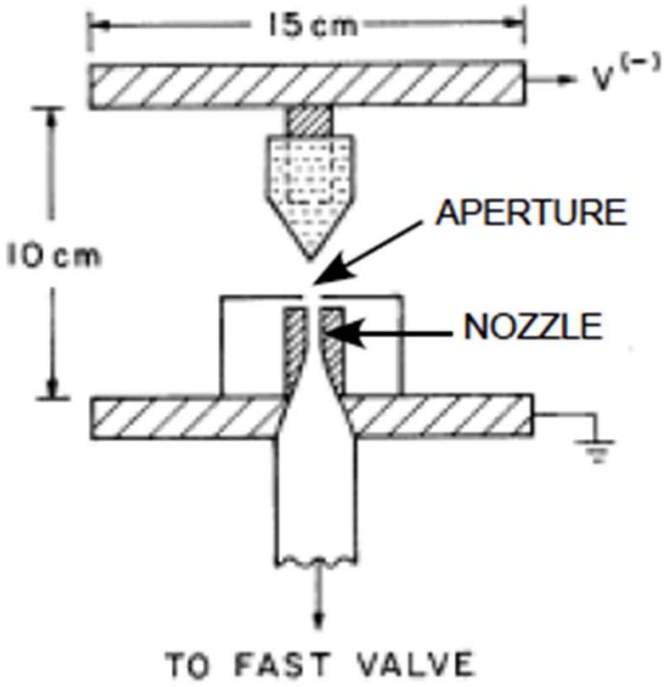

Fig. II-1. Schematic of the experimental setup for the first gas puff Z-pinch. Reprinted figure with permission from [II-1]. Copyright 1978 by the American Physical Society.

The gas delivery system consisted of a fast valve, nozzle, and an aperture, as shown in Fig. II-1, along with a miniature spark gap below the nozzle to detect that gas had been released before triggering the generator (gas-puff assembly components are described in Section IV-A). Unlike most later designs for gas-puff loads, where the nozzle is the cathode and the downstream anode is a wire mesh, here the downstream electrode is the cathode and it was a solid cone. The anode nozzle had an opening of 0.25-cm diameter for the gas to flow into the evacuated anode–cathode (A–K) gap. If the delay between the valve opening and firing the generator was too short, the pinch acted more like a spark gap; if it was too long, there would be a voltage flashover at the insulator stack. By 20 μs after the valve was opened, the neutral Ar gas reached a density of $\sim 10^{17}$ cm^{-3}. At this time, the gas puff had an outer diameter (OD) of 0.25 cm near the anode (valve face) and 0.4 cm at the conical high-voltage cathode 0.8 cm away. About 300 ns after the initial gas breakdown, the gas reached a radial velocity of 20 cm/μs and pinched to a few millimeter diameter, with an electron density of $n_e > 10^{19}$ cm^{-3}. At this time, the voltage spiked and there was a burst of X-rays lasting ~20 ns. Hard X-rays (>200 keV) were also observed. It was suggested that gas puffs, as opposed to a wire on axis, offer the advantage of a higher shot rate since there was no need to break vacuum between shots, at least for moderate currents.

In [II-2], it was shown that the gas-puff Z-pinch would be an excellent source for spectroscopic observations of highly ionized noble gases and that the ionization fractions in the pinched plasma were not in LTE. *Ab initio* atomic structure calculations were brought to bear on the spectra and line ratios

from H- and He-like Ar ions indicated a plasma temperature of ~1 keV based on a collisional radiative equilibrium (CRE) kinetics model from the Naval Research Laboratory (NRL). (LTE and CRE are discussed in Section VI-B.)

A natural application of the gas-puff Z-pinch was to investigate its utility as a neutron source. Bailey *et al.* [II-3] found that for high-density pinches ($\sim 2 \times 10^{19}$ cm^{-3}), adding 10% Ar to a D_2 puff produced a more uniform and stable pinch with a similar neutron yield (5×10^7) as pure D_2. It was estimated that the product of density and confinement time was larger with the Ar than in pure D_2. This was attributed to the observed radial separation of deuterium from the Ar and the latter acting as a stabilizing blanket around the inner deuterium plasma.

Another paper from the UCI group deserves mention for its demonstration that discovery by serendipity can follow invention. The gas-puff geometry of the UCI system was modified and the nozzle was changed to a form a gas shell of OD = 4 cm to study the stability of the pinch. With a hollow anode and a recessed cathode as part of the nozzle, Chang *et al.* [II-4] reported a significant improvement in the pinch stability over a previous design. But after a few hundred shots, suddenly the hard X-ray output increased by about an order of magnitude. Suspecting a failed diode filter, the machine was opened only to find that the pinch had drilled a hole through the recessed part of the cathode into the Kr gas plenum, thereby forming a central jet in addition to the gas shell. A new nozzle configuration with a central hole and plunger was fielded to control the central jet and they reported that the radiation above 1 keV was ~1.5 J without the jet but ~8 J with the central jet.

About one year after the initial paper [II-1], Stallings *et al.* [II-5] reported on an Ar gas puff using the 4-TW PITHON generator at Physics International (PI). Note that subsequently PI became MPI, which became Titan Corporation Pulse Sciences Division (TPSD), and is now L-3 Applied Technologies Inc. (L-3 ATI). Stallings *et al.*'s [II-5] objective was to form a hollow shell to maximize the implosion velocity and attain high temperatures at stagnation, converting kinetic into thermal energy, for radiation production. The A–K gap was varied from 2 to 8 cm, but no X-rays were observed beyond 4 cm. This was attributed to the rapid flaring of the initial, neutral gas shell such that at 4-cm downstream of the nozzle, the annular shell feature was lost. Similar temperatures to those previously obtained in [II-2] were derived from the same CRE modeling. According to [II-6], PI also investigated an approach at current-pulse rise-time reduction (which was thought to improve stability) wherein an outer gas shell would implode on an inner one and, with a transfer of current, the inner one was to rapidly compress to the axis. This concept again appears in Section VII on hybrid pinches. Sincerny *et al.* [II-7] reported that the conjecture was not confirmed, but noted that the stability of the entire pinch was improved. Baksht *et al.* [II-8] were the first to demonstrate increased radiation near ~1 keV using a cascade, or equivalently a double-shell gas puff, compared with a single annular shell. Actually, a triple-shell gas puff was reported that gave by far the most radiation, but the implications of this result for the control of magnetic Rayleigh–Taylor (MRT) instability (discussed in Section V-C) was not appreciated by the community for nearly a decade.

By the mid 1980s, other groups were beginning to experimentally study gas-puff Z-pinches. Clark *et al.* [II-9] used a high-Mach-number nozzle to limit the flow divergence and imploded an Ar puff on the Blackjack 5 generator (3.5 MA, ~200 ns) at Maxwell Laboratories Inc. [(MLI), later merged with PI to become MPI around 2001]. The time history of the plasma radius was measured with a visible streak camera and matched to a radius computed from a 0-D snowplow model derived from [II-10]. Marrs *et al.* [II-11] employed time-resolved vacuum ultraviolet (UV) spectroscopy to observe the time-dependent ionization of an Ar puff on a 350-kA pulser at Lawrence Livermore National Laboratory. Using an Ar puff on the PITHON generator at PI, Perez *et al.* [II-12] made spectral measurements perpendicular to the pinch axis and reported Doppler shifts of emission lines during the implosion as a result of the radial motion of the plasma shell away from and toward the observation point. Stewart *et al.* [II-13], [II-14] also used the PITHON generator to study the spectroscopic details of emission lines from Ne-like Kr and L-shell Ar (Ne-like Ar means the Ar ion has 10 bound electrons, and L-shell Ar means that there are 3 to 10 bound electrons). The latter paper reported radial velocities associated with Doppler shifts similar to [II-12], ~70 cm/μs, but also saw shifts looking in the axial direction corresponding to ~20 cm/μs.

Kania and Jones [II-15] reported the first measurement of electron beams in a gas puff on a generator at Los Alamos National Laboratory (LANL). Of the 600-kA total current they estimated 10 kA in a 20-keV electron beam from filtered Faraday cup measurements. The spectroscopy of [II-16] from the LANL experiments showed the inner shell transitions from L-shell Ar and suggested that electron temperatures had been overestimated by neglecting the ionizations by the beam. Hares *et al.* [II-17] performed absolute measurements of the suprathermal electrons on a capacitively driven Ar pinch and showed that they could not be the dominant energy source. At Imperial College, Choi *et al.* [II-18] found that the soft X-ray emission from hot spots in an Ar pinch was temporally preceded by hard X-ray emission resulting from high-energy electrons.

The earliest paper we found to suggest that Z-pinches could be used as a radiation source was by Turchi and Baker [II-19], although this was for a metallic foil load. The pulsed-power group at NRL was seeking to eliminate any current prepulse from the Gamble II generator and shorten the current rise time. Stephanakis *et al.* [II-20] successfully engineered the combination of a plasma opening switch (POS) with a neon gas-puff shell as the load. The success at producing high temperature plasmas and radiation through gas puffs [II-2], [II-5], [II-20] motivated the theoretical studies of gas puffs to determine how the radiation could be enhanced. Duston *et al.* [II-21] developed the hot spot model that advanced the state of the art for non-LTE theory by utilizing a CRE model to calculate the ionization kinetics. The plasma was assumed to be stationary and optically thin.

Apruzese and Davis [II-22] improved on the hot spot model by including radiation transport and opacity effects for emission lines. A proper treatment of the emission lines is driven by the fact that the observed spectra from Z-pinches are dominated by emission lines. They found that opacity effects reduce the power from the optically thin approximation of [II-21], but that a mixture of Na and Ne could increase the combined K-shell radiative power from the pinch over either pure Na or Ne.

The radiation from a gas puff Z-pinch was also proposed as an X-ray laser source. Such a source requires a homogeneous medium with a long radiation path length to achieve high gain. Spielman *et al*. [II-23] noted that implosions of annular gas shells produced irregular hot spots when assembled on axis, so the objective of their initial study was to produce a homogeneous pinch in the stagnation phase using a hybrid design. The experiments were performed on Proto-II (3 MA, 40 ns) with a Xe annular shell of radius 1.25 cm imploding onto a thin (0.2-cm diameter) low-density (4.5×10^{-3} g/cm^3) foam of polyacrylic acid on axis. Even though the foam mass was roughly twice that of the Xe puff, the X-ray yield near 1 keV only decreased from 4.3 kJ without the foam to 4.1 kJ with the foam. Furthermore, based on time-integrated pinhole images (>1 keV), the foam did act to produce a more uniform pinch on axis. An X-ray laser was not investigated in [II-23].

Another early application of an imploding gas-puff Z-pinch plasma, but with commercial implications, was lithography [II-24]–[II-26]. This work built on the previous research with gas puffs [II-1], [II-2]. Using a simple capacitive discharge driving a hollow shell of Kr gas at ~0.7 MA, ~20 J of >1-keV radiation was observed. The capacitive discharge was thought to be more easily scaled to a repetitively pulsed production capability. Approximately 60% of the >1-keV radiation was in the range of 1.7–1.88 keV, mostly line radiation from Ne-like Kr. This was thought to be the ideal range of photon energy for lithographic applications [II-24]. A lower power, repetitively pulsed system (3 Hz) for this application, utilizing a neon gas puff, was also demonstrated [II-27]. The neon produced an X-ray yield of up to ~200 J at a ~350-kA peak current. Radiation in the range of 0.9–1.4 keV was dominated by resonance lines of He-like and H-like Ne.

We arbitrarily end this section on the early history at this point, and note that many of the engineering and physics concepts highlighted from the above early papers, such as the dependence of pinch quality on the initial density profile noted by [II-4] and [II-7], continued to play a major role in the subsequent research.

III. Theoretical Background

In this section, we introduce a number of theoretical concepts and define terms that are used in the remainder of this review. The discussion is somewhat tutorial but does establish a framework that supports the motivation and trends of the experiments described later. Section III-A presents the fundamental plasma equations typically used to describe the resistive MHD physics of dense gas-puff Z-pinches. Section III-B describes the connection between the above equations for a Z-pinch and the generator treated with a circuit model. The 0-D snowplow model is developed in Section III-C. Though many researchers have employed this simple model in the past, its application with a distributed density and a coupled circuit does not seem to have been presented. Admittedly, the 0-D model is a gross simplification. In particular, there is no mechanism for heating the plasma. As a result, there is no dynamic feedback from plasma pressure and no accounting for the effects of radiation on the energy balance. All of this notwithstanding, the solutions from the 0-D model highlight features of the pinch dynamics that are important for a general understanding, and this is presented in Section III-D. Section III-E describes scaling models employed to understand pinches as K-shell radiation sources.

A. Equations of Resistive MHD

Most models of gas-puff Z-pinches have employed the MHD description with charge neutrality and the neglect of the displacement electric field. This assumes that ion gyroradius is small compared with the magnetic sheath thickness controlled by the resistivity and that electrostatic fields are not important. Maxwell's equations for the magnetic (**B**) and electric (**E**) fields are then Faraday's law, the absence of magnetic monopoles, and Ampere's law for the current density (**J**). In centimeter-gram-second units (used throughout this paper), these are

$$\frac{\partial \mathbf{B}}{\partial t} = -c\nabla \times \mathbf{E} \tag{III-1}$$

$$\nabla \cdot \mathbf{B} = 0 \tag{III-2}$$

and

$$\mathbf{J} = \frac{c}{4\pi}\nabla \times \mathbf{B} \tag{III-3}$$

where c is the speed of light and t is the time variable. Because of the assumption of charge neutrality noted above, the electric field is not determined from Coulomb's law. Instead, the electric field is specified through an Ohm's law, which in the simplest case is a resistive term in addition to the relation from ideal MHD

$$\mathbf{E} = -\frac{\mathbf{u}}{c} \times \mathbf{B} + \eta_{\text{res}}\mathbf{J} \tag{III-4}$$

where $\mathbf{u}$ is the mass velocity and η_{res} is the scalar resistivity. The first term on the right is the motional electric field and the second is the electric field associated with the plasma resistivity.

For the hydrodynamics, one starts with the continuity equation for a single fluid

$$\frac{\partial \rho}{\partial t} + \nabla \cdot (\rho \mathbf{u}) = 0 \tag{III-5}$$

where ρ is the mass density. The momentum equation is

$$\frac{\partial}{\partial t}(\rho \mathbf{u}) + \nabla \cdot (\rho \mathbf{u}\mathbf{u}) + \nabla(p_i + p_e) + \frac{\partial \Pi_{\alpha\beta}}{\partial x_\beta} = \frac{1}{c}\mathbf{J} \times \mathbf{B}. \tag{III-6}$$

The ion ($p_i = n_i k_B T_i$) and electron ($p_e = n_e k_B T_e$) pressures are distinctly noted because the ion (T_i) and electron (T_e) temperatures can be quite different in a Z-pinch (k_B is the Boltzmann constant). n_i (n_e) is the ion (electron) number

density. $\Pi_{\alpha\beta}$ is the ion viscosity stress tensor. Its divergence in (III-6) is written in generalized coordinates where repeated subscripts indicate a sum over all the three coordinates. The ion thermal energy equation is

$$\frac{\partial}{\partial t}(n_i\varepsilon_i) + \nabla\cdot(n_i\varepsilon_i\mathbf{u}) + p_i\nabla\cdot\mathbf{u} + \Pi_{\alpha\beta}\frac{\partial u_\alpha}{\partial x_\beta} + \nabla\cdot\mathbf{q}_i = -Q_{ie}. \quad \text{(III-7)}$$

For an ideal ion plasma component with a ratio of specific heats $\gamma = 5/3$, the ion thermal energy is $\varepsilon_i = (3/2)k_BT_i$. The term $\Pi_{\alpha\beta}(\partial u_\alpha/(\partial x_\beta)$ represents ion viscous heating. $\mathbf{q}_i = -\kappa_i\nabla T_i$ is the ion thermal conductive flux with the ion thermal conductivity κ_i. Q_{ie} is the ion-electron thermal equilibration term proportional to $\overline{Z}^2 n_i n_e(T_i - T_e)$, where $\overline{Z}$ is the mean ion charge state. Finally, the electron energy equation is

$$\frac{\partial}{\partial t}(n_e\varepsilon_e + n_i\varepsilon_x) + \nabla\cdot[(n_e\varepsilon_e + n_i\varepsilon_x)\mathbf{u}] + p_e\nabla\cdot\mathbf{u} + \nabla\cdot\left[\mathbf{q}_e - \frac{\mathbf{J}}{en_e}(n_e\varepsilon_e + p_e)\right] = Q_{ie} - \Lambda + \mathbf{J}\cdot\left(\mathbf{E} + \frac{\mathbf{u}}{c}\times\mathbf{B}\right) \quad \text{(III-8)}$$

where $\varepsilon_e = (3/2)k_BT_e$, $\mathbf{q}_e = -\kappa_e\nabla T_e$ is the electron thermal conductive flux with electron thermal conductivity κ_e, and Λ is the radiation loss from the plasma. Here, ε_x is the ionization plus excitation energy per ion. Because electron thermal energy through collisions and radiation through photon interactions are responsible for the ionization and excitation state of the ions, the term $n_i\varepsilon_x$ is included in the electron energy equation. Note that for the electric field of (III-4), the last term on the right of (III-8) reduces to the resistive heating $\eta_{\text{res}}\mathbf{J}^2$.

We now perform some manipulations of these equations. First, multiply the momentum equation by the velocity to derive the kinetic energy equation

$$\frac{\partial}{\partial t}\left(\frac{1}{2}\rho u^2\right) + \nabla\cdot\left(\frac{1}{2}\rho u^2\mathbf{u}\right) + \mathbf{u}\cdot\nabla(p_i + p_e) + u_\alpha\frac{\partial\Pi_{\alpha\beta}}{\partial x_\beta} = \frac{\mathbf{u}}{c}\cdot(\mathbf{J}\times\mathbf{B}) = \mathbf{J}\cdot\left(-\frac{\mathbf{u}}{c}\times\mathbf{B}\right). \quad \text{(III-9)}$$

The time and space integral of the right side of this equation can be written as

$$E_{j\times b} = \int dt\int dr^3\frac{\mathbf{u}}{c}\cdot\mathbf{J}\times\mathbf{B} \quad \text{(III-10)}$$

and is referred to as the $\mathbf{J}\times\mathbf{B}$ energy in the Z-pinch literature. It is the energy coupled to the plasma through the Lorentz force. More will be said on this term shortly. Next combine the ion internal energy equation (III-7) with the kinetic energy equation (III-9) to obtain a total ion energy equation

$$\frac{\partial}{\partial t}\left(n_i\varepsilon_i + \frac{1}{2}\rho u^2\right) + \nabla\cdot\left[\mathbf{u}\left(n_i\varepsilon_i + \frac{1}{2}\rho u^2 + p_i + p_e\right)\right] - p_e\nabla\cdot\mathbf{u} + \frac{\partial}{\partial x_\beta}(u_\alpha\Pi_{\alpha\beta}) + \nabla\cdot\mathbf{q}_i = -Q_{ie} + \frac{\mathbf{u}}{c}\cdot(\mathbf{J}\times\mathbf{B}) = -Q_{ie} + \mathbf{J}\cdot\left(-\frac{\mathbf{u}}{c}\times\mathbf{B}\right). \quad \text{(III-11)}$$

The total plasma energy equation is the sum of (III-11) and the electron energy equation (III-8)

$$\frac{\partial}{\partial t}\left[n_i(\varepsilon_i + \varepsilon_x) + n_e\varepsilon_e + \frac{1}{2}\rho u^2\right] + \nabla\cdot\left\{\mathbf{u}\left[n_i(\varepsilon_i + \varepsilon_x) + n_e\varepsilon_e + \frac{1}{2}\rho u^2 + p_i + p_e\right]\right\} + \frac{\partial}{\partial x_\beta}(u_\alpha\Pi_{\alpha\beta}) + \nabla\cdot\left[\mathbf{q}_i + \mathbf{q}_e - \frac{\mathbf{J}}{en_e}(n_e\varepsilon_e + p_e)\right] = -\Lambda + \mathbf{J}\cdot\mathbf{E}. \quad \text{(III-12)}$$

A complete presentation of (III-1)–(III-12), except for the term ε_x, can be found in [III-1], including the transport coefficients for the ion and electron thermal conductivities, ion viscosity stress tensor, and resistivity. The ion viscosity coefficients vary as $T_i^{5/2}/\overline{Z}^4$. The inverse and strong dependence on the ion charge state arises from the ion-ion cross section for Coulomb collisions. The viscous stresses are generally small for gases with a high $\overline{Z}$, except within shock waves where the velocity gradients are large. Lagrangian-based MHD simulations use an artificial viscosity to capture shock fronts, while many Eulerian-based simulations solve a total energy equation, including the magnetic energy, and use the Riemann jump conditions to capture shock fronts.

To derive Poynting's theorem, multiply Faraday's law (III-1) by the magnetic field

$$\frac{\partial}{\partial t}\left(\frac{\mathbf{B}^2}{8\pi}\right) + \nabla\cdot\left(\frac{c}{4\pi}\mathbf{E}\times\mathbf{B}\right) = -\mathbf{J}\cdot\mathbf{E}. \quad \text{(III-13)}$$

The energy density of the electric field ($\mathbf{E}^2/8\pi$) is small compared with that of the magnetic field by $\mathbf{u}/c$, as in (III-4), and will be neglected in the time derivative term.

Equations (III-12) and (III-13) show that the energy exchanged between the magnetic field and the plasma is through the $\mathbf{J}\cdot\mathbf{E}$ term. For the electric field of (III-4), there are two contributions to this term: 1) from the motional and 2) from the resistive component of the electric field. Integrating Poynting's theorem over a volume fixed in time and rearranging gives

$$\frac{d}{dt}\int\frac{\mathbf{B}^2}{8\pi}dr^3 + \int\frac{\mathbf{u}}{c}\cdot\mathbf{J}\times\mathbf{B}dr^3 + \int\eta_{\text{res}}\mathbf{J}^2dr^3 = -\oint\frac{c}{4\pi}\mathbf{E}\times\mathbf{B}\cdot\hat{\mathbf{n}}dA. \quad \text{(III-14)}$$

The middle term on the left is the $\mathbf{J}\times\mathbf{B}$ power from (III-10) and the third term is the resistive heating that matches the last term on the right in (III-8). The integral on the right is over the surface enclosing the volume and $\hat{\mathbf{n}}$ is the unit normal vector. For this volume, consider the cylinder of fixed radius r_o and an A–K gap ℓ, as in Fig. III-1. Take the region $r \geq r_o$ to be a vacuum, and assume that the power flow is axisymmetric. Since the total axial plasma current (I) is contained within r_o, by (III-3)

$$B_\varphi(r \geq r_o) = -\frac{2I}{rc}. \quad \text{(III-15)}$$

Manheimer [III-2] derives an expression for the electric field in the vacuum region. Assume that the electrodes in the surface

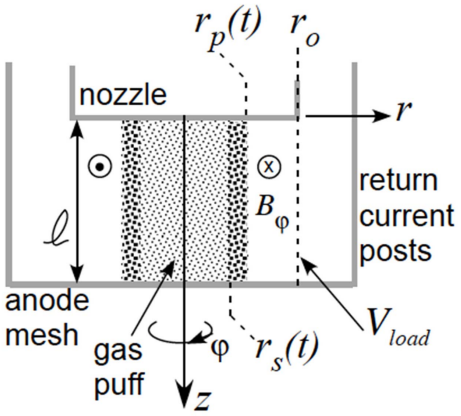

Fig. III-1. Coordinate system for the gas puff Z-pinch with initial outer radius r_o and plasma radius during implosion $r_p(t)$ and shell inner radius $r_s(t)$.

integral of (III-14) are perfect conductors. Then from (III-15)

$$-\oint \frac{c}{4\pi}\mathbf{E}\times\mathbf{B}\cdot\hat{\mathbf{n}}dA = I\int_0^\ell E_z(r_o,z,t)dz. \quad \text{(III-16)}$$

B. Coupling to a Circuit

The Z-pinch is connected to the outside world through the generator current I. We consider a simple equivalent circuit description of the generator described by a time-varying generator voltage $V_g(t)$ fed through a circuit of fixed inductance L_g and resistance R_g to the load

$$L_g\frac{dI}{dt} + R_g I + V_{\text{load}} = V_g(t). \quad \text{(III-17)}$$

The Z-pinch load consists of a time-varying inductor and resistor in series with voltage

$$V_{\text{load}} = \frac{d}{dt}(L_{\text{load}}I) + R_{\text{load}}I. \quad \text{(III-18)}$$

We use Poynting's theorem in integral form (III-14) to specify the load inductance and resistance. Following [III-3], the load inductance is defined in terms of the magnetic energy

$$\frac{1}{2}L_{\text{load}}I^2 = \int\frac{\mathbf{B}^2}{8\pi}dr^3. \quad \text{(III-19)}$$

This integral is over the volume within r_o of Fig. III-1, and includes any magnetic field within the plasma. Another approach to evaluating V_{load} is to use Faraday's law with L_{load} defined as the flux inductance [III-4]. The present approach through Poynting's theorem is more readily connected with energy conservation in simulation codes. The power flow into the pinch from (III-18) is

$$IV_{\text{load}} = \frac{d}{dt}\left(\frac{1}{2}L_{\text{load}}I^2\right) + \frac{I^2}{2}\frac{dL_{\text{load}}}{dt} + R_{\text{load}}I^2. \quad \text{(III-20)}$$

The first term on the right is time rate of change of the magnetic energy in the load (III-19). For the remaining terms, comparison of (III-20) with (III-14) and (III-16) demonstrates that

$$\frac{1}{2}I^2\frac{dL_{\text{load}}}{dt} = \int\frac{\mathbf{u}}{c}\cdot\mathbf{J}\times\mathbf{B}dr^3 \quad \text{(III-21)}$$

$$R_{\text{load}}I^2 = \int\eta_{\text{res}}\mathbf{J}^2dr^3 \quad \text{(III-22)}$$

$$V_{\text{load}} = -\int_0^\ell E_z(r_o,z,t)dz. \quad \text{(III-23)}$$

Equation (III-21) explicitly relates the $\mathbf{J}\times\mathbf{B}$ power from (III-10) to the time rate of change of the load inductance, as defined in (III-19). Equations (III-21) and (III-22) provide expressions for L_{load} and R_{load} in terms of the field and plasma conditions that can be used to solve for V_{load} in (III-18). Note that V_{load} is evaluated along the initial outer radius of the plasma. The constant inductance bounded by the annular region between r_o, the return current radius, and the arrow denoting the radial coordinate in Fig. III-1 is considered part of the generator inductance L_g. This evaluation of V_{load} permits a useful nondimensional formulation of the snowplow model in Section III-D.

In [III-1], a generalized Ohm's law was derived there from the electron momentum equation by dropping terms proportional to the electron mass

$$\mathbf{E} = -\frac{\mathbf{u}}{c}\times\mathbf{B} + \frac{\mathbf{R}_{\text{ei}}}{\text{en}_e} + \frac{1}{c}\frac{\mathbf{J}}{\text{en}_e}\times\mathbf{B} - \frac{1}{\text{en}_e}\nabla p_e \quad \text{(III-24)}$$

where in addition to the motional electric field (first term), there are, in order from left to right, the resistive, Hall, and grad p_e electric field components. The resistive electric field term $\mathbf{R}_{\text{ei}}$ has six tensor components, three varying with the current density, and three with the gradient of the electron temperature. Equation (III-4) contains only a scalar coefficient for the $\mathbf{R}_{\text{ei}}$ components proportional to the current density, and also neglects the Hall and grad p_e electric fields.

Regardless of the complexity of the electric field, such as displayed in (III-24), the last term on the right side of (III-8) indicates that all components of the electric field, other than the motional one, act as a source in the electron energy equation, which includes the electron thermal as well as the ionization and excitation energies in the ions. In general, this is Ohmic heating. From (III-9), the motional component of the electric field is clearly a source for the ion kinetic energy. Furthermore, from (III-11), this component is also a source for the ion thermal energy, and the mechanism for ion heating is the nonisentropic process of viscous heating in shock fronts during implosion of a Z-pinch. The term for viscous heating in (III-7) is contained in the terms on the left side of (III-11). The $\mathbf{J}\times\mathbf{B}$ energy, which appears as ion thermal and kinetic energies, is usually the dominant channel for energy coupling from the driver circuit to a Z-pinch. The dynamics and measurements of energy coupling will be addressed in Section VI-C, where other channels will be examined.

C. 0-D Snowplow Implosion Model

The snowplow model has a long history. The basic elements together with extensions can be found in [I-12], [II-10], and [III-5]–[III-7], as well as others. The version presented

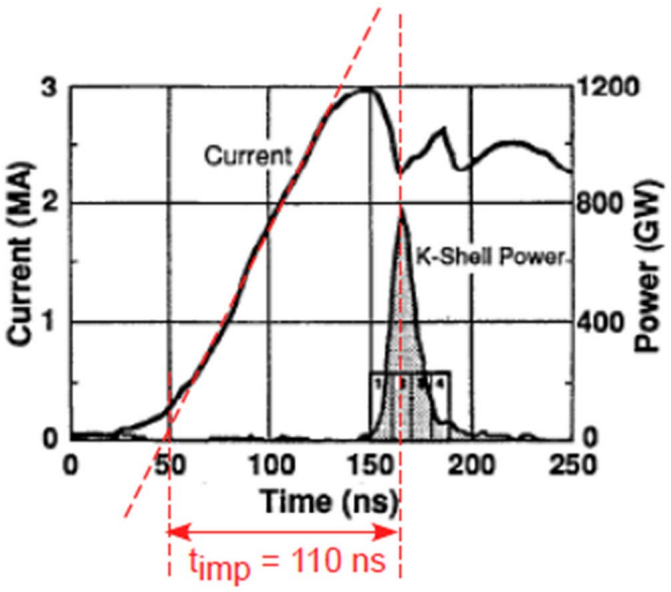

Fig. III-2. Example of the load current and the K-shell X-ray power pulse Ar gas-puff pinch of the Double-EAGLE generator. The initial gas profile was a shell of diameter 2.5 cm. The power pulse marks the time of pinch assembly on axis, i.e., stagnation, and the turnover in the current at stagnation is the inductive notch, or current bite. The implosion time is the duration between a temporal fiducial defined by the linear current rise and the peak of the K-shell pulse. Reprinted with permission from [III-11] (slightly adapted). Copyright 1994, AIP Publishing LLC.

here emphasizes the coupling of the pinch dynamics to a generator. There are several assumptions in the snowplow model as described here. First, as the pinch implodes, all of the material is swept up into a shell that moves with a radial velocity (u_p). This is depicted in Fig. III-1, where r_p is the outer plasma radius and r_s is the inner edge of the shell. Second, the pinch is axisymmetric with only an azimuthal magnetic field (B_φ) and an axial electric field (E_z). Third, the plasma is considered a perfect conductor, so that there is no magnetic field within the plasma, resistive heating can be ignored, and there is only a surface current. Outside of the plasma, (III-15) now becomes

$$B_\varphi(r \geq r_p) = -\frac{2I}{rc}. \tag{III-25}$$

Under the above assumptions for the snowplow model, we have from (III-19) and with $\eta_{\text{res}} = 0$

$$L_{\text{load}} = \frac{2\ell}{c^2}\ln\left(\frac{r_o}{r_p}\right) \text{ and } R_{\text{load}} = 0 \tag{III-26}$$

and the load voltage from (III-18) is

$$V_{\text{load}} = L_{\text{load}}\frac{dI}{dt} - \frac{2\ell}{c^2}\frac{u_p}{r_p}I. \tag{III-27}$$

The second term on the right contains the motional impedance, also called the inductive reactance, $(-2\ell/c^2)(u_p/r_p)$. As the pinch implosion proceeds, the velocity increases and its radius decreases. Thus, the inductive reactance (>0) can grow large enough to cause a turnover, or inductive notch, in the load current just before stagnation. This effect is illustrated in Fig. III-2, along with a graphical definition of the term implosion time. The plasma outer radius r_p is determined from the dynamics. Let $\rho_o(r, t = 0)$ be the initial density profile. In the 0-D feature of the snowplow model, all the mass is swept up into an infinitely thin shell ($r_s \rightarrow r_p$), so the continuity equation (III-5) for the time-dependent mass in the shell (M) becomes

$$\frac{dM}{dt} = -2\pi r_p u_p \rho_o \ell. \tag{III-28}$$

For the momentum equation (III-6), the magnetic pressure acting on the shell is $B_\varphi^2/8\pi$ and one finds

$$\frac{d}{dt}(Mu_p) = -\frac{\ell I^2}{r_p c^2}. \tag{III-29}$$

No energy equation is needed because in the 0-D approximation the plasma radiates away all of its internal energy.

The instantaneous power delivered from the generator to the load region is directly from (III-20)

$$\frac{d}{dt}E_{\text{load}} = IV_{\text{load}} = \frac{d}{dt}\left[\frac{\ell}{c^2}\ln\left(\frac{r_o}{r_p}\right)I^2\right] - \frac{\ell}{c^2}\frac{u_p}{r_p}I^2. \tag{III-30}$$

The first term on the right of (III-30) is the time derivative of the magnetic energy in the vacuum region of the load [see (III-19)]

$$\frac{d}{dt}E_{\text{vac}} = \frac{d}{dt}\left(\frac{1}{2}L_{\text{load}}I^2\right) = \frac{d}{dt}\left[\frac{\ell}{c^2}\ln\left(\frac{r_o}{r_p}\right)I^2\right] \tag{III-31}$$

and the second term is the time derivative of the $\mathbf{J}\times\mathbf{B}$ energy as defined in (III-10) and (III-21)

$$\frac{d}{dt}E_{j\times b} = \frac{1}{2}I^2\frac{dL_{\text{load}}}{dt} = -\frac{\ell}{c^2}\frac{u_p}{r_p}I^2. \tag{III-32}$$

From (III-29) and (III-32), one finds that in the 0-D snowplow model, the kinetic energy of the pinch is less than the energy coupled to the pinch

$$\frac{d}{dt}E_{\text{kin}} = \frac{d}{dt}\left(\frac{1}{2}Mu_p^2\right) = \frac{d}{dt}E_{j\times b} - \frac{u_p^2}{2}\frac{dM}{dt}. \tag{III-33}$$

In the context of the 0-D snowplow model, the difference must be the coupled energy lost to radiation during the run in. As a consequence of (III-33), if the initial gas distribution is initially a thin annulus where all the mass is swept up early while the velocity is low, then the kinetic energy is close to $E_{j\times b}$. This is why a thin annulus gas puff was initially thought to be the preferred configuration for producing radiation at stagnation, as will be discussed in later sections. On the other hand, if the gas is distributed throughout $0 \leq r \leq r_o$, then the second term on the right of (III-33) can be a significant fraction of $E_{j\times b}$ and the lost energy in the snowplow model is likewise significant. Calculations for the radiated energy and internal energy of the plasma require a treatment of the ionization kinetics as described for scaling laws in Section III-E and more generally in Section VI-B. Note that if the velocity is constant then the kinetic energy of the pinch would be only half of the $\mathbf{J}\times\mathbf{B}$ energy.

Based on dimensional analysis, the final velocity (u_f), i.e., the velocity at stagnation, is roughly the initial radius divided

by the implosion time $u_f \sim r_o/t_{\rm imp}$. From (III-29), the kinetic energy, final velocity, and implosion time vary with the total mass M_o and the peak current $I_{\rm pk}$ as

$$M_o u_f^2 \sim \frac{\ell}{c^2} I_{\rm pk}^2, \quad u_f \sim \frac{r_o}{t_{\rm imp}}, \quad M_o r_o^2 \sim \frac{\ell}{c^2} I_{\rm pk}^2 t_{\rm imp}^2. \quad \text{(III-34)}$$

The proportionality coefficients for these relations depend on the circuit properties, initial density profile, and the compression factor. They are presented in (III-49), (III-50), and (III-51), respectively.

D. Example

To demonstrate the behavior of the implosion for different density profiles, we integrate the set of equations for the 0-D snowplow model: (III-17) with (III-26) and (III-27) for the circuit and (III-28) and (III-29) for the dynamics. For the driving voltage, we adopt a profile characteristic of a water-line, pulsed-power generator

$$V_g(t) = V_{go}\psi(t/t_g) = V_{go}\left(\frac{t}{t_g}\right)^2 \exp[1-(t/t_g)^2] \quad \text{(III-35)}$$

where t_g is the time the drive voltage attains its maximum V_{go}. For inductive storage or linear transformer drivers a different circuit and voltage profile would be used, but the general results derived here are applicable to reasonable driving voltage waveforms. For the circuit parameters in (III-17) and (III-35), we take, as an example, generator properties that are characteristic of the water-line driver Double-EAGLE during the 1990s: $L_g = 35$ nH, $R_g = 0.3\ \Omega$, $V_{go} = 2.5$ MV, and $t_g = 95$ ns, along with a pinch length of $\ell = 4$ cm. We consider three different initial density profiles for the gas puff

$$\text{shell: } \rho_o = \begin{cases} \rho_{oo}, & \text{for } 3/4 \le r/r_o \le 1 \\ 0, & \text{otherwise} \end{cases} \quad \text{(III-36.a)}$$

$$\text{uniform fill: } \rho_o = \rho_{oo} \quad \text{(III-36.b)}$$

$$\text{central peak: } \rho_o = \frac{\rho_{oo}}{1+(10r/r_o)^{2.5}}. \quad \text{(III-36.c)}$$

The value of the density scale factor ρ_{oo} is determined from the total mass

$$M_o = \rho_{oo}\int_0^{r_o} \theta\left(\frac{r}{r_o}\right) 2\pi r dr \ell \quad \text{(III-37)}$$

where θ is one of the functions in (III-36).

Fig. III-3 shows three initial density profiles for the same conditions: $M_o = 300\ \mu$g and $r_o = 2$ cm. The value of ρ_{oo} from (III-37) is different for each choice in (III-36). The remaining panels in Fig. III-3 show the implosion histories for the radius (r_p), velocity ($u_p = dr_p/dt$), and current for each profile. The calculations were stopped when the compression factor r_o/r_f, where r_f is the final r_p value, has reached the canonical value of 10. u_f is the value of u_p at the time. The centrally peaked profile implodes earlier than the solid-fill or shell profile and the peak current is the least. As discussed below, the radius and/or mass are not well matched to the generator characteristics for this profile. The velocity curves indicate some notable behavior. The kink in the shell velocity occurs at the time all of the mass in the shell has been swept

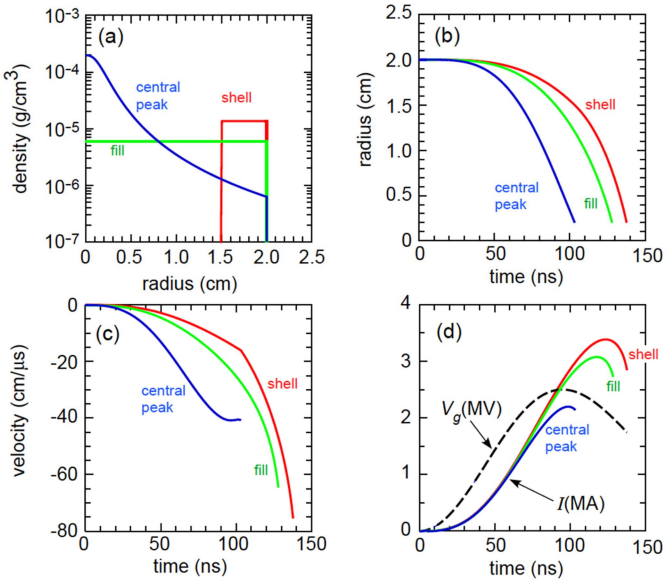

Fig. III-3. (a) Three initial density spatial distributions for: (III-36.a) shell in red; (III-36.b) fill in green; and (III-36.c) centrally peaked in blue. Shown in (b)–(d), respectively, are the radius, velocity, and current (solid) of the implosion from a 0-D snowplow calculation as a function of time. The specified generator voltage of (III-35) is also shown in (d) (dashed).

up and subsequently one sees an increase in the acceleration toward the axis. The velocity of the solid-fill has a smooth increase and comes to a final value that is close to that of the shell. Its velocity is greater in magnitude than that of the shell at a given time, but the final velocity is less because it reaches the compression factor sooner. The velocity of the peaked profile is quite different. Initially, it is larger than the other two at a given time. This is as expected because of the lower mass that has been entrained in the snow plow. But as the final radius is approached, the velocity becomes nearly constant because the density near the axis grows faster than $1/r^2$ by (III-36.c), leading to a balance between the mass accretion and the driving $\mathbf{J}\times\mathbf{B}$ force on the right side of (III-29). This difference in velocity produces a smaller motional impedance [see (III-27)] and hence a smaller inductive notch in the current.

A nondimensional formulation of the above equations is useful to succinctly present the dependency of the solutions on various parameters. Toward this end, let us define

$$I_g \equiv \frac{V_{go}t_g}{L_g} \text{ and } \Delta L \equiv \frac{2\ell}{c^2}\ln\left(\frac{r_o}{r_f}\right). \quad \text{(III-38)}$$

The first expression will be used to normalize the current and is derived from circuit parameters. The second expression is the inductance change in the load as the pinch implodes from its initial to its final position. Next we set

$$\begin{aligned} t &= \tau t_g, \quad r_p = \xi r_o, \quad M = \sigma M_o \\ u_p &= \upsilon\frac{r_o}{t_g}, \quad I = \imath I_g \\ E_{\rm kin} &= \varepsilon_{\rm kin}\Delta L I_g^2, \quad E_{\rm vac} = \varepsilon_{\rm vac}\Delta L I_g^2 \\ E_{j\times b} &= \varepsilon_{j\times b}\Delta L I_g^2 \end{aligned} \quad \text{(III-39)}$$

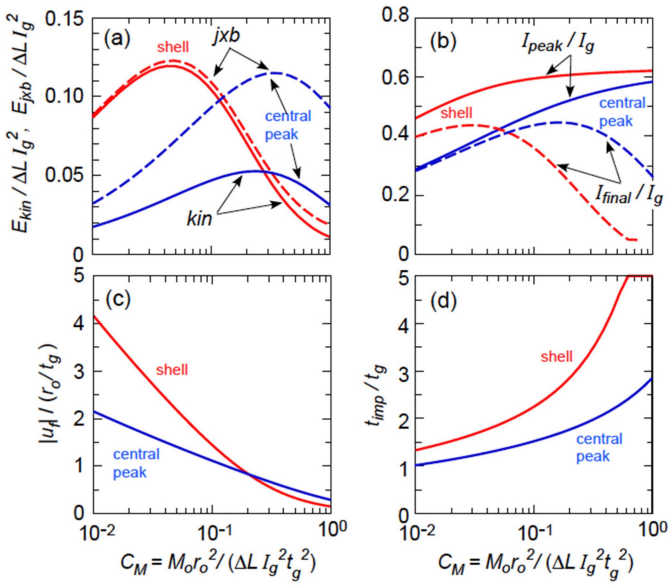

Fig. III-4. Normalized solutions for 0-D snowplow model as a function of the parameter C_M of (III-46). Shell (red) and centrally peaked (blue) refer to the initial density profiles in Fig. III-3(a). (a) Kinetic (solid) and $\mathbf{J}\times\mathbf{B}$ (dashed) energies. (b) Peak (solid) and final (dashed) currents. (c) Final velocities and (d) implosion times.

with lower case Greek characters representing nondimensional quantities.

Using these expressions, the circuit equation (III-17) with (III-18), (III-26), and (III-35) becomes

$$\frac{d}{d\tau}\left[\left(1+C_L\frac{\ln\xi}{\ln\xi_f}\right)\imath\right]+C_R\imath=\psi. \tag{III-40}$$

The equation for the swept-up mass (III-28) together with (III-37) can be written as

$$\frac{d\sigma}{d\tau}=-\frac{\xi\upsilon\theta}{\left(\int_0^1\theta\xi d\xi\right)} \tag{III-41}$$

and the momentum equation (III-29) becomes

$$\frac{d}{d\tau}(\sigma\upsilon)=\frac{1}{2}\frac{\imath^2}{\xi}\frac{1}{C_M\ln(\xi_f)}. \tag{III-42}$$

For the energies in (III-31)–(III-33), one finds

$$\frac{d\varepsilon_{j\times b}}{d\tau}=\frac{1}{2}\frac{\upsilon\imath^2}{\xi}\frac{1}{\ln(\xi_f)} \tag{III-43}$$

$$\varepsilon_{\text{vac}}=\frac{\imath^2}{2}\frac{\ln(\xi)}{\ln(\xi_f)} \tag{III-44}$$

and

$$\frac{d\varepsilon_{\text{kin}}}{d\tau}=\frac{d\varepsilon_{j\times b}}{d\tau}-\frac{1}{2}\upsilon^2\frac{d\sigma}{d\tau}C_M. \tag{III-45}$$

The constant parameters in (III-40), (III-42), and (III-45) are

$$C_L\equiv\frac{\Delta L}{L_g},\ C_R\equiv\frac{R_g t_g}{L_g},\ \text{ and } C_M\equiv\frac{M_o r_o^2}{\Delta L I_g^2 t_g^2}. \tag{III-46}$$

Fig. III-4 shows the variation of the normalized final kinetic ($\varepsilon_{\text{kin},f}$) and $\mathbf{J}\times\mathbf{B}$ ($\varepsilon_{j\times b,f}$) energies, peak ($\imath_{\text{pk}}$) and final ($\imath_f$), currents, final velocity (υ_f), and implosion time (τ_{imp}) as the parameter C_M is varied for both the shell and centrally peaked profiles. For these calculations, we used the values from the sample circuit mentioned after (III-35): $C_L=0.52$ and $C_R=0.81$, with a compression ratio of 10. The most significant point is that the coupled energies $\varepsilon_{j\times b,f}$ and $\varepsilon_{\text{kin},f}$ from (III-39) display a peak in Fig. III-4(a) as a function of C_M. The simplest way to understand the abscissa axis is to consider the circuit properties (I_g and t_g) and inductance change ΔL as fixed. Then the quantity $M_o r_o^2$, which characterizes the load, increases along the abscissa. For $M_o r_o^2$ smaller than the value at which $\varepsilon_{j\times b,f}$, or $\varepsilon_{\text{kin},f}$, is a maximum, the implosion occurs before the maximum current that the circuit can deliver, as seen in Fig. III-4(b). For $M_o r_o^2$ larger than the value giving the peak energy, the plasma implosion is delayed until after the peak current at which time the current decreases because of the turnover in the driver voltage. In this case, the final kinetic and $\mathbf{J}\times\mathbf{B}$ energies are low because the final current in Fig. III-4(b) and the final velocity in Fig. III-4(c) are low [see (III-32), (III-33)]. In the extreme case of $M_o r_o^2\to\infty$, there is no motion of the load and no coupled energy. Thus, there is an optimal value of C_M, which couples the maximum energy to the load and this optimal value is different depending on the density profile, the circuit parameters, and the compression ratio. For fixed circuit parameters, one can equivalently say that there is an optimal value of $M_o r_o^2$ at which the generator is matched to the load.

Fig. III-4(a) also shows notable differences between the two initial density profiles. First the C_M value where the maximum $\mathbf{J}\times\mathbf{B}$ energy occurs is an order of magnitude greater for the centrally peaked than for the shell profile. Because the mass is more concentrated near the axis for the former than the latter profile, the implosion time is shorter as shown in Fig. III-4(d). Thus, for the distributed profile one must move to a larger $M_o r_o^2$ to take advantage of the maximum current that the circuit can deliver. Second, for the centrally peaked profile, $\varepsilon_{j\times b,f}$ is significantly larger than $\varepsilon_{\text{kin},f}$, while for the shell the two energies are almost the same, and would be the same for an infinitely thin shell of the same mass. Solutions for the uniform solid-fill profile lie between the two curve sets displayed in this figure. As mentioned above, all of the difference $\varepsilon_{j\times b,f}-\varepsilon_{\text{kin},f}$ is assumed to be radiation loss in the 0-D snowplow model. In more accurate models that include the equations for the ion thermal (III-7) and electron (III-8) energies, the energy difference is only partly lost to radiation with the remainder in plasma internal energy. In particular, according to (III-11), the $\mathbf{J}\times\mathbf{B}$ energy produces ion heating (through the viscosity in shock waves) in addition to kinetic energy. As the pinch assembles on axis, the ion energy from the $\mathbf{J}\times\mathbf{B}$ coupling is transferred to the electrons through thermal equilibration Q_{ie}, and the electrons produce the radiation through ionization and excitation. If at stagnation there is a rapid rise in density, then ion–electron thermal equilibration rate can also be rapid because this rate varies as the square of the density (see the text following (III-7). This has important implications for achieving K-shell radiation from large-radius distributed density profiles, as discussed in Sections VI-A and VI-C.

It is important to emphasize that the proceeding discussion applies to the energy delivered to the pinch

(be it E_{kin} or $E_{J\times B.}$). For a particular application, e.g., maximizing K-shell radiation, the energy per ion must be optimized. For example, given a value of $M_o r_o^2$ that maximizes either it E_{kin} or $E_{J\times B.}$, the individual values of M_0 and r_0 must be found that maximize the K-shell radiation for a particular species. This is discussed in the following section.

The calculations for Fig. III-4 were performed for an assumed compression factor of 10. All the curves shift only slightly to the left if instead one assumes a compression of 20 because the ordinate is normalized to the change in inductance. This limited change arises from the use of ΔL defined in (III-38) and in the normalizations of (III-39). If the length of the pinch is increased while keeping the same mass per unit length and other circuit properties fixed, then the parameter C_M in (III-46) does not change. However, L_g increases due to the added inductance between r_o and the return current posts, which increases linearly with ℓ.

Each of the solution curves in Fig. III-4 depends on the parameter C_M and the initial density profile: $\varepsilon_{j\times b,f} \equiv \varepsilon_{j\times b,f}(C_M, \rho_o)$, and similarly for the dimensionless kinetic energy $\varepsilon_{\text{kin},f}$, final velocity v_f, peak current ι_{pk}, and implosion time τ_{imp}. Then, from (III-39), we can write

$$E_{j\times b,f} = \varepsilon_{j\times b,f}\Delta L I_g^2, \quad E_{\text{kin},f} = \varepsilon_{\text{kin},f}\Delta L I_g^2$$
$$u_f = v_f(r_o/t_g), \quad I_{\text{pk}} = \iota_{\text{pk}} I_g, \quad t_{\text{imp}} = \tau_{\text{imp}} t_g. \tag{III-47}$$

These relations can be readily combined into

$$E_{j\times b,f} = \left(\frac{\varepsilon_{j\times b,f}}{\iota_{\text{pk}}^2}\right)\Delta L I_{\text{pk}}^2 \tag{III-48}$$

$$\frac{1}{2}M_o u_f^2 = \left(\frac{\varepsilon_{\text{kin},f}}{\iota_{\text{pk}}^2}\right)\Delta L I_{\text{pk}}^2 \tag{III-49}$$

$$u_f = (v_f \tau_{\text{imp}})\frac{r_o}{t_{\text{imp}}} \tag{III-50}$$

$$M_o r_o^2 = \left(\frac{2\varepsilon_{\text{kin},f}}{\tau_{\text{imp}}^2 v_f^2 \iota_{\text{pk}}^2}\right)\Delta L I_{\text{pk}}^2 t_{\text{imp}}^2 \tag{III-51}$$

which specify that the coefficients in the relations of (III-34) depend on C_M, the initial density profile, and ΔL. Note that t_{imp} as used in (III-50) and (III-51) for the 0-D snowplow model is the duration from the time of zero generator voltage to the time when r_p reaches the chosen r_f. This will be longer than the implosion times reported for some experiments as described in Fig. II-3.

E. Scaling Laws for K-Shell Radiation

One of the primary applications of research on gas-puff Z-pinches has been the improvement of K-shell radiation sources. In this section, we review some of the scaling laws developed primarily at NRL to understand the connection between the coupled energy and the radiation yield. Consider a species of atomic number Z_A, and following [III-8], we estimate the energy per ion that must be invested in order to produce strong K-shell radiation. First, based on ionization equilibrium in hydrogenic ions, the electron temperature for which K-shell occupation and excitation is significant scales as

$$T_e(\text{K-shell}) \sim 0.27 Z_A^{2.9}\ \text{eV}. \tag{III-52}$$

For $T_i = T_e = T$, the thermal energy per ion of such a plasma is $3/2(1+\overline{Z})T$, where $\overline{Z}$ is the mean charge state. If this state is H-like, $\overline{Z} = Z_A - 1$ and the thermal energy per ion scales as

$$E_{\text{th}}(\text{K-shell}) \sim 0.4 Z_A^{3.9}\ \text{eV/ion}. \tag{III-53}$$

Second, the ionization energy expended to produce K-shell ions must also be included in the invested energy. The sum of the ionization energies starting from the neutral state and ending with the K-shell fractional populations of 50% He-like and 50% H-like can be approximated as

$$E_{\text{ioniz}}(\text{K-shell}) \sim 3.83 Z_A^{2.64}\ \text{eV/ion} \tag{III-54}$$

for Z_A between Ne and Kr. Thus, the minimum energy invested to produce a strongly radiating K-shell ion is the sum of (III-53) and (III-54), or approximately [III-9]

$$E_{\min}(\text{K-shell}) \sim 1.012 Z_A^{3.662}\ \text{eV/ion}. \tag{III-55}$$

A fundamental concept for the scaling laws is the relation between the energy coupled to the pinch and $E_{\min}$. Suppose all the energy coupled to the plasma during implosion is kinetic so that the energy available per ion is $1/2\ m_i u_f^2$, where m_i is the mass of the ion and u_f is its final velocity. Then Whitney *et al.* [III-8] and others (see the following) have made extensive use of the ratio:

$$\eta \equiv \frac{\frac{1}{2}m_i u_f^2}{E_{\min}(\text{K-shell})} \tag{III-56}$$

in K-shell scaling laws. In practice, η needs to be >1 because energy is expended in excitation with subsequent radiation while the plasma is undergoing ionization.

Let us apply (III-56) to the snowplow solutions of the previous two sections. For Ar with $E_{\min} = 40$ keV/ion, $u_f = 62.2$ cm/μs is required for $\eta = 2$. For the shell profile, the coupled energy maximizes at $C_M = M_o r_o^2/\Delta L I_g^2 t_g^2 \approx 0.05$ from Fig. III-4(a). This corresponds to $|u_f|t_g/r_o \approx 2.2$ from Fig. III-4(c). For $t_g = 95$ ns as mentioned below (III-35), one would require an initial shell radius of ~2.7 cm in order to attain the required velocity. Again from Fig. III-4(a), for the centrally peaked profile, the coupled kinetic energy peaks at $C_M = M_o r_o^2/\Delta L I_g^2 t_g^2 \approx 0.25$, but $|u_f|t_g/r_o$ is only ~0.75. In this case, the initial radius to attain u_f is much larger, namely, 7.9 cm. If the difference between the kinetic energy and $E_{j\times b}$ was not lost to radiation, as assumed in the snowplow mode, but kept in the plasma as internal energy, then the energy available for ionization to the K-shell would be as large for the centrally peaked profile as for the shell. [For the remainder of this review, internal energy will refer to the sum of the thermal, excitation, and ionization energies: $n_i(\varepsilon_i + \varepsilon_e) + n_e\varepsilon_e$ as in (III-11).] An extension of the definition in (III-56) to address the $\mathbf{J}\times\mathbf{B}$ energy is simply from [III-10]

$$\eta^* \equiv \frac{m_i E_{j\times b}/M_o}{E_{\min}(\text{K-shell})}. \tag{III-57}$$

In the 0-D snowplow model, η^* can be evaluated from the first relation in (III-48)

$$\eta^* = \left(\frac{\varepsilon_{j\times b,f}}{\iota_{\rm pk}^2}\right)\frac{m_i}{M_o}\frac{\Delta L I_{\rm pk}^2}{E_{\rm min}(\text{K-shell})}. \qquad \text{(III-58)}$$

More generally, (III-10) would need to be used for $E_{\rm jxb}$.

The above examples indicate that moving out in radius, but lowering M_o to keep $M_o r_o^2$ constant, would give the same coupled energy but at a higher velocity and a higher η^*. This would seem to be the most direct way of achieving K-shell radiation from Ar on a ~1-MA generator or from Kr on a large current machine. However, there are consequences and tradeoffs to consider. The first is that implosions from large radii can be MHD unstable, so that the 0-D model is not applicable. This problem will be discussed in Section V-C. A second tradeoff is that moving out in radius with $M_o r_o^2$ fixed lowers the number of radiators. This feature was observed for the Ar K-shell yield on Double-EAGLE [III-11]. The tradeoff between mass and radius can be addressed with a model of the ionization and excitation kinetics, which is beyond the simple 0-D model but has been treated in the work on scaling laws.

The ionization/excitation kinetics for Z-pinch K-shell radiation sources does not satisfy LTE because the density at stagnation is too low. The criterion for LTE is [III-12]

$$n_e > 7\times 10^{18}\overline{Z}^7 (T/\text{IP}_Z)^{1/2}\ \text{cm}^{-3}$$

where $\overline{Z}$ is the mean ionization state and IP_Z is the ionization potential of that state. For K-shell temperatures specified by (III-52), the required electron density even for Ne is many orders of magnitude beyond that achieved in any pinch experiment. The appropriate treatment for the ionization dynamics is that of collisional-radiative (CR) kinetics. For a two-level ion in a uniform plasma with ground-state and excited-state densities n_1 and n_2, respectively, the population of the excited state would be determined by

$$\frac{dn_2}{dt} = n_e n_1 \text{CX}_{12} - n_e n_2 \text{DX}_{21} - n_2 A_{21} P_{21} \qquad \text{(III-59)}$$

where CX_{12} and DX_{21} are the electron collisional excitation and de-excitation rates (functions of electron temperature), respectively, A_{21} is the radiative decay rate, and P_{21} is the probability-of-escape for the transition. The latter would be determined by a radiative transport calculation. In the optically thin limit, P_{21} would be unity. For a pulselength of Δt, the radiative yield from this two-to-one transition would be

$$Y_{21} = n_2 h\nu_{21}(A_{21}P_{21})\pi r_f^2 \ell\,\Delta t \qquad \text{(III-60)}$$

where $h\nu_{21}$ is the energy of the transition. Under the conditions of CRE, where equilibrium means $d/dt = 0$, (III-59) and (III-60) can be combined as

$$Y_{21} = \frac{n_e n_1 \text{CX}_{12}}{1+(n_e \text{DX}_{21}/A_{21}P_{21})} h\nu_{21}\pi r_f^2 \ell\,\Delta t. \qquad \text{(III-61)}$$

The term $n_e \text{DX}_{21}/A_{21}$ in the denominator is the quenching ratio, or the ratio of collisional de-excitation to radiative decay. If this term was large or the plasma very optically thick (P_{21} very small), the populations would be in LTE since collisions would dominate the kinetics as can be seen from (III-59).

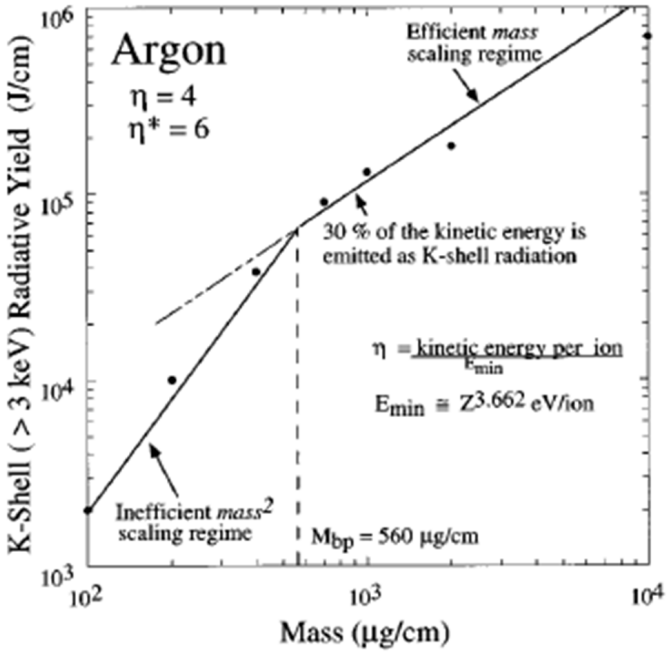

Fig. III-5. Calculated Ar K-shell yield from 1-D simulation with phenomenological transport coefficients as a function of the mass loading. The mass break point ($M_{\rm bp}$) where the yield scaling transitions from M_o^2 to M_o is denoted. Reprinted with permission from [III-10] (slightly adapted). Copyright 1996, AIP Publishing LLC.

For Z-pinches, the quenching ratio for K-shell emission is $\ll 1$. The densities in the numerator of (III-61) both scale as the load mass, and so for low n_e (low mass load) the yield should scale as M_o^2. Of course, this cannot hold indefinitely as the yield must be limited by the kinetic energy coupled to the pinch. Beyond some load mass, the radiation can at best grow with the total kinetic or $\mathbf{J}\times\mathbf{B}$ energy, and the radiation would scale M_o. This point is discussed further as follows.

Whitney *et al.* [III-8] first used a 1-D radiation MHD (RMHD) code to determine how the K-shell yield (Y_K) varies with η and evaluate the mass break point, which is the mass where the yield transitions from M_o^2 to M_o scale. This paper was done for Al and used 41 singly excited levels in a CRE model instead of the single-level system outlined earlier. The ionization kinetics and a probabilistic radiation transport were self-consistently coupled to the Lagrangian MHD code. To obtain reasonable results using a 1-D simulation, and not suffer radiative collapse, the current was turned off when the plasma began to stagnate. Thornhill *et al.* [III-10], [III-13] used phenomenological transport coefficients to limit the unphysical densities and broaden the narrow radiation pulses produced by simple 1-D simulations. The classical transport coefficients for resistivity and thermal conduction were enhanced, which heats the plasma, softens the implosion, and increases the radiation pulsewidth. The multipliers were determined by matching data to existing Al and Ar pinches. Fig. III-5 shows the curve for $\eta = 4$ (equivalent in these models to $\eta^* = 6$) and the mass break point determined with this model for Ar. Here, the gas puff was assumed to begin as a thin shell, but because the 1-D RMHD simulation could follow the diffusion of the

magnetic field into the plasma during implosion the integral in (III-10) for the $\mathbf{J} \times \mathbf{B}$ energy could be explicitly calculated. Above the mass break point $M_{\rm bp}$, the simulations showed that $\sim$30% of $E_{j\times b}$ appeared as K-shell radiation. This region was termed the efficient scaling region where the yield scaled linearly with the coupled energy, which in turn scales with M_o. Below $M_{\rm bp}$, where $Y_{\rm K}$ varies as M_o^2, is called the inefficient region because the yield was less that the maximum fraction of coupled energy. The purpose of scaling relations is to estimate potential results beyond the experimental capabilities at the time. Based on the developed scaling relations, it was estimated that if one couples 150 kJ/cm to a 1-mg/cm load, then the Ar K-shell yield would be $\sim$40 kJ/cm for $\eta^* = 1.5$. The corresponding scaling for K-shell Kr was also shown in [III-10]. Of course, much more coupled energy is needed to produce Kr scaling because of the large radiation losses associated with the numerous atomic levels, and the analysis suggested that the assumption of equilibrium kinetics may not be valid for Kr.

An alternative approach to using a simulation tool for establishing K-shell scaling was developed in [III-14] and [III-15]. This is a phenomenological approach where equations for a two-level ion, as in (III-59)–(III-61), were used to describe the kinetics for a K-shell resonant transition. The total coupled energy at stagnation was taken to be the sum of internal + losses (in neglected processes) + K-line yield. Various approximations for these terms, along with an additional relationship for the implosion time scaling with current and mass (see III-34), allowed them to obtain closed form expressions for the K-line yield in the weak emission (inefficient) regime and the strong emission (efficient) regime, and for a smooth transition between these regimes. The model was validated for neon experiments on the Hawk generator [III-16], [III-17], and for Al wire arrays on Saturn [III-14]. The model was also successfully compared with data from a variety of Ar gas-puff experiments for short- and long-implosion times [III-15]. The optimum mass for maximum K-shell radiation is derived for all regimes. In the inefficient regime, the K-shell yield is not an important factor in the overall energy balance leading to the following:

1) the optimum mass for K-shell yield scales as $E_{j\times b} \sim I_{\rm pk}^2$ [see (III-48); this is the same scale needed to match the generator output [see (III-51)]];
2) the K-shell radiation scales as $(E_{j\times b})^2 \sim I_{\rm pk}^4$.

These scalings have important implications when increasing the current while keeping all the other generator parameters and Z_A fixed (see Section V-D).

Although the above ideal scaling laws all contain the essence of the essential physics that affect the changeover from $M_o^2(I_{\rm pk}^4)$ to $M_o(I_{\rm pk}^2)$ scaling, it was recognized that none of these relations was very reliable from the standpoint of their ability to accurately predict the K-shell scaling as a function of coupled energy, load mass, and atomic number for all possible load configurations. The reason for this is that every load has its own nonideal physics associated with it, such as different initial density distributions, and the fact that large-radius loads are more prone to the MRT instability described in Section V-C. All of these individual load characteristics will ultimately affect how coupled energy is thermalized and radiated during the stagnation phase of an implosion and in turn will affect the K-shell yield scaling characteristics for that particular load design.

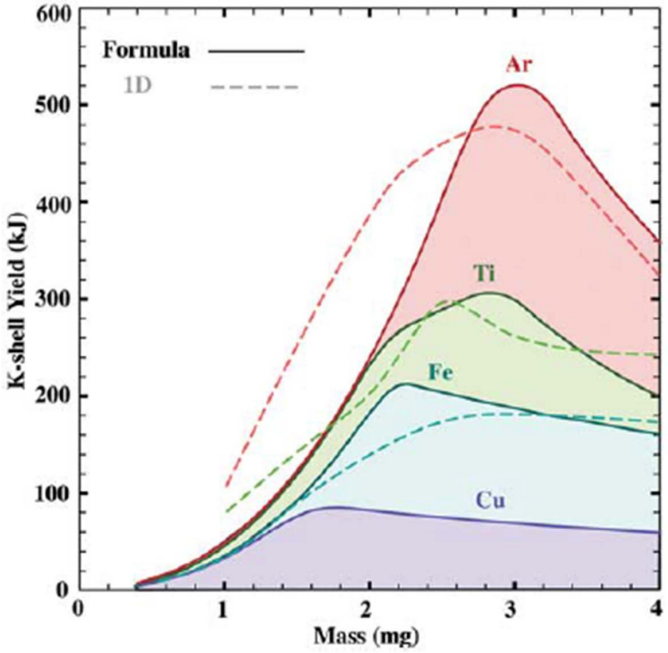

Fig. III-6. Predicted K-shell yields for the ZR generator from an empirical scaling law and 1-D phenomenological simulations. The Ar estimates assumed a double-shell gas puff nozzle of outer radius 4 cm and >25 MA into the load. Reproduced from [III-18].

To account for the particular nonideal load behavior that is associated with any specific load design, an empirical scaling relationship was developed in [III-18] that grounded the relation to existing experimental results through a factor determined from previous experiments using similar load designs. This empirical scaling was developed in preparation for experiments on the ZR generator. The resultant yields from this revised scaling law and 1-D phenomenological simulations, shown in Fig. III-6, suggest that $\sim$500 kJ of Ar K-shell was possible. We now know that these calculations from 2006 turned out to be excessive, primarily because the ZR machine was unable to deliver the projected 25-MA currents to the load. For large-current generators (>6-MA short-circuit current), the most significant unknown that can affect K-shell yields is the load current. Based on simulations coupling a transmission line circuit model to an RMHD code, Jennings *et al.* [III-19] found that there must be multiple current losses in the ZR generator to account for the observed electrical data. Because of unknown current losses that occur prior to the load region, there is large uncertainty in the amount of current that is coupled to the load. Understanding and reducing these current losses is a priority in present-day Z-pinch and pulsed-power research.

For a better understanding of the scaling of high-Z gas puffs with current and atomic number, there are theory and experimental efforts that can be pursued. Being able to compute that factor η^* for Kr would be useful for determining the optimum

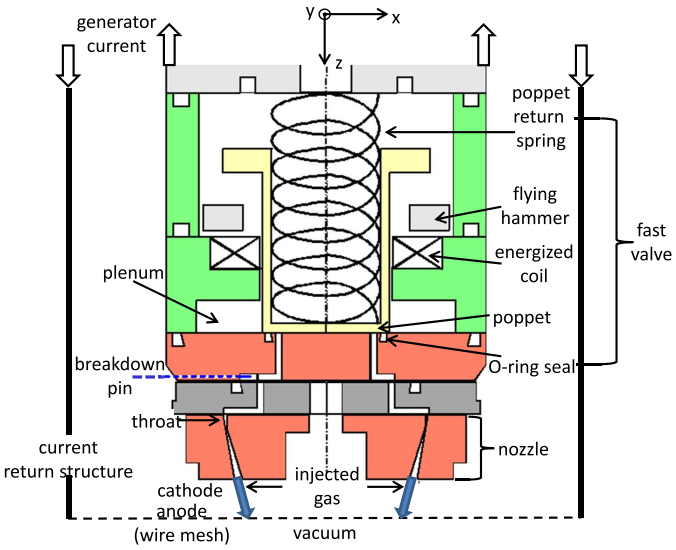

Fig. IV-1. Schematic of conical-annular gas puff nozzle similar to that used on the Phoenix pulsed-power generator. The return current structure is azimuthally symmetric. Coordinate system is defined at the top of the figure. The xy plane where $z = 0$ is located at the nozzle exit plane. Adapted from [IV-2] and [IV-3].

mass for maximum K-shell emission. To do this, the highly complex L- and M-shell atomic physics must be delineated. Also, to find the optimum gas-puff density distribution for a given generator, it would be useful to be able to systematically vary the gas-puff radius as well as the mass for a fixed radius, all the while keeping the product $M_o r^2$ constant to ensure that the maximum generator current is accessed.

IV. Initial Conditions of a Gas Puff

The properties of the gas-puff nozzle determine the radial and axial mass distributions of the neutral gas that is then ionized, heated, and compressed. As discussed in Section III-D for Fig. III-4, the initial conditions determine the ability of the pulsed-power generator to couple its available energy to the imploding pinch (i.e., matching the load to the generator). The initial conditions can also influence the stability of the implosion, and the subsequent temperature and density of the stagnated plasma. The gas injected into the vacuum between the electrodes of the pulsed-power generator should not find its way into the power feed as this could lead to power flow losses. As a very important practical matter, the pulsed-power generator must be given a trigger signal from the nozzle so that the appropriate time-dependent gas distribution exists between the generator electrodes at the time the generator is discharged.

A. Gas-Puff-Assembly Hardware, Design, and Operation

Here, we describe typical gas-puff-assembly hardware. A representative gas-puff assembly is illustrated in Fig. IV-1, which is a simplified cross section of a design that was used on the Phoenix generator [IV-1]–[IV-3], [III-17]. We discuss newer designs in what follows, but refer to the gas-puff assembly in Fig. IV-1 to describe the major gas-puff-system components. The gas is stored, prior to injection between the electrodes, in the plenum that is sealed from the vacuum downstream of it. The plenum is usually pressurized by a gas line (not shown in the figure) that connects the assembly to a gas reservoir far from the gas-puff region. Depending on the mass required to obtain the desired gas distribution and the pulsed-power generator current and rise time (see Sections III-C and III-D), plenum pressures typically vary between 10 and 100 psia.

The fast valve must open quickly and symmetrically to allow the gas in the plenum to flow reproducibly downstream through the throat and the nozzle and be subsequently injected between the pulsed-power generator electrodes. The valve should also close quickly to avoid continual injection of neutral gas into the main vacuum chamber. Such fast valves have been used in a variety of experiments and their design has evolved over time. For the gas-puff system illustrated in Fig. IV-1, the fast acting valve [IV-4] consists of a poppet, a coil, a flying hammer, and a poppet return spring. A current pulse through the coil (generally several kiloamperes with a rise time of tens of microseconds) causes the flying hammer (usually aluminum) to accelerate upward because the current in the coil and the induced current in the hammer repel each other. An *ab initio* analysis of this process can be found in [IV-5] and an experimentally verified model relating the current in the coil to axial motion can be found in [IV-6] and [IV-7]. The mechanical impulse thus imparted to the poppet momentarily lifts it off the O-ring seal it makes with the plenum, causing the gas to flow out into the nozzle region. Variations on this fast-valve approach include: making the hammer from soft iron so that it is attracted to the energized coil rather than repelled by it [IV-8], [IV-9], eliminating the poppet and having the flying hammer itself make and break the plenum seal directly [IV-5], [IV-6], [IV-10]–[IV-17], or having a low-mass coil serve as the plenum seal as well as be accelerated to break the seal (flying coil) [IV-7]. The poppet spring helps to maintain a good seal between the plenum and vacuum and provides additional force to close the valve. Valve opening times (closing times) of $\sim$100 μs (500 μs) have been achieved and are representative of what is currently fielded.

It is interesting to note that other mechanisms have been used to achieve a fast opening valve that have not proved useful for gas-puff Z-pinch applications, but might for other applications. Some of these mechanisms include the following.

1) Mechanically dropping a weight to release the valve seal [IV-10].
2) Using magnetic forces to distort/bend the valve seal [IV-18].
3) Releasing an over-compressed seal by electrically exploding a wire [IV-19].
4) Electrically rupturing a thin diaphragm (spark puncture) separating the plenum from the vacuum [IV-20].
5) Using magnetic forces to push a preionized gas in the plenum though very narrow silts that are differentially pumped with respect to the main vacuum chamber [IV-21].

Referring again to Fig. IV-1, the breakdown pin is a dc-biased electrode ($\sim$1 to a few kilovolts, usually negative), insulated from the gas-puff assembly and inserted into the

gas path [IV-8]. At a particular value of the gas density that depends on the applied voltage, a breakdown occurs. The resultant voltage pulse is used as a timing marker for triggering the pulsed-power generator. The neutral gas radial and axial distributions (see Section IV-B) are usually measured off line so as to not occupy generator pulsing time needed for other applications. Upon synchronizing the time history of the measured distribution with the breakdown pin signal, the current from the pulsed-power generator can be applied at the time when the desired distribution exists between the electrodes. This approach also ensures that there actually is gas between the electrodes before the pulsed-power generator is triggered, avoiding an open-circuit load and the associated, possibly catastrophic, hardware damage. This approach of course depends on the reproducibility of the fast valve opening and the timing between the breakdown-pin pulse and gas-flow conditions (the breakdown pin jitter). Measured gas flows that are synchronized with the breakdown pin are quite reproducible. Such synchronization reduced the spread in arrival time of gas flow measured 1 cm from the nozzle face from 50 to 5 μs, compared with the gas flow rise time of several 100 microseconds [IV-22]. While the breakdown pin itself can change its characteristics with repeated use and requires periodic refurbishment, it is currently the standard method for achieving correct trigger timing between the pulsed-power generator and the desired gas distribution. To provide redundancy, one can install additional breakdown pins (both in the nozzle and at the anode plane) [IV-7], [IV-23] and monitor the coil current [IV-7], [IV-22]. Although not quite as straightforward to field, a laser interferometer measuring the actual gas density as it exits the nozzle [IV-24] was successfully demonstrated as a trigger for the pulsed-power generator [IV-25].

The next components in the gas-puff assembly are the throat and nozzle. The throat is an azimuthal aperture of small area (relative to the exit area of the nozzle) that defines a region of so-called choked flow. The gas speed at this point is the sound speed as determined by the gas temperature and the mass of the gas molecule or atom in the plenum. Conservation of mass requires that the speed of the gas exiting the throat be supersonic. The mass per unit length that is injected through the nozzle is proportional to the product of the plenum pressure and throat area. The throat opening must be azimuthally uniform to provide an azimuthally symmetric flow into the nozzle. Azimuthal asymmetries can lead to limitations on the minimum final radius (or, equivalently, maximum compression ratio) [IV-26]. Ensuring this uniformity can be a hardware-design challenge (see below).

The last element of the gas-puff assembly illustrated in Fig. IV-1 is the nozzle proper. The purpose of the nozzle is to form a nonturbulent, supersonic, axially directed, gas flow into the interelectrode region. The remainder of this section will review different types of gas-puff assemblies, nozzle designs, and nozzle geometries that have been developed as understanding has evolved of what mass density profiles are optimal for creating a hot, dense plasma at stagnation (see Section VI for details of physics results). We review methods for measuring the mass density profile and compare some measurements with hydrodynamic gas flow calculations in Section IV-B.

The nozzle portion of the gas-puff assembly illustrated in Fig. IV-1 is an example of a conical nozzle design that produces a single annular shell [IV-27], [IV-28]. A variation of this conical nozzle design (but not the actual gas-puff assembly shown in Fig. IV-1) was used successfully on several water-line generators: PITHON ($\sim$3 MA in $\sim$ 100 ns, Ar) with OD $\approx$ 3 cm [II-5] and Gamble II ($\sim$1 MA in 60 ns, Ne) with OD $\approx$ 3 cm [II-20], [IV-29]. The actual gas-puff assembly shown in Fig. IV-1 was used on Phoenix ($\sim$3.5 MA in 100 ns, Ar) with OD $=$ 3.5 cm [IV-1]. A variation of this conical nozzle design was also used on the direct-drive capacitor-bank UCI pinch facility ($\sim$500 kA in 600 ns) with OD $=$ 4 cm [II-4] and on the Hawk inductive storage generator ($\sim$0.6 MA in $\sim$ 100 ns using a plasma opening switch, discussed in Section V-D) with OD $=$ 2.0, 3.5, and 5.0 cm [III-16]. The term conical refers to the shape of the nozzle walls, i.e., the walls are straight as in a cone. This shape is meant to produce an azimuthally symmetric, annular, or shell/ring-like gas distribution, which was thought to be important for maximizing the kinetic energy of the implosion (see Section III-D). Because the gas-puff nozzle can experience a high-current density, it is often replaced after each high-current discharge. This nozzle design is fairly straightforward to manufacture compared with the contoured nozzle walls described below. Mach numbers (ratio of gas flow speed to sound speed of the gas in the plenum) as high as 3.5 were measured [IV-27]. Note the inward tilt angle of the nozzle in Fig. IV-1. The purpose of this feature is to compensate for radial expansion by the gas as it moves away from the nozzle face. In practice, this type of nozzle results in a mass distribution with axial nonuniformities, with the gas near the nozzle being annular while 1.5–2-cm downstream from the nozzle the radial distribution is filled in (more distributed in radius). The mass per unit length can vary with the axial distance from the nozzle as a result of a time-changing flow rate from the nozzle [III-16], [III-17] (also see Section IV-B). Axial nonuniformity can result in stagnation occurring at the optimum time for only a portion of the pinch length, reducing the radiation production efficiency [III-16], [III-17]. It can also lead to the so-called zippering phenomena (see Section V-B), where the implosion along the z-axis varies in time, possibly giving rise to maximum K-shell emission varying with time and axial location (see [IV-30]). Zippering can produce a much longer radiation pulse than expected from a 1-D implosion [IV-31]. The desire for better control over the radial and axial gas distribution led to the development of contoured nozzle surfaces. The shape of these contours can be determined analytically by the so-called method of characteristics or computationally by a fluid code.

As discussed in Section V-C, it became clear the MRT instability would not allow high-density, axially uniform stagnation on axis from the large-radius, annular gas distributions (see Sections V-C–V-E) that convert all the $E_{j\times b}$ implosion energy into enough kinetic energy (see Sections III-D and III-E) to heat electrons to the temperature

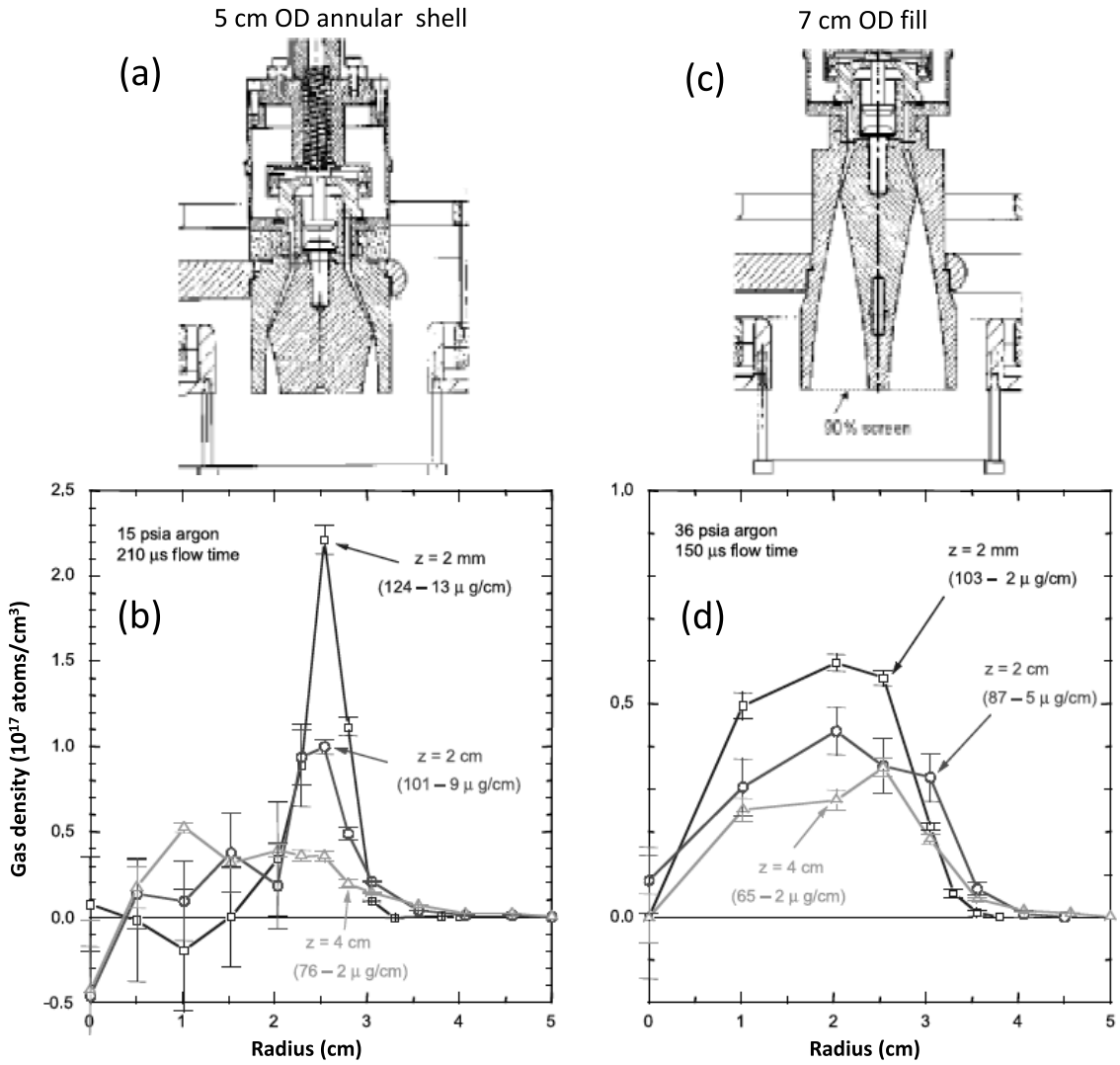

Fig. IV-2. (a) Cross section of gas-puff assemblies used on DM2, ACE 4, and Double-EAGLE for the $r_N = 1.75$–2.5-cm annular shell. (b) Corresponding density distributions at the time the pulsed-power generator is triggered obtained with the NRL 1-D high-sensitivity interferometer. (c) and (d) Corresponding figures for the $r_N = 3.5$-cm solid-fill design. Adapted from [I-16].

required to ionize and excite K-shell radiation from high Z_A elements such as Ar and Kr. Similar arguments regarding large-radius annular puffs can be made in the cases of scaling a particular high Z_A element to higher current, moving from the inefficient to efficient regime where the yield scales as M_o ($I^2_{\rm pk}$, see Section III-E), while keeping t_g constant and/or allowing longer implosion-time pulsed-power generators (see Section V-D) [I-16], [III-11], [III-16], [IV-32]–[IV-34]. This recognition led to new gas-puff-assembly designs whose goal was to achieve stabilization of the MRT instability. These new designs featured nozzles that provided a variety of radial gas distributions that replaced the single annular shell: solid-fill; shell-on-shell or double puff (multiple concentric annular nozzles); and structured or triple puff comprised of a central jet within a double puff and producing an increasing density with decreasing radius. These distributed density profiles can reduce the total kinetic energy, as shown in Fig. III-3 and discussed in Section III. However, as also discussed in Section III-D, the coupled $E_{j\times b}$ can be as large as the $E_{\rm kin}$ of a thin annular shell. The connection between diagnostic methods for measuring the initial neutral gas distribution, the mitigation of the MRT instability due to the density profile, and the improvement in the K-shell radiation production at stagnation are discussed in Sections IV-B, V-E, and VI-A.

We now describe in more detail several such gas-puff assemblies and their associated nozzles. We pick representative designs, rather than present an exhaustive compilation. Here, it is useful to clarify and define some nomenclature for the geometry of the nozzle at its exit plane. In the literature, a nozzle can be described by the OD of its largest opening; however, the individual openings at the exit plane of the nozzle are described in terms of their inner and outer radii. Unless the OD is explicitly stated, we will use the symbol r_N to describe the radial geometry of the exit plane openings. If the nozzle produces a single annular shell, the outer radius is stated. If the inner radius of the nozzle is relevant to the discussion, then both radii are given separated by a dash. If the thickness of the shell is nearly the same as the outer radius of the nozzle

exit plane, then the gas puff is termed a solid-fill, or simply fill, and only the outer radius is noted. A double shell, double puff, or shell on shell means there are two concentric nozzles meant to form two annular gas shells and the inner and outer radii of both shells are stated with a solidus between the pair. For instance, $r_N = 1$–2/3–4 cm means that the exit plane of the nozzle has one opening between $r_N = 1$ and 2 cm, and a second opening between $r_N = 3$ and 4 cm. Unless otherwise stated, a triple shell, triple puff, or shell on shell on center jet refers to a double-shell geometry with a central jet on axis. Here, the outer radius of the central jet is stated and separated from the geometry of the double puff by another solidus, as in $r_N = 0.5/2$–3/5–6 cm.

Examples of a single-shell and solid-fill nozzles are shown in Fig. IV-2(a) and (c), respectively, from [I-16]. In Fig. IV-2(b) and (d), the measured neutral gas distributions are compared at a time when the pulsed-power generator is triggered for a single puff ($r_N = 1.75$–2.5 cm) and a solid-fill ($r_N = 3.5$ cm), respectively. Clearly, near the nozzle exit the radial gas distribution for the shell is very different from that of the solid-fill, but by 4-cm downstream the distributions are similar. These gas-puff assemblies were fielded on DM2, Double-EAGLE, and ACE-4 [I-16].

In a double puff nozzle, the outer annulus carries the current initially and is accelerated radially inward until it reaches the inner annulus where the total acceleration is reduced. Assuming conservation of energy and momentum, the masses associated with the outer and inner shells implode together, effectively starting the implosion at a smaller radius with all the mass at a higher current. This configuration was used in many experiments. One such nozzle was described in [IV-35]. Fig. IV-3(a) and (b) from [IV-35] shows a cross section ($r_N = 1$–2/3–4 cm) and a photo of this nozzle, respectively. The two plenums are independent and can be filled to different pressures. A single flying hammer opens both seals at the same time. The independent plenums allow selective admixtures of trace gases, the radiation from which could be used to help diagnose the pinch [IV-30]. This assembly was used successfully on Double-EAGLE [IV-30] and the Z generator at SNL [IV-36]. Note that the shell-on-shell distribution has neutral gas between the shells (see Section IV-B). The design of a triple gas-puff assembly with three distinct shells was also reported in [IV-37].

Motivated by the success of this double-shell design, as reviewed in Section VI-A, a new triple-puff, or double-puff assembly of a 12-cm OD and a center jet was developed at TPSD [IV-23], [IV-38], [IV-39]. Initially, two variations of the inner and outer radii for the two nozzle openings were explored [IV-23]: either $r_N = 2$–3/5–6 cm or $r_N = 1.5$–3/4.5–6 cm. Also nozzles with a 1- or 2-cm recess were examined, i.e., with the exit plane of the recessed nozzles set back from the OD of the outer nozzle. For this paper, the center jet was a straight hole drilled through the center of the inner nozzle (varied from 0.12 to 0.28-cm diameter) that shared the same plenum as the inner nozzle.

A schematic cross section (from [IV-40]) and photograph of the final version of this TPSD-designed gas-puff assembly is shown in Fig. IV-4(a) and (b), respectively. Very successful

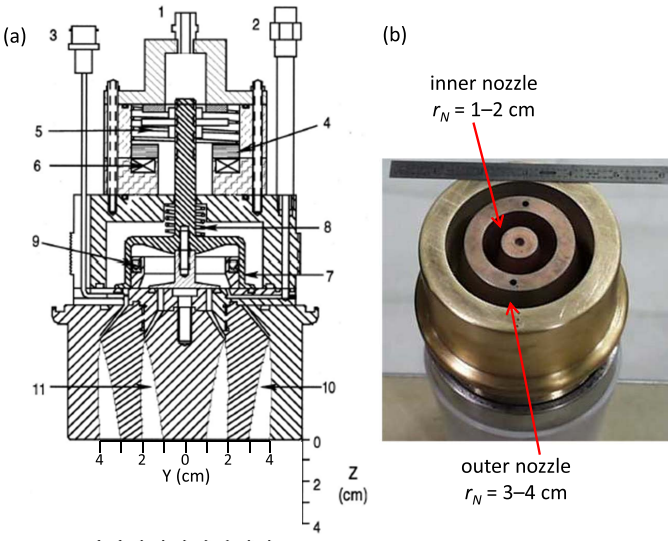

Fig. IV-3. (a) Cross section of an $r_N = 1$–2/3–4-cm shell-on-shell gas-puff assembly: (1) outer plenum gas inlet; (2) inner plenum gas inlet; (3) breakdown pin output; (4) hammer; (5) hammer reset spring; (6) solenoid; (7) poppet; (8) poppet reset spring; (9) sliding seal; (10) outer nozzle; and (11) inner nozzle. Reprinted with permission from [IV-35] (slightly adapted). Copyright 2000, AIP Publishing LLC. (b) Photograph of the same gas-puff assembly (courtesy of Levine).

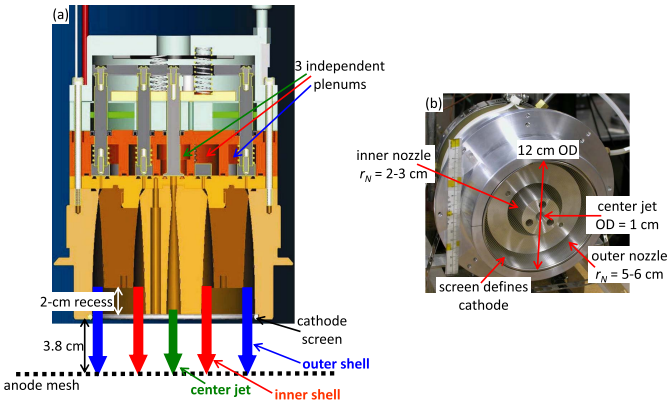

Fig. IV-4. (a) Cross section of the TPSD shell-on-shell-on-center-jet assembly ($r_N = 0.5/2$–3/5–6 cm). Adapted from [IV-40]. (b) Photograph of the same gas-puff assembly (courtesy of Jackson). Outer and inner nozzles are recessed; center jet is not recessed.

experiments using this gas-puff assembly were reported in [IV-38] and [IV-39] (see Section VI-A). A single flying hammer simultaneously opens the seals for the three independent plenums. The region between the inner and outer nozzle is recessed [2-cm recess shown in Fig. IV-4(a)]. This is to allow the gas additional axial extent to fill in the radial gaps between the nozzles before reaching the interelectrode region for snowplow stabilization. The center jet is a contoured nozzle that is a 1-cm diameter at the exit plane, connected now to an independent plenum. The cathode screen produces a well-defined surface for current connection. The screen also affects the density distribution, as will be discussed in Section IV-B. Note that results for Ne implosions using a gas-puff assembly featuring three distinct shells plus a center jet was reported in [IV-41].

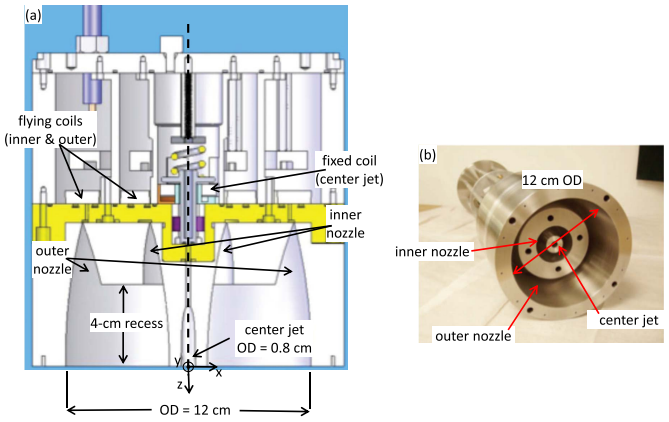

Fig. IV-5. (a) Cross section of recent AASC 12-cm-OD, shell-on-shell-on-center-jet assembly (r_N = 0.4/1–2/4–6 cm). Arrows point to location of energized coils, but the coils themselves are not shown. Outer and inner nozzles are recessed. (b) Photograph of a similar gas-puff assembly with the center jet recessed. Adapted from [IV-7].

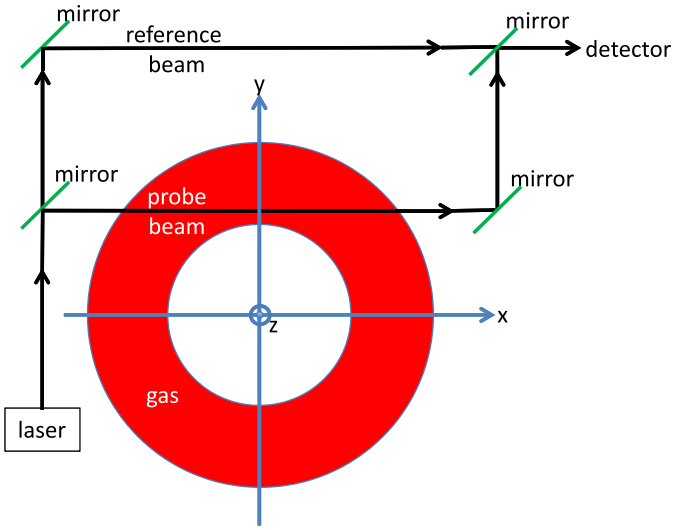

Fig. IV-6. Schematic of 1-D interferometry (in Mach–Zehnder configuration). Adapted from [IV-3].

As an electrode in a high-current circuit, the nozzle can suffer damage in a high-current-density environment. Usually (but not always), the gas-puff nozzle is the cathode and, as noted in Fig. IV-4, there can be either a transparent screen or a mesh (spider-web like wire array) across it. The purpose of the screen or mesh is to electrically define a cathode plane, especially if portions of the nozzle are recessed (see Fig. IV-4). The mesh also serves as a connecting surface for the current, thereby minimizing damage to nozzle components. Another mesh or set of crossed wires usually defines the anode plane. Without such defining surfaces, determination of the gas-puff inductance can be uncertain, especially for recessed-nozzle designs. These wire structures can affect the neutral-gas distribution in important ways [IV-31], [IV-40] (see Section IV-B).

The final gas-puff assembly described here (r_N = 0.4/1–2/4–6 cm) is a 12-cm-OD triple-nozzle system designed and built by Alameda Applied Sciences Corporation (AASC) for use on the Z generator at (SNL, ~25 MA in 100 ns) [IV-7], schematically illustrated in Fig. IV-5. There are several unique features for this system that are worth noting. The fast acting valves for the outer and inner nozzles use a light-weight energized coil to seal these plenums from the vacuum as well as move to break the seal; i.e., a flying coil (the center jet employs a flying hammer). There are independent valves for each plenum that can be separately triggered to time the gas flow from each nozzle, providing an additional control over the gas profile if needed. Rather than align the nozzle hardware to establish an azimuthally symmetric, small-opening (130–380 μm) throat, a throat plate was used. The desired throats are machined into a 127-μm-thick stainless steel foil with a $\pm$25-μm tolerance using a laser. The plate is then checked offline using a desktop scanner so that only those plates whose average gap differs by no more than $\pm$2.5% are used in the gas-puff assembly. This allows the nozzles to be machined with a more manageable tolerance and simplifies their assembly procedure. The individual gas flows can be highly annular (estimated Mach number is 7), so they do not merge until ~2.5-cm downstream from the nozzle face.

Independent of the design, the gas-puff assembly can be located in the high-voltage electrode of the pulsed-power generator that can exceed MV levels. This requires the gas-puff triggering and sensing circuits as well as the gas reservoir to be electrically isolated from the high voltage. This is accomplished by use of an inductive isolator (sometimes referred to as transit-time isolator for short-pulse generators). A description of one such isolator can be found in [IV-7].

Finally, for all gas-puff assemblies used as radiation sources, the current into the gas-puff is delivered in a coaxial geometry, with the return current structure usually constructed with individual rods, or from a cylinder with machined slots, so that radiation can be measured. The return-current structure could impress an azimuthal nonuniformity on the imploding plasma [IV-26].

B. Gas Density Measurements

Unlike a wire-array Z-pinch, where the detailed characteristics of the initial configuration (e.g., mass and mass distribution, wire characteristics, and wire composition) can be very accurately determined under static conditions, the mass distribution of a gas-puff Z-pinch at the time current is applied from the pulsed-power generator must be measured under dynamic conditions. A detailed knowledge of the initial mass distributions is of critical importance for understanding experimental results and as input for computational simulations. Fortunately, several approaches have been implemented to measure the time history of the radial and axial distribution of neutral gas as it evolves with time. While these methods have not been implemented *in situ* and rely on the demonstrated reproducibility of the gas-puff nozzle, they have provided crucial insight into the behavior of the pinch. Measurements of electron density characterizing the implosion and stagnation phases of the Z-pinch plasma, discussed below, combined with the initial mass distribution give a complete picture of the pinch dynamics for which analytic models can be developed and against which simulations can be compared. Techniques for

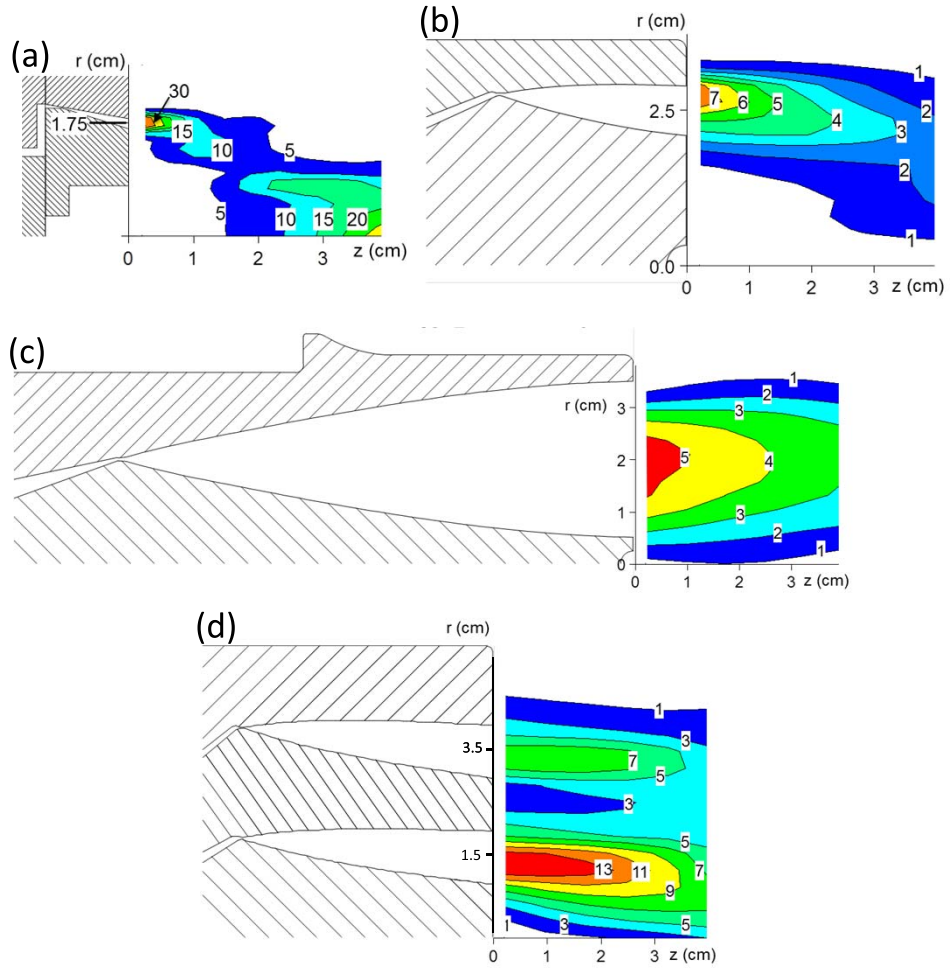

Fig. IV-7. Sample of Ar density measurements (~500 μs after the fast valve was actuated), for various MPI (now L-3 ATI) nozzles expressed as density contours, made using the high-sensitivity, 1-D interferometer at NRL. From [III-17], reproduced with permission. (a) $r_N = 1.75$-cm annular nozzle illustrated in Fig. IV-1, (b) $r_N = 2.5$-cm annular nozzle, (c) $r_N = 3.5$-cm fill nozzle illustrated in Fig. IV-2(b), and (d) $r_N = 1$–2/3–4-cm nozzle shown in Fig. IV-3. Density contours are in units of 10^{16} cm^{-3}.

measuring the space-and time-resolved mass distributions of the neutral gas comprise two primary categories: 1) interferometry and 2) laser-induced fluorescence (LIF). Each has 1-D and 2-D implementations. Both have advantages and drawbacks. Pressure transducers, which have been used to measure the time history of gas flow (see [IV-7], [IV-28]) but not for detailed number density distribution measurements, will not be discussed.

As shown in Fig. IV-6 [IV-3] for a Mach–Zehnder geometry, 1-D interferometry uses a single laser probe beam that traverses the gas along a chord perpendicular to the gas flow at some axial location (y', z'). The line-integrated neutral-gas number density at (y', z'), namely, N_o (y', z'), is proportional to the phase difference, $\Delta\phi(y', z')$ resulting from the difference in the optical paths of the probe beam and a reference beam that does not traverse the gas

$$N_o(y', z') \equiv \int_{-x_o}^{x_o} n_o(x, y', z')dx = \frac{\lambda}{2\pi}\frac{n_{o,\mathrm{STP}}}{(\chi_o - 1)}\Delta\phi(y', z') \qquad \text{(IV-1)}$$

where λ is the laser wavelength, χ_o is the index of refraction at the gas density $n_{o,\mathrm{STP}}$, (taken at standard temperature and pressure), and n_o (x, y, z) is the number density distribution of the neutral gas [IV-3]. To construct number density distribution in the xy plane at a given z', one must measure $N_o(y', z')$ for enough chordal (y') locations to construct the function $N_o(y, z')$. The number density distribution in the xy plane at z' is then obtained by Abel inversion, which requires the assumption of azimuthal symmetry. Defining $r^2 = (x^2 + y^2)$, we have for the radial number density distribution at z'

$$n_o(r, z') = -\frac{1}{\pi}\int_{y=r}^{\infty}\frac{dN_o(y, z')}{dy}\frac{dy}{\sqrt{y^2 - r^2}}. \qquad \text{(IV-2)}$$

Many measurements are needed at different chords to construct $N_o(y, z')$ and ultimately $n_o(r, z')$. The process is repeated at several axial locations to arrive at $n_o(r, z) = n_o(x, y, z)$ (again assuming azimuthal symmetry). The mass distribution is obtained simply by multiplying $n_o(r, z)$ by the mass of the gas atom or molecule. The crucial assumption of azimuthal symmetry can be checked by rotating the gas-puff assembly about z and observing the reproducibility [III-17]. The number

of gas-puff-assembly pulses can be reduced by employing a multiple-beam system. As a continuous wave laser is generally used for this approach, the time history of the density distributions can be obtained and used to determine the timing between activating the fast valve and application of the current from the pulsed-power generator. Usually, this current is applied at the time when the flow rate has ceased to increase and the axial mass gradient is minimized (typically about 500 μs after the fast valve is actuated). However, one approach to eliminating zippering of the pinch is to fire the generator while the flow rate is still increasing and take advantage of the radial expansion and axial gradient in the mass/length along the axis (see Section V-B).

A unique, vibration-isolated, high-sensitivity, 1-D interferometer at NRL [IV-2] was used extensively for characterizing the neutral gas density distributions of many types of gas-puff assemblies and to better understand gas-puff Z-pinch behavior [III-17], [IV-3], [IV-30], [IV-35], [IV-42]. Researchers at the High Current Electronics Institute (HCEI) in Tomsk, Russia, used NRL measurements to extrapolate to other nozzle designs [IV-43]. This system uses two lasers with different wavelengths (two-color) running simultaneously through the same line-of-sight and can be used to detect electrons as well as neutrals [IV-2] (see Section IV-C). The unique high sensitivity of this system is especially useful for measuring small gas densities at the periphery of the radial distribution (see below). Based on data recorded without gas, Weber and Fulgum [IV-2] report a minimum phase sensitivity of 0.036° corresponding to a minimum line-integrated density for Ar (at $\lambda = 532$ nm) of 5×10^{14} cm^{-2} at the time of interest (~600 μs after the fast valve was actuated). Vibrational noise over the ~millisecond time scale required for neutral density measurements appears to be the limiting factor for the minimum sensitivity. The typical dynamic range between the highest and lowest line-integrated density relative to the vibrational noise is 1000. In [IV-40], using a new, diode-pumped, frequency-doubled, Nd:vanadate laser at $\lambda = 532$ nm in the same system, but with nonideal vibrational isolation, a minimum phase sensitivity of 0.3° corresponding to a minimum resolvable line-integrated density for Ar of about 4×10^{15} cm^{-2} at the time of interest (500 μs after the fast valve was actuated) was reported. This minimum phase resolution, while higher than originally obtained, is still quite respectable and allowed a local density measurement as low as 7×10^{14} cm^{-3} [IV-40]. The spatial resolution for 1-D systems is limited in practice by how many pulses one is willing to carry out and how precisely the probe beam can be moved from one position to the next. A practical limit is 1–2 mm, using a mechanical manipulator. Examples of measurements for a variety of gas-puff types are given in Fig. IV-7 [III-17]. Several other systems were developed using the 1-D approach with a minimum phase resolution of ~3° [IV-44]–[IV-46].

The high-sensitivity interferometer also revealed some important aspects of the gas injection process. One is the effect of injecting gas through a semitransparent screen, as would happen when a cathode mesh is used. Another is neutral gas appearing at radii larger than the nozzle radius that

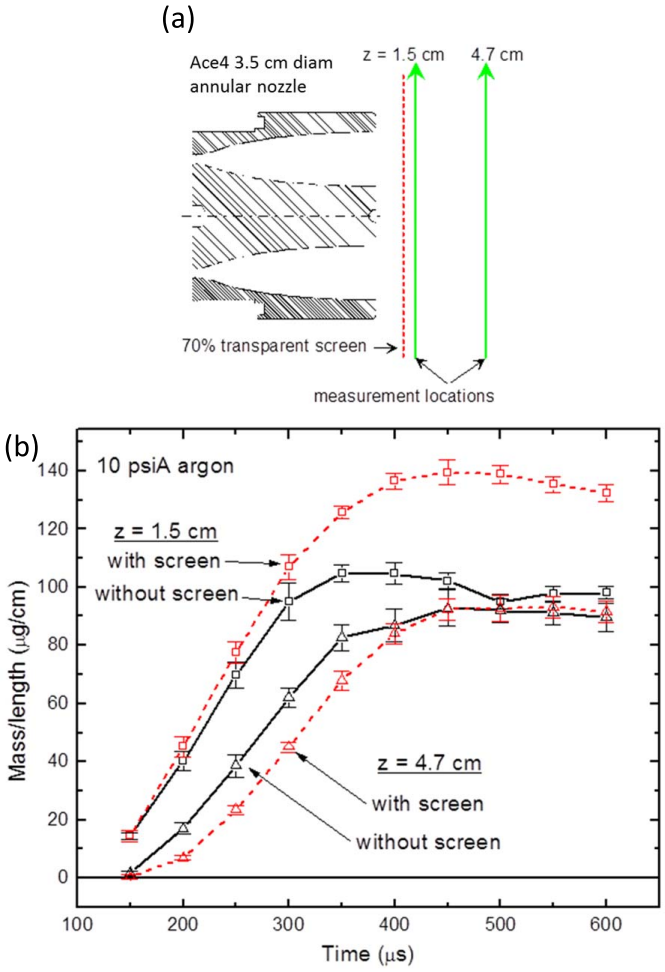

Fig. IV-8. (a) Illustration of setup for measuring effect of cathode screen on flow. (b) Measured mass/length at two axial locations from the nozzle face with (squares, red-dashed lines) and without (triangles, black-solid lines) the 70% transparent screen. Unpublished data courtesy of [IV-47].

can possibly influence the initial phases of the power flow. Fig. IV-8 [IV-47] shows results from measuring the gas flow at two axial locations with and without a screen. When the screen is present, the mass/length increases near the nozzle and decreases away from the nozzle, clearly influencing the axial gradient. This effect can be important to account for when modeling the pinch. Using the high-sensitivity capability of the 1-D interferometer, gas density was measured, starting at ~200 μs after the fast valve was energized, at radii significantly larger the nozzle radius, as shown in Fig. IV-9 [IV-47]. Note the vertical sale is logarithmic and the high-frequency feature early time for $y < 3.66$ cm is digitizer noise resulting from the large dynamic range of the measurement. This radius is large enough that the neutral gas could influence the initial stages of the power flow.

Using the reference beam as a second probe beam, a differential phase shift technique was developed [IV-48] as a common-mode-rejection approach to improving the precision of the data used in (IV-2). Additional optics were employed to position the reference beam a small distance ($\Delta y = 1$ mm) from the probe beam. The measured phase shift is then proportional to the difference in the line-integrated densities

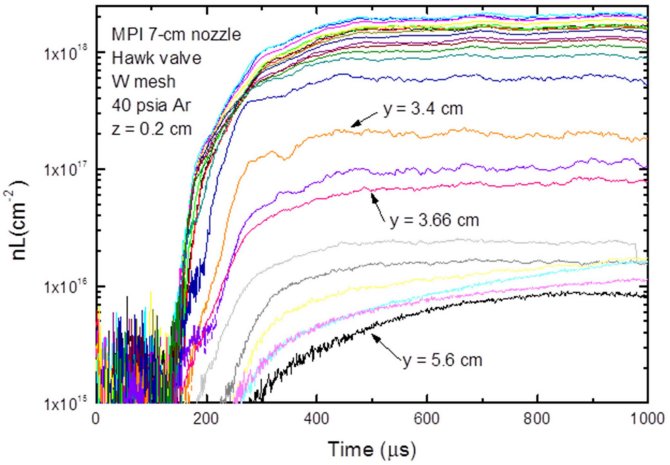

Fig. IV-9. Measured line integrated density, nL (logarithmic scale), of neutral gas 0.2 cm from the nozzle face for the solid fill nozzle shown in Figs. IV-2(c) and IV-7(c) as a function of chordal location y (see Fig. IV-6). Decreasing integrated line density corresponds to increasing y. Note the neutral gas at values of y greater the associated nominal 3.5-cm radius of the nozzle. Unpublished data courtesy of [IV-47].

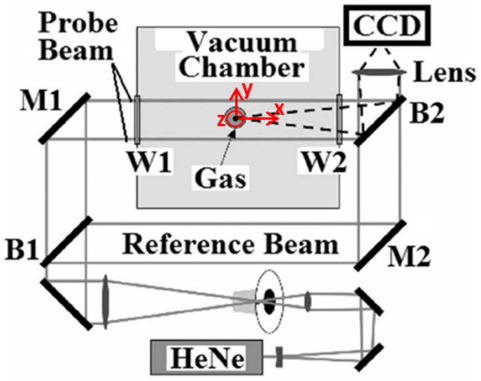

Fig. IV-10. Schematic of 2-D interferometer (in Mach–Zehnder configuration) built by AASC (axes superimposed). Reprinted with permission from [IV-49]. Copyright 2012, AIP Publishing LLC.

along the two beam paths, ΔN, giving a direct measurement of the average derivative of the line density ($dN/dy \cong \Delta N/\Delta y$). The Abel-inverted density distributions obtained using this technique were not superior to those using the standard interferometer measurements, but the differential technique appears to be a good diagnostic of gas turbulence.

In 2-D interferometry, a pulsed laser exposes the full y-z (or x-z) cross section of the interelectrode region of the gas puff and the phase information is recorded as an interference pattern generated by the interaction between the probe beam and reference beam. This 2-D approach has an advantage over the 1-D system in that it eliminates the need for repeated pulses of the gas-puff assembly to obtain the density distribution at a given time. Early 2-D interferometers for measuring neutral-gas distributions were reported by [IV-45] and [IV-46]. A more recent 2-D system, developed by AASC, is illustrated in Fig. IV-10 [IV-49]. As shown in Fig. IV-11, the 2-D fringe patterns from this system with and without gas present are recorded on a gated charge-coupled device (CCD) and are

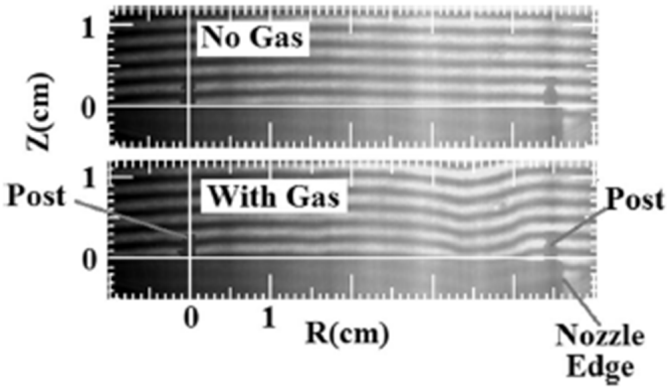

Fig. IV-11. Sample fringes from 2-D (Mach–Zehnder configuration) interferometer system illustrated in Fig. IV-8. Reprinted with permission from [IV-49]. Copyright 2012, AIP Publishing LLC.

compared to ascertain the net line density associated with the gas in the entire yz plane, $N(y, z)$, at a given time of interest (usually ~500 μs after the fast valve is actuated). Time resolution for the system was obtained from the CCD, which can be repetitively pulsed and read out every 0.3 ms with an exposure time of 10 μs. Exposures before gas is injected, during the time gas is injected, and after the gas is injected are analyzed to obtain the net fringe shift from the gas. Abel inversion is again used to infer $n(r, z)$. As with 1-D interferometry, azimuthal symmetry must be verified. Additional gas-puff discharges at different times can be used to study the time evolution of the neutral gas density.

For the system illustrated in Fig. IV-10, a minimum phase resolution of 7° was reported [IV-49]. For Ar gas using a HeNe laser at 633 nm, this corresponds to a minimum resolvable integrated line density of about 1×10^{17} cm^{-2}. The minimum phase resolution for the 2-D interferometer is in part determined by the fringe spacing, which is determined by a tradeoff between spatial resolution and phase resolution. While the system described here is ~200 times less sensitive than demonstrated by the high-sensitivity 1-D system described above, it is adequate for quickly determining the operational integrity of a gas-puff assembly and the general characteristics of its gas flow, particularly with large mass loads. This system has high intrinsic spatial resolution, ~0.4 mm [IV-49]. However, tradeoffs again involving fringe spacing increase the minimum spatial resolution to ~1 mm in both axial (z) and chordal (y) coordinates [IV-7]. Another version of a 2-D Mach–Zehnder system has been described that uses a 3-ns full-width at half-maximum (FWHM) pulsed laser for time resolution [IV-45]. To date, 2-D spatial interferometry has been used less extensively than 1-D interferometry for characterizing the neutral gas distribution from gas-puff assemblies.

The LIF approach differs from interferometry in that the laser-induced fluoresce of a dopant added to the gas (usually 5% acetone by partial pressure) is measured whereas interferometry directly responds to the gas. The spatially resolved fluorescence induced by the laser (preferentially in the UV, 266 nm) is recorded on a CCD. As long as the dopant and the gas density remain in the same proportion and the line of

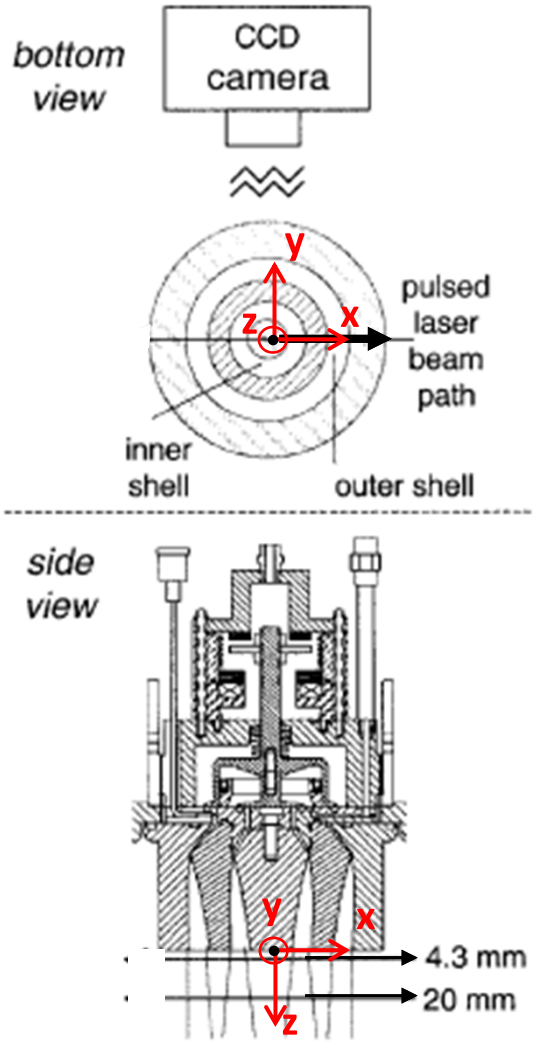

Fig. IV-12. Schematic of 1-D LIF system on the r_N = 1–2/3–4-cm shell-on-shell gas-puff assembly shown in Fig. IV-3 (axes superimposed). Reprinted with permission from [IV-50] (slightly adapted). Copyright 2003, AIP Publishing LLC.

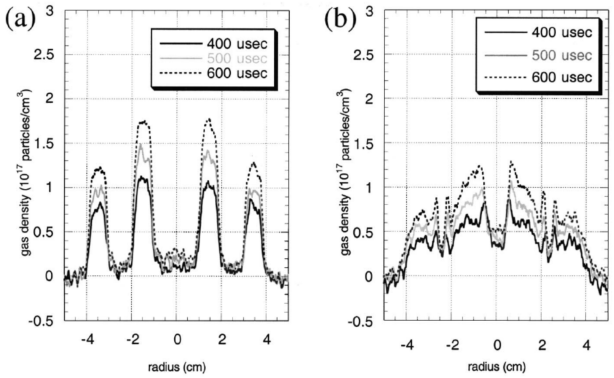

Fig. IV-13. Gas-density data for the r_N = 1–2/3–4-cm shell-on-shell gas-puff assembly shown in Figs. IV-3, IV-7(d), and IV-12 obtained with the TPSD 1-D LIF system at different times and at two distances from the nozzle exit plane. (a) 0.43 and (b) 2.0 cm. Reprinted with permission from [IV-50]. Copyright 2003, AIP Publishing LLC.

sight is through a diameter of the neutral gas column, the fluorescence is proportional to the neutral gas density and the density distribution can be inferred from the measured fluorescence with no Abel inversion required. The principles of this measurement technique in 1-D and 2-D are described in [IV-50]. The 1-D LIF system developed by TPSD is illustrated in Fig. IV-12 [IV-50]. The system in Fig. IV-12 gives the radial distribution at a given axial location. A 2-D system uses a sheet beam along a diameter in the xz plane that extends between the exit plane of the nozzle and the location of the anode (wire mesh or screen). If the entire fluorescence from the xz plane is imaged perpendicular to the laser beam (i.e., in the y-direction), $n(x, z)$ can be obtained at the time the laser is pulsed with one puff of gas. This approach is termed planar laser-induced fluorescence (PLIF). Additional gas-puff discharges at different times can be used to obtain $n(r, z)$ at different times. Azimuthal variations are automatically measured in the plane of the laser beam and can be checked in the entire xy plane at a given z by sending the sheet beam through the xy plane and viewing the fluorescence axially. Submillimeter spatial resolution with a minimum resolvable density of 10^{15} cm^{-3}, limited by the CCD, was reported [IV-51]. A modern CCD might increase the sensitivity by a factor of 5. An example of a PLIF measurement with an r_N = 1–2/3–4-cm shell-on-shell gas-puff assembly shown in Figs. IV-3, IV-7(d), and IV-12 is shown in Fig. IV-13 [IV-50].

This approach has the advantages of being able to ascertain $n(x, y, z)$ with a minimum number of gas-puff pulses without requiring an Abel inversion, but there are some issues. The fluorescent signal is proportional to (among other parameters): the number density of absorbing, ground-state molecules; the molecular absorption cross section; and the fluorescent quantum yield. All of these quantities are temperature dependent. Also, the assumption of uniform dopant concentration under transient conditions might not hold. The calibration is done under static conditions with known density and at room temperature. These conditions can change as a result of the gas being puffed at supersonic speeds into the interelectrode region. In principle, the increase in absorption cross section can be offset by a decrease in fluorescent yield [IV-50]. All this leads to an uncertainty in the calibration. In addition, scattered light from metallic parts of the gas-puff assembly can mix with the fluorescent signal. This makes taking measurements near electrodes, wire meshes, or screens problematical (see below).

Density distributions for the r_N = 1–2/3–4-cm shell-on-shell [see Figs. IV-3, IV-7(d), and IV-12] gas-puff assembly measured with the 1-D LIF and 2-D PLIF [IV-50] have been compared with those measured using 1-D interferometry. Data from 1-D LIF are compared with 1-D interferometry in Fig. IV-14 [IV-50]. The LIF measurements were taken at 0.43 and 2.0 cm from the nozzle exit plane while the 1-D interferometer measurements [IV-35] were at 0.2 and 2.0 cm from the nozzle exit plane. There is general agreement at the 2.0-cm location but about a factor of 2 discrepancy near the nozzle face. Some of that discrepancy is a result of the measurements being at two axial locations. In this comparison, the 1-D interferometry generally gives higher densities than the 1-D LIF.

TABLE I
COMPARISON OF REPORTED NEUTRAL GAS DENSITY MEASUREMENT TECHNIQUES

Approach	refs.	Comment	Minimum sensitivity for Ar
1-D high sensitivity interferometry	[IV-2], [IV-3], [IV-45], [III-17], [IV-40]	- measure gas - Abel inversion required - many gas-puff discharges required - highest density - dynamic range of ~1000	0.036° or 5×10^{14} cm^{-2} (line integrated) [IV-2] to 0.3° or 4×10^{15} cm^{-2} (line integrated) and 7×10^{14} cm^{-3} (density) [IV-40] (both at 532 nm)
2-D interferometry	[IV-45], [IV-49], [IV-7]	- measure gas - Abel inversion required - moderate sensitivity - rapid characterization of gas distribution	7° or ~1×10^{17} cm^{-2} (line integrated) (at 633 nm)
2-D planar laser-induced fluorescence	[IV-50], [IV-51], [IV-23], [IV-38]	- measure fluorescence of dopant in gas - calibration subject to uncertainties - no Abel inversion required - high sensitivity - rapid characterization of gas distribution	1×10^{15} cm^{-3} (density) (at 226 nm)

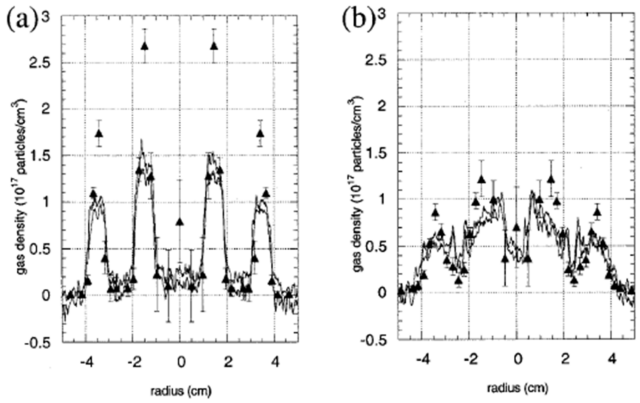

Fig. IV-14. Comparison of Ar gas density profiles measured with LIF (continuous lines representing ± one standard deviation from the mean value) and 1-D high-sensitivity interferometry (triangles) for the r_N = 1–2/3–4-cm shell-on-shell gas-puff assembly shown in Fig. IV-3 at different axial locations from the nozzle exit. (a) 0.2 cm for 1-D interferometry and 0.43 for 1-D LIF and (b) 2.0 cm for both. Reprinted with permission from [IV-50]. Copyright 2003, AIP Publishing LLC.

In [IV-40], a more detailed comparison was carried out between 2-D PLIF and 1-D interferometry for the TPSD r_N = 0.5/2–3/5–6-cm shell-on-shell-on-center-jet gas-puff assembly used for Saturn shot 3565. Shown in Fig. IV-15(a) is the mass between radius r and $(r+dr) \propto n(r,z)\times r$ (where, again, $r^2 = x^2 + y^2$), measured with 1-D interferometry and PLIF, plotted as a function of r at three axial locations (z = 0.5, 2.0, and 3.5 cm), with and without a cathode screen, at the time the Saturn current began to flow (500 μs after the fast valve was actuated). Measurements for 1-D interferometry are made with (blue) and without (red) a cathode screen while the PLIF measurements (green) are made without the cathode screen only. The 1-D interferometry measurements show that the mass near the cathode (z = 0.5 cm) increases in the presence of the cathode screen as discussed above (see Fig. IV-8 and the associated text). There are clear differences between 1-D interferometry and PLIF, especially near the cathode, for the case where both measurements are done without the cathode screen. The cathode screen was used in the Saturn experiment. Shown in Fig. IV-15(b) is the axially resolved Ar K-shell emission from a zipper diagnostic [IV-31] as a function of time for Saturn shot 3565 using this nozzle. Superimposed on the K-shell radiation is the 1-D snowplow-predicted stagnation time at each axial location, using the three measured profiles in Fig. IV-15(a) for initial conditions. The stagnation times from the 1-D interferometer distribution measured with the cathode screen match the onset of K-shell emission at different z positions whereas the PLIF data and the 1-D interferometer data, both taken without the screen, do not. If PLIF could have been used near the cathode screen, the density would have been even higher (based on the interferometer data, also see Fig. IV-8), resulting in even later predicted stagnation times for K-shell emission. This type of discrepancy using PLIF to measure the neutral gas density for this 12-cm-OD gas-puff assembly was also alluded to in [IV-23]. These issues notwithstanding, the PLIF method has been successfully used to match the gas-puff load and generator as well as understand the implosion dynamics and heating for the 12-cm-OD gas-puff assembly shown in Fig. IV-4 [IV-23], [IV-38], [IV-39], [IV-51]–[IV-56].

The approaches for measuring the neutral gas density for gas-puff Z-pinches described above are summarized in Table I. Note that only reported characteristics are given and improvements can be made. Researchers should pick the approach that suits their needs. In general, PLIF offers the advantage of quickly determining the operational integrity of a gas-puff assembly and the general characteristics of its gas flow, particularly with large mass loads, with good sensitivity without

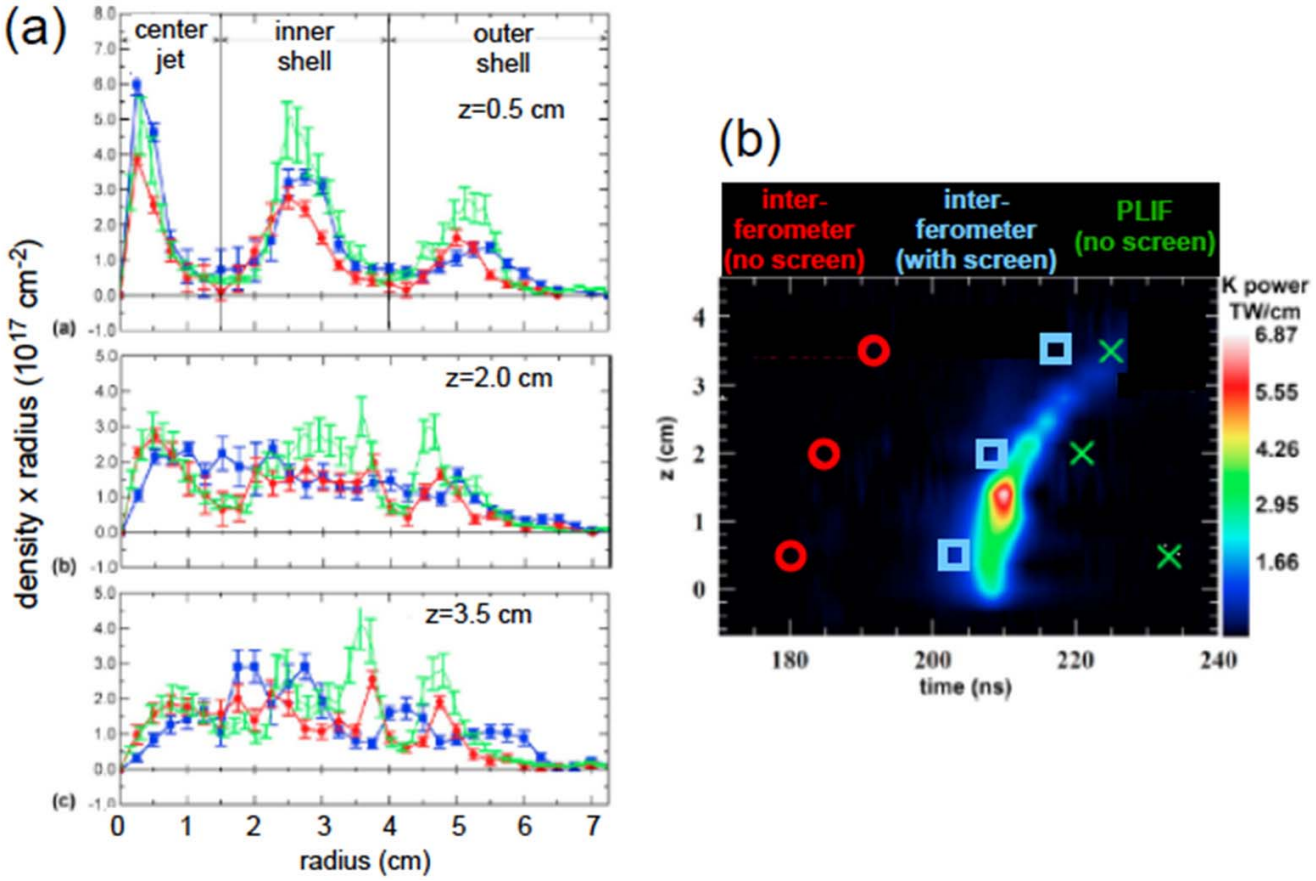

Fig. IV-15. (a) Comparison of PLIF and 1-D, high-sensitivity interferometry measurements of neutral Ar (density) × (radius) profiles for the triple-nozzle gas-puff assembly (r_N = 0.5/2–3/5–6 cm) shown in Fig. IV-4 at the time of application of Saturn current (∼500 μs after the fast valve was actuated) at z = 0.5, 2.0, and 3.5 cm. Measurements for 1-D interferometry are with (blue) and without (red) cathode screen. Measurements using PLIF are without cathode screen (green). (b) Axially resolved K-shell emission as a function of time from Ar on Saturn (Shot 3565, cathode screen used) compared with the predicted stagnation time for the measured profiles on the left-hand side of the figure using a 1-D snowplow at each axial location. Adapted from [IV-40].

Abel inversion. There are issues with absolute calibration and possibly stray light from nearby surfaces that might result in systematic errors, thereby affecting details in the modeling of the implosion. 2-D interferometry also can used be to rapidly characterize a gas-puff assembly with useful phase resolution, but requires Abel inversion. Both PLIF and 2-D interferometry provide a level of characterization that can be useful for some modeling. The 1-D high-sensitivity interferometer requires many pulsings by the gas-puff assembly and Abel inversion. However, it offers the highest phase resolution and is preferred for detailed physics studies of the gas-puff Z-pinch.

Predicting the mass distribution from a gas-puff nozzle assembly is a daunting but laudable task for fluid-dynamics experts. For example, it is advantageous to have a fluid code that could be used to help to improve the design of gas-puff nozzles based on understanding derived from diagnosed and analyzed behavior. Fig. IV-16 [IV-45] shows a comparison between measured phase change from a gas-puff assembly and phase change computed using two physics models. A brief description of the code used (ARES) and assumptions made in the computations are presented in [IV-45] and the references therein. The computations were made with two unsteady-flow models: Euler (nonviscous gas) and Navier–Stokes (viscous gas). A 2-D Mach–Zehnder system [IV-45] was

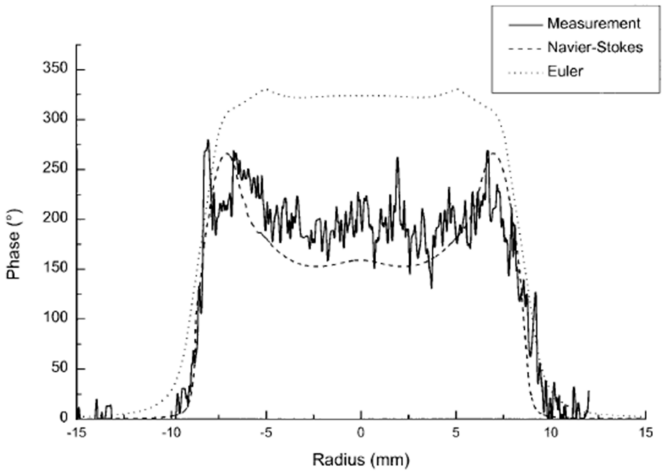

Fig. IV-16. Measured phase as a function of radius (y) near the nozzle exit plane of an 1.8-cm-OD Ar annular gas puff using a 2-D Mach–Zehnder interferometer compared with the results of computations using a 2-D code with (Navier–Stokes) and without (Euler) viscosity. Reproduced from [IV-45].

used to measure the variation of phase change with chordal position (y) at an axial location near the nozzle exit plane of a 1.8-cm-OD gas puff at ∼500 μs after the fast valve was actuated. It is clear that the viscous-gas

approach results in a superior fit to the data. In [IV-3], computations of the radial density distribution 3.2 cm (0.2 cm) from a 5-cm-OD (7-cm OD) nozzle face using a Navier–Stokes code (2RZDelta, developed at MLI by Murphy—no reference available) agreed with the radial density distribution measured at the same locations and times by the 1-D, high-sensitivity interferometer when the computed values were increased by 20%.

For high-density flows of noble gases, the rapid expansion of the gas from the throat region results in cooling (conversion of thermal energy into directed kinetic energy) that can lead to condensation in the form of microdroplets or clusters. Qi *et al*. [IV-51] used PLIF, as well as Rayleigh and Raman scattering, to measure the gas distribution for the r_N = 0.5/2–3/5–6-cm shell-on-shell-on-center-jet gas-puff assembly (see Fig. IV-4). They found direct and indirect evidence for the presence of clusters in the double-shell configuration of the nozzle. The gas distribution based on the PLIF and Raman scattering were similar, but the Rayleigh scattering, which varies strongly with the diameter of the scattering particles, was notably different. It was concluded that clusters are formed in the high density regions of the shells but not in the low-density intershell regions. For the indirect evidence, clusters were required to explain the higher than-expected gas flow speed measured using PLIF, which was attributed to the energy released in condensation. While the fractional mass of these clusters is small and their presence does not affect the gross behavior of the pinch (rapid ionization in the early stages of the pinch leads to rapid disassembly of clusters), they must be accounted for energetically in simulations if such simulations are to accurately reproduce the measured gas flow and distribution.

Though the above evidence for clusters did not include a central jet, one can reasonably conclude from the Hagena parameter [IV-57], [IV-58] that cluster formation occurs in the central jet of all Ar gas puff Z-pinch experiments. Based on the formulation in [IV-59], this parameter depends on the gas composition, pressure, and temperature in the plenum, the half-angle of the jet expansion, and the diameter of the circular throat part of the nozzle. The plenum is always at room temperature, T_o. We further chose typical parameters for an Ar central jet: 15° for the half-angle of the jet expansion and a throat diameter of 0.1 cm. The plenum pressure can cover a large range: 5.2 psia [IV-15] to 250 psia [IV-49]. The respective Hagena parameter ranges from 4×10^3 to 2×10^5, significantly larger than the threshold value of ~300 for cluster formation. The cluster size depends on this parameter, and for the high-pressure case there could be close to 10^4 atoms/cluster. For Kr under the same conditions, cluster formation is more pronounced, but for Ne clustering would occur only at the high pressure. The Hagena model does not apply to an annular opening as used in the nozzle to make shell profiles.

An analytic approach was developed for modeling flows from nozzles called the ballistic-flow model (BFM) [III-17], [IV-60]. The BFM treats the gas flow as emerging from a thin annulus with a Gaussian distribution in angle about the nozzle tilt angle. This

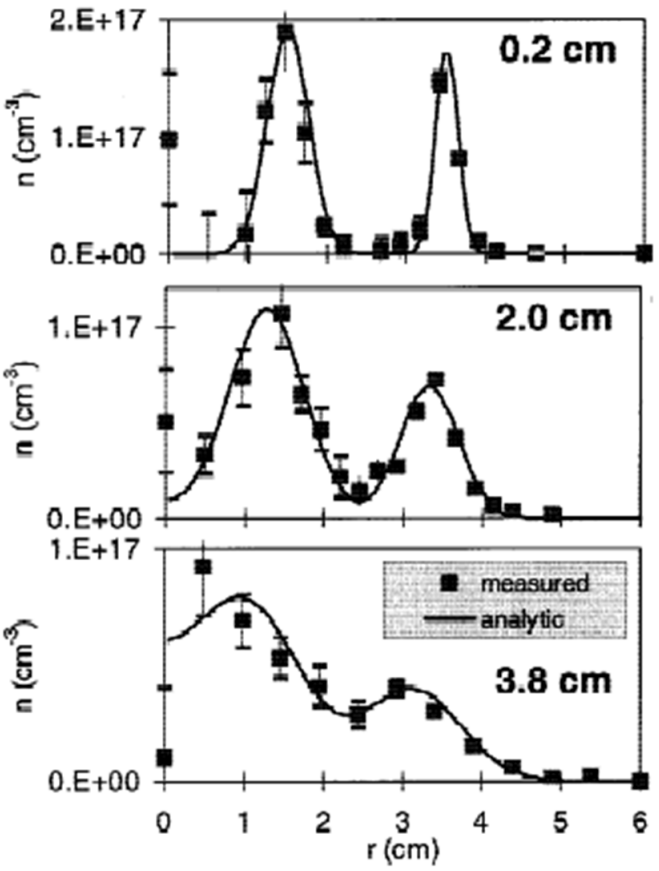

Fig. IV-17. Comparison of Ar neutral density profiles measured with the NRL high-sensitivity interferometer at z = 0.2, 2.0, and 3.0 cm, ~500 μs after the fast valve is actuated (square data points) and the BFM fit (solid line) for the r_N = 1–2/3–4-cm shell-on-shell gas-puff assembly illustrated in Figs. IV-3, IV-7(d), and IV-12. From [III-17], reproduced with permission.

distribution is then propagated forward ballistically in z. The model is described in detail in [III-17]. There are four parameters for the model: two are determined from the nozzle geometry (the radius of the annulus and the tilt angle) and the remaining two (an angle describing the Gaussian distribution and an offset of the annular source from the nozzle exit plane) are chosen to simultaneously provide the best overall fit to the measured density profiles. The model then provides a smooth analytic function for all values of z that can be used, e.g., as initial conditions in 2-D simulations of the implosions. It may also be used to help evaluate the effect changes in the nozzle design might have on the gas distribution. Fig. IV-17 [III-17] shows an example of this approach for the r_N = 1–2/3–4-cm shell-on-shell. The model fits the data well. For multiple-shell cases such as this, the distributions from each nozzle are added to obtain the total distribution. Note that the model assumes that the flows from each shell are independent and does not account for interacting flows. In cases where flows interact, the BFM method is not expected to work well for fine details of the density distribution [IV-51].

It is somewhat surprising that the BFM works as well as it does, given that the model assumes collisionless flow while the gas puff itself is highly collisional, at least within the jet and shells at the nozzle exit. A measure of collisionality

is the Knudsen number, which is the ratio of the mean free path ($\lambda_{\rm mfp}$) to a characteristic system length. For example, consider the $r_N = 0.5/2$–$3/5$–6-cm shell-on-shell-on-center-jet nozzle with an Ar mass loading of 200 μg/cm. If the mass ratio in the jet/inner/outer is 20/40/40, then the average atom density at the exit plane of the nozzle and within the openings specified by r_N would be $n_a = 7.7 \times 10^{17}/7.7\times^{16}/3.5 \times 10^{16}$ cm^{-3}, using the same ordering as the mass ratio. The hard sphere cross section for Ar–Ar collisions is $\pi\sigma^2 = 4.16\times10^{-15}$ cm^2 [IV-61], and the corresponding mean free paths are $\lambda_{\rm mfp} = 1/\sqrt{2}n_a\pi\sigma^2 = 2.2 \times 10^{-4}/2.2 \times 10^{-3}/4.9\times10^{-3}$ cm. These lengths are much smaller than the nozzle openings (small Knudsen number) and so the flow at the exit plane within the jet and shell regions is quite collisional. At this location in between the shells or between the inner shell and central jet, the density may be several orders of magnitude lower. Downstream where the flow intermingles, the density is closer to uniform but the Knudsen number would still be small, using the outer nozzle diameter for the characteristic length. A factor of 10 smaller mass loading would not change the conclusion of a strongly collisional gas flow.

The gas flow between the throat and the exit plane may be turbulent due to the nonslip boundary condition along the nozzle surface. A metric for a turbulent boundary layer is the Reynolds number, $R_{\rm ey} = UD/\nu_{\rm vis}$. Here, U and D are a characteristic velocity and length scales, and $\nu_{\rm vis}$ is the kinematic viscosity, given by $(1/3)\langle c\rangle\lambda_{\rm mfp}$ in the hard sphere model of atomic collisions [IV-61], with $\langle c\rangle$ the average molecular speed $= (8k_BT/\pi m_a)^{1/2}$ for an atom of mass m_a. Thus

$$R_{\rm ey} = 3\frac{U}{\langle c\rangle}\frac{D}{\lambda_{\rm mfp}} = 3\sqrt{2}\frac{U}{\langle c\rangle}Dn_a\pi\sigma^2. \tag{IV-3}$$

At the throat the flow transitions from sonic to supersonic, $U \sim \langle c\rangle$ and $R_{\rm ey} \sim 3D/\lambda_{\rm mfp}$. At the throat, the density is larger by the ratio of the opening at the exit plane to that of the throat, $\sim$10, and $\lambda_{\rm mfp}$ is thereby 10 times smaller than the above estimates. For a characteristic length of the nozzle surface of $D \sim 2$ cm, $R_{\rm ey}$ is $>10^4$, which indicates the development of a turbulent boundary layer. Downstream of the throat for a steady isentropic flow of a perfect gas, the velocity asymptotes to

$$U \approx \left(\frac{2\gamma}{\gamma-1}\frac{k_BT_o}{m_a}\right)^{1/2} \tag{IV-4}$$

into a vacuum if the expansion angle of the nozzle is not too great. The factor $U/\langle c\rangle$ increases as $\sqrt{T_o/T}$, but the fall off in density probably exceeds this ratio and the Reynolds number decreases. Beyond the exit plane in the boundary free region, the flow is highly supersonic so the Reynolds number for turbulence does not apply; however, the boundary layer from the nozzle may have a residual effect on the gas flow structure.

C. Gas Breakdown and Preionization

The neutral gas injected between the electrodes of the pulsed-power generator must become a good conductor, i.e., break down and become a plasma, so that it can conduct the generator current and subsequently pinch. The initial ionization process can occur in several ways. One way is through the natural breakdown process associated with the driving power pulse, where the applied voltage exceeds the Paschen minimum along some trajectory between the generator electrodes determined by the radial and axial distributions of the injected gas at the time the generator voltage is applied. The radial gas distribution can vary with axial location (see Figs. IV-7 and IV-15) and time.

For many pulsed-power generators, the final stage of pulse compression results in a capacitive coupling to the vacuum assembly, called the prepulse, that precedes the main driving power pulse. If this coupling is sufficiently high, the gas can break down from the prepulse voltage and conduct the associated displacement current, resulting in further ionization. If this happens, an initial current path is already established when the main power pulse arrives. Sometimes, the prepulse is mitigated through clever design such as the use of prepulse switches. However, depending on the generator architecture, the mitigation approach can be complex and/or costly. Many high-current generators have prepulse.

Another way is to ionize the gas through an external process, e.g., using microwaves, electron beams (e-beams), e-beams in a magnetron-like discharge, or UV irradiation. In this way, there is a known initial current path reproducibly established before the prepulse or main pulse arrives. This is generally termed preionization (while one could call ionization by a prepulse also preionization, we will keep it in the category of breakdown). Again, depending on the process, ionization occurs along some trajectory and over some radial extent between the generator electrodes determined by the radial and axial distribution of the injected gas at the time the preionization is applied.

Independent of how it is done, reproducible and uniform initial ionization is thought to beneficially influence reproducibility and symmetry. Shot-to-shot reproducibility is a highly desired feature for any application. Azimuthal asymmetry, for example, can limit the final, stagnated-pinch radius, thus limiting the achievable density [IV-26]. Knowledge of the initial current path is also of primary importance for understanding experimental results and for input to simulations.

The breakdown process in gas-puff Z-pinches has been discussed in [I-12]. It is pointed out in that discussion that for a breakdown to occur, the voltage (electric field) across the gas must increase to a high-enough value that between successive electron-neutral collisions, the electrons can obtain sufficient energy to cause an ionizing collision with a neutral. Assuming that the voltage applied across the gas-puff electrodes rises rapidly enough, they estimate that to achieve 10 such ionizing collisions the neutral density should be $\sim2\times10^{16}$ cm^{-3} (for an A–K gap of 1.5 cm and typical ionization cross sections). This could be characteristic of the neutral density at the radial periphery of a neutral-density distribution (see Fig. IV-7). At this density, the time for significant ionization to occur is estimated to be $\sim$5 ns. In [IV-62], a model is described and extended to 2-D that characterizes the formation of the current sheath in the Z-pinch from this breakdown process. Filamentary structure in the current sheath

is observed in 2-D. Measurements on early ionization from prepulse and subsequent initial evolution of the current flow—with no external preionization—are reported [IV-44], [IV-63]. As stated in [I-12], the breakdown process itself is statistical, depends on the details of the injected gas and generator characteristics, and can lead to individual current-carrying channels thereby imprinting azimuthal nonuniformities and unstable filamentary structure at an early stage of the discharge. Thermal instabilities are discussed in [I-12]. In fact, for low neutral densities and under appropriate generator conditions, gas breakdown does not occur at all [IV-64]. This leads to the desire to establish a uniform, conductive current path before the generator current is applied, i.e., preionization. For high-current generators that rely on large prepulse or high dI/dt to initiate the gas breakdown (e.g., the most recent gas-puff experiments at Z, discussed in Section VI), the radius at which the breakdown occurs will depend on the Paschen minimum for the particular gas-puff and generator parameters. When large-radius, structured profiles are used, the radius at which the implosion begins might not be the nominal radius of the nozzle and might vary with axial location.

The use of microwaves for preionization was reported by [II-5] in conjunction with Ar gas-puff experiments on PITHON using a single-shell, conical nozzle, but the system was not described. The use of direct e-beam irradiation for preionization was investigated at UCI [IV-65]. The UCI Z-pinch driver was used (several hundred kiloamperes in 1.25 μs) with a 4-cm-OD, single-shell nozzle. The electron density distribution during the implosion for a low-density ($<10^{17}$ cm^{-3}), He gas Z-pinch was measured using a pulsed (5 ns), nitrogen-laser-based, 2-D, Mach–Zehnder interferometer both with and without preionization. Magnetic probes were also used to compare the strength of the inductive notch or current bite [drop in current associated with the increased circuit inductance see (III-27) and the accompanying text] that results from the pinch imploding. This is a qualitative and relative measure of compression ratio. The e-beam preionization system consisted of a 2-cm-diameter carbon bristle brush (as in a test-tube cleaner) bent as a circle whose radius is the nominal gas-puff nozzle radius and whose center is placed on the gas-puff axis but in a plane that is 1-cm axially outside the honeycombed anode (the nozzle is the cathode). Electrons emitted from the tips of the carbon bristles and axially directed toward the gas-puff assembly pass through the highly transparent honeycomb anode and interact with the cylindrical gas column. The electrons are driven by a capacitor discharge that generates $\sim$100 A of $\sim$20-keV electrons. The authors found that for this low-density gas puff, e-beam preionization resulted in a more axially uniform implosion and higher compression ratio than without preionization. Their analysis suggests that the amplitudes of the MRT instabilities are reduced with preionization.

A variation of this e-beam approach is employed on the capacitor-bank-driven, Ne gas, Z-pinch experiments carried out at the Weizmann Institute of Science (WIS). Details of the preionization system and its performance are described in [IV-66]. With this system, eight carbon-brush sources are fielded azimuthally symmetrically in a polyurethane ring located 9 cm below the midplane of the A–K gap. These sources point toward the center of the A–K gap on the axis of symmetry. The capacitor (0.5 μF at 14 kV) driving the e-beam sources in parallel is triggered $\sim$74 μs after the gas injection and 400 ns prior to the generator current pulse, delivering a peak total current of 1.1 kA in $\sim$600 ns. The carbon-brush sources emit electrons that interact with the gas inside the A–K gap and ionize it before the axial current starts to flow. Time-resolved visible light images suggest a reasonable degree of azimuthal and axial uniformity. While no systematic studies of the effects of preionization with this system have been performed, there are indications that the preionization contributes to the stability of the implosion, the reproducibility of the compression, and an increase in the total K-yield at stagnation [IV-67]. In addition, the influence of the preionization system on the implosion time was measured and showed the implosion time increasing when preionization was used, indicating that more gas was accreted by the pinch current [IV-66]. This system is currently used in all the WIS Z-pinch experiments (see [I-21], [IV-68]).

A series of preionization experiments and associated analyses was carried out at HCEI using the IMRI-4 capacitor bank (370–470 kA in 0.75–1.1 μs) and the GIT-4 inductive-storage generator (1.7 MA in 120 ns using a POS (see Section V-D and [IV-64], [IV-69], [IV-70], [IV-71]) with Ar gas in both a 6-cm-OD single-shell and an $r_N = 1.4/3.0$-cm shell-on-shell configuration. The motivation for this paper was the fact that the GIT-4 generator had a small prepulse because of its inductive-store architecture (see Section V-D) and gas puffs so driven responded in an irreproducible manner without preionization. For example, it was observed that for a shell-on-shell gas puff without preionization, the initial breakdown in both the inner and outer shells occurred in a random manner, allowing generator current to be initially shared between the shells at the beginning of the current pulse, defeating the desired snowplow stabilizing influence from the two shells. While IMRI-4 was a relatively low-current generator, it was used to test preionization concepts before they were fielded on the higher current, more-costly-to-operate GIT-4 device.

Three types of preionization schemes were studied extensively at the HCEI. The first, termed spark preionization, utilized the UV radiation generated by three localized, externally driven, surface flashover sources. These spark sources were embedded in the nozzle itself at three azimuthal locations, as shown in Fig. IV-18(a). The second and third were termed magnetron preionization: either in the planar, illustrated in Fig. IV-18(b), or cylindrical geometries. In the cylindrical case, the external electric field was applied radially, across the output of the nozzle itself and the relevant magnetic field component was in the axial direction. With the magnetron approach, the preionization is achieved by electrons emitted from the cathode and drifting azimuthally in externally applied, crossed electric and magnetic fields resulting in impact ionization of the neutral gas. The use of the term magnetron is somewhat misleading, as microwaves are not generated, but crossed electric and magnetic fields do cause electrons to drift azimuthally, as they do in a magnetron. In all cases, the preionization level was measured with an

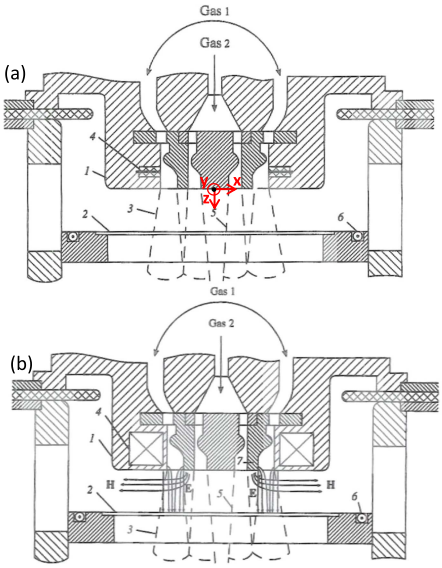

Fig. IV-18. Schematic of two preionization approaches developed at HCEI. (a) Spark preionization and (b) planar magnetron preionization. For both (a) and (b): (1) cathode, (2) grid anode, (3) outer gas-puff shell (6-cm OD), (5) inner gas-puff shell (2.8-cm OD), and (6) Rogowski coil. For (a): (4) spark illumination system and for (b): (4) external magnetic field coil and (7) additional electrode. Reprinted from [IV-71] (slightly adapted) with permission of Springer Science and Business Media.

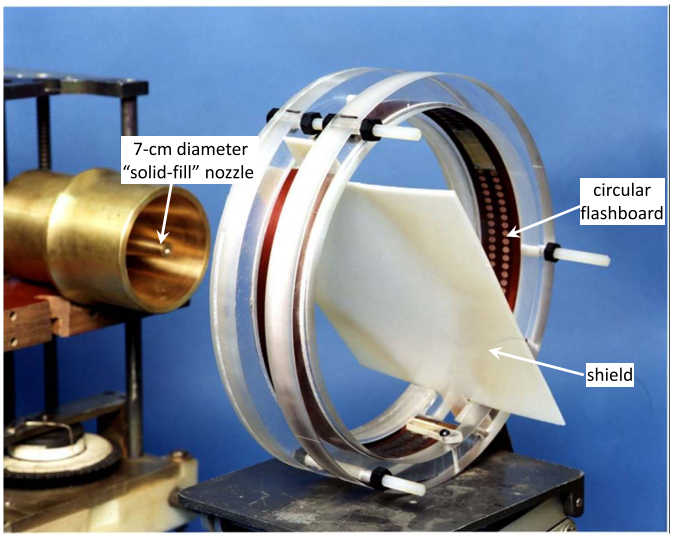

Fig. IV-19. Photograph of prototype circular-flashboard preionizer system developed at NRL, shown with a 7-cm-OD solid-fill nozzle shown in Figs. IV-2(c) and IV-7(d). The preionizer was generally fielded far enough from the gas-puff assembly that the generator was fired before flashboard plasma arrived at the gas-puff region. The shield is required to inhibit plasma flow to the gas-puff region. (Photo courtesy of Weber.)

electric probe at several axial locations in the interelectrode region [IV-64] and it varied between 1% and 100% of the neutral density.

The results of these experiments showed that the spark preionization scheme resulted in azimuthally nonuniform preionization, associated with the finite number of spark-source sites, while the magnetron approach gave an azimuthally uniform preionization. The magnetron approach was required for the initial current to always be carried in the outer shell only of shell-on-shell configurations (the spark preionization was irreproducible in this regard and depended on the polarity of the gas-puff-assembly electrodes). For single shell, Ar gas puffs, however, neither type of magnetron-induced, azimuthally uniform preionization resulted in higher compression ratios and higher K-shell yields (most evident in the faster rise time, higher current GIT-4 generator). This surprising result was explained by the fact that the induced axial magnetic field became frozen into the generator-current-carrying plasma and was compressed along with the plasma to a level comparable with the azimuthal magnetic field associated with the generator current. For the shell-on-shell gas-puff assembly, however, the planar magnetron did result in an ~25% higher K-shell power and somewhat better reproducibility than either the spark or cylindrical magnetron cases. This was explained by the following.

1) The electrical circuit required the planar magnetron discharge to be formed using the electric field associated with the voltage existing across the A–K gap during the conduction phase of the POS (see Section V-D), which resulted in a delay of ~1 μs before the initiation of the main driving current.
2) The stable outer shell and frozen-in magnetic field compressed and heated the gas associated with the inner shell.

Photoionization, utilizing UV radiation, has been used extensively for a variety of gas-puff experiments on Double-EAGLE, Saturn, and in the early Ar gas-puff shots on *Z* (see Section VI-A). The first approaches featured individual flashboards (sometimes referred to as flashcards) placed radially outside the pinch region in the axial midplane of the A–K gap and in azimuthally symmetric locations that were noninterfering with radially viewing radiation diagnostics. A capacitor drives a flashover across the surface of the boards producing plasma [IV-72] and intense UV. The hope was to produce enough photoionization so that the generator could be fired before the discharge plasma that is accelerated away from the flashboard could reach the gas-puff and vacuum feed region, possibly adversely affecting power flow. The UV emission of this type of surface flashover was characterized by [IV-73]. More than 60% of the UV emission was from photons of energy 20–70 eV, making the surface flashover appropriate for Ar photoionization as there is a broad maximum in the Ar photoionization cross section between 16 and 30 eV.

A different geometry for flashboard-generated photoionization was developed at NRL [IV-74], [IV-75]. A photograph of a prototype system is shown in Fig. IV-19. The nozzle shown in the photograph is a 7-cm-OD, solid fill nozzle [see Figs. IV-2(c) and IV-7(c)]. The NRL system comprises two semicircular flashboards arranged in a complete circle and axially separated from the gas-puff region. Shown in Fig. IV-20(a) is a drawing of this system as fielded to measure the neutral gas without preionization as well as the preionized electron density distribution caused by UV from the axially displaced, circular arrangement of flashboards. The high-sensitivity, two-color interferometer (described in Section IV-B) working at 1064 and 532 nm

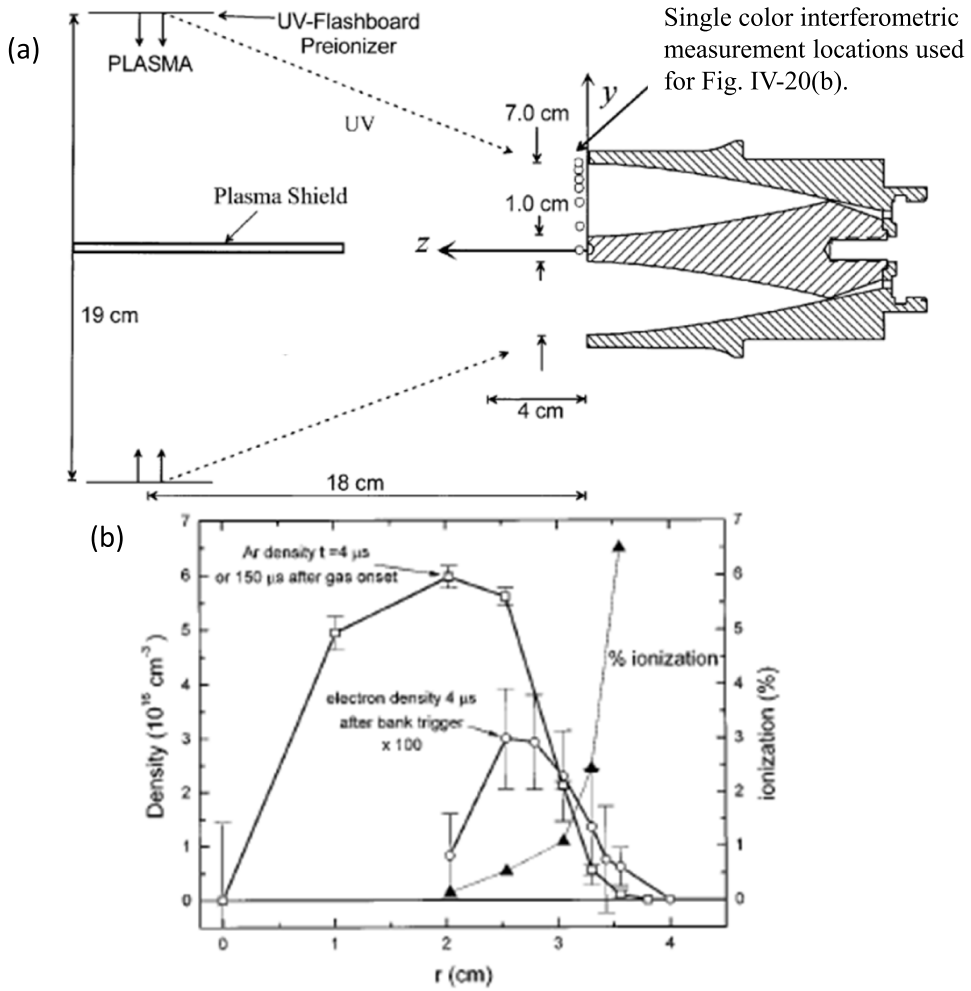

Fig. IV-20. (a) Side view of the nozzle and NRL prototype preionizer. (b) Radial density profiles of neutral gas and preionization electrons produced from photoionization. Also shown is the ionization percentage as a function of radius. Measurements taken 2 mm from nozzle exit plane. Reprinted with permission from [IV-75] (slightly adapted). Copyright 1999, AIP Publishing LLC.

was used to determine the neutral and preionized electron radial distributions [IV-74], [IV-75]. Referring to Fig. IV-6 and the accompanying text in Section IV-B, but considering the phase shift produced by electrons only, the line-integrated electron density at location (y', z'), namely $N_e(y', z')$, is proportional to the phase difference, $\Delta\phi_e(y', z')$ resulting from the difference in the optical paths of the probe beam and a reference beam that does not traverse the gas-puff region

$$N_e(y', z') = -\frac{\Delta\phi_e(y', z')}{r_e \lambda} \tag{IV-5}$$

where r_e is the classical radius of the electron (2.82×10^{-13} cm) and λ again is the laser wavelength. Note that while the phase shift for neutrals is inversely proportional to λ, the phase shift for electrons is proportional to λ and has the opposite sign to a neutral phase shift. According to Moosman *et al.* [IV-75], (IV-1) and (IV-5) can be used separately, and together at two wavelengths, to determine $\Delta\phi$ and $\Delta\phi_e$. The associated neutral and preionized electron density distributions can then be determined by Abel inversion. Fig. IV-20(b) shows a plot of the measured Ar neutral and preionized electron density as a function of radius for the 7-cm OD nozzle (shown in Fig. IV-19) 150 μs after the fast valve is actuated and 4 μs after the preionization capacitor bank is fired at an axial location of 2 mm from the nozzle exit plane (determined by separate neutral and electron density measurements) [IV-74], [IV-75]. For Ar, resonance fluorescence effects that could alter the index of refraction were shown not to be an issue for this measurement. Also, the plasma from the flashboard was diagnosed separately and shown not to be in the interferometer line-of-sight for the measurement times in Fig. IV-20(b). As can be seen, a preionized region is formed at the periphery of the neutral Ar distribution that extends ~1.5 cm into the neutral gas with fractional ionization from 1% to nearly 10%. At axial locations closer to the flashboard assembly, but within the expected 4-cm A–K gap, the fractional ionization is higher with no influence from flashboard plasma.

Comparisons of Ar K-shell yield with and without this preionization method for DM2 (2.25 MA in 300 ns) using the 7-cm-OD solid-fill nozzle in Fig. IV-19 have been reported [IV-42], [IV-74], [IV-76]. An additional variation was the inclusion or removal of cathode wires. There are a limited number of data points and some scatter in the data but

trends could be identified [IV-74]. Without cathode wires, the yield was considerably higher with preionization than without preionization. For the case where cathode wires were used, the yields with preionization generally define the upper boundary of the yields obtained without preionization. The wires and preionization increased the probability of a high-yield shot [IV-42]. A limited number of shots on Similar experiments were performed with Ar on Double-EAGLE were devoted to comparing Ar K-shell yield using a 12-cm-OD shell-on-shell-on-center jet (see Fig. IV-4 and the accompanying text in Section IV-B) with and without a preionization scheme similar to the NRL circular flashboard geometry (see Fig. IV-19). The results were not published, but it was observed that the average yield with preionization was higher than the average yield without preionization. The highest yield shot, however, had no preionization [IV-77]. Also, the scatter in the yield was less with preionization [IV-77]. A UV preionizer similar to the NRL prototype was used in most all MPI and TPSD Ar gas-puff development work [IV-77]. The NRL team attempted to measure the level of preionization (unpublished) but concluded that if there was preionization, it was below the sensitivity of the system [IV-47]. It was concluded that the UV radiation was absorbed by gas at large radius downstream of the A–K gap [IV-47]. The 19-cm diameter of the flashboards being too small compared with the 12-cm-OD nozzle (plus radial expansion of the gas) to allow direct irradiation of the radial periphery of the gas puff in the A–K gap region.

Similar experiments were performed with Ar on Double-EAGLE by the AASC team (again unpublished) using a 12-cm-OD, shell-on-shell nozzle with no center jet but designed to have a density distribution peaked on axis [IV-78]. In addition, in this set of experiments, the initial current distribution investigated using local magnetic probes [IV-79]. With limited statistics, the K-shell yield was observed to increase by $\sim$30% and the K-shell reproducibility was better with preionization. The localized magnetic probes and a zipper diagnostic exhibited very different behavior regarding the detailed current flow patterns and zippering depending on whether or not preionization was used.

The question of whether or not preionization is helpful for improving the quality of implosions remains somewhat open. For generators with low prepulse or low dI/dt, it seems that preionization is helpful in producing a more stable implosion with a higher compression ratio and higher K-shell yield. The picture is murky for generators with high dI/dt, e.g., Double-EAGLE, Saturn, or Z. Here, the cost of empirically determining the benefits of preionization precludes a thorough investigation of that option. Relying on breakdown to set the initial conditions for the implosion can lead to uncertainties in modeling and analysis, especially for large-diameter nozzles. However, preionization techniques do produce a reproducible initial plasma distribution that can be measured. Knowing the axial and radial distribution of electrons produced by a preionization process should be quite valuable for analysis, modeling, and simulation purposes, independent of the generator characteristics.

V. Implosion Phase

The implosion phase of a gas puff begins after a conducting plasma sheath has formed on the outer layers of the gas and the $\mathbf{J}\times\mathbf{B}$ force starts to accelerate the material radially inward. Section V-A primarily describes measurements of the plasma conditions during implosion of an annulus by two groups of researchers. The researchers disagree on whether or not the resistivity is classical. Typically, the plasma radius at the time of these measurements is about half the initial radius.

We then change our viewpoint from the microscopic properties of density and temperature to consider the global nature of the implosion. Section V-B describes zippering in Z-pinches, which is a natural consequence of the fact that the axial flow velocity from a nozzle is not infinite. The following section discusses the MRT instability. This is the most disruptive mechanism of a gas-puff Z-pinch during the implosion phase. There is extensive literature on this instability so we only highlight a few points relevant to gas puffs. Section V-D examines the design of pulsed-power generators and the problem of high voltages needed for high current. It would appear that these last two sections are not related; however, the concern about MRT instabilities and generator operation both arose from the requirement of greater K-shell yields. It is remarkable that both disparate problems can be partially resolved using the concept of snowplow stabilization presented in Section V-E.

A. Plasma Properties Early in the Implosion

In a series of papers, researchers at WIS reported on spectrally, temporally, and spatially resolved spectroscopic measurements during the early implosion phase. The pinch was a 4-cm-OD annular shell, 1.5-cm long, and $\sim$0.5-cm wide, of CO_2 on a capacitive generator that reached a peak current of 200–300 kA in about a half microsecond. Foord *et al.* [V-1] observed the pinch radially and used the red and blue Doppler shifted emission lines from oxygen ions OII–OVI to determine the radial velocity of the plasma. Ions in the lowest ionization state are at the leading, inward moving, edge of the plasma and those in higher ionization states are found at larger radii. In viewing the plasma axially they could determine the ionization front velocity from OII emissions. It was found that the radial velocity of the ionization wave was larger than that of the gas, and this wave velocity was consistent with heating by an electron thermal conduction front. Following this paper, Gregorian *et al.* [V-2]–[V-4] used the oxygen emission lines to measure the electron density and temperature in this gas puff. Another paper from the WIS team reported on the magnetic field radial distribution during the implosion using the Zeeman effect for the oxygen emission lines. Davara *et al.* [V-5] viewed the gas puff along the axial direction, which is perpendicular to the azimuthal field. Stark broadening dominates the linewidth in this plasma, so that polarization optics was employed to distinguish the π and σ polarization components of the lines. As noted above, the higher ionization states are found at larger radii and axial spectra at various distances from the axis allowed the team to obtain mapping up to $\sim$90 ns before stagnation and down to 0.7-cm radius of the plasma. The data for the magnetic field at two times during

the implosion were fit with a 1-D model for the diffusion and the best fit to the data provided an estimate for the electrical conductivity. The classical (Spitzer) formula for the electrical conductivity was evaluated using an electron temperature obtained from OII and OV emission lines. They found that magnetic diffusion was consistent with classical values. These magnetic field measurements, together with the previously measured ion velocity distributions, allowed the determination of the time-dependent relative contributions of the magnetic and thermal pressure to the ion radial acceleration across the plasma shell. Using the total measured current in the circuit and the outer plasma radius, it was also found that during the implosion, the plasma conducted the entire circuit current.

Often the Zeeman splitting of emission lines in Z-pinches can be smeared out due to Doppler and Stark broadenings. Tessarin *et al*. [V-6] describe the Zeeman broadening technique that works for certain atomic transitions, but can be used in quasi-isotropic field distributions. Under the Zeeman effect, the linewidths of the doublet components $^2S_{1/2}$–$^2P_{1/2}$ and $^2S_{1/2}$–$^2P_{3/2}$ would differ and thus can be used to measure the magnitude of the magnetic field. They proposed that the $1s^2 3s$–$1s^2 3p$ doublet at 4.39 and 4.33 eV of Li-like Ne would be a good candidate for this technique on ~1-MA generators. Detailed line profile calculations are needed for the analysis. To date, this spectroscopic technique for measuring magnetic fields has not been employed in Z-pinches.

Qi *et al.* [V-7] fielded an alternative diagnostic approach to spectroscopy for measuring the electron density in an imploding pinch. In [V-7], the operation and analysis of a laser shearing interferometer (LSI) is described and applied primarily to a neon gas-puff annular shell (3.5-cm OD) on the Hawk generator. Subsequently, Qi *et al.* [V-8] employed a laser wavefront analyzer (LWA) for the same purpose and on the same machine. The LWA has a polarized laser beam that traverses the plasma and is then focused into 10^4 spots on a CCD camera. Density gradients in the plasma cause the spots to move from their null position and the magnetic field induces a rotation of the polarized beam. Through Abel inversion, one can obtain the local electron density as a function of radius and axial extent. The LWA diagnostic works well before stagnation because afterwards the density gradients become so large that the spots are lost. The LSI experimental results were compared with RMHD simulations using the Mach2 code with Spitzer resistivity and the two were found to agree [V-9]. Subsequently, Qi *et al*. [IV-54] applied both the LSI and LWA to study the Ar plasma implosion from the TPSD triple nozzle (r_N = 0.5/2–3/5–6 cm) on Double-EAGLE in the long-pulse regime. The electrons were observed to be confined to a high-density layer at ~75 ns before stagnation. If all the ions are swept up into this layer, the mean charge state is known. The electron temperature was estimated from a non-LTE ionization model. With this information, the Spitzer resistivity was evaluated and used in an analytic model to calculate a skin depth. They found that this classical skin depth was much smaller than twice the thickness of the electron layer. The latter agrees with the skin depth based on an expression for an anomalous resistivity which is 20–60 times larger than the Spitzer resistivity. This conclusion for Ar on the Double-EAGLE generator at 3.5 MA contrasts sharply with that reported by [V-5] for CO_2 on a much smaller machine. However, the connection between the electron layer thickness and the magnetic skin depth needs proper supporting evidence based directly on magnetic field measurements.

B. Zippering

Since the early days of gas puffs it has been known that the gas outflow emerging from the nozzle forms an expanding cone from each orifice between the cathode and the anode because the gas has a finite temperature. Also, during the time to reach steady-state outflow from the nozzle, the mass per unit length is smaller at the downstream electrode than at the nozzle side (as a result of the finite transit time of the gas). However, when the generator is discharged, the pinch occurs much faster than the crossing time for the gas between electrodes, so the density profile is frozen at the instant of the discharge as far as the pinch dynamics is concerned. These features can lead to zippering, i.e., the implosion of the gas proceeds sequentially in time along the z-axis rather than simultaneously at all axial locations. This limits the aggregate maximum K-shell power, as the radiation is emitted over a longer time [IV-31]. An example measurement of this phenomena is shown in Fig. IV-15(b). Hussey *et al*. [V-10] described a simple extension of the snowplow model to account for the nonuniform gas distribution. The gas shell is divided into a number of axial segments and the equation of motion was used to calculate the radial and axial velocity components of each segment. The mass of each segment is just the volume swept over by that segment times the local density. When this model is applied to the expanding flow from an annular nozzle, the zippering time is given by the delay between the first and last segments to reach the axis. Based on this model, three approaches were proposed to remove the zippering. The first approach is to design a nozzle with a high-Mach-number flow such that the outflow is less divergent. The model showed that a Mach number of >10 would be needed to reduce the zippering time to a couple of nanoseconds. However, such nozzles have never been employed for gas-puff Z-pinches. The second approach is to make use of the fact that the outflow from the nozzle takes >100 μs to reach steady state. Even for a large flow velocity of 1 cm/μs and an A–K gap of 2 cm, the transit time is ~2 μs. Hence, if the generator is fired while the mass flow rate is still increasing and the implosion is only ~100 ns, then the mass per unit axial length on the downstream (anode) side of the gap is less than near the nozzle exit, compensating for the downstream implosion starting at a larger radius. The model indicated that a mass decrease of ~20% would minimize the zippering time. Firing before steady state also has the advantage of limiting the time during which the gas can leak back into the vacuum power flow region and potentially cause shorting. The third approach was simply to employ nozzles with an inward tilt toward the axis. Hsing and Porter [V-11] tested these ideas by fielding three different nozzles. The control was a Mach-4 nozzle that produces a radiation pulsewidth from neon of $\Delta t \sim 10$ ns.

The same nozzle with a 10° tilt reduced the pulsewidth to 4 ns. The same improvement was achieved with a third nozzle of Mach-8 flow only if the generator was fired early in the mass flow rate rise time.

Deeney *et al*. [V-12] showed that tilting the nozzles to remove zippering also had a dramatic improvement on the K-shell yield. A 2.5-cm-OD Mach-4 nozzle with a 10° inward tilt produced 13 kJ of Ar K-shell on Double-EAGLE, but only 3.5 kJ if there was no tilt. Another approach to controlling zippering was described in [IV-42]. Through a choice of the plenum pressure and timing of the discharge relative to the opening of the valve, Levine *et al*. [IV-42] found that they could control the direction of the zippering from the cathode to the anode, or vice versa. Thus, for solid fill loads they could minimize the effect of zippering on the K-shell power and yield.

C. Magnetic Rayleigh–Taylor Instability in Gas Puffs

If a diffuse cylindrical Z-pinch plasma is perfectly conducting and in pressure equilibrium, then it only exhibits the $m = 0$ (sausage) and $m = 1$ (kink) modes of MHD instability, whereas the modes with higher values of m (filamentation, screw, etc.) do not grow. Moreover, if the diffuse density and pressure profiles are smooth enough, satisfying the so-called Kadomtsev stability criterion [I-14], [V-13], as in magnetic confinement configurations, then the sausage mode is stabilized and the kink mode dominates. The MRT instability of an accelerated imploded plasma is different because modes with all values of m are unstable independently of the unperturbed density and pressure profiles. The growth rate of the kink $m = 1$ MRT mode is close to that of the dominant sausage $m = 0$ MRT mode. The stabilizing factor $\boldsymbol{k} \cdot \mathbf{B}$, which is only nonzero for the kink mode, tends to reduce its growth rate. Development of the kink mode is typically observed close to and after stagnation, when the radius of the narrow stagnated plasma column becomes the relevant length scale, and the column sometimes starts to twist. The geometry of the magnetic field in a Z-pinch without an externally applied magnetic field favors azimuthal correlations of perturbations characteristic of the sausage MRT modes, particularly for short wavelengths, which are thereby seen to dominate during the run-in phase.

The classical Rayleigh-Taylor (RT) instability occurs when a light fluid supports a heavy fluid against a gravitational field (g) directed from the heavy to the light fluid. Perturbations of the interface grow exponentially according to $\exp(t\sqrt{kg})$, where $k_{\mathrm{RT}} = 2\pi/\lambda_{\mathrm{RT}}$ is the RT wavenumber and t is the time. In the nonlinear regime, spikes of heavy fluid fall (move in the direction of g) and bubbles of the light fluid rise (move opposite to the direction of g). In a Z-pinch, the magnetic field in the vacuum outside the pinch represents the light fluid and it accelerates the pinch inward toward the axis, so the effective gravity points outward. By dimensional analysis, the change in the pinch radius is related to the acceleration g as $\Delta r = gt^2/2$, so the amplitude of a perturbation grows as $\exp[2\sqrt{(\pi\,\Delta r/\lambda_{\mathrm{RT}})}]$. For a pinch that implodes from 2 cm and a long wavelength of 0.5 cm, the perturbation would amplify >1000 times. Note that

$$\#\text{ of MRT e-foldings } = t\sqrt{\mathrm{kg}} = 2\sqrt{\pi r_o/\lambda_{\mathrm{RT}}} \qquad \text{(V-1)}$$

is independent of the implosion time and depends only on the ratio of the radius to the wavelength. Deeney *et al*. [III-11] measured the dependence of the Ar K-shell yield (>3 keV) on Double-EAGLE as the radius of a gas puff was increased from 0.75 to 2 cm. The nozzle formed a thin annular shell and the mass loading was decreased as the radius increased to roughly maintain matched conditions. The idea was that by increasing the radius at a fixed implosion time the η parameter for Ar would be larger and a greater yield might be expected. However, for two different generator charge voltages the maximum yield of 18.7 kJ at 60 kV (12.5 at 55 kV) was found at a radius of 1.25 cm, and Y_K dropped at a 2-cm radius to 14.5 kJ at 60 kV (11 kJ at 55 kV). The falloff in yield was attributed to a lower density at stagnation, but more likely due to disruption by MRT instabilities. For instance, the Kr simulations of Cochran *et al*. [V-14] showed that thin shells of initial radius greater than ~2 cm would breakup before the implosion onto the axis could be completed. Systematic increase in radii from 1 to 1.75 to 2.5 cm on Hawk with Ne, under conditions of constant implosion kinetic energy, also showed a decrease in K-shell yield at a 2.5-cm radius [III-16]. Analysis suggested this decrease resulted from a lower compression ratio that was related to the MRT instability.

The above simple analysis for (V-1) implies that the shortest wavelengths are the fastest growing, but a theoretical analysis in [V-15] shows that a finite resistivity imposes a minimum unstable wavelength. Resistive MHD simulations in [V-16] supported this theory. Baksht *et al*. [IV-32] at the HCEI found a sharp decrease in the K-shell emission from Ar on GIT-4 as the load mass in a 2.8-cm-OD puff was decreased but a much more gradual fall off in yield as the load mass increased. This later feature was attributed to a lower electron temperature in more massive loads. The larger classical resistivity (proportional to $1/T_e^{3/2}$) causes a greater penetration of magnetic field into the plasma shell, and short-wavelength structures diffuse away. Furthermore, multimode simulations by Douglas *et al*. [V-17] found an inverse cascade, i.e., short-wavelength structures combine into ever larger ones.

The most deleterious wavelengths in the nonlinear regime would be those on the order of the shell thickness, for then the bubbles can break apart the imploding shell. A time lapse simulation illustrating the growth and nonlinear development of the MRT instability in isodensity contours is presented in Fig. V-1 from [V-18]. The initial radius was 2 cm and shell thickness 0.1 cm. Actually, the calculation was for tungsten but the start-up conditions are equivalent to a thin shell of tungsten gas with random perturbations. By 100 ns [Fig. V-1(b)], there is one large bubble and by 110 ns [Fig. V-1(c)], there is a collection of nonlinear spikes and bubbles. The visible images of a neon gas puff in Fig. I-1 show the development of spikes and a bubble has turned into large wings near the cathode side. Hussey *et al*. [V-19] approximated the nonlinear development of the MRT instability with a heuristic model. The bubble and spike structure of the implosion was related to the width of the radiation pulse at stagnation, and in turn this was related

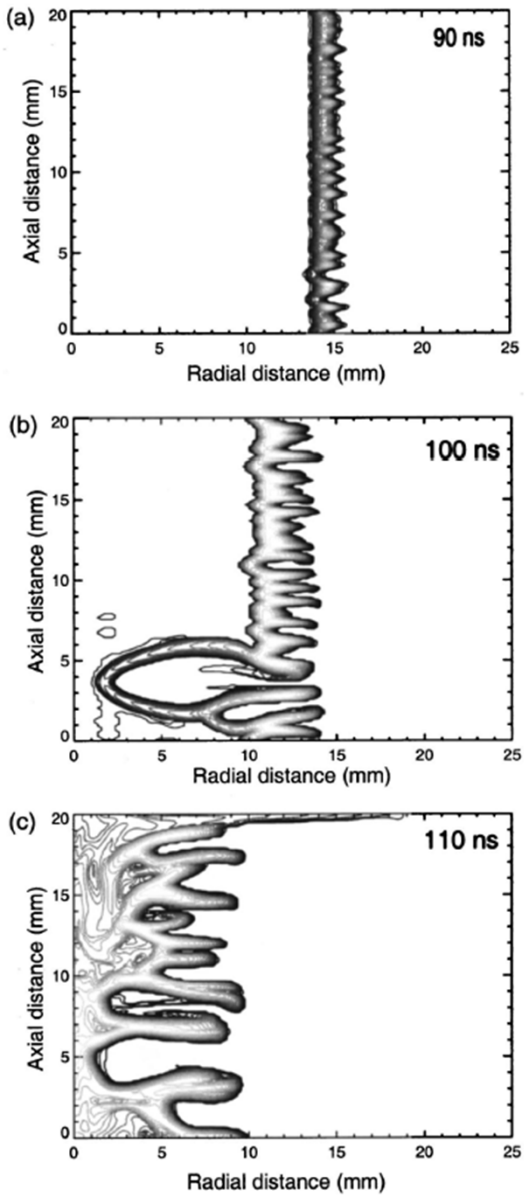

Fig. V-1. Simulation showing the development of the MRT instability from an initially thin shell of a 2-cm radius and a 0.1-cm thickness. The instability was seeded by 5% cell-to-cell density perturbations. The times are (a) 90, (b) 100, and (c) 110 ns after the current initiation. Reprinted with permission from [V-18]. Copyright 2001, AIP Publishing LLC.

through the model to the initial perturbations. Comparison of the theory with data from gas puffs on Double-EAGLE suggested that the initial perturbations in gas puffs increase with their diameter. Shishlov *et al.* [IV-43] developed a simple extension of the snowplow model to 2-D to study the bubble and spike formation, though the dynamics is questionable when the shells interpenetrate.

As the MRT instability develops into the nonlinear stage, mass moves from the bubble to the spikes. Even if the mass per unit length, $m(z,t) = \int_0^{r_o} \rho 2\pi r dr$, is fairly uniform as a function of the axial coordinate z at the start ($t = 0$), by the end of the implosion phase, $m(z, t_{\text{imp}})$ can be a highly irregular. This is illustrated in Fig. V-2 taken from simulations of Ar pinches on Decade Quad in [V-20]. The initial $m(z,0)$

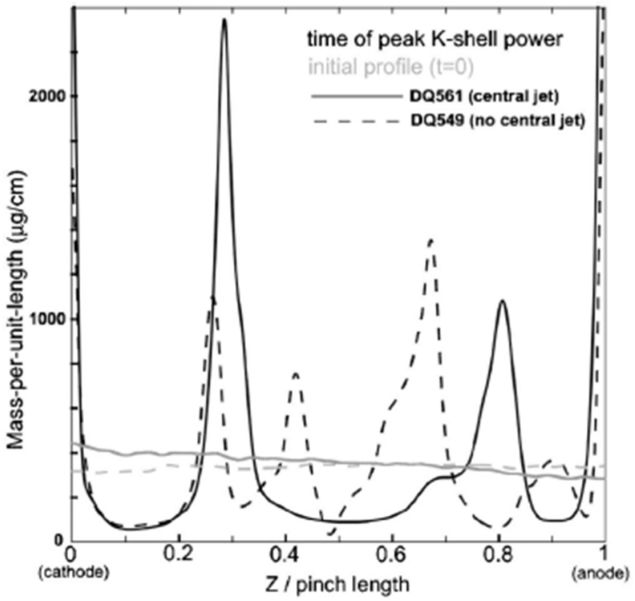

Fig. V-2. Simulations showing how the mass per unit length changes along the A–K gap from the initial, nearly uniform distribution to that near the time of peak power. The axial redistribution of mass results form the development of the spikes and bubbles of the MRT instability. Reprinted with permission from [V-20]. Copyright 2007, AIP Publishing LLC.

is shown for two different initial density profiles and both exhibit a slight decrease from the cathode (nozzle) to the anode. However, by the time of assembly on axis, the mass per unit length can vary by factors of ~20 along the axis where the bubbles have lost mass to the spikes.

The above is a cursory review of the MRT instability in Z-pinches. Douglas *et al.* [V-21] presented a review of the MRT instability up to 2001 with a strong emphasis on wire arrays. In the same time period, there are also reviews of the fundamental physics of the MRT instability in [I-12] and [I-14]. The reader can consult these articles for more extensive discussions.

D. Pulsed-Power Considerations

Sources of current are required to drive the gas-puff Z-pinch load. These drivers can take the form of capacitor banks that deliver current directly to the gas-puff load or pulsed-power generators that use additional forms of power conditioning. The differences between these drivers are the inherent rise time, t_{rise}, of the output current (usually defined as the time to peak current for a matched load) and the driving voltage. In the first case, the capacitors are configured electrically in parallel in air or in a Marx configuration (parallel charging, series discharging through a switch array, usually in oil). For these drivers, $t_{\text{rise}} \sim 0.5$–1 μs and the driving voltage can be several tens of kilovolts to many hundreds of kilovolts (e.g., the UCI facility, the WIS facility, Hawk, and IMRI-4, all referred to in the previous sections). In the second case, additional power-conditioning stages, either through pulse charging and switching out of successively lower inductance capacitors (usually using water as the dielectric, thus the connotation water-line generators) or through inductive storage techniques,

can have $t_{\rm rise}$ ~100–500 ns and output voltages of hundreds of kilovolts to several megavolts (e.g., Double-EAGLE, Saturn, Z, GIT-4, also all referred to in the previous sections). For the remainder of this section, we focus on the second case of pulsed-power generators.

Let us emphasize why the MRT instability and (V-1) had such an impact on the development of plasma radiation sources. Suppose one has a matched load for a generator in the sense that the load allows the generator to deliver close to its peak output current, i.e., maximum energy at or near the time of implosion. The parameter C_M in (III-46) is specified by the value at which $\varepsilon_{{\rm kin},f}$ of (III-47) is a maximum for a shell-like density profile. We consider this profile and the kinetic energy because before the mid 1990s it was believed that one needed to optimize the final kinetic energy per ion for maximum K-shell production. For this matched load, the coefficients within parentheses of (III-48)–(III-51) are fixed. There are three scenarios for which a larger initial radius for the load would be beneficial to the design of radiation sources: 1) an increase in the Z_A of the load; 2) an increase in the load current; and 3) an increase in the pulsewidth of the electrical driver. Identifying methods to mitigate the expected increased deleterious effects due to the MRT instability associated with larger radius loads (V-1) becomes an essential aspect of any effort to improve K-shell sources. We discuss each of these scenarios in turn.

1) For fixed generator parameters (e.g., V_g, t_g, L_g, R_g, and ΔL as defined in Section III-D), to reach the K-shell of a larger Z_A requires an increase in the kinetic energy per ion to account for the increase in $E_{\rm min}$ in the denominator of (III-56), and an increase in η to account for the additional radiation losses at higher Z_A. This can be achieved by increasing the final velocity u_f, which in turn increases with the initial radius r_o by (III-50). To maintain matched load conditions in (III-51), the product $M_o r_o^2$ must be the same so that M_o must be decreased. In principle, one would perform an $M_o r_o^2$ scan to verify these scaling arguments. In practice, time constraints limit the experimental variations with various nozzle radii that can be performed on a high-current, pulsed-power generator so that detailed variations in radius as well as mass are rarely carried out to find the optimum combination of mass and radius for maximum radiation from a given generator. In addition, without very good atomic physics models of the higher lying shells (e.g., L- and M-shell), it is difficult to compute η *ab initio* and thus computationally determine the optimum mass and radius for maximizing the K-shell radiation. Moreover, for high-current generators (>6 MA) with convolutes connecting separate magnetically insulated transmission lines, there can be significant current losses near the convolute. At present, this phenomenon is not well understood and must be estimated in simulations.
2) According to (III-49), an increase in the load current for a fixed compression ratio and $Z_A$could be used to increase the mass load at the same final velocity and thereby increase the radiation output. However, as has been pointed out in Section III-E, as the mass (current) increases, the optimum mass for maximum K-shell radiation scales less than $I_{\rm pk}^2$ while the mass needed to maintain a matched load condition continues to scale as $I_{\rm pk}^2$. Thus, to maintain matched conditions in (III-51) with a fixed $t_{\rm imp}$, higher current, and optimum mass for radiation, one would increase r_o. There are issues associated with scaling to higher $I_{\rm pk}$ with fixed $t_{\rm imp}$ that involve details associated with the electrical design, size, and cost of the higher current pulsed-power generator. From (III-47) at the matched condition, $I_{\rm pk} \propto I_g$ and $t_{\rm imp} \propto t_g$. By the first definition in (III-38) a higher $I_{\rm pk}$ with fixed $t_{\rm imp}$ can be achieved only by increasing the voltage of the pulsed-power generator (V_{go}) and/or by lowering its inductance (L_g). But higher voltage presents design challenges for the vacuum insulator (usually a vacuum–water interface), generally results in a large footprint for the generator, and involves relatively high-cost capacitive-power-conditioning technology. Lowering the inductance, i.e., smaller gaps in the magnetically insulated transmission lines, might lead to power flow issues in the vacuum (e.g., breakdowns and current loss) at high voltage.
3) In contrast to the above issues, increasing the electrical pulse width of the generator, i.e., t_g in (III-35), has some advantages. From (III-38), the same I_g can be obtained by lowering V_{go} and/or increasing L_g, exactly the opposite of the case in 2). Again at the matched condition, $I_{\rm pk} \propto I_g$ and $t_{\rm imp} \propto t_g$, and for the same peak current, (III-51) can be satisfied by increasing r_o as much as $t_{\rm imp}$ is increased. This approach would not increase η because the final velocity would be the same, nor the kinetic energy by (III-49). The primary advantage of this approach is that, if the MRT instability can be overcome, then high-current generators could be designed and built of smaller size and cost for the same radiation output. Finding methods to allow larger radius gas-puff Z-pinches without incurring the deleterious effects of the MRT is an important goal. In the following section, we discuss possible mitigation schemes for the MRT.

An alternative design for a generator that adopted the approach of 3) but used small-radius loads to bypass the MRT problem was to decouple t_g from $t_{\rm imp}$. Inductive store techniques (see [V-22], [V-23]) can be used to reduce the rise time of the current into the Z-pinch ($t_{\rm imp}$) while the generator current has a long rise time. In the inductive-storage approach, an opening switch shorts out the generator electrical pulse so that a significant fraction of the originally capacitively stored energy is stored in the circuit inductance. At peak current, ideally, the switch opens, driving current to the Z-pinch in a time that is short compared with the switch conduction time. The faster rise time will lead to a smaller radius gas puff than would have been required for the longer intrinsic rise time of the generator and the Z-pinch will be less susceptible to MRT. In principle, high-voltage issues can be minimized and current transfer optimized if the opening switch is located as close to the gas-puff load as possible. One can take an alternative approach and increase the radius even more to accommodate

the longer rise time. The inductive store approach transfers the inherent electrical risks in a high-voltage, low-inductance driver to the rapid and efficient coupling of the current from the storage inductance to the load.

An example of such an opening switch is the POS (also known as the plasma erosion opening switch) [V-23]–[V-29]. The plasma is injected in vacuum between the electrodes of the generator upstream of the gas-puff load, shorting out the electrical pulse from the generator. At a prescribed set of conditions that depend on the plasma density, species, electrode geometry, and current time history, the plasma will cease conducting, i.e., open, and transfer current to the gas-puff load in a time that is short compared with $t_{\rm rise}$. The high voltage is generated only at the time of the switch opening, in vacuum, and in proximity to the gas puff. An extension of the opening switch approach is to use several opening switches in parallel that sequentially steepen the current rise time [V-22], [V-30], [V-31]. An inherent drawback to the inductive-store approach is that as a consequence of magnetic flux conservation, the peak current delivered to the gas puff will be less than the peak current conducted, even for an ideal opening switch [V-22], [V-32]. Several experiments using a POS with a gas-puff Z-pinch are described briefly in the following.

Early on, the POS was used to decrease the rise time of two water-line generators that had fast (less than 100 ns) rise times. First-order comparisons were made of the power flow and behavior of the Z-pinch load with and without the use of the POS for the same Z-pinch load configuration. No attempt was made to reduce the radius of a gas-puff assembly whose mass had already been optimized. The first use of the POS was on the PITHON generator (operated at ~3 MA in ~80 ns) at PI [V-33], [V-34]. For this paper, the POS was coupled to a Ti wire array load. The POS resulted in a decrease in the rise time of the current getting to the load and there was some evidence of reduced current loss in the vacuum feeds upstream of the array compared with the no-POS case. We conjecture that this could be a result of generating high voltage at a time when significant current is flowing, leading to better magnetic insulation of vacuum-flowing electrons. Time-integrated pinhole camera images show that the usually axially twisted and irregular-shaped pinch was axially more uniform when the POS was used. No radiation yield measurements were reported. The first time a POS was used with a gas-puff Z-pinch was on the Gamble II generator (operated at 0.94–1.45 MA in ~60 ns) [II-20]. A Ne gas puff was used with the nozzle described in Fig. IV-1 [IV-28]. Data with no POS were taken over a range of plenum pressures for five different peak driving currents and an optimum plenum pressure (mass) for a given current was obtained. The optimum pressures corresponded to ~15–45-μg/cm initial mass per unit length at the lowest and highest currents, respectively, in the gas puff (computed under the assumption of a thin, annular shell). The POS reduced the current rise time into the gas puff from 60 to 20 ns and the peak value of the current was reduced by as much as a third (1.25 MA with no POS versus 0.8 MA with POS). While there was significant scatter in the data, comparing their upper bounds suggests that there is as much as a 2.5-fold increase in the Ne K-shell yield with POS compared with the non-POS case at optimum pressure for each peak driving current. This is a remarkable result because of the lower current with the POS. Spatially resolved spectroscopy showed that the POS also improved the pinch quality in both the axial (as with [V-33] and [V-34]) and radial directions. The authors speculate that eliminating the early portion of the current rise limits the growth of instabilities, resulting in a better radiator. We conjecture that for the nozzle radius used, the nozzle was better match in terms of energy per ion (η^*) to the faster rise time afforded by the POS.

The group at HCEI was a leader in using inductive storage for high-power electrical pulses. The lower cost and reduced high-voltage design aspect of inductive store was an important influence for the development of the GIT generators at HCEI [V-25]. GIT 4 was used extensively to study gas-puff designs to maximize the Ar K-shell (Section VI-A).

The design for the Decade Quad (5.7 MA in 220 ns with a Ar gas-puff load) [V-35], [V-36], [IV-39], [IV-53] was based on a long-implosion time and inductive store. This effort spurred research on using an ~1-μs-conduction-time POS to drive both a bremsstrahlung diode and an Ar gas puff. Neon gas-puff experiments were carried out [V-37] using a Decade Quad prototype generator called Falcon at PI, which provided 3 MA in 1.2 μs without the POS and up to 1.8 MA in as little as 190 ns with the POS. The annular, conical nozzle used was of the type illustrated in Fig. IV-1. By varying the POS plasma density, current rise times between 170 and 350 ns could be generated. The highest Ne K-shell yield obtained was for the case with a 190-ns rise time and a peak current of 1.8 MA. In this case, the K-shell yield was 13.5 kJ with a mass per unit length of 90 μg/cm compared with 4.5–7.6 kJ without the POS at comparable currents but rise times of ~500 ns. The authors ascribe the higher yield to higher kinetic energy with the shorter rise time.

A microsecond-conduction-time POS was used to drive an Ar gas puff using the ACE 4 generator (~2.9 MA, 200-ns implosion time) at MLI. ACE 4 was also a prototype device in the decade development program that featured novel capacitor design. Experiments were carried out to access the efficacy of different nozzle designs [I-16], [IV-33] (see Section IV-A). Work at the NRL Hawk generator (~0.6 MA in ~100 ns) used an ~1-μs conduction time POS to assess the effect of increasing nozzle radius while keeping the kinetic energy per particle constant (see [III-16] and the references therein). (See Section IV-A.)

It is interesting to note that based upon simple scaling relationships, it was argued that a POS was necessary in order to achieve significant K-shell radiation [V-38]. In order to produce K-shell radiation from a given species the η (III-56) or more generally η^* (III-58) must be a few. This specifies the final velocity u_f which scales as $r_o/t_{\rm imp}$ (III-50). Now r_o and $t_{\rm imp}$ can change by the same factor, but (III-49) implies that for a fixed peak current and u_f, the total mass M_o is constant. From (III-61), the K-shell radiation scales as $Y_K \sim n_e n_i \pi r_f^2 \Delta t$, with the neglect of quenching, But for a fixed mass, $n \sim 1/r_f^2$ and one can scale the pulsewidth as

$\Delta t \sim r_f/u_f$. Finally, for a fixed compression ratio, $r_f \propto r_o$, and one is forced to conclude that

$$Y_K \sim 1/r_o \sim 1/t_{\text{imp}} \tag{V-2}$$

i.e., the above argument concludes that the K-shell yield decreases with increase in radius or, equivalently, implosion time (see [IV-39], [IV-55]). For some time this argument pushed the research in the direction of fast implosions with a fast rise to the current to maximize K-shell emission. Hence the interest in a POS, wherein a slow, less expensive generator could be turned into a fast one. The limitation in this relation will be shown not to hold in Section VI-A.

E. Snowplow Stabilization

As discussed in Section III-E and many places in the immediately preceding sections, increasing the radius of a gas-puff shell would attain higher η values. This could be done at a fixed implosion time by increasing the initial radius, such that on moderate current generators (few MA) one could achieve efficient Ar K-shell radiation or inefficient Kr K-shell on a high-current machine (>15 MA). Likewise from Section V-D on pulsed-power considerations, it would be advantageous for generator design and facility cost if long implosion times from large radii puffs could be stably imploded to produce powerful radiation sources. However, by (V-1) the MRT instability is the more disruptive, the larger the radii. The inability to produce intense radiation sources with large radii and/or long implosion times was a serious impediment to further progress in gas-puff Z-pinches [III-11], [V-39]. During the 1990s, there grew intense interest in devising means to mitigate the MRT instability. Deeney *et al.* [II-6] reviewed the research on long-time implosions and, in an associated article, Douglas *et al.* [V-21] reviewed many proposed and some tested means of stabilization. Those potentially applicable to gas puffs include: 1) magnetic shear with the introduction of an ambient axial magnetic field; 2) azimuthal velocity or rotation; 3) loads of higher atomic number that enhances the resistivity ($\eta_{\text{res}} \propto \overline{Z}/T_e^{3/2}$) and the magnetic diffusion length scale; 4) viscous damping due to large ion–ion mean free paths; 5) gyrokinetics effects in the low-density, large-radii region of a gas puff; and 6) tailored density profiles. The review by Ryutov *et al.* [I-12] made similar points on stabilization. For reference in a later section on K-shell radiating puffs with an embedded axial magnetic field, we note a simple stabilization criterion. If the initial axial magnetic field is B_{zo} and it is flux frozen into the pinch of initial radius r_o, its value at the final radius is $B_z = B_{\text{zo}}(r_o/r_f)^2$. The azimuthal field at this time is $B_\phi = 2I_{\text{pk}}/r_f c$. To first order, the axial field would stabilize the pinch if $B_z > B_\phi$, or

$$B_{\text{zo}}(\text{kG}) > 200\frac{I_{\text{pk}}(\text{MA})}{r_o(\text{cm})}\left(\frac{r}{r_o}\right). \tag{V-3}$$

Stabilization of the MRT instability by tailored density profiles refers to structuring the radial gas distribution produced by the nozzle such that the MRT growth is controlled or eliminated. As mentioned in Section II on early history, Baksht *et al.* [II-8] were the first to report that double-shell gas puffs led to a significant improvement in an ~1-keV radiation output compared with single-shell ones, but they did not discuss the MRT instability. Gol'berg and Velikovich [V-40] attributed the improved implosion to a accretion by a dense shell. They showed that the nonmagnetic RT instability of a dense planar layer accelerated by a light gas can be suppressed if the layer accretes mass through a shock front moving into an unperturbed gas. A linear stability analysis was developed for the self-similar solutions describing the gas between the accelerating piston and the shock front. Perturbations of wavelength λ did not grow until the thickness of the accelerated layer exceeded λ, and such disturbances can be damped if the acceleration was constant or negative. This process was termed snowplow stabilization.

Cochran *et al.* [V-14] performed r-z RMHD simulations on a hypothetical 60-MA generator to study the MRT instability for shells and uniform solid-fills of Kr. Starting with initial perturbations in each density configuration, growth rates were determined from the increase in the axial kinetic energy over the entire computational plane. The growth rates and disruption were smaller for uniform solid-fills than shells, either single or multiple. Roderick *et al.* [V-41] also compared the MRT instability through r-z RMHD simulations for a Kr shell versus a solid-fill on the Saturn generator. Fig. V-3 shows that the annular shell has broken apart but the uniform solid-fill is still intact just before the axis is reached. The OD for both profiles was 4.5 cm. Douglas *et al.* [V-39] discuss further results on mitigating the MRT instability in gas puffs.

Other tailored profiles were also investigated. Velikovich *et al.* [V-42] proposed a profile composed of an outer region with increasing density toward the axis as $\rho \sim 1/r^3$ bounded by an inner vacuum region. As mass is accumulated in a layer sweeping through the outer region, the pressure driving the layer varies as $B^2 \sim I^2/r^2$. This will balance the ram pressure ρu^2 that the layer experiences, and the velocity varies as $u \sim (I/r)\sqrt{\rho}$. For the chosen density profile, the layer will decelerate at constant current until the inner region is reached. If the radius of the inner vacuum is not too large, the layer will then accelerate toward the axis but the MRT instability will not disrupt the layer because of the limited growth periods. Fig. V-4 shows that the axial kinetic energy, representing MRT growth, is damped after an initial acceleration and until the inner vacuum is reached for the initial density profile in the inset. RMHD simulations [V-43] showed that such a tailored profile starting at 10-cm radius could produce tens of terawatts power in Ar K-shell radiation on a 5-MA generator.

In principle, the ultimate tailored density profile for MRT stabilization would have no acceleration, but a constant velocity throughout the implosion. Hammer *et al.* [V-44] showed that if one assumes a constant velocity, $r_p = r_o - |u_p|t$, then (III-18) and (III-26) with $R_{\text{load}} = 0$ can be used in the circuit equation (III-17) to give a closed-form integral solution for the current. For a constant u_p, (III-28) and (III-29) can be combined into to $\rho(r) = (I/c)^2/(2\pi r^2 u_p^2)$. Thus, for a specified driver voltage, an initial density profile can be determined that implodes

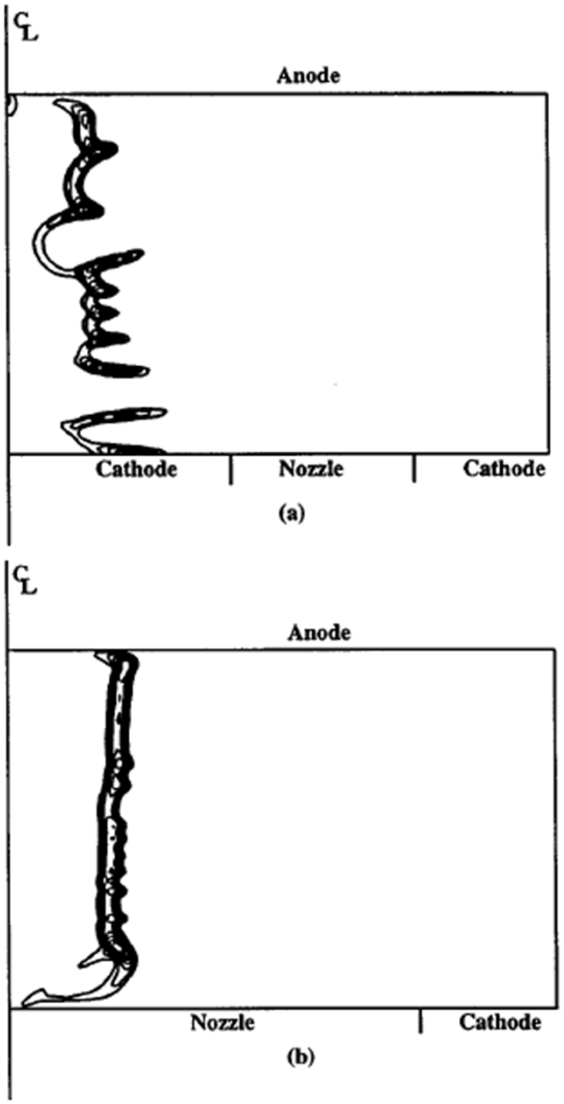

Fig. V-3. Isodensity contours of a simulated implosion on the Saturn generator of a Kr gas puff showing improved stability for a fill compared with a shell. (a) Initial density profile was a shell from a 4.5-cm-OD nozzle. (b) Fill distribution of the same diameter. Reprinted with permission from [V-41]. Copyright 1998, AIP Publishing LLC.

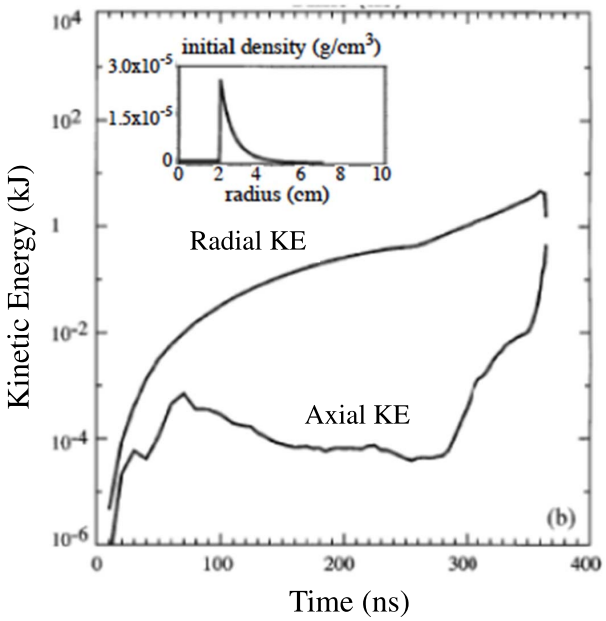

Fig. V-4. Radial and axial kinetic energies versus time for a simulated Ar gas puff driven by a constant 5-MA current. Stagnation occurs at 360 ns. Inset: initial density distribution. Reprinted figure with permission from [V-42]. Copyright 1996 by the American Physical Society.

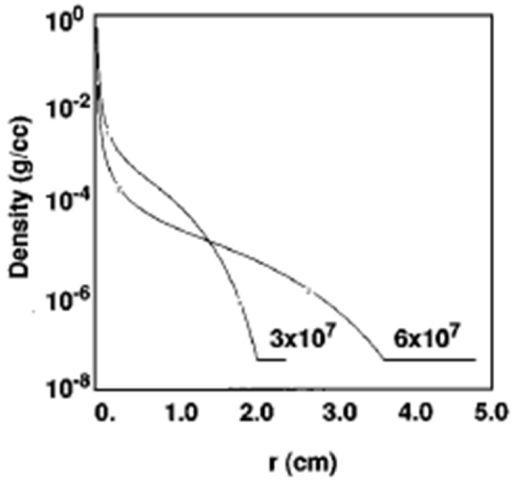

Fig. V-5. Centrally peaked initial density profiles that produce a constant velocity implosion computed for parameters of the Saturn generator. The velocities are noted in cm/s. Reprinted with permission from [V-44]. Copyright 1996, AIP Publishing LLC.

without acceleration. Such profiles for the Saturn generator are shown in Fig. V-5 for two velocities. Obviously, the concept of a constant velocity implosion arising from a calculated initial density profile is idealized. Even though the density falls orders of magnitude in the outer region from the central peak, the gas must be accelerated up to the constant velocity as the current turns on. The analysis in [V-44] ignores this phase where the MRT instability would be active. However, the basic concept of stabilizing the implosion by accreting mass from a centrally peaked density profile became a target of future nozzle development. The centrally peaked profile in (III-36) used in the 0-D calculations of Figs. III-3 and III-4 was chosen to represent a more realistic distribution with $d\rho/dr < 0$. It is important to note from Fig. III-4 that the matched condition (the value of C_M where the coupled $\mathbf{J} \times \mathbf{B}$ energy peaks) is much more favorable for structured profiles than for shells: for a structured profile, compared with shell loads, one could design a generator with a larger peak current (larger I_g) and longer implosion time (larger t_g) and field a larger value for $M_o r_o^2$. For an efficiently radiating element, one could use the design to increase the load mass for more K-shell yield, and in the inefficient regime one could increase the initial radius to produce $\eta^* > 1$.

It is intriguing that the serendipitous central jet discovered by [II-4] (see Section II) must have been centrally peaked. According to the above discussion, the increase in the radiation output might be attributed to MRT stabilization, but apparently this experimental result was not known to the above researchers.

The theoretical ideas during the 1990s, namely that a tailored density profile could damp the MRT growth and prevent disruption during implosion, whether it extends to the axis

with $d\rho/dr < 0$ everywhere or only in an outer region, led to improved experimental results for K-shell, gas-puff radiation sources.

VI. Stagnation Physics

This section contains the culmination of the forgoing discussions, namely, a review of the radiation and neutron output from gas-puff Z-pinches. Section VI-A describes the experimental development and successful results with Ar K-shell plasma radiation sources. The following section is a more general theoretical discussion of the non-LTE physics in radiation sources as applied to gas puffs. Theoretical analysis for the plasma properties at stagnation based on observed spectra are included here. Several of the basic issues in Z-pinch physics, such as the thermal versus hydrodynamic ion temperature and the energy coupling from the generator to the load, have been studied using gas puffs. These topics are addressed in Section VI-C on the energetics and dynamics of gas-puff radiation sources. There is recent interest in magnetic flux compression in both Z-pinches and laser targets. Research on flux compression is extensive and deserves its own review, but some gas-puff experiments have included an axial magnetic field in addition to the azimuthal compressing field. Section VI-D reviews how this feature affects the radiation yield. Deuterium gas-puff Z-pinches have also been used as a plasma neutron source and such experiments are described in Section VI-E.

A. Ar Plasma Radiation Sources

As noted in Section II, [II-2] and [II-5] observed K-shell lines from Ar. In the late 1980s, Spielman *et al.* [VI-1] performed a survey of noble gas pinches using a single-shell nozzle of mean radius $\langle r_N \rangle = 1.25$ cm with a 1-cm exit aperture on the Saturn pulsed-power generator (~7 MA in ~60 ns). As much as 39 kJ of Ar K-shell radiation (>3 keV) was measured. In the early 1990s, Deeney *et al.* [III-11] used single-shell nozzles of increasing dimension to study the Ar K-shell yield on Double-EAGLE as a function of shell radius. The yield peaked at $\langle r_N \rangle = 1.25$ cm and fell off at larger $\langle r_N \rangle$ even with larger generator voltages.

Following the concept of tailored density profiles during the 1990s to mitigate the MRT instability (Section V-E), there was a surge of experiments with Ar gas puffs that demonstrated the effectiveness of this mitigation by achieving K-shell radiation sources with large radius. One can see from Fig. III-4 that the matched condition for a generator changes with the density profile. Moreover, for a distributed profile, the $\mathbf{J} \times \mathbf{B}$ energy does not decrease as does the kinetic energy. The snowplow model assumes the difference between these two energies is radiated away, but in reality this is only partly true. Much of the coupled energy during implosion resides in internal energy. This energy is available at stagnation for producing K-shell radiation.

The collection of experiments producing Ar K-shell radiation with large-radius loads were performed on different generators, of different peak current, and with various nozzle configurations. The strictly historical record is somewhat chaotic with the same nozzle fielded on different generators and reports of results appearing over several years. To impose some structure in reviewing the publications, we present these experimental results from three complementary viewpoints:

1) a table listing details of some of the data;
2) a figure of selected entries from this table showing the transition of the Ar K-shell yield from an $I_{\rm pk}^4$ to an $I_{\rm pk}^2$ scaling;
3) a historical narrative.

For the first viewpoint, we have organized the results according to the generator and the load current in Table II. The acronym for each generator is stated along with a selection of a few shots. The data, when available, include: the shot number, the gas profile, the nozzle configuration, the pinch length, mass loading, implosion time, peak current, Ar K-shell yield, peak K-shell power, K-shell pulsewidth, pinch size at stagnation, η^*, and the reference. For the gas profile, single, [as in Figs. IV-1, IV-2(a), and IV-7(b)] means an annular shell of mean or outer radius as listed in the next column. For a solid-fill [as in Figs. IV-2(c) and IV-7(c)], the outer radius of the nozzle is listed. Double means two concentric annular shells with the mean radius of each in the next column separated by a /. If the exit dimension for each opening is known, these are presented according to the nomenclature described in Section IV-A. For a triple nozzle (as in Figs. IV-4 and IV-5), the outer radius of the central jet is listed, and then the dimensions for the double puff. In most cases, the pinch diameter is that of the K-shell-emitting radius. The parameter η^* is evaluated according to (III-38) and (III-58) using the table entries for the outer nozzle radius as r_o, the pinch length ℓ, $I_{\rm pk}$, M_o, and half the listed pinch diameter for r_f. This diameter is typically that of the K-shell-emitting plasma at stagnation, which may be smaller than the diameter of all the material in the pinch, and so the value of η^* is larger than assuming a factor of 10 for the compression ratio. The factor $(\varepsilon_{j\times b,f}/\iota_{\rm pk}^2)$ in (III-58) is not the same for each generator, but we have set it to 0.5 based on Fig. III-4. Thus, the values of η^* are rough estimates meant to indicate a general trend toward higher values as the current increases. From this table, one can also see how the K-shell yields vary on a given generator as different nozzles are used. Many of the data entries in this table were collected by Apruzese *et al.* [VI-2] from articles and spreadsheets from various researchers as background for a summary of the best Ar K-shell results.

For the second viewpoint, we plot in Fig. VI-1, the Ar K-shell yield from many generators as a function of the peak current. Similar plots of Ar K-shell yield of an earlier date and with some different data points were presented in [I-16] and [IV-36]. Here, we have symbolically distinguished between single, solid-fill, double, and triple gas puffs and whether the implosion time was short or long (≥150 ns). All the data plotted in Fig. VI-1 can be found in Table II (but not vice versa). For gas puff loads properly matched and optimized to the generator current drive, the K-shell yield is larger for generators that produce larger currents. Note the current break point where the K-shell yield scaling changes from $I_{\rm pk}^4$ at low current to $I_{\rm pk}^2$ at high current. In Section III-E,

TABLE II
PARAMETERS FOR Ar K-SHELL RESULTS ON VARIOUS GENERATORS

Generator[a]	shot #	gas profile[b]	nozzle radius[c] (cm)	A-K gap (cm)	mass (μg/cm)	implosion time (ns)[d,e]	peak current (MA)	K-shell yield (kJ)	peak K-shell power (TW)	K-shell FWHM (ns)	pinch diam. (mm)	η^*	Ref.
GIT-4	378	single	1.4	2	180	120/POS	1.6	0.35	0.034	-	-	-	[VI-3]
GIT-4	396	double	1.4/3	2	115	120/POS	1.6	0.44	0.059	-	3.4	0.7	[VI-3]
GIT-12	83	single	1.4	2	82	214/POS	1.7	0.42	0.068	-	1.5	1.1	[IV-43]
GIT-12	94	single	4	2	479	306/POS	2.3	0.47	0.014	-	4.6	0.3	[IV-43]
GIT-12	71	double	1.4/4	2	439	334/POS	2.4	0.53	0.13	-	2.1	0.5	[IV-43]
GIT-12	109	double	1.4/4	2	158	278/POS	2.2	1.28	0.38	-	2.2	1.1	[IV-43]
DM2	471	single	2.5	3	-	300	2.3	1.5	0.057	20	2.5	-	[VI-4]
DM2	619	fill	3.5	4	-	348	2.3	1.7	0.056	29	3.3	-	[IV-42]
PITHON	5469	single	~1	3.3	~50	72	2.5	4.7	0.59	8	2.5	3.9	[VI-4]
ACE 4	1763	fill	7	5.1	103	231/POS	3.6	6.5	0.23	28	4.4	4.5	[VI-4]
ACE 4	2082	single	2.5	3.3	146	87/POS	3.2	2.0	0.043	16	5.3	1.6	[IV-33]
ACE 4	2142	fill	3.6	3.6	45	99/POS	2.6	4.7	0.43	8.4	2.1	5.5	[IV-33]
DE	2339	single	1.25	3	85	110	3	12.5	1.06	14	2	2.8	[III-11]
DE	-	single	1.25	3	94	107	3.4	18.7	-	11	7	1.6	[III-11]
DE	4059	fill	3.5	3.8	180	178	3.5	11	1	13	1.6	2.7	[VI-22]
DE	4428	double	1-2/3-4	3.8	113	187	3.7	12	1.2	10	3.1	4.1	[IV-30]
DE	5351	double	2-3/5-6	3.8	114	212	3.3	10.5	1.1	7.1	2.1	4.0	[IV-77]
DE	5556	triple	0.5/2-3/5-6	3.8	135	205	3.5	21	2.9	7.3	1.5	3.5	[IV-38]
Sphinx		triple	0.5/3/7	2.1	-	500	3.6	4.8	-	-	-	-	[VI-9]
DQ	498	double	1-2/3-4	3.8	286	214	4.6	29	2.3	13	3.1	2.5	[VI-6]
DQ	549	double	2-3/5-6	3.8	348	248	5.8	28	1.9	16	2.6	3.8	[VI-7]
DQ	563	triple	0.5/2-3/5-6	3.8	415	228	5.9	72	19.4	4.6	1.8	3.6	[IV-39]
Saturn	570	single	1.25	2	-	70	9	39	3.9	-	-	-	[VI-1]
Saturn	2121	fill	2.25	2	313	62	7	38	3.6	7.8	2.5	4.7	[VI-5]
Saturn	3565	triple	0.5/2-3/5-6	3.8	436	206	6.5	72	14	5	2.3	4.0	[IV-52]
Saturn	2733	double	1-2/3-4	2	-	160	6.3	32.8	-	7.5	-	-	[I-16]
Z	663	double	1-2/3-4	2.4	800	112	15	274	14.4	12	3.6	9.0	[IV-36]
Z	1590	double	1-2/3-4	3.2	870	112	13.9	300	35	11	3	7.6	[VI-4]
ZR	2381	double	1-2/3-4	2.5	1000	107	13	250	16.5	9	4	4.8	[VI-10]
ZR	2559	double	1-2/3-4	2.5	1000	104	15	319	26.4	8.5	3	7.6	[VI-11]
ZR	2560	double	1-2/3-4	2.5	1000	103	15	363	29	7.6	3	7.6	[VI-11]
ZR	2561	double	1-2/3-4	2.5	1000	104	15	309	26.9	7.5	3	7.6	[VI-11]

[a] GIT = Literally Russian for generator current pulsed, DM2 = Decade Module 2, DE = Double Eagle, DQ = Decade Quad, ZR = refurbished Z.
[b,c] See text for an explanation.
[d] See text for an explanation. The implosion time is defined in Fig. III-2.
[e] POS = Plasma Opening Switch

we described the mass break point in the K-shell scaling relations where the yield scaling must change from M_o^2 to M_o by energy conservation, and because the radiation loss plays a major role in the energy balance. From (III-48)–(III-51), at matched conditions, there is a connection between the mass loading and the square of the peak current. Hence, there is also a current break point. Beyond this transition, the optimum mass for radiation scales less than linearly with $E_{J\times B}$, and the radius must be increased to match the generator. As a point of interest, Apruzese *et al*. [VI-2] found that there is no mass break point if the K-shell radiation is plotted against the K-shell-emitting mass (M_K). The latter was determined from a spectral diagnosis of some shots listed in Table II. They found that $Y_K \sim M_K^{1.9}$ over the range covering the generators DM2 to Z. Scaling laws have been worked out in [III-14] using a simple 2-level model.

Note that Fig. VI-1 shows yield per unit length. This approach might suggest that increasing the pinch length can proportionally increase the yield, but we point out that this is not the case. In the nondimensional development leading to Fig. III-4, for a fixed mass load per unit length M_o/ℓ, changing the pinch length ℓ only changes the parameter C_L in (III-46). For a larger ℓ, the result is a lower peak current and lower total coupled energy, but a larger total mass and potential number of K-shell-radiating ions. Hence, the nonlinear interplay between length and yield needs to be experimentally examined for each generator. For example, compare shots 663 and 1590 on Z in Table II. The latter was a third longer, had a 9% greater K-yield, but an 18% lower yield per unit length. A similar comparison can be made among the ACE 4 shots.

For the third viewpoint, we present an approximately historical narrative of the experimental results that closely matches the diameter of the gas-puff nozzle, from smaller (oldest) to larger (recent). The review of K-shell radiation laws in Section III-E noted that for a fixed generator, i.e., same implosion time and peak current, one could increase η^* using a larger radius load. From Section V-D, a high-current generator could be more easily designed if the current rise time was lengthened. But likewise to reach an η^* of a few, one needs to also implode from a larger radius. With snowplow stabilization (Section V-E), either by uniform solid-fills or by tailored density profiles, the path forward

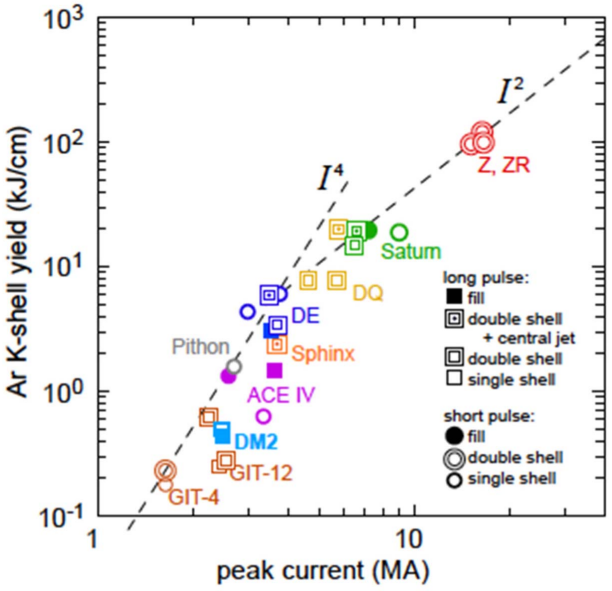

Fig. VI-1. Ar K-shell yield per unit length versus peak load current on various generators. Data are taken from Table II. Long pulse means an implosion time of >150 ns.

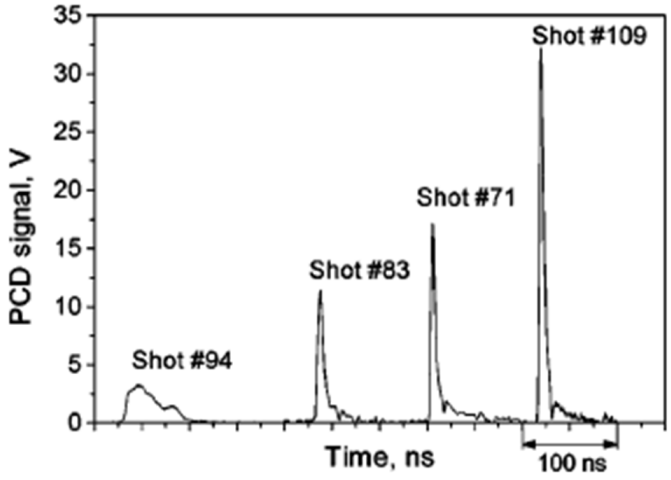

Fig. VI-2. Ar K-shell power pulses for shots on GIT-12. See Table II for the parameters of these shots. Shots #94 and #83 are single shell, $r_N = 1.4$ cm. Shots #71 and #109 are double shells, $r_N = 1.4/3.0$ cm. In addition, for the double puff shot #71 the inner-to-outer shell mass ratio was 0.3, and on shot #109 it was 1.37. Note the signals are time shifted for clarity. Reprinted with permission from [IV-43]. Copyright 2000, AIP Publishing LLC.

offered a potential solution to the MRT stability problem expressed as the number of e-foldings in (V-1).

Baksht *et al.* [IV-32], [VI-3] at HCEI compared the Ar K-shell yield from single and double-puff loads. The experiments were performed on the inductive store generator GIT-4 (∼1.6 MA), which uses a POS (Section V-D) to reduce the inherent 2-μs current rise time from the machine to ∼100 ns for the load current. In [IV-32], it was reported that Y_K dropped sharply as the single-shell radius increased from 1.4 to 3 cm, despite the large η and attributed this to the deleterious effect of the MRT instability. In a later work, Baksht *et al.* [VI-3] formed a double-shell puff of $r_N = 1.4/3.0$ cm. They proposed that the instability was mitigated since Y_K improved to 440 J and the K-shell Power (P_K) to 51 GW compared with 350 J and 34 GW from a single shell at a 1.4-cm radius. Subsequently, the inductive generator at HCEI was improved to GIT-12 and Shishlov *et al.* [IV-43] reported on similar experiments as above with single shells of a 1.4- or 4-cm radius, and double shells when the two were combined. The photoconductive device (PCD) signals from two single-shell shots (#94 and #83) and two double-shell shots (#71 and #109) (data listed in Table II) are shown in Fig. VI-2 and demonstrate the significant increase in K-shell power moving from single to double shells. Increasing the mass in the inner shell resulted in higher K-shell power. Based on the experiments and simulations, the authors concluded that the pinch is stable against the MRT instability when the mass of the inner shell is greater than that of the outer shell. This condition requires that the density of the inner shell be much larger than that of the outer one (to account for the decreased radius), consistent with the relation $d\rho/dr < 0$ used in the tailored density profiles of [V-42] and [V-44].

The first results with a solid-fill [see Figs. IV-2(c) and IV-7(c)] were reported in [VI-5] using the Saturn generator (∼7 MA in ∼80 ns). The Ar K-shell radiation for a 4.5-cm-OD solid-fill nozzle and a previously optimized 2.5-cm-OD annular nozzle was compared at the same ∼7-MA peak generator current. The K-shell yield for the solid-fill nozzle relative to the annular nozzle was 1.5–5 times higher and the radiated K-shell power was two to three times higher. Coleman *et al.* [IV-33] also examined Ar K-yields from a solid-fill on the inductive store generator ACE 4 (∼3 MA in 200 ns). The 7.2-cm-OD solid-fill produced over twice the K-shell yield, 10 times the K-shell power, and half the pulsewidth as a single annular shell of a 5-cm OD. The larger pulsewidth of the single shell arises from its breakup during implosion. Levine *et al.* [IV-42] studied long-implosion Ar solid-fills on DM2 (2.3 MA in 250 ns), Double-EAGLE (4 MA in 200 ns), and Saturn (6.5 MA in 200 ns). The objective was to determine the load development issues if the pulsed-power risks for large-current high-voltage generators were eliminated with a long pulsewidth and a POS for the driver, as was expected for the 200-ns rise time on Decade Quad. The K-shell yield from the 7-cm-OD solid-fill on DM2 and Double-EAGLE followed an $I_{\rm pk}^4$ scaling, but the results on Saturn were only 19 kJ, far below even an $I_{\rm pk}^2$ scaling. The use of a 10-cm-OD solid-fill on DM2 and Double-EAGLE were poor. For the 7-cm-OD solid-fill on Saturn, the presence of a cathode plane of wires at the nozzle increased the Y_K by a factor of two. There were no null tests for Double-EAGLE and the wires did not improve Y_K on DM2.

In 2000, MPI developed the $r_N = 1$–2/3–4 double nozzle [see Figs. IV-3 and IV-7(d)]. Sze *et al.* [IV-30] initially fielded this nozzle on Double-EAGLE in long-pulse mode. The best result was 12-kJ yield, indicating that the performance of the double-shell puffs at a 4-cm outer radius was similar to that of solid-fills at a 3.5-cm radius. The inner-to-outer mass ratio of the shells varied from 0.6 to 1.1, but, unlike [IV-43], no definite trend of K-shell yield with the mass ratio between the inner and outer shells was observed. It was thus concluded that the

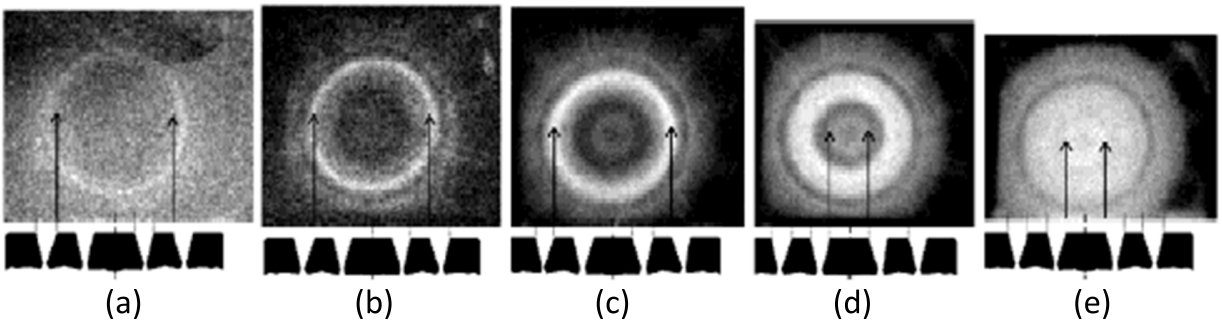

Fig. VI-3. (a)–(e) Sequence of optical images (axial) of an Ar implosion from the double-shell r_N = 1–2/3–4 nozzle (see Fig. IV-3) on Double-EAGLE. This is from shot #4428 in Table II. A sketch of the nozzle lies below each image to illustrate the position of the nozzle openings. The timings relative to peak K-shell power for (a)–(e) are −103, −82, −60, −39, and −17 ns, respectively. Reproduced from [I-16] with the kind permission of Cambridge University Press.

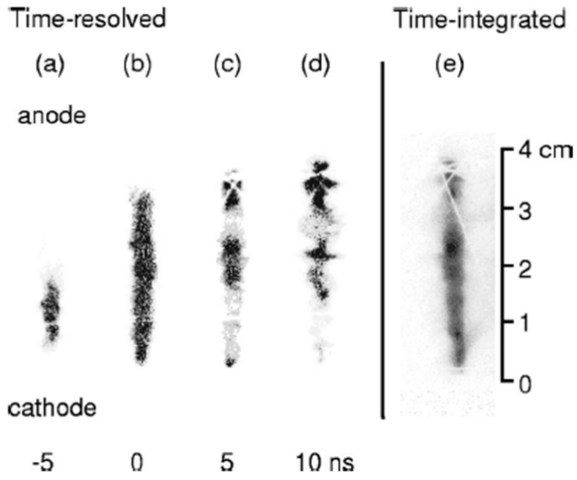

Fig. VI-4. (a)–(d) Time-resolved K-shell X-ray pinhole images for the double-shell r_N = 1–2/3–4 nozzle (see Fig. IV-3) on Double-EAGLE. This is from shot #4428 in Table II. (e) Time-integrated K-shell image of the same shot. Times are relative to the peak K-shell power. Reprinted with permission from [IV-30]. Copyright 2000, AIP Publishing LLC.

subtleties of the shell-on-shell interaction are of second order in the conversion of the coupled energy into K-shell radiation. A chlorine tracer was added and the Cl Ly-α line was clearly seen if the tracer was in the inner shell, but very weak if only in the outer shell. The apparently low level of mixing suggests that the inner shell damps and resists the penetration of any MRT bubbles that developed in the outer shell. Fig. VI-3 shows optical images of the double-shell implosion from the axial direction for shot #4428. Fig. VI-4 shows images of the Ar K-shell emission for the same shot. At peak K-shell power (t = 0), the pinch is nearly uniformly lit up along the z-axis and then goes unstable into an apparently helical mode by +10 ns. The bright spots in the time-integrated image appear to persist after peak power.

Coleman *et al.* [I-16] present a review of the work covering [IV-30], [IV-33], and [IV-42] at MPI up to 2001. They also reported on a series of shots on the Saturn generator at SNL in long-pulse mode with the r_N = 1–2/3–4 nozzle. The pinch length was reduced to 2 cm from the Double-EAGLE shots at 3.8 cm to obtain good power flow. They found a maximum of ∼16 kJ Ar K-shell yield at ∼160 ns in a 7.5-ns pulsewidth.

The double-shell r_N = 1–2/3–4 nozzle was next fielded on the Z generator at SNL (∼15 MA, 110 ns). From the series on Double-EAGLE, it was learned that the downstream section of the flow, where the distinctness of the double-shell structure was washed out, produced most of the yield. So the inner nozzle was recessed 1 cm behind the cathode wire mesh. The series in [IV-36] was planned as a mass variation. Two shots with a greater length of 2.4 cm, instead of 2 cm, performed the best, and the one with the lowest mass loading (0.8 mg/cm, #663) produced 274-kJ Ar K-shell, which was a surprising jump from the exiting record on Saturn of 39 kJ. With this data point, the $I_{\rm pk}^2$ scaling is clearly evident in Fig. VI-1. It was thought that the shots of shorter length inadvertently cutoff the most productive section. But subsequently Coleman *et al.* [VI-6] published data on the K continuum arising from recombination radiation to H- and He-like ions from shot #663 and similar later ones but of a greater length. They were all found to produce ∼28% of the total radiation yield in the K-shell (>3 keV), and ∼8% of the total was above the K continuum (>4.4 keV). The r_N = 1–2/3–4 nozzle was also fielded on Decade Quad in [VI-7]. At the highest Marx charging, the K-shell yield was ∼29 kJ, which is consistent with a current break point of ∼5 MA.

The last and largest nozzle in this series developed by TPSD was a 12-cm triple design with a central jet, an inner shell from 2 to 3 cm, and an outer shell from 5 to 6 cm (r_N = 0.5/2–3/5–6). (See Fig. IV-4.) Levine *et al.* [IV-23] studied the importance of the central jet and the nozzle recess on Double-EAGLE in long-pulse mode. Whether the nozzles were recessed from an outer lip by 1 or 2 cm, the central jet made a notable difference. In the best configuration, the central jet increased Y_K by 17% and P_K by 40%, even though the mass in the central jet constituted only a few percent of the total mass load. The nonrecessed and 1-cm recess produced double peaks in the K-shell pulse, but for the 2- and 3-cm recess the double pulse was eliminated and the K-yield was marginally improved. An unresolved feature of the pinches was that for the shots with a double radiation pulse, the nozzle end of the pinch imploded first even though the mass loading per unit length, as measured using PLIF (see Section IV-B), was greater on the nozzle side.

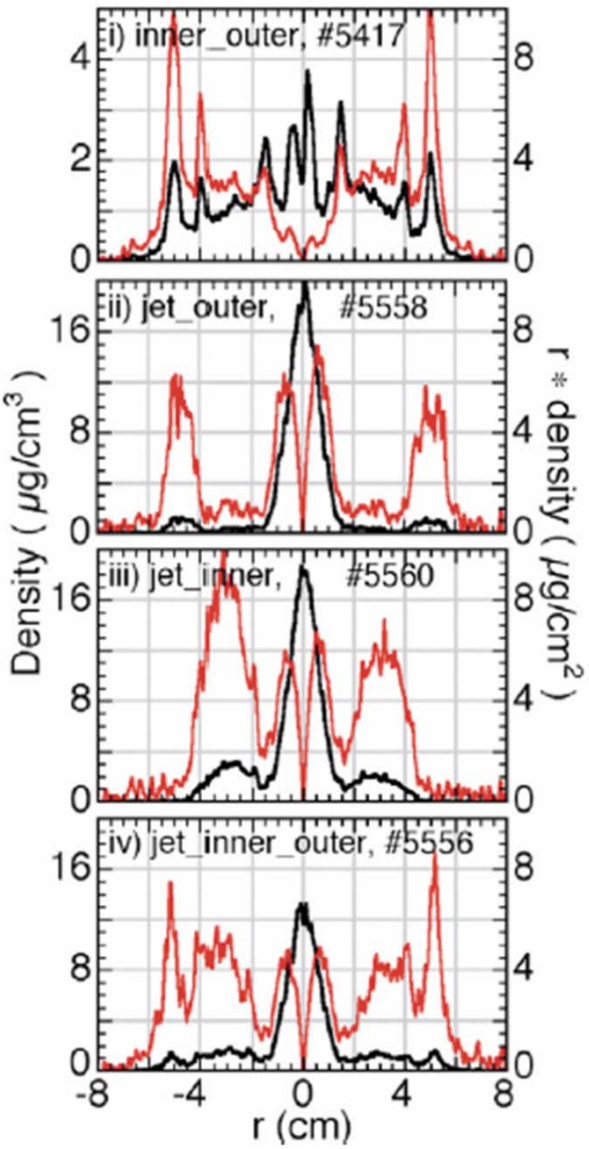

Fig. VI-5. Radial distributions of the Ar mass density (black curves) and radius times mass density (red curves) for four different configurations of the $r_N = 0.5/2–3/5–6$ nozzle at the midplane of a 3.8-cm-long puff. Reprinted figure with permission from [IV-38]. Copyright 2005 by the American Physical Society.

Based on the success with the center jet, the 12-cm-diameter triple nozzle was reconfigured such that the jet was fed by an independent plenum [see Fig. IV-4(a)] instead of from the inner nozzle plenum (the outer nozzle was already separated from the inner one), and the throat of the jet was increased to allow a greater mass flow on axis (see Section IV-A). Sze *et al*. [IV-38] took advantage of the three separate plenums to study with the same generator the impact of the density profile on Y_K. By selectively filling either shell or the jet they looked at four combinations: 1) inner and outer shells; 2) central jet and outer; 3) central jet and inner; and 4) central jet with both shells. The return current posts were fixed at a 7.8-cm radius for all shots. Fig. VI-5 shows the different density distributions for the four configurations, measured with PLIF (see Section IV-B). The case with a double shell and the jet with a 205-ns implosion time produced the maximum Ar K-shell yield of 21 kJ on Double-EAGLE. This yield is comparable with the previous maximum obtained on the same generator at smaller radii: 18.7 kJ for a single shell at a 1.25-cm radius and 110 ns [III-11], and 12 kJ with the $r_N = 1–2/3–4$ nozzle and 200 ns [IV-30]. The physics of the implosion and stagnation was described in terms of a pusher (outer), stabilizer (inner), and radiator (jet) interaction. This paper demonstrated that long implosions of large radii could produce comparable radiation sources to fast ones of small radii. As noted in this paper, the jet-inner configuration had two-thirds of the yield and half the pulsewidth (3.7 ns) of the load with the best yield. Thus, this last point suggests that proper load design may also allow smaller radii loads to achieve similar yields on long-pulse generators. The inner-outer and jet-outer configurations were less productive in both the K-shell yield and power.

Levine *et al*. [IV-39] presented a more complete discussion of the data from the shots using the 12-cm triple nozzle on Double-EAGLE, particularly in regard to the initial density profile. For the best shot, the mass in the center region ($0 < r < 1.5$ cm) was ~20% of the total mass load, 40% in the inner region ($1.5 < r < 4$ cm), and the remainder in the outer region ($r < 4$ cm). This density profile is analogous to the centrally peaked profiles used in the snowplow analysis of Sections III-C and III-D, and to the ideal distribution with no acceleration in [V-44]. The stagnated pinch showed little zippering. As in [IV-30], a Cl dopant was used and indicated that the central jet was the primary K-shell radiator: 65% of the K-shell yield originated from the central jet in the jet–inner–outer configuration, and 75% for the jet–inner configuration. This result is consistent with the pusher–stabilizer–radiator model [IV-38]. Qi *et al*. [IV-56] presented results from these same shots using PLIF for the initial density, and LSI and LWA for the plasma conditions during implosion. Fig. VI-6 compares the electron density from LWA measurements at two instances for the jet–outer and the jet–inner–outer configurations. The breakup of the accreting layer for the jet–outer shot, as opposed to the more uniform one for the jet–inner–outer case, conclusively demonstrates the stabilizing effect of tailored density profiles in large-radius Z-pinch gas puffs.

Levine *et al*. [IV-39] also fielded the jet-inner-outer configuration of the 12-cm-diameter triple nozzle on the Decade Quad facility (see Section V-D). An impressive 80 kJ of Ar K-shell at 6-MA peak current was achieved with a pulsewidth of only 5.7 ns in a 227-ns implosion. This was almost a factor of three larger than the yield and better than half the pulsewidth from the $r_N = 1–2/3–4$ nozzle on Decade Quad [VI-7]. Sze *et al*. [IV-55] present a summary of the research on Double-EAGLE, Saturn, and Decade Quad performed by L-3 Pulse Sciences (originally MPI) team using the 12-cm-OD triple nozzle. The key to the above success with the triple nozzle was having a center jet that provided ~20% of the initial injected mass on axis.

A double puff 12-cm-OD nozzle, designed by AASC, was also fielded on Double-EAGLE in the same time frame as the TPSD 12-cm-OD triple gas puff. The AASC nozzle

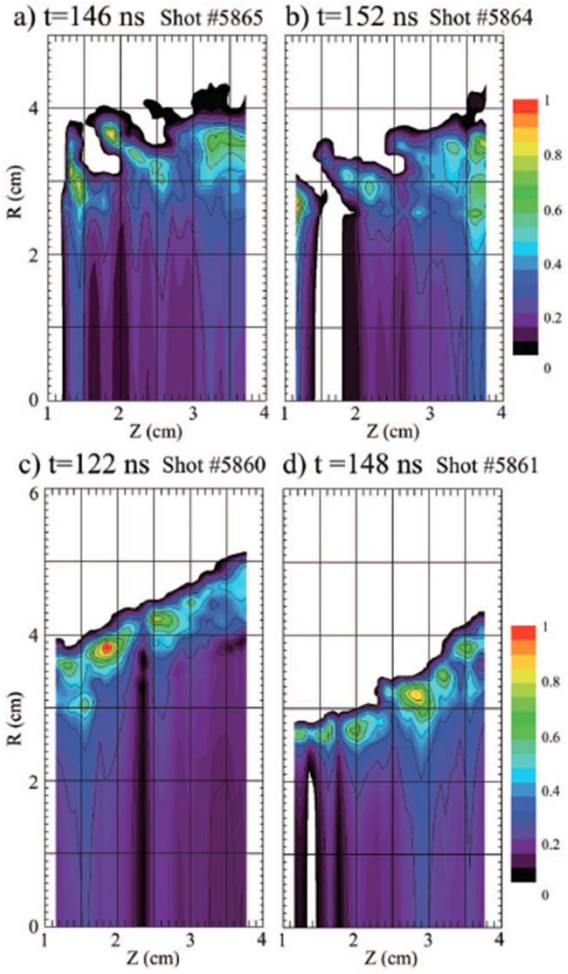

Fig. VI-6. Electron density derived from LWA measurements of the $r_N = 0.5/2–3/5–6$ nozzle. (a) and (b) For the jet-outer profile at two times showing the structuring due to MRT instabilities. (c) and (d) For the jet-inner-outer profile showing the effect of snowplow stabilization for the large-radius implosion. Reprinted with permission from [IV-56]. Copyright 2008, AIP Publishing LLC.

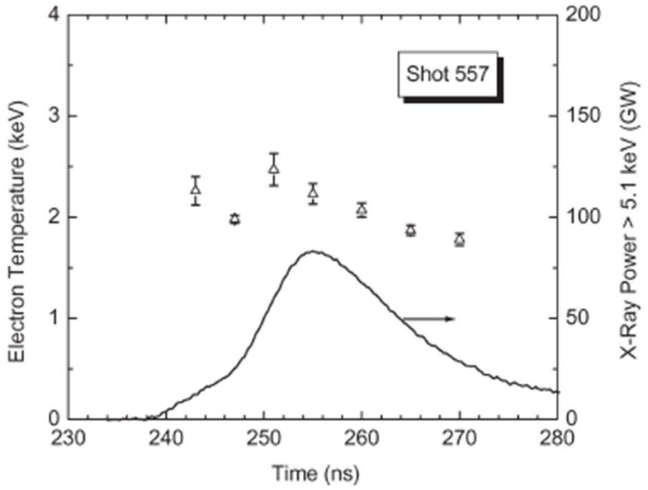

Fig. VI-7. Temporal evolution of the electron temperature based on the slope of the spatially averaged continuum for an Ar gas puff on Decade Quad using a double-puff nozzle $r_N = 1–2/4–6$ cm. Reproduced from [VI-8].

($r_N = 1–2/4–6$ cm) did not have a center jet but was able to achieve a neutral gas distribution that was peaked on axis and continuously decreased with increasing radius. This nozzle, without a center jet, achieved peak argon K-yields that were about 20% lower than were reached with the TPSD nozzle with an optimized center jet.

Young *et al.* [VI-8] used a crystal spectrometer with time-resolved detectors to perform absolute measurements of the K-continuum from Ar in the range of 5–10 keV on Decade Quad. Measurements were taken for two, 12-cm diameter nozzles without central jets: for nozzle A, $r_N = 2–3/5–6$ cm; and for nozzle B, $r_N = 1–2/4–6$ cm. The electron temperature was obtained from the slope of the continuum given that the emissivity varies as $\exp(-h\nu/k_B T_e)$. For both nozzles, the spatially averaged, time-resolved continuum T_e is largest at the beginning of the K-edge continuum (~5.1 keV) pulse and starts decreasing prior to the peak in that band. Fig. VI-7 shows the results for nozzle B. For nozzle A, the continuum T_e is similar to the temperature derived from the ratio of K-shell lines (see Section VI-B). However, for nozzle B, the continuum temperatures are about 15% larger than the line ratio temperatures. These results suggest that for nozzle B, the high-temperature continuum emission is generated in a region of the pinch different from the case of the line emission. For instance, the smaller initial linear mass density on axis for nozzle B than for nozzle A may have led to a higher temperature, lower density plasma on the axis. Similar to the findings of Coleman *et al.* [VI-6] mentioned above for the *Z* generator, 20%–25% of the total yield appears as K-shell emission and 6%–10% lies in the free-bound continuum.

The two largest nozzles ever fielded on generators were both beset by poor energy or current coupling to the load. Zucchini *et al.* [VI-9] studied Ar gas puffs on the linear transformer driver Sphinx in Gramat, France, using a 20-cm diameter nozzle. This was a triple nozzle with very wide exit apertures that produced a density profile with $d\rho/dr < 0$ everywhere. The pressure in the plenum of the central jet was varied but the large divergence of the jet led to zippering and hot spots near the cathode. The measured peak current was ~3.6 MA in a ~500-ns implosion. By reducing the pinch length to 2.1 cm, the current was increased by ~10% and K-shell yield rose to 4.8 kJ, about twice that at 4 cm. Labetsky *et al.* [IV-41] reported on a 24–27-cm diameter nozzle with three annuli and a central jet. The work was performed on GIT-12 at the HCEI without a POS so that the rise time was ~1 μs and the peak current ~3.5 MA. The gas puff here was neon rather than Ar. It was claimed that the MRT instability did not affect the implosion and the diameter of the K-shell-emitting region was quite small, just 3–4 mm. A number of magnetic probes were placed throughout the load region to follow the dynamics of the current sheath. 10%–15% of the current loss was attributed to electron Hall conduction in the low-density region beyond the outer shell. At stagnation, it was surprisingly found that less than ~30% of the supplied current flows within a diameter of 5.5 cm. The current losses were observed to grow

monotonically during the course of the implosion, and to increase abruptly at stagnation. Probe measurements of the magnetic field in high-current, high-density plasma environments can suffer flashover issues, making interpretation of results difficult.

As noted above, the initial Ar gas-puff implosions on the Z generator were reported in [IV-36]. Following the recent refurbishment of the generator, now ZR, the capability to field gas-puff loads was reestablished in [VI-10]. The double-shell gas-puff assembly with the $r_N = 1$–2/3–4-cm nozzle was fabricated by AASC [IV-7]. The face of the nozzle is the cathode, i.e., there is no cathode screen and no recess. The ZR discharge occurs after the mass flow from the nozzle has reached steady state. Also no preionization is employed. The inner to outer mass ratio of the shells was 1.6:1. For the initial experiments, the charging voltage (and associated maximum current) on ZR was reduced to 70 kV from the maximum of 85 kV to prevent potential damage to the insulator stack. For the one shot reported in [VI-10] (Z2381), 250 kJ of Ar K-shell radiation was measured, which was one-third of the total radiation. Over half of the peak total X-ray power is composed of K-shell radiation.

Very recently, the same double-shell AASC nozzle and mass loading was used on ZR at a larger Marx charging voltage (~85 kV) for three shots. The result reported in [VI-11] are the largest Ar K-shell yields ever measured: 309, 319, and 363 kJ. Data for these shots are listed in the bottom three rows of Table II. Furthermore, the K-shell pulsewidth and line ratios among the He-like and H-like emission lines were remarkably similar. The results represent a mature, and reproducible capability with an ~30% efficiency in the conversion of coupled energy into Ar K-shell radiation.

B. Non-LTE Physics of Radiation Sources

The radiative output from the stagnation phase of a Z-pinch is controlled by microscopic processes: atomic physics and radiation transport. A complete understanding of the phenomena would require the self-consistent coupling of 3-D MHD with the atomic structure for the energy levels, knowledge of collision rates and photo-cross sections, and the plasma emissivity and absorptivity along every photon's path. This is a complex, nonlinear problem that is very difficult to fully simulate in a computational model. We discuss the theoretical and modeling efforts to date, moving from stationary plasmas through 1-D to 2-D simulations.

To begin, let us schematically represent a more complete version than (III-59) of the CR kinetic equation for a level of an ion. Index 1 represents any excited levels in an ionization stage of lower energy than level 2, index 3 represents any excited levels of higher energy than level 2, and index 4 represents states of the next higher ionization stage

$$\begin{aligned}\frac{dn_2}{dt} &= n_e n_1 \mathrm{CX}_{12} + n_e n_3 \mathrm{DX}_{32} n_3 + (n_e)^2 \mathrm{BB}_{42} n_4 \\ &\quad - n_e n_2 \mathrm{DX}_{21} - n_e n_2 \mathrm{CX}_{23} n_2 - n_e n_2 \mathrm{CI}_{24} n_2 \\ &\quad + n_1 \mathrm{PX}_{12} + A_{32} n_3 + n_e \mathrm{RR}_{42} n_4 \\ &\quad - n_2 A_{21} - n_2 \mathrm{PX}_{23} - n_2 \mathrm{PI}_{24}. \end{aligned} \tag{VI-1}$$

The rate of change of the population in state 2 is dn_2/dt [units of $1/(\mathrm{cm}^3\mathrm{s})$]. The reactions in addition to those in (III-59) are three body recombination (BB), collisional ionization (CI), photoexcitation (PX), radiative recombination (RR), and photoionization (PI). The first six reactions in (VI-1) are driven by collisions with electrons. The last six involve photon processes. If photons did not impact on the population kinetics, then, under the condition of equilibrium ($dn_2/dt = 0$), the ionization balance would be given by the Saha equation and the excited-state populations would obey the Boltzmann relation [VI-12]. The photoprocesses depend on the mean intensity $J_\nu = (1/4\pi)\int I_\nu d\Omega$, which is the angle average of the local radiation intensity I_ν. [units of ergs/(cm^2 s Hz steradian)]. For an absorption cross section σ_ν^{ij} at frequency ν

$$\mathrm{PX}_{ij} = \int \sigma_\nu^{ij} \frac{4\pi J_\nu}{h\nu} d\nu \tag{VI-2}$$

and similarly for the photoionization PI_{ij} (units of PI and PX are 1/s). Clearly the impact on the population kinetics due to photons requires, in principle, the determination of the angle dependent I_ν, and hence, the solution of the radiative transfer equation along rays. In the optically thin coronal limit, only upward collisions (CX and CI) and radiative decay (A and RR) enter the kinetics. Fig. VI-8 presents a schematic of many reactions for a He-like ion, including doubly excited states which are not included in (VI-1). A tutorial on radiation transport in Z-pinches can be found in [VI-13].

Apruzese and Davis [II-22] solved a set of equations analogous to (VI-1), under the CRE condition taking opacity into account. They treated the Na–Ne mixture as a static hot spot. Coupling coefficients connecting different parts of the plasma were used to treat the transport and absorption of emission lines within the probability-of-escape formalism. In an axially uniform, cylindrically symmetric pinch (1-D) the implementation of radiation transport could be accomplished with one ray per zone [VI-14], [VI-15]. Apruzese and Kepple [VI-16] also reported on a CRE model for Kr with atomic structure among L-shell ionization stages. They compared the optically thick results against the case for thin emission and a case with velocity gradients using the Sobolev approximation [VI-17]. Clark *et al.* [VI-18] extended the probabilistic transport treatment of radiation to the continuum emission, such as free-bound radiation. The continuum radiation above the ionization energy of the H-like ion stage can be an important contribution to the total K-shell yield. A non-LTE analysis of this component was presented in [VI-19]. An example of a non-LTE synthetic spectrum at stagnation from a simulated Ar Z-pinch is shown in Fig. VI-9. The L- and K-shell lines are denoted along with the underlying continuum.

Coulter *et al.* [VI-20] developed an especially important technique for diagnosing plasma conditions in a Z-pinch using CRE models of stationary plasmas. The application was initially done only for Al and Apruzese *et al.* [VI-21] revised the technique and applied it to Ar. Consider a cylindrical plasma of uniform electron temperature T_e and ion density n_i. Also, a radius for the plasma is needed to account for the

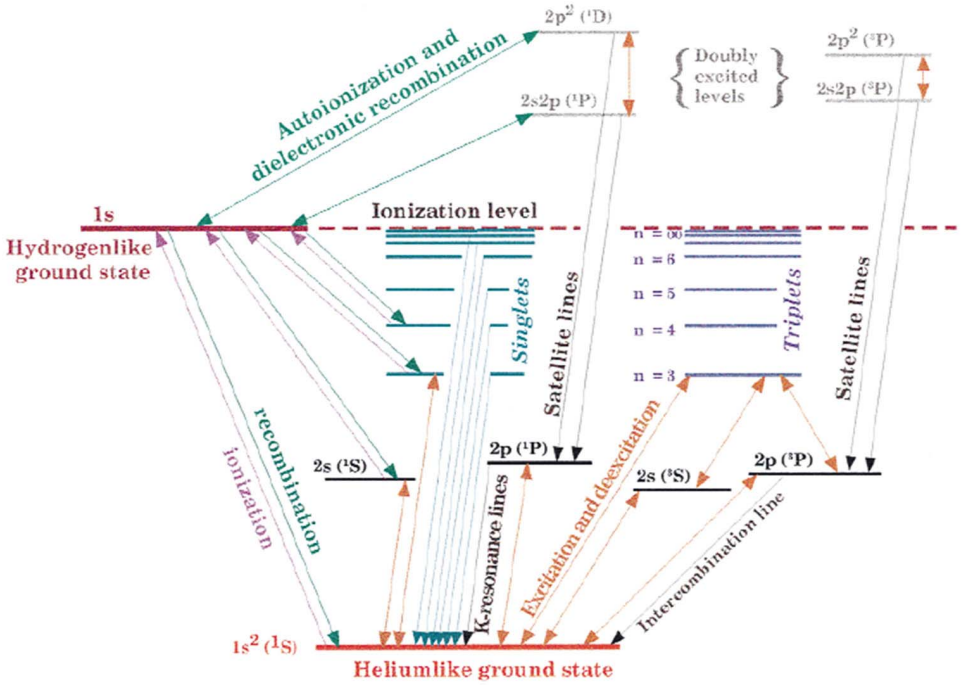

Fig. VI-8. Energy level diagram for a He-like ion, showing various atomic coupling processes among the levels. From [VI-29], reproduced with permission.

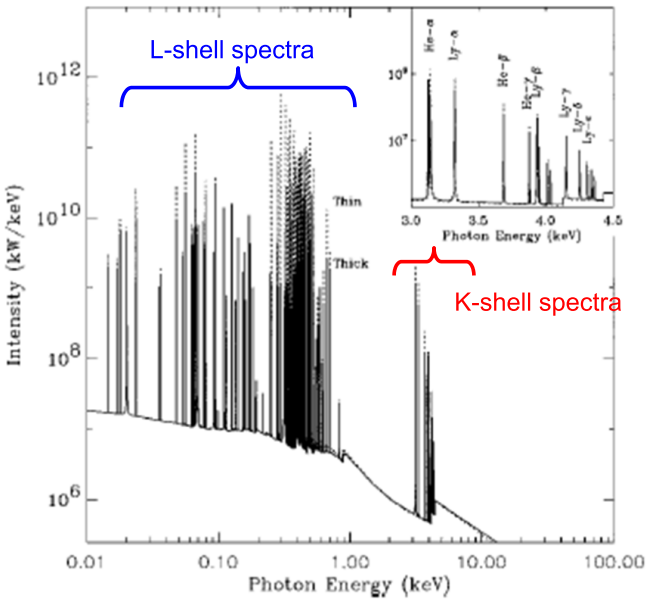

Fig. VI-9. Typical synthetic spectra computed from a 1-D non-LTE simulation of an Ar Z-pinch. The optically thin result is shown as a dashed line. The L-shell and K-shell regions are denoted along with a blow-up of the latter. Reprinted with permission from [V-43] (slightly adapted). Copyright 1998, AIP Publishing LLC.

effect of opacity. A CRE model for the K-shell and nearby L-shell ionization stages is calculated for the populations and the emitted K-shell total and line radiation. Note that although T_e and n_i are uniform, the level populations are not necessarily so. A line photon emitted near the edge of the plasma sees a lower opacity, the trapping is less, and therefore upper level populations are lower than in the center. From the calculations, the ratio is formed of the power in the Ly-α emission line to that in the He-α plus intercombination lines. For the same radius, T_e and n_i are varied to calculate the total K-shell emission for each combination. A graph with T_e along the ordinate and n_i along the abscissa leads to contours of a constant line ratio that tend to run horizontally. On a separate $T_e - n_i$ graph contours of the total K-shell power tend to run vertically. An example for Ar is shown in Fig. VI-10 [VI-4]. The plots in Fig. VI-10 update those shown in [VI-21] and use an ion temperature of 20 keV, and a 0.3-cm diameter cylindrical plasma. From observed K-shell spectroscopy and X-ray images of a Z-pinch, one can extract the Ly-α/(He-α + IC) line ratio, total K-shell power, and radius of the K-shell-emitting region. For the fixed diameter, these two values specify particular contours on each of the two separate $T_e - n_i$ graphs made for the observed diameter, and when overlaid, the point of intersection provides the T_e and n_i of the plasma. Failor *et al.* [VI-22] used this technique with axially resolved data to analyze Ar puffs of length 2, 4, and 6 cm on Double-EAGLE with the 1–2/3–4 nozzle. They found that the K-shell-emitting plasma varied along the length in temperature from 1.2 to 2 keV, and in density from 5 to 35 $\times$ 10^{18} cm^{-3}. Also for the shorter pinches, more mass per unit length is radiating from the K-shell than for longer pinches.

A recent application of the spectroscopic technique by Apruzese *et al.* [VI-23] was to investigate whether the high intensities of hot spots seen in pinches are due to high temperatures, high density, or some combination of the two. Most of the discussion was on wire arrays, but at the end of the paper they compared two Ar gas puffs taken five years apart that are the entries for the Z generator in Table II. Even though load conditions are very similar, as is Y_K, it was found from the spectral analysis that T_e and n_i differed by a factor of two,

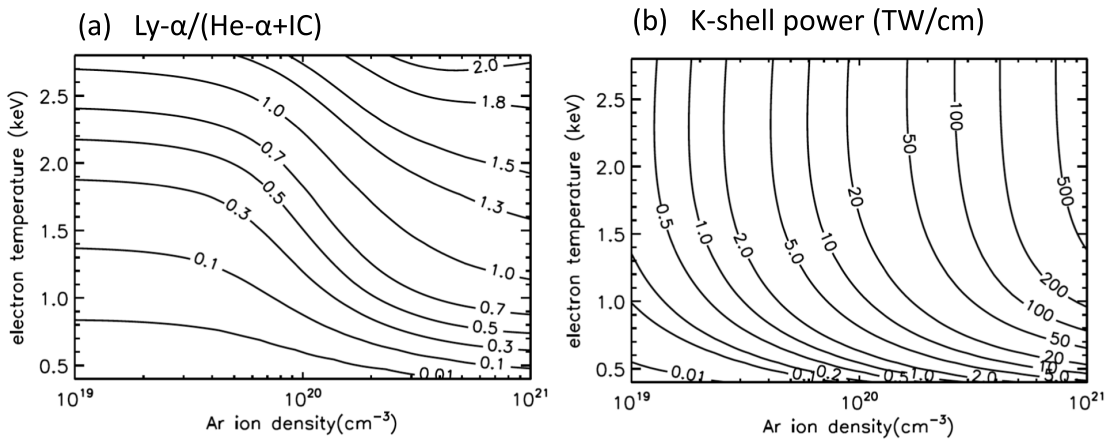

Fig. VI-10. (a) Contours of the ratio of the radiated power in the Ly-α line to the to He-α plus intercombination lines for a cylindrical Ar plasma of a 0.3-cm diameter as a function of the ion density and electron temperature. (b) Contours of the K-shell power above 3 keV for the same conditions. Unpublished data courtesy of [VI-4].

with their product nearly the same. This indicates that a pinch can produce the same yield but with very different plasma conditions. Another application of this spectroscopic diagnostic was the analysis of several K-shell line ratios from Ar puffs on the ZR generator [VI-11], [VI-24]. In these papers, the technique was extended to a two-component plasma at the time of peak K-shell emission to best match several line ratios among the He- and H-like ions.

Static plasma calculations for the ionization kinetics and radiation output are useful for diagnostics. Incorporation of a CRE model into a dynamic simulation of a Z-pinch was a challenge in the 1980s and 1990s because of the memory and speed limitations of the computers of those decades. Because a substantial fraction of the energy coupled to a plasma radiation source (PRS) Z-pinch is emitted as radiation, the non-LTE kinetics and radiation losses can have a significant impact on the dynamics. Furthermore, the treatment must be done self-consistently because the motional dynamics changes the internal energy, and the ionization kinetics changes the distribution of internal energy between thermal and ionization/excitation components, which in turn affects the radiation transport and the radiative loss, which then feedbacks on the compression of the pinch. Clark *et al*. [VI-25] combined a reduced CRE model with a 1-D hydrodynamic code to simulate an imploding neon gas puff. In addition to the ground states of all ionization stages, there were only 16 excited levels spread over the B- to H-like ions, and without an MHD solver, the plasma shell was given an initial inward velocity. Subsequently, the CRE model was expanded to ~100 levels by Clark *et al*. [VI-26]. They found that the distribution among ionization stages at stagnation was substantially different from the case of LTE or coronal ionization. Today, 1-D MHD simulations are able to include 50–100 levels per ion in the L- and K-shells.

Davis *et al*. [VI-27] combined a circuit model with a 1-D Z-pinch MHD simulation and CRE kinetics. The objective was to examine how much the L-shell kinetics would affect the K-shell emission of a Kr puff. To reach H-like Kr, a theoretical 60–100-MA generator was used to drive the load. The generator design was an extrapolation from a Decade Quad transmission line [VI-28]. Generators of higher power can drive more massive loads, but such loads may perform no better in terms of densities and temperatures. However, if more mass can be driven to the same n_e and T_e as a lower power generator, then the yield would increase, especially for Kr with low opacity. The overall radiative efficiency was found to be greater with a more complete atomic model, both because more radiative transitions are treated and because the pinch is more compressed. However, this efficiency is not from the K-shell emission but rather from the L-shell. Fig. VI-11 shows that as the L-shell model is made more complete for Kr, there is a progressively narrower domain in load mass for optimizing the K-shell radiation. This result implies that not only does one need a large η^* as in (III-57) for K-shell production, but also, as the generator current and the atomic

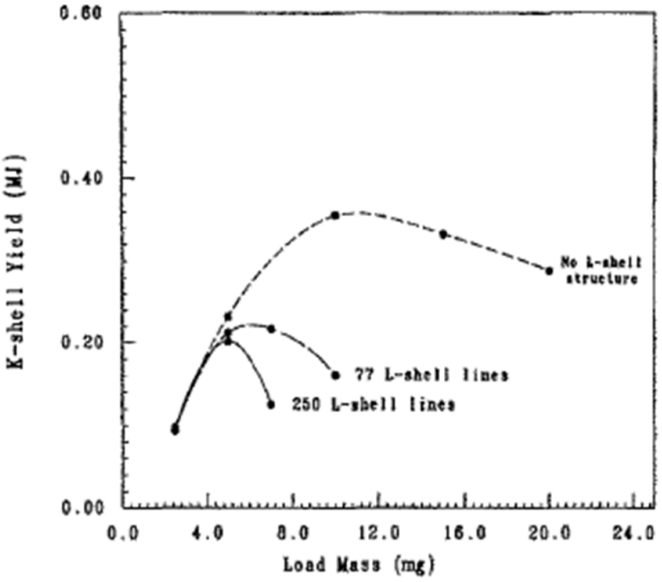

Fig. VI-11. K-shell yield (MJ) as a function of the load mass (milligram) and the atomic L-shell structure from an MHD simulation of a 5-cm radius Kr gas puff on a hypothetical 60-MA generator. Reprinted with permission from [VI-27]. Copyright 1995, AIP Publishing LLC.

number of the load increases, η^* must grow ever bigger (see Sections III-E and V-D). Whether this indicates a fundamental limit to thermally driven K-shell plasma sources has yet to be considered. Davis *et al*. [VI-29] examined further issues of LTE versus CRE ionization kinetics for Kr, such as time-dependent ionization. One can find a section there discussing dense plasma effects upon atomic physics, such as level shifts and ionization lowering.

An approach different from the ionization kinetics was taken in [VI-30] to study an Ar puff-on-puff load. In an LTE equation-of-state table, all the properties of the plasma are determined by two parameters: 1) the temperature and 2) density. Busquet [VI-31] proposed that non-LTE ionization could be approximated with a temperature from a radiation-dependent, modified Saha equation in equation-of-state tables, instead of the plasma temperature from the internal energy. The primary interest of [VI-30] was a load design wherein a heavy outer shell would implode upon, and transfer its energy to, a low-density central solid-fill. The outer shell need not have a large velocity as the solid-fill would be heated quasi-adiabatically. In this manner, T_e would rise simultaneous with T_i rather than first having the ions thermalize their kinetic energy followed by equilibration of ion thermal energy with the electrons. This picture was described as analogous to the heating in laser fusion targets. Simulations were performed with a 1-D MHD code driven by a specified current rather than a circuit model. The results showed that about twice the mass participated in emitting K-shell photons with a shell-on-solid-fill compared with the load without the solid-fill. This design looks essentially like an outer shell on a central jet, i.e., the jet–outer of [IV-38]. As the proposed non-LTE ionization model of [VI-31] has not been verified against more accurate treatments nor validated against experimental data, it is unclear if the model is appropriate for K-shell sources.

The incorporation of non-LTE into multidimensional simulations of Z-pinches cannot be done as a straightforward extension of the 1-D approach with coupling coefficients: a coefficient for each emission feature connecting each zone to every other zone would be too memory and computationally intensive. Existing reports of multidimensional Z-pinch modeling used radiation diffusion and LTE ionization kinetics and opacities. An example would be the test of the MRT stabilization by a centrally peaked profile reported for Kr in [V-44].

Thornhill *et al*. [VI-32] advanced a unique technique for CRE kinetics applicable to multidimensional codes. Basically, a 3-D table is precalculated for the CRE kinetics, and hence the name tabular CRE (TCRE). The table entries are formed by calculating all the properties of interest for a uniform plasma of a given ion density, internal energy, and size. The size parameter is replaced by a catalog of the escape probability of the dominant emission line from each ionic stage. For a material of atomic number Z_A, there are Z_A lines. When coupled to an MHD code, the radiation transport is solved for the Z_A lines along a discrete set of ordinates emanating from each zone. The angle average of the escape probabilities over the rays is used to characterize that zone. For the on-the-spot (OTS) approximation, any absorption along a ray is attributed to the emitting zone. This approach is superior to diffusion because: 1) it goes to the correct optically thin and thick limits; 2) the impact of line absorption and photoexcitation are taken into account; and 3) non-LTE source functions are included, i.e., the source function is not Planckian as assumed in diffusion. The technique was verified by comparison with 1-D calculations where the more rigorous transport with coupling coefficients can be used. As a demonstration, the role that MRT plays in the K-shell radiation was studied in 2-D using TCRE.

The TCRE non-LTE model was subsequently combined in [V-20] with the 2-D (r-z) Mach2 MHD code [VI-33] to simulate the Ar experiments on Decade Quad with the 12-cm-diameter nozzle. The initial density profile from PLIF measurements was used for the initial gas distribution and an equivalent circuit description of the generator drove the pinch. In agreement with the experimental yield data, but unlike 1-D simulations, the 2-D modeling showed that the configuration with a central jet is superior to the configuration without the jet. The 2-D simulations showed that the presence of the central jet dampened the instabilities and produced a high-density K-shell-emitting region. Recently, the ZR generator was configured for gas-puff loads and the Mach2-TCRE code was exercised to ascertain which, among several, would be the optimal initial density profile for Ar K-shell. The predictions from [VI-34] were in the range 280–340 kJ for the double-shell puffs of the AASC design [IV-7] at a mass loading of 1 mg/cm. The experiments measured 250 kJ [VI-10] at a reduced Marx charging. Given that the measured current in the feed was $\sim$15 MA but the calculations used 18 MA from an estimated circuit, the agreement was satisfactory.

In the first paper on the TCRE technique, it was stated that one of the major drawbacks of the model was the OTS approximation. In a paper within this Special Issue on Z-pinches, Thornhill *et al*. [VI-35] have shown how to replace this approximation with a nonlocal absorption model. The more exact simulations using nonlocal absorption have larger peak total and K-shell powers, in comparison with the simulations using OTS. In the former case, there is some spatial propagation of photopumping over a larger volume than in the latter case. This reduces the opacity within a zone near the edge of the K-shell-emitting region and enhances its emissivity.

C. Energetics and Dynamics of Radiation Sources

The previous two sections have concentrated on experiments for K-shell radiation sources and the non-LTE ionization kinetics producing such radiation. In this section, we turn to considerations of the dynamics during stagnation. In particular, the discussion will focus on the difference between the ion and electron temperatures, the energy sources leading to heating and radiation emission, and the energy balance.

The thermal electron temperature can be determined spectroscopically, for example, using line ratios as described in the previous section or the free-bound continuum slope described in Section VI-A. On the other hand, the thermal

ion temperature does not enter any kinetic reactions for a Z-pinch, and so cannot be measured by those particular spectroscopic techniques. Instead, one measures the FWHM of the profile of an emission line ($\Delta\nu_{\rm FWHM}$) using high-resolution spectroscopy. There are several known components that contribute to the measured linewidth, such as Doppler broadening due to ion motion ($\Delta\nu_{\rm Doppler}$), the microscopic physics of Stark broadening ($\Delta\nu_{\rm Stark}$), opacity broadening ($\Delta\nu_{\rm opacity}$), and even instrumental broadening ($\Delta\nu_{\rm instrum}$). For Gaussian profiles, these effects add in quadrature and the Doppler broadening can be deconvolved from the other components as follows:

$$\Delta\nu_{\rm FWHM} = \sqrt{(\Delta\nu_{\rm Doppler})^2 + (\Delta\nu_{\rm Stark})^2 + (\Delta\nu_{\rm opacity})^2 + (\Delta\nu_{\rm instrum})^2}.$$

An effective ion temperature ($T_i^{\rm eff}$) is then associated with $\Delta\nu_{\rm Doppler}$ using (FWHM)

$$\Delta\nu_{\rm Doppler} = 2\sqrt{\ln 2}\sqrt{\frac{2k_B T_i^{\rm eff}}{m_i}}\frac{\nu_o}{c} \tag{VI-3}$$

where ν_o is the line center frequency. Here the derived temperature is called effective because $\Delta\nu_{\rm Doppler}$ may include hydrodynamic motion as well as thermal broadening.

For a Ne/Ar mixture on Saturn, Wong *et al.* [VI-36] used the Rydberg series in He-like Ar to determine the Stark broadening as it scales as the square of the principal quantum number of the emitting level. From a best-fit Gaussian profile to the lines they found $T_i^{\rm eff} \sim 36$ keV, much larger than the peak $T_e \sim 1$ keV from the continuum slope. In their summary table of K-shell yields for Ar solid-fills, Levine *et al.* [IV-42] listed $T_i^{\rm eff}$ of ~20 keV for Double-EAGLE and ~12 keV for Saturn, while T_e was also ~1 keV. Details of the measurement technique were not presented. The most detailed study of $T_i^{\rm eff}$ has been performed with neon puffs on two small generators at WIS. Kroupp *et al.* [VI-37] initially worked on an ~320-kA pulser with an ~750-ns implosion time. A gated, high-resolution spectrometer measured the width of the Ne Ly-α satellite line $2p^2\ {}^1D_2 - 1s2p\ {}^1P_1$. This line is optically thin, isolated with the 6400 resolution used, and not affected by Stark broadening. During stagnation, the $T_i^{\rm eff}$ decreased from ~2.3 keV to ~200 eV over 4 ns while T_e increased from ~150 eV to a maximum of 250 eV at the time of peak power. Subsequently, Kroupp *et al.* [IV-68] used the diagnostic instrument for the Ly-α satellite line on a 500-kA, 500-ns capacitor discharge. On this device $T_i^{\rm eff}$ decreased from ~3.8 keV to ~500 eV and T_e peaked at ~200 eV over the 10 ns of stagnation. The above review of the large difference between $T_i^{\rm eff}$ and T_e was limited to gas puffs, but the phenomenon is also seen in wire arrays [VI-38]–[VI-40]. For those experiments wherein the electron density is also measured, one also finds that the ion–electron thermal equilibration time is much shorter than the pulsewidth of the total power. In [IV-68], the measured ion effective and electron temperatures were used in an equilibration rate equation to obtain an ion thermal temperature (T_i) that was $\sim 1/10 T_i^{\rm eff}$ early in the stagnation 4 ns before and remained half of $T_i^{\rm eff}$ as late as 7 ns after the time of peak power. The remaining questions are what is the origin of the large effective temperatures derived from linewidths? and what role do they play in heating during stagnation?

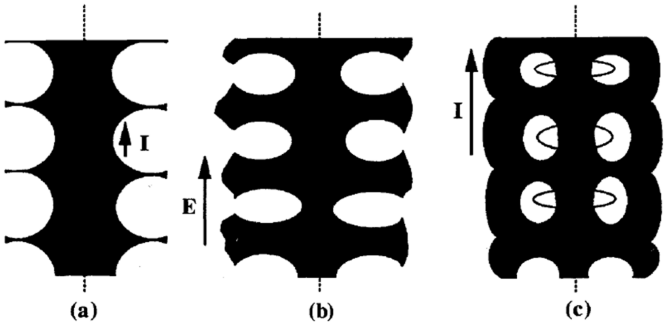

Fig. VI-12. (a) Initial development of $m = 0$ structures. (b) Expanding cusps begin to reconnect the current. (c) Pinch current flows on the outside with trapped cells of azimuthal magnetic field. Reprinted with permission from [VI-41]. Copyright 1994, AIP Publishing LLC.

Suggestions for the large $T_i^{\rm eff}$ included hydrodynamic motion, 3-D effects, rotation, or small-length scale turbulence [VI-36], [IV-68]. In a prescient paper, long before the observations of large $T_i^{\rm eff}$ in gas puffs, Lovberg *et al.* [VI-41] proposed that the rapid expansion of a D_2 fiber pinch results from the $m = 0$ instability and subsequent drag heating. When the outer region of the fiber goes unstable, the nonlinear evolution leads to a bubble or, in azimuth, a loop containing azimuthal magnetic field (B_φ). The neck of the bubble, located at the outer radius of the pinch, shorts out due to the electric field and the flux becomes entrapped within the plasma. The energy inside the plasma then consists of internal thermal energy, kinetic energy, and isolated loops of magnetic energy. These loops contract toward the axis due to the curvature stress ($-B_\varphi^2/4\pi r$), and in so doing the magnetic energy does work to displace the plasma. According to [VI-41], the ions pick up most of this drag heating and, as the fiber does not break up, the process repeats and is akin to boiling of a heated fluid. Fig. VI-12 shows a schematic of the process as envisioned by [VI-41]. The thermal ion heating process is described by an equivalent enhanced resistance which is nonlinear, i.e., depends on the current

$$R_{\rm bub} = \varsigma\frac{\ell I}{c^3 a\sqrt{M_o/\ell}} \tag{VI-4}$$

where a is the pinch radius and the numerical factor $\varsigma = 2$. The rate at which magnetic flux detaches from the external circuit is $R_{\rm bub}I$, and the total power pumped into ion heating would be $R_{\rm bub}I^2$.

The concept of entrained flux loops in a pinch was independently developed in [VI-42] and applied to radiating pinches. The entrained magnetic flux resulting from MRT instabilities leads to a macroscopic MHD turbulent pinch that is prevented from radiative collapse. In some wire array pinches it was observed that the total radiated energy was larger than the $\mathbf{J}\times\mathbf{B}$ coupled energy for any reasonable final radius, as estimated from (III-32) using the peak current in 1/2 $\Delta L_{\rm load} I_{\rm pk}^2$. Velikovich *et al.* [VI-43] and Rudakov *et al.* [VI-44] addressed this problem by extending the work of [VI-42]. They presented

a thorough derivation of enhanced heating resulting from magnetic entrapment by formulating mass, momentum, and energy equations including the presence of magnetic bubbles, and separate induction equations for the plasma and the bubbles. The plasma energy equation includes heating of the plasma from the compressional pdV work performed by the bubbles as they contract within the plasma toward the axis, heating of the ions from the energy dissipated by the drag force, and heating of the electrons from resistivity. The equivalent resistance of the total heating term has the same form as (VI-4) but with $\varsigma = 1/2$.

Haines *et al.* [VI-39] addressed the problem of large T_i^{eff} by claiming that short-wavelength $m = 0$ MHD interchange instabilities at stagnation lead to ion viscous heating, as contained in (III-7). These modes would be hard to detect as $ka \sim 200$, for wavenumber k and pinch radius a [I-13]. Haines [VI-45] objected to the closure of the bubbles at the constricting neck, as in Fig. VI-12, because the $\mathbf{J} \times \mathbf{B}$ force would oppose the axial motion. The enhanced resistance derived in [I-13] has the same form as (VI-4) with $\varsigma = 2.26$. The relevance of ion viscous heating for a pinch can be estimated by comparing the viscous Reynolds number $R_A = v_A a/\nu_{\text{ii}}$, where v_A is the Alfven velocity and ν_{ii} is the ion viscosity, against the magnetic Reynolds $S = v_A a/(c^2\eta/4\pi)$. R_A is basically a measure of advective motion relative to momentum diffusivity and S measures the advective motion relative to the magnetic diffusivity. If $R_A \gg S$, the pinch is viscous. Another way to express this is that if the magnetic Prandtl number $P_M = 4\pi\nu_{\text{ii}}/c^2\eta$ is >1, then ion viscous heating is more important than resistive heating. Both the bubble and the ion viscous mechanisms produce thermal heating rather than large hydrodynamic motions.

Let us now return to the neon experiments performed at WIS mentioned above. Kroupp *et al.* [VI-37] studied the energy balance in a neon pinch and found that they could account for the total radiation from the K-shell region during stagnation using the measured change in T_i^{eff}. The same results held for [IV-68], even though the ion thermal temperature T_i was much smaller. For both of these pinches on generators of $\leq$500 kA, the energy source for the radiation is accounted for, but the nature of the motion that dominates the ion kinetic energy as measured by T_i^{eff} was not resolved. Using a 2-D MHD code with the TCRE ionization kinetics (see Section VI-B), Giuliani *et al.* [VI-46] showed that the time-dependent data for the temperatures T_i^{eff} and T_e from [IV-68] could be reproduced, as well as the visible imaging, electron density, K-shell radius, and K-shell pulse. The results are shown in Fig. VI-13. The simulated T_i^{eff} were determined computationally in a manner analogous to the diagnostic: the atomic-level populations from the simulation were used to solve the radiation transport through the plasma and the linewidths for the calculation of T_i^{eff} were derived from synthetic spectra. Sharp gradients in the radial velocity near the axis and the corresponding Doppler shifts, combined with the shock heating of the ions [see (III-7)] early in the stagnation phase, produced the broad lines. T_i rapidly decreases to T_e before peak power. Continued thermalization of the motion does not produce further ion heating because of the short equilibration time between ions and

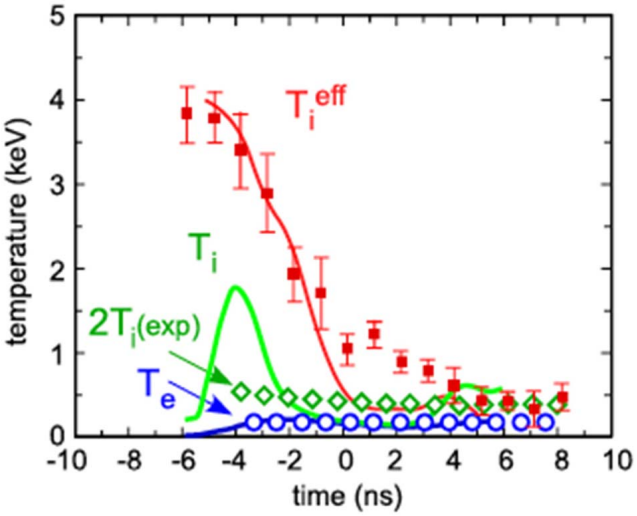

Fig. VI-13. Electron temperature (blue line), thermal ion temperature (green line), and effective ion temperature (red line) from an MHD simulation of a neon gas puff. Data from [IV-68] are shown as symbols. Reprinted with permission from [VI-46]. Copyright 2014, AIP Publishing LLC.

electrons and the strong radiation that keeps the electrons cool. Understanding the discrepancy between the measured and simulated thermal T_i early in the stagnation remains for further research. Another point of interest is that an accurate knowledge of the initial density profile as well as the location of the plasma breakdown was important in obtaining the agreement.

Maron *et al.* [VI-47] further examined the energy balance in pinches using spectroscopic data from the neon experiments at ~500 kA at WIS and Al wire experiments on the Z accelerator at ~20 MA. They envision the stagnation hydrodynamic geometry as a shock wave propagating outward from the axis and encountering the imploding plasma driven by a magnetic piston. However, the magnetic field does not play a major role in the radiation production within the stagnation region, i.e., Bennett equilibrium is not applicable. Instead the kinetic energy described by T_i^{eff} that is thermalized across the accretion shock demarking the outer radius of the K-shell-emitting plasma is sufficient to account for the total radiation from this region. The observed data from both experiments are used to show that the hydrodynamic shock jump conditions are satisfied without including magnetic terms. As noted in their paper, their conclusion raises the question of how the magnetic field can produce the high acceleration of the imploding plasma and heating at stagnation while most of the current remains far outside of the emission region.

A similar description of the stagnating region was earlier described in [VI-48] based upon 2-D simulations of a single temperature plasma and a simple radiation model. The focus of this paper was the temporal radial variation of the hot plasma core. The magnetic piston drives an imploding region which produces an outward expanding shock once it reaches the axis. The kinetic energy of the inflowing gas is balanced by the pressure behind the shock. The subsequent contraction of the emitting plasma occurs when the piston collides with the shock. At this point, the plasma in the unstable outer region of the magnetic piston produces turbulence in the core.

In contrast to the above MHD view of a stagnating pinch composed of shock waves, magnetic bubbles, or viscous heating from $m = 0$ instabilities, Coleman *et al.* [IV-31] suggested an alternative picture based on Ar data from filtered zipper arrays and high-resolution pinhole images taken on several different generators. Instead of a smooth emitting region, the K-shell-radiating elements of a pinch are discrete thin (0.1 mm), long (few millimeters), dense ($>10^{20}$ cm^{-3}), low-temperature (<1.5 keV) filaments that are kink unstable and move transversely at ~40 cm/μs. Each filament radiates at a fixed power and their lifetime defines the radiation pulsewidth rather than the transit time of a shock wave. This concept has not received further research though the collection of filaments might display spectroscopic properties that differ from those of a homogeneous emitting plasma.

Besides spectroscopic and simulation analyses of the energy balance during stagnation, there have also been studies using electrical diagnostics. Soon after the concept of magnetic bubbles was developed by [VI-41]–[VI-44], Labetsky *et al.* [VI-49] devised a diagnostic for the presence of such bubbles and to determine any effective resistance, as in (VI-4). The loads were single (3-cm radius) and double shell puffs (3- and 1.4-cm radii) of Ne, Ar, and Kr fielded on the IMRI-4 generator (~350 kA in 1.1-μs rise time). A three-channel instrument obtained simultaneous interferometry, polarimetry, and shadowgraphy images. The results indicate regions of trapped magnetic field within the plasma of similar magnitude to that exterior to the pinch. Electrical measurements using an active voltage divider at the load were performed on the single-shell puffs. This voltage was taken to consist of inductive and active resistive components, as in (III-18). The current was measured and the terms $L_{\rm load}$ and $dL_{\rm load}/dt$ were calculated using the snowplow model. A number of experiments were performed with the three gases over a range of mass loadings. For all the three species at the higher mass loadings they found that $R_{\rm load}$ was two to four times larger than the value from (VI-4). Furthermore, while $R_{\rm bub}$ should increase as M_o decreases, the opposite trend was observed for $R_{\rm load}$. We remark that a snowplow model was used to calculate $L_{\rm load}$ and $dI_{\rm load}/dt$, and hence derive $R_{\rm load}$, but there were no corroborating observations to confirm the temporal variation of the plasma radius.

A detailed measurement of the energy balance using electrical and broad-band spectral data was performed on the Saturn generator. In a multi-MA water-line, pulsed-power generator the current is measured with B-dot probes in the final feed to the load region but the voltage is generally measured far upstream on the water side of the vacuum interface. A circuit analysis must be used to estimate the load voltage. Murphy *et al.* [VI-50] developed a vacuum voltmeter to directly measure the load voltage. This was possible because the Z-pinch set up on Saturn allows access to the high-voltage electrode from inside the vacuum chamber above the diode. From temporal measurements of the voltage and current at practically the same location, one first of all has the total energy that the generator has delivered to the load region up to time t. If resistive heating

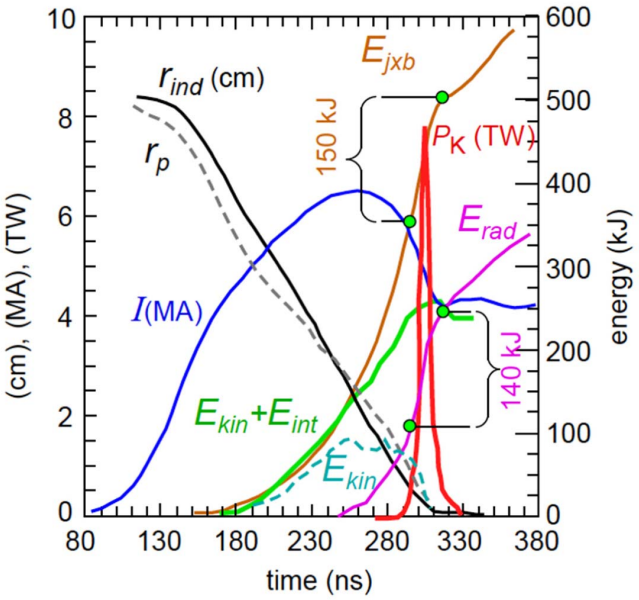

Fig. VI-14. Data from a Saturn Ar gas puff showing that the energy coupled to the pinch ($E_{j\times b}$) balances the sum of the kinetic ($E_{\rm kin}$), internal ($E_{\rm int}$), and radiated ($E_{\rm rad}$) energies. A vacuum voltmeter was used to measure the load voltage. The data indicate that during the time of K-shell pulse the increase in $E_{j\times b}$ is radiated away. See the text for the details of the analysis.

is negligible, then the energy coupled to the plasma is the $\mathbf{J}\times\mathbf{B}$ energy and (III-32) and (III-18) give

$$E_{j\times b}(t)=\int_0^t \frac{I^2}{2}\frac{L_{\rm load}}{dt'}dt'=\int_0^t V_{\rm load}I\,dt'-\frac{1}{2}L_{\rm load}I^2. \quad \text{(VI-5)}$$

From (III-18), the load inductance is obtained from the measured load voltage

$$L_{\rm load}(t)-L_{\rm load}(t=0)=\Delta L_{\rm load}=\frac{1}{I}\int_0^t V_{\rm load}(t')dt'. \quad \text{(VI-6)}$$

If it is further assumed that the imploding plasma is perfectly conducting and 1-D, as in the snowplow model, then one can obtain the sheath radius as a function of time from (III-26)

$$r_{\rm ind}(t)=r_o\exp\left(-\frac{c^2}{2\ell}\Delta L_{\rm load}\right) \quad \text{(VI-7)}$$

where $r_{\rm ind}$ can be thought of as an effective radius where the entire pinch current flows in a thin sheet. It agrees quite well with the radius determined from a snowplow calculation using the measured initial density distribution and current. At any time t, the coupled energy should be the sum of the kinetic, thermal, excitation/ionization, and radiated energies

$$E_{j\times b}(t)=\frac{1}{2}{\rm Mu}_p^2+\frac{3}{2}(k_BT_i+\overline{Z}k_BT_e)+E_x+E_{\rm rad} \quad \text{(VI-8)}$$

where $\bar{Z}$ is the mean ionic charge, E_x is the excitation/ionization energy, and $E_{\rm rad}$ is the emitted radiation energy. This equation explicitly shows the terms accounting for the energy difference between the $\mathbf{J}\times\mathbf{B}$ and kinetic energies discussed near the end of Section III-D.

Commisso *et al.* [IV-52], [IV-53] analyzed the vacuum voltmeter and current data for Ar shot 3565 on Saturn according to the above equations. Fig. VI-14 shows the evolution of various quantities for this shot. During the time

period that the pinch radiates in the K-shell, the $\mathbf{J} \times \mathbf{B}$ energy increases by $\sim$150 kJ which is balanced by an increase of $\sim$140 kJ in the radiation (72 kJ of which is K-shell radiation). The kinetic energy 1/2 $M(dr/dt)^2$, which was evaluated from (III-28), the time derivative of (VI-7), and the measured initial density profile and current, was negligible during this time. Also the second and third terms in (VI-8) inferred from the measured $E_{j\times b}$ and $E_{\rm rad}$ were approximately constant during this time. Thus, the loss of kinetic energy within the snowplow model of the pinch does not account for the gain in radiated energy. The authors conclude that during this time period, the $\mathbf{J} \times \mathbf{B}$ energy is rapidly converted into radiation. The authors speculate that this process is indirect, and that the high temperature ions heat lower temperature electrons that then collisionally excite the K-shell radiation. However, the actual mechanism for converting the $\mathbf{J} \times \mathbf{B}$ energy into radiation requires more detailed research.

In summary, the physics of the dynamics, thermalization, and energy balance during stagnation may involve several competing processes. For gas puffs on low-current generators ($\leq$500 kA) as studied in [IV-68] and [VI-37], the measured $T_i^{\rm eff}$ of $\sim$4 keV appears to arise from the radial velocity of the implosion [VI-46], and the radiated energy can be accounted for by just the inflowing kinetic energy [VI-47]. For these puffs, the magnetic Prandtl number is $\ll$1 so the theory of ion viscous heating [VI-45] would not apply. On the other hand, on multi-MA generators, the Prandtl number can be much larger, for instance, the magnetic Prandtl number $P_M \sim 67$ for Ne/Ar experiments by [VI-36] on Saturn ($\sim$7 MA). The implosion velocity is about 4 times larger on Saturn than on the WIS generator (80 cm/μs versus 23 cm/μs, respectively), but Doppler shifts arising from this velocity would not be sufficient to account for $T_i^{\rm eff} \sim 36$ keV. Jones *et al.* [VI-51] measured red and blue Doppler shifts of He-like Ar and Cl dopant lines from a gas puff on the Z generator. They found that the implosion velocities decreased from $\sim$70 cm/μs at 6 ns before peak power to 58 cm/μs at -3 ns. The deceleration near stagnation may produce heating and large $T_i^{\rm eff}$, but Doppler widths through stagnation were not reported. Further research is needed to see if the origin of effective ion temperatures differs from small- to large-current generators. The $\mathbf{J} \times \mathbf{B}$ energy determined with a vacuum voltmeter on Saturn satisfies the energy balance without any resistive term [IV-52], unlike the case with the small generator IMRI-4, where it appears to require a substantial active resistive in the load [VI-49], even beyond that from the dissipation of magnetic bubbles.

D. Axial Magnetic Fields in Radiation Sources

The initial interest in axial magnetic fields within gas-puff pinches focused on flux compression. The theory was presented in [VI-52] and subsequent experiments in [VI-53] on the small generator at UC Irvine (470 kA in a 1.25-μs rise time) demonstrated a compression ratio of 180 times the initial field to $\sim$1.6 MG. This value was measured by Faraday rotation through a fused silica quartz fiber mounted along the pinch axis [VI-54]. The initial field ($B_{\rm zo}$) was generated by a pair of Helmholtz coils and the nozzle (cathode) was fabricated from a carbon–carbon fiber composite of high electrical resistivity in order that the field could diffuse through it prior to the pinch discharge. The puff was a 2-cm-radius annulus and the highest compressions were found with Kr and Xe. Gases of lower Z_A tended to bounce off the compressed field. This may have reflected the lower mass loading for such gases due to plenum pressure constraints, or to such gases being poor radiators. (See [VI-55] for a more thorough discussion of these results.) Felber *et al.* [VI-56] inferred, based on flux conservation because of the measured high temperature of the imploding gas shell, an initial seed field of 100 kG could be compressed to 42 MG using an Ar pinch on the Proto-II generator (7.5 MA in 60 ns). If this high value for the compressed field was actually measured it would be larger than the best achieved to date (28 MG) on explosive generators [VI-57]. The Omega laser was used to compress a cylindrical target with an embedded field of $\sim$50 kG and measured compressed fields of 30–40 MG using proton deflectrometry [VI-58]. Finally, Felber's result has only recently been superseded by magnetized liner experiments on the ZR generator (more than twice the current of Proto-II) wherein peak axial fields of $\sim$90 MG are estimated from kinetic modeling of the observed tritium production from the D_2 solid-fill [VI-59].

Several general points were mentioned in [VI-53] and [VI-55] relevant to radiation sources. As $B_{\rm zo}$ increased for a fixed mass loading, both the implosion time and the final radius increased, while the total X-ray intensity decreased. Moreover, the pinch column was stable before and after stagnation, even for $B_{\rm zo}$ as low as 1 kG. Mitigation of the MRT instability by an axial magnetic field was mentioned in Section V-E. By far, most of the experimental effort for improving radiation sources has been with tailored density profiles as evidenced in Section VI-A.

Chaikovsky *et al.* [VI-60] and Shishlov *et al.* [VI-61] at the HCEI tested one load design of a radiation source that combines both stabilization mechanisms. This double-puff gas configuration consists of an outer annular shell and a central solid-fill with the radius of the shell five times larger than the outer radius of the solid-fill. An initial axial field serves to stabilize the run-in of the annular shell and, at contact with the inner solid-fill the snowplow effect stabilizes the final stage of implosion. Note that this configuration, in terms of the initial density profile but not the magnetic field, is similar in radii and mass ratios to the jet-inner load of [IV-38] and [IV-39] described in Section VI-A, which produced the highest power among the four pusher-stabilizer-radiator concepts. Chaikovsky *et al.* [VI-60] performed the first of these experiments with the magnetized shell-on-solid fill configuration using neon on IMRI-5 (400 kA in 300 ns). Four different radii of the outer annulus were studied: 2.2, 3, 4, and 5 cm. A number of scans were made over the mass of the annulus, the mass of the solid fill, and the initial magnetic field to determine the optimal conditions for Y_K. In general for all the shots, the addition of an axial field reduced the shot-to-shot variability and produced a more axially uniform pinch, i.e., less hot spots. This was interpreted as indicating a more stable pinch, but the pinch radius was about the same.

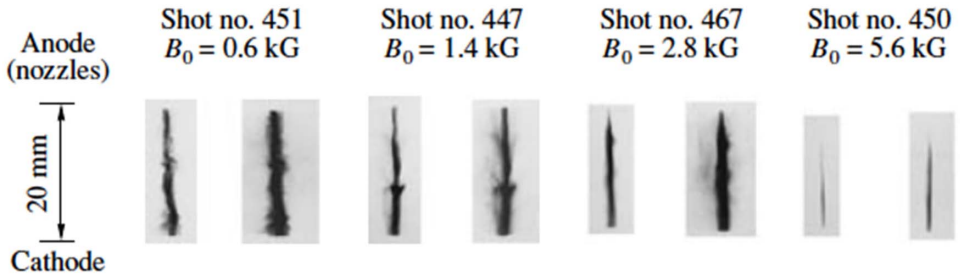

Fig. VI-15. Time-integrated pinhole images at stagnation for an Ar gas puff on GIT-12 with different initial axial magnetic fields (B_o). For each magnetic field value, the left image is the Ar K-shell radiation and the right image is soft X-rays (>0.8 keV). Reprinted from Fig. 6 of [VI-61], copyright 2006, with kind permission from Springer Science and Business Media.

However, in spite of the extensive scans to find optimal conditions, the axial magnetic field did not improve the K-shell neon yields. The optimal yields with and without a B_{zo} occurred for the same shell radius (3 cm) and nearly the same mass ratio (outer:solid-fill ~2:1). For the case with B_{zo} (=0.66 kG), the K-shell power was twice that of the case without B_{zo}, but the yield was ~30% less.

The magnetron discharges used for preionization on IMRI-4 and GIT-4 at HCEI (described in Section IV-C) embedded an axial magnetic field into the outer shell of a shell-on-shell gas puff. As described in [IV-71], the planar magnetron resulted in an increase of ~25% of Ar K-shell power and better reproducibility. No improvement was found with just a single shell.

Shishlov *et al*. [VI-61] used the same shell-on-solid-fill load concept for Ar on GIT-12 (2.5 MA, 300 ns with a POS) at HCEI. In these experiments, the configuration was fixed with a shell of a 4-cm radius and the central solid-fill was 0.8 cm. As was found for Ne on IMRI-5, the pinch on GIT-12 was observed to be more stable with a magnetic field, but the yield was substantially less: a maximum of 1.1 kJ/cm without a magnetic field but at best 0.39 kJ/cm with B_{zo} at a low value of 1.4 kG. It was argued that the lower yield could be solely due to the energy expended in compressing the axial field. The pinhole images in Fig. VI-15 clearly demonstrate that increasing the initial magnetic field makes the pinch straighter and tighter. The visible light streak images in Fig. VI-16 indicate that without a magnetic field both the outer shell and inner solid fill imploded together. This current division was not observed with an axial magnetic field. For both the Ne and Ar experiments, the axial magnetic field that produced stable pinches, as defined by the uniform X-ray pinhole images, was only 1/4 to 1/2 of that in (V-3). This equation is only a rough estimate, but the experimental data allow one to estimate values of B_{zo} needed for stabilization at stagnation. The largest value for B_{zo} (5.6 kG) produced the tightest pinch (0.01-cm radius) based on pinhole images of radiation >0.8 keV. Assuming that this emitting region consists of the gas in the inner solid-fill, the compression factor was 80, a notable record. However, there was no measured Ar K-shell radiation from this pinch, indicating that a tight, uniform pinch is not the bellwether for a good K-shell source.

We note that both of the above experiments [VI-60] and [VI-61] may be in the inefficient

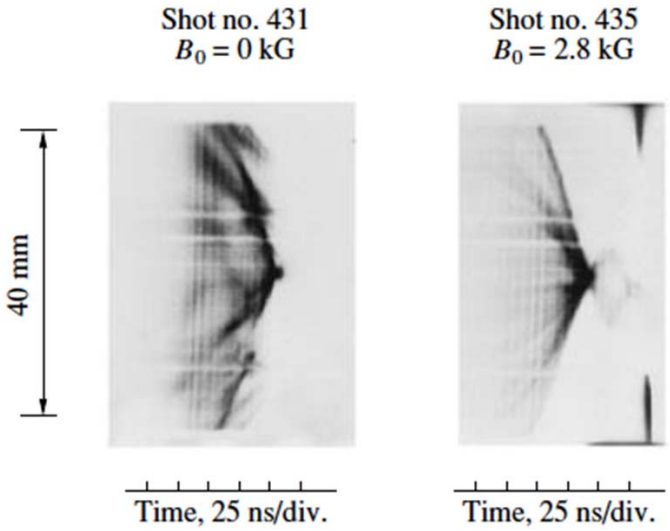

Fig. VI-16. Visible light streak images of two Ar gas puff pinches on GIT-12 without and with an initial axial magnetic field (B_o). Reprinted from Fig. 9 (top only) of [VI-61], copyright 2006, with kind permission from Springer Science and Business Media.

regime for the given currents and gases. From Fig. VI-1, a current of 2.5 MA on GIT-12 is clearly below the current break point for Ar, and the 400 kA of IMRI-5 may also be low for Ne. If hot spots are the primary source of K-shell radiation in the inefficient regime, then Y_K would be less for those experiments with $B_{zo} > 0$. A test of this conjecture would be the study of Y_K from Ne gas puffs with and without a B_{zo} at ~1 MA.

The report by Sorokin [VI-62] on Ar and Ne puffs with a B_z differs from some of the results of [VI-60] and [VI-61], and runs counter to the stated conjecture. In these experiments the axial field was not embedded in the pinch but instead was generated by a helical return current cage on the MIG generator (2 MA in 80 ns). In this Z-θ pinch, the axial field rises with the azimuthal field and becomes part of the driving force compressing the plasma. The ratio of the axial to the azimuthal field component scales as the radius over the fixed pitch of the helical returns, so the more the pinch compresses the smaller B_z/B_φ becomes. The load was a double shell puff of radii 1.8 and 0.5 cm for Ar and 1.5 and 0.5 cm for Ne. As in the above experiments with an embedded B_{zo}, the helical cage

produced axially uniform pinches without the characteristic hot spots, as observed with straight returns. However, unlike the above experiments, for both Ne and Ar double-shell loads the K-shell yield were similar for the straight and helical return current cages: 0.8–1 kJ for Ar and 4–5 kJ for Ne. Based on the assumed velocities, the η for Ar was up to 1.9. But from Fig. VI-1, the current for the generator puts it in the inefficient regime, and the reported Ar yields are consistent with the I^4 scaling line on the figure. On the other hand, Ne should be in the efficient regime, which is consistent with $Y_K > 25\%$ of the estimated coupled energy ($1/2\ \Delta L_{\text{load}} I^2$ with $r_f \sim 0.2$ cm). The generated B_z in these experiments produces homogeneous Ar and Ne pinches, but their K-shell yields are not changed from straight returns showing hot spots, even though Ne is in the efficient regime and Ar is not.

Gourdain *et al.* [VI-63] applied an axial magnetic field from a single turn loop on the Cobra generator (described in Section VII) to study compression of B_z in a Ne double-shell gas puff. Miniature B-dot probes [VI-64] were oriented to pick up changes in axial magnetic flux and an optical fiber aligned with the center of the pinch measured the B_z-induced Faraday rotation in a double pass arrangement. Both instruments recorded a change in the axial flux only at the time of the X-ray pulse and the amplitude of the change was similar whether the applied field was energized or not. These results are consistent with the snowplow model sweeping up mass and applied field, but such signals in the absence of an applied B_z indicate the generation of azimuthal currents in all cases.

E. Plasma Neutron Sources

Up to this point the review has only discussed gas-puff Z-pinches as plasma radiation sources. This section addresses deuterium puffs as plasma neutron sources. Similar to the discussion on the Ar K-shell yields, we organize the data on Z-pinch neutron sources into a figure of yields and a historical narrative. A recent review of DPFs in [I-20] included some comments on gas puffs as neutron sources. The following are more recent data on gas puffs.

There are two scenarios in which fusion neutrons are produced from a deuterium gas puff and they are distinguished by the energy distribution function of the deuterons. First there is the beam–target interaction. A small fraction of the deuterons are accelerated by some means to an energy much greater than the thermal energy of the parent distribution. This beam, with a characteristic energy E_b for each deuteron, interacts with target deuterons from the parent distribution and 50% of the reactions produce H_e^3 and a 2.45-MeV neutron. At $E_b = 10$ keV, the cross section for the neutron producing reaction [III-12] is $\sigma_{\text{DD}}(10\text{ keV}) \sim 5 \times 10^{-30}$ cm^{-2}. The cross section rises rapidly [$\sigma_{\text{DD}}(100\text{ keV}) \sim 1.7 \times 10^{-26}$ cm^{-2}] and peaks at $\sim 10^{-25}$ cm^{-2} for $E_b \sim 3$ MeV. In the center-of-mass frame of the interaction, the neutrons are emitted isotropically, but in the lab frame the neutron energy distribution would be more anisotropic the larger E_b is. In the second scenario, the deuterons have a thermal (Maxwellian) distribution of a few keV temperature and the self-interactions within the deuterium bath produces fusion neutrons. High-energy beam deuterons have a larger fusion cross section than the deuterons in a Maxwellian of a couple of keV temperature. On the other hand, in a hot thermal distribution the high-energy tail can be sufficiently populated to compensate for their smaller fusion cross section compared with the MeV beam deuterons. DPFs and Z-pinches on low-current generators produce neutrons via the beam–target interaction. High-current pinches (>5 MA) produce neutrons via both scenarios.

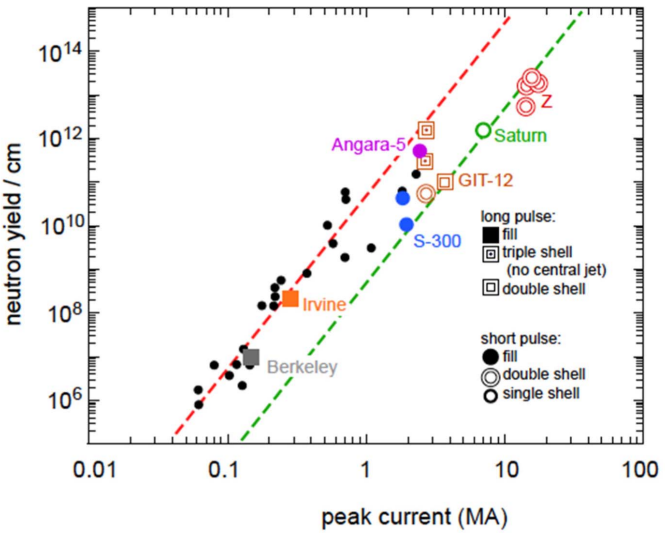

Fig. VI-17. Neutron yield per unit length versus DPF current for the small dots and Z-pinch current for all other symbols. See the text for the data sources and meaning of the two trend lines. Long pulse means an implosion time of >200 ns. Adapted from [I-20].

Krishnan [I-20] developed arguments and presented data showing that the current scaling law for both beam and thermally generated neutrons follow a $Y_n \propto I^4$ relation, where Y_n is the total neutron yield, but the coefficient of proportionality is smaller for the thermonuclear than for the beam–target process. The trend line for these two mechanisms along with data from DPFs and Z-pinches are presented in Fig. VI-17, which has been adopted from [I-20] and [VI-65]. All of the D_2 DPF data from [I-20] are shown as smaller dots in the figure while the data from D_2 Z-pinches are symbolically distinguished by their nozzle configuration and implosion time, as was done in Fig. VI-1. The upper trend line represents beam generation of neutrons and is based on the DPF data. The lower trend line represents a mixture of beam and thermonuclear generation. The references for the gas puff data are: Berkeley [III-5]; Irvine [II-3]; S-300 [VI-66], [VI-67]; Angara-5 [VI-67], [VI-68]; GIT-12 [VI-69], [VI-70]–[VI-72]; Saturn [VI-74]; and Z [VI-75]–[VI-77].

The earliest reported study of neutrons from a D_2 pinch emerged from Project Sherwood in 1958 under the Atoms for Peace initiative. Anderson *et al.* [III-5] used a 45-cm-long gas embedded pinch in the Radiation Laboratory at the University of CA, Berkeley and Livermore. They theorized that the $\sim 10^8$ total neutrons per discharge arose from the $m = 0$ instability. Bailey *et al.*'s work [II-3], using the first true gas puff at the University of CA, Irvine, was reviewed in Section II. In a

1998 internal SNL report, Spielman *et al*. [VI-74] were the first to interpret their neutron yield data as indicative of the thermal production mechanism. This conclusion was based on the fact that both the radially and axially mounted indium activation detectors gave similar yields of $\sim 3 \times 10^{12}$ neutrons. These experiments were 2.5-cm-diameter D_2 single shells, 2 cm in length, on the Saturn generator. Almost a decade later, Coverdale *et al*. [VI-75], [VI-76] returned to gas-puff neutron source development on the recently commissioned Z facility ($\sim$15 MA in 100 ns). They studied double-shell D_2 loads with the $r_N = 1$–2/3–4 nozzle described in Fig. IV-3 and previously used for Ar K-shell pinches. The largest neutron yield, 3.7×10^{13} for a 2-cm length, was an order of magnitude larger than on Saturn, and gave a current scaling of $I^{3.5}$ between the two machines. Both indium activation and neutron time-of-flight (nTOF) detectors were fielded radially and axially to verify isotropy, but the gas-puff hardware precluded a clean interpretation of the axial data. Within the error bars, the neutron data appeared isotropic. While any observed anisotropy is a sufficient condition for the beam–target mechanism, isotropy is necessary but not sufficient for the thermonuclear mechanism. Velikovich *et al*. [VI-77] presented analytic models for the beam–target and thermal yield of neutrons on these experiments. They argued that if all the observed Y_n was due to beams alone, then 6%–9% of the magnetic energy coupled to the plasma would need to be converted into deuteron beams for E_b anywhere between 100 keV and 1 MeV. This efficiency would surpass existing light ion accelerators. Furthermore, 1-D and 2-D MHD simulations produced similar yields to the data. It was concluded that a substantial fraction of Y_n on the Z facility was thermonuclear in origin.

Definitive proof of thermonuclear neutrons from a D_2 gas-puff Z-pinch must await further experiments. However, particle-in-cell (PIC) simulations have supported the conjecture of [VI-75] and [VI-77] regarding thermonuclear processes. The PIC approach intrinsically accounts for kinetic effects, such as beam generation. Welch *et al*. [VI-78], [VI-79] presented the first fully kinetic PIC simulation in their large-scale plasma code of a D_2 Z-pinch that included collisions and self-consistent electromagnetic effects. In these simulations, large inductive electric fields of the order 10–15 MV/cm develop in the low-density, highly magnetized regions between the MRT spikes. McCall [VI-80] presents an analytic model for the acceleration of ions by the inductive field across the neck of a growing $m = 0$ instability. The process would also apply to the gap between MRT spikes. Welch *et al.* [VI-78], [VI-79] mention that kinetic instabilities in these regions drive energetic ions up to $\sim$100 keV and form a non-Maxwellian tail in the distribution. Corresponding studies of a DPF with the same simulation code suggest that the lower hybrid drift instability could be important for the ion acceleration [VI-81]. For the Z-pinch PIC simulations at low currents, such as 1 MA, a high-energy, non-Maxwellian population of the deuterons produces all the neutrons from beam–target interactions. However, at high currents of $\sim$10–15 MA, this population was responsible in the modeling for only half of the neutrons, and the remainder were thermonuclear in origin. It is interesting to note that for the low-current cases, 2-D simulations produce about 10 times more neutrons than 1-D PIC simulations because the MRT structures are absent from the latter. Welch *et al*. [VI-82] continued their PIC study up to an idealized 40-MA machine and predicted $>10^{16}$ neutrons. At these currents, 2-D and 3-D effects reduce the 1-D yield, so that the effect of the simulation dimensionality on Y_n is completely flipped from the low-current case.

We now review recent experimental results by Klir and collaborators for D_2 gas puffs on low-current generators wherein the neutrons are all attributed to the beam–target mechanism. These experiments used an extensive suite of nTOF diagnostics to extract the neutron energy distribution function. On S-300 (2 MA in $\sim$100 ns) Klir *et al*. [VI-66] measured $\sim 10^{10}$ neutrons from a 1-cm long conical solid-fill that expanded from a 0.5- to 0.75-cm radius. At a peak current of $\sim$2 MA, this point is on the lower scaling line of Fig. VI-17. The nTOF detectors arrayed radially and axially around the pinch showed that the peak of the neutron distribution function was 2.6 MeV along the direction of current flow, 2.3 MeV in the opposite direction, and 2.4 MeV for the side-on view. The average kinetic energy of the deuterons producing the neutrons was $\sim$100 keV. Further experiments [VI-67] on S-300 increased Y_n by a factor of six at the lower current of 1.5 MA and longer lengths (1.1–2 cm). It was noted that some of the gunpowder used to drive the puff was mixed with the D_2 puff producing an excessive mass loading. The combined energy of all of the fast deuterons producing the fusion reactions was $\sim$15% of the energy ($\sim$9 kJ) coupled to the plasma. This efficiency is impressive: it is larger than the value [VI-77] estimated to argue against a pure beam–target origin for the neutrons on the Z generator. Next Klir *et al*. [VI-69] used double-shell D_2 loads ($r_N = 1.5/4$ cm) and a 2-cm length on the GIT-12 generator. With a POS and 80-μg/cm total mass loading, the current rise time was $\sim$200 ns but the implosion time was $\sim$450 ns as given by the initial rise of the neutron pulse. Without a POS, the mass loading was 70 μg/cm and the implosion time was $\sim$650 ns. In both cases, the current at implosion was between 2 and 3 MA and the average yield was $1\text{–}2 \times 10^{11}$. The similar yield despite the different implosion time is likely due to the stiffness of the GIT-12 generator and the long neutron pulses (>100 ns). One result from these experiments was the strong correlation of Y_n with what they termed the peak effective voltage. The latter was determined in a similar manner to [IV-53] and [VI-49]. The voltage V_{up} was measured upstream from the load. Let L_o be the fixed inductance between the measurement position and the initial load radius. Note that V_{up} is not the same as the generator voltage V_g and L_o is not the same as the generator inductance L_g in (III-17). Then one can calculate the time history of the load inductance from

$$V_{\text{eff}} = I \frac{dL_{\text{load}}}{dt} = V_{\text{up}} - (L_o + L_{\text{load}}) \frac{dI}{dt} \qquad \text{(VI-9)}$$

where the left-hand side is their effective voltage neglecting any resistive component. Whether the opening switch was used or not, the result was $Y_n \propto (V^*_{\text{eff}})^{3.8}$, where V^*_{eff} is the

peak effective voltage in kilovolts. A large effective voltage indicated a large change in inductance, which was attributed to the spread of the light molecule D_2 to large radii within the A–K gap before the generator was triggered. Up to a 40-ns delay between the peak of the soft X-rays and the neutron was reported in [VI-69], but later attributed in [VI-70] to the neglect of an internal signal delay.

Klir *et al.* [VI-70] added an outer shell of 8-cm radius to their nozzle and examined triple-shell D_2 puffs on the GIT-12 machine. They reported double neutron pulses, as in [VI-67] and [VI-69]. The first one occurs at the beginning of stagnation while the plasma looks stable and there were no electron beams from the absence of high-energy bremsstrahlung. The second, and primary, pulse occurs after the disruption of the pinch by $m = 0$ and $m = 1$ instabilities, arises from beam–target interactions, and is accompanied by >1-MeV photons. These experiments did not use a POS and the best shot produced $\sim 3\times 10^{11}$ neutrons for a 92 μg/cm total mass load over a 3.7-cm length with an implosion time of 790 ns at a stagnation current of 2.8 MA. Heavier loads with higher stagnation current levels produced a smaller Y_n. Such loads required a longer delay time between the valve opening and the generator trigger, and hence more spreading of the D_2 as inferred in [VI-69]. This dispersal affects the dynamics and potentially leads to current leakage in the feed region. Another result was that the energy spectrum of the neutrons from the primary neutron pulse depended strongly on the mass loading. The highest ion beam energies increased as the load mass was reduced. Klir *et al.* [VI-70] were the first to report >10-MeV neutrons for low mass loads. This implies that the deuterons in the beam–target interaction must have energies >7 MeV. The correlation of the peak effective load voltage with Y_n was found as before, but its value of ~400 kV is far below the inferred deuteron beam energy. The load design for the maximum neutron yield on GIT-12 is discussed in the following section.

The tendency of greater ion beam energies at lower mass loading found in [VI-70] does not necessarily translate into higher neutron yield. Klir *et al.* [VI-71] show that the neutron yield for GIT-12 experiments displays a peak when plotted as a function of the parameter $I_{\text{stag}}/\sqrt{(M_o/\ell)}$, where I_{stag} is the current at stagnation of the D_2 gas puff and M_o/ℓ is the mass per unit length. At low values of the parameter, the heavy gas-puff load provides more deuterons but the lower energy of the accelerated deuterons reduces the number of fusion reactions. At large values the ion beam energy is higher, but there are too few targets. The result is an optimum over the range of the parameter studied with GIT-12, as shown in Fig. VI-18. This parameter was developed to compare with the drive parameter used for DPFs. It is interesting to note that the parameter $I_{\text{stag}}/\sqrt{(M_o/\ell)}$ squared is proportional to the numerator in the expression for η^* (III-58). This could suggest that there is an optimum energy per particle for radiation as well as neutron production, although the authors propose a kinematic rather than an energetic explanation for the observed optimum.

The importance of pinch disruption and MHD instabilities in producing neutrons is supported by the influence of an axial magnetic field on Y_n found in [VI-62]. Double-shell gas-puff

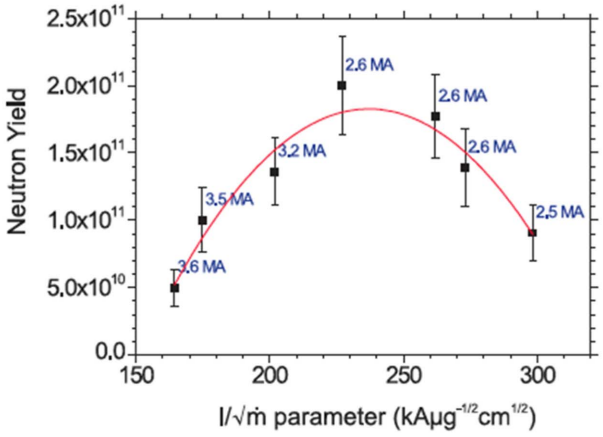

Fig. VI-18. Dependence of the neutron yield as a function of the current at stagnation divided by the mass per unit length. The data are for 2-cm-long, double-shell D_2 gas puff loads on the GIT-12 generator. Reprinted from [VI-71].

pinches of D_2 were studied using different geometries for the return current cage. Although the Ne and Ar K-shell yields were not much different with or without the helical return cage (see Section VI-D), the neutron yields with helical returns were five times smaller compared with the straight returns ($2–4\times 10^9$ versus $1–2\times 10^{10}$). The lack of $m = 0$ constrictions in the pinch due to the presence of axial magnetic fields with the helical cage was responsible for the decrease in Y_n.

VII. Hybrid Gas Puffs

With one exception [II-23], all of the previously described gas puffs consisted of a single material, or with the addition in a small percentage of a dopant for spectroscopic diagnostic. In this penultimate section, we turn to various hybrid versions of gas puffs that have been proposed or fielded in the laboratory. In brief summary, these puffs include the use of different gases in distinct shells, puffs on a single wire, puffs on wire arrays, puffs on foams, and the recent development of puffs of metallic plasmas.

The development of nozzles that produce multiple gas shells from separate plenums readily facilitates the study of how a pinch performs with different species in segregated shells. Levine *et al.* [VII-1] used the TPSD r_N = 1–2/3–4 nozzle to study combinations of Ar and Kr in the different shells. Of course with the Double-EAGLE (3.5 MA) generator they could not achieve the Kr K-emission, so they measured the Kr L-shell (1–2.5 keV) and the Ar K-shell emission (3–4.5 keV). For this set of experiments, the masses for each shell where set equal by appropriately adjusting the plenum pressures by a factor of two. Four variations were investigated: 1) Kr (80%) plus Ar (20%) on Ar (with admixture of dopant)—three shots; 2) Kr (80%) plus Ar (20%) on Kr (with admixture of dopant)—one shot; 3) Ar on Kr (with admixture of dopant)—one shot; and 4) Ar (with admixture on dopant) on Kr—one shot. The total (Ar K-shell plus Kr L-shell) from the Kr-plus-Ar on Ar shots was comparable with the total (same sum) radiation from the Kr-plus-Ar on Kr shot. The argon K-shell yield for the Kr-plus-Ar on argon shots was slightly more than half of the argon K-shell yield obtained

from the pure Ar on Ar shot. With a Cl dopant added to the inner shell, the spectroscopy indicated that compared with the Ar-on-Ar shot, the stagnated electron density and temperature were significantly reduced for Ar-on-Kr and Kr-on-Kr, but only slightly reduced for Kr-on-Ar. The fact that Kr on the inside reduces the pinch temperature is consistent with the theoretical study in [VI-27] which showed that the Kr L-shell has a high radiation efficiency.

Shishlov *et al*. [VII-2] reported that streak camera images of He and Ar single-shell pinches suggested that pinches with lower Z_A species were more stable. So on GIT-12 (2 MA in ∼300 ns) at HCEI they fielded an Ar/H_2 mixture in the outer shell (4-cm radius) and pure Ar in the inner shell (1.4 cm) of a double puff. The results with H_2 showed a decrease in the implosion velocity, compression ratio, stagnation density, and temperature. For $H_2 < 5\%$ by mass there was some effect, but for $H_2 > 20\%$ the decrease in Ar K-yield and power was drastic. It was suggested that even though H_2 starts in the outer shell, reflection from the anode grid spread H atoms throughout the pinch, and as hydrogen is far less compressible than Ar, the pinch conditions were poor. Recall that Bailey *et al*. [II-3] found a radial separation of deuterium from Ar in a mixed pinch and suggested that the heavier species acted to stabilize the inner deuterium pinch. Separation by species mass under the influence of a driving magnetic field has been spectroscopically observed in a low-density, coaxial plasma discharge [VII-3].

After a hiatus of more than a decade from Shishlov *et al.*'s [VII-2] study, the concept that shells of different species may provide stable implosions has recently received renewed attention. The WIS was commissioned by NNSA to manufacture a small, versatile nozzle for university research. The primary designer was Fisher, who constructed the very first gas-puff nozzle (Section II). The triple-shell nozzle (r_N = 0.5/0.7–1.8/2.1–3.1 cm) has independent plenums and the center plenum can be removed for diagnostic access along the axis. Qi *et al*. [VII-4] fielded this nozzle on the Cobra generator (∼1 MA in 200 ns) at Cornell University to investigate the stability of implosions with Ne and Ar. From a comparison of time-gated extreme UV images, they found that the Ne-on-Ar implosions showed smaller MRT development prior to stagnation than either Ar-on-Ne or Ne-on-Ne implosions. For the Ne-on-Ar shots, the maximum implosion speed was 25 cm/μs and the plasma started to decelerate 25 ns before stagnation, which damped the MRT instability growth [V-42], [V-43]. For the opposite configuration, the maximum speed was larger and deceleration did not occur until 10 ns before stagnation. For the Ne-on-Ne implosions, the plasma continuously accelerated toward the axis. There was an attempt to maintain the same initial mass density profile among the different configurations by adjusting the plenum pressure; however, the interaction between the shells of different species could have led to differences in the initial profiles. The current waveform on Cobra is doubly peaked and by adjusting the timing of the two Marx output switches one can make the first peak the larger or smaller of the two. For the same load, the two different current waveforms impose a different acceleration history on the pinch and, as a consequence, different MRT behaviors. The contrary results among [VII-1], [VII-2], and [VII-4] on the stabilizing influence of double puffs with species-segregated shells clearly suggest that further investigations are needed.

Double-shell nozzles with different species have also been computationally studied as neutron sources. Rahman and associates at the UCI have promoted the staged Z-pinch, which in recent papers refers to the implosion of a dense gas shell composed of a high Z_A gas onto a D_2 or DT inner solid-fill. In [VII-5] and [VII-6], the interest was to model fusion on a low-current generator. The outside edge of a dense Kr shell becomes MRT unstable but the magnetic field rapidly diffuses through this shell and accelerates an inner layer to compress the inner D_2 fuel, this fuel being the second stage of the pinch. The D_2-Kr interface remains stable because a heavier mass shell is accelerating a lower mass one. In [VII-7], the model used a Xe outer shell on a larger driver of 17 MA, predicting an energy gain from the DT burn of 42 times the stored energy in the driver. The extremely large compressions calculated by their simulations, ∼200, are well beyond any observed value from laboratory experiments.

In the next set of hybrid pinches for consideration, the inner gas is replaced by a foam cylinder on axis, a single wire on axis (puff-on-wire configuration), or a wire array. The puff-on-foam by Spielman *et al*. [II-23] was described in Section II.

The phrase staged Z-pinch was originally used to describe a Kr puff on an Al wire in [VII-8], or on a fiber [VII-9]. Wessel *et al*. [VII-10] performed experiments on ACE 4 (3.2 MA in 400 ns) with a Ne puff-on-single wires of various species: Cu, Mo, Ag, and W. The configuration was referred to as a tandem-puff. Spectra were taken covering 0.8–2.3 keV and silicon p-i-n diodes measured the 6–300-keV photon energy range in nine channels (each channel having energy range ε_i). Compared with the gas-only cases, the yield in high-energy photons >6 keV increased twofold for Cu and five times for the W wires with the Ne puff. This enhancement cannot be a result of a difference in the compression. Extrapolating the slope of the continuum from the spectra near 1.4 keV was not consistent with the high-energy data. Considering all the targets, this yield scaled linearly with the Z_A of the wire, which is characteristic of beam–target bremsstrahlung. For thin targets, such radiation has an intensity independent of the beam energy. For thick targets, the bremsstrahlung intensity varies as $\varepsilon_o - \varepsilon_i$, where ε_o is the end point energy. But the intensity from the p-i-n diode channels varied as $1/\varepsilon_i$.

Chuvatin *et al*. [VII-11] and Branitskii *et al*. [VII-12] simultaneously proposed that the puff-on-wire configuration could lead to a rapid current rise of the target wire, and hence a power multiplication in the wire. As the outer shell implodes, it becomes MRT unstable. If the shell were to break apart before hitting the wire, or become thinner than the collisionless skin depth, then the magnetic field would rapidly penetrate into the region between the disrupted shell and the wire. This process could be timed, depending on the mass of the shell, to occur close to the wire, and thereby drive a rapidly rising electric field and current in the wire. In [VII-11], the GIT-4 generator (1.5 MA in 150 ns) imploded an Ar puff on a Ni wire, calling it a composite pinch. With the

optimal delay between the valve opening and the pinch, a rapid rise ($\sim$1 ns) by an order of magnitude in the emission of high-energy photons ($>$4 keV) was taken to indicate the shell breakup and the staged energy transfer to the wire with power amplification. In [VII-12] Xe, Ar, or propane was imploded onto a foam target doped with Mo, KCl, and NaCl on the Angara-5 generator ($\sim$2 MA in 150 ns with a POS). With a low-mass gas shell, a rapidly rising burst of soft X-rays was observed that coincided with a drop in the dI/dt curve and a maximum in the dissipated power. The total energy in soft X-rays was 15–20 kJ. While [VII-11] attributed the high-energy continuum radiation to recombination into the K-shell of Ni, [VII-12] saw little evidence for K-shell lines from the dopants. Based on the presence of Ne-like Mo lines, [VII-12] suggested the generation of energetic electrons at the wire, which is similar to the observations of [VII-10]. Whether it is called a staged pinch, composite pinch, or tandem puff, an optimally tuned (by mass) gas puff imploding onto a single central wire might be a controllable source of high-energy electron beams that remains to be fully optimized.

Some of the recent experiments on the Cobra facility described above also employed a central wire, but in these shots the wire primarily served to prevent damage to the generator if the valve did not function properly. With an Al wire on axis, the Ne-on-Ar puffs displayed a tighter pinch (0.3-cm OD) than without (0.5-cm OD). Qi *et al.* [VII-4] proposed that the ablated plasma from the wire reduced the MRT instability just like a center jet did in [IV-38] and [IV-39].

There have also been experiments with an outer gas puff imploding onto, and possibly through, an inner array of wires, or puff-on-array pinches. Baksht *et al.* [VII-13] contended that the on axis plasma precursor, which forms during the ablation stage of a wire array, dampened the compression at stagnation as the trailing mass imploded and thereby reduced the potential K-yield. An outer gas shell might switch its current to the array at the moment of interaction. If the current rise is rapid enough, the ablation phase would become an explosive phase and the wires could implode ahead of the gas onto the empty central axis. Experiments were initially carried out on GIT-4 (1.5 MA in 120 ns) with a 4-cm-radius single-shell Ar gas puff on an Al array. For a fixed array mass, the Ar mass load and array radius were varied to find optimal conditions. For shots with the same Ar mass and array radius, the average Al K-yield increased by 30% and the power by $\sim$80% with the gas puff compared with those without. Shishlov *et al.* [VII-14] also looked at puff-on-arrays but with very different conditions. The GIT-12 generator provided a higher current (3.5 MA) and was configured without a POS, so the implosion times were long: 0.7–1.1 μs. To match the long implosion time, a large double-shell nozzle ($r_N = 4/8$ cm) was used with Ne gas. As opposed to the emphasis on the wire array emission in [VII-13], here Shishlov *et al.* [VII-14] found that the Ne K-yield increased on average by more than a factor of two with the wire array in place. The reasonable assumption was noted that the Ne passed through the array and, after current switching, the Al implosion acted to compress the Ne on axis. One problem both of these puff-on-array experiments encountered was a large variability in the K-yield and power from the species of interest. Both teams attributed this feature to the fact that the fraction of current switched from the gas to the array is not consistent shot to shot.

The most recent hybrid gas puff, one that is quite different from those above and potentially the most fruitful, is the development of the metallic puff Z-pinch by Russian scientists. The basic design is described in [VII-15]. A set of plasma guns is arranged in a cylindrical array as part of the high-voltage electrode. The guns are driven simultaneously by a single power supply and the resultant vacuum arc discharges propel a metallic plasma into the electrode gap forming an annular shell. The mass load of the shell formed by the combined jets is controlled by the delay between firing the guns and the main pulsed power for the pinch. The advantages of these metallic puffs are as follows.

1) One can use materials other than room temperature gases.
2) The puff can be composed of materials for which fine wires may not be available.
3) The material is already ionized.
4) Azimuthal symmetry is possible as opposed to wires with gaps.

The disadvantages are as follows.

1) A high current of 80–100 kA is needed to ignite the many discharges.
2) The mass loading is dependent on the erosion rate, which differs among materials.

In [VII-15], 10 guns were arranged in a cylinder of 2-cm radius. The electrodes were Mg, and the discharges ignited within 3 ns of each other. The A–K gap was 1 cm. A schematic of the system and images of the plasma shell are shown in Fig. VII-1. The initial implementation was performed on IMRI-5 (450 kA in 450 ns). For a mass loading of 14 μg/cm, the metallic puff imploded to a radius of 0.15 cm, but only produced $\sim$7 J/cm of Mg K-shell radiation. The same experiment, but with Al arc discharges, also produced $\sim$7 J above 1 keV [VII-16].

Baksht *et al.* [VII-17] implemented a metallic puff-on-puff pinch, i.e., both the 2-cm-radius shell and the central jet were formed from vacuum arc discharges. For the same IMRI-5 generator as above (450 kA in 450 ns), this configuration produced a 33-fold compression that was axially uniform and 32 J/cm of Al K-shell with a peak power of 8 GW. For comparison, the $\sim$1-MA Zebra generator ($\sim$100 ns) at the University of Nevada, Reno, produced 100–500 J/cm with a 2-cm long Al cylindrical array of radius 0.8 cm [VII-18]. According to [III-14], the current break point separating the I^4 from the I^2 scaling is 1.8 MA for Al (analogous to the Ar current break point in Fig. VI-1). Thus, scaling the metallic puff K-shell result for Al up to 1 MA in the I^4 regime could produce $\sim$780 J/cm, exceeding the Zebra wire array data, and using a long pulse.

Work has been done very recently to control the density profile formed by the vacuum arc discharges. In [VII-19], the plasma guns were modified to form either a narrow annular shell at 2-cm radius or a broad density profile that diverges from the 2-cm radius across the A–K gap. The later distribution is referred to as isotropic flow. Again using

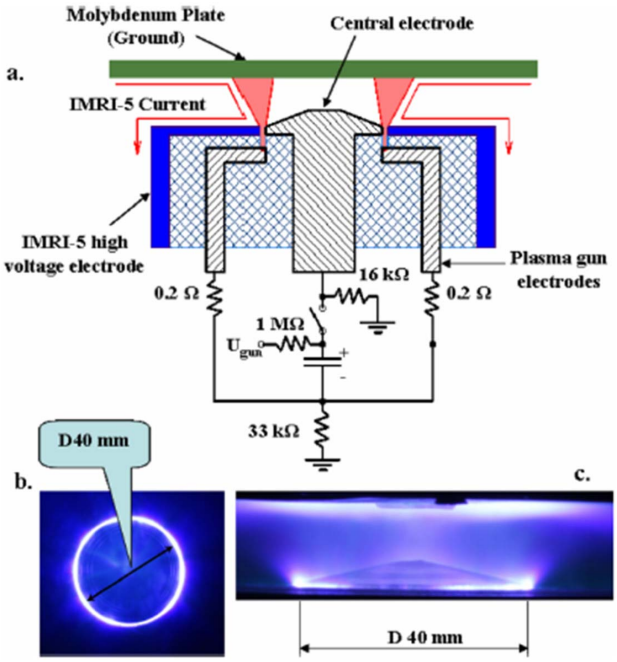

Fig. VII-1. (a) Schematic of a metallic gas puff Z-pinch system. A metallic plasma (red) forms between the gun electrodes and escapes into the A_K gap. Photograph of the escaping plasma looking at the cathode (b) face on and (c) side on. Reprinted with permission from [VII-15]. Copyright 2011, AIP Publishing LLC.

IMRI-5, images show that Mg pinches in the isotropic flow were stable all the way to the axis, unlike those for the narrow shell. Apparently, the isotropic flow spreads out to the return current radius (7.25 cm), and the pinch current initiates in this region before sweeping inward. The large-radius, tailored density profile from the isotropic flow satisfies the criteria for stability against the MRT instability described in [V-42] and [V-44]. The Mg K-shell yields of the stable pinch were 6–9 J/cm, but when a central discharge was added to the initial profile, the yield jumped to 73 J, the K-power was 5.8 GW, and the pinch was remarkably uniform in the axial direction.

We note that an alternative way to produce a metallic puff of plasma was devised in [VII-20] on the MAGPIE generator (1.4 MA in 250 ns) at Imperial College. The load comprised two arrays in parallel. One array (A) was an inverse pinch with a central cathode stalk, and the second array (B) with a standard configuration would become the imploding array. Initially, the drive current was inductively divided between the two arrays with most of the current in array A. The current in array B acted as a prepulse and vaporized all of the wire material with little ionization. After a temporal delay of ~140 ns, array A exploded, the current was interrupted as in an opening switch, and the current transferred to array B leading to its implosion in only ~80 ns. Streak photography and interferograms indicated that there was no trailing mass and no precursor formation on axis, as is usual for standard wire arrays on MAGPIE. Array B of diameter 1.7 cm was comprised of only eight wires, so the metallic vapor from each of the wires did not form an azimuthally symmetric metal shell as in [VII-15]. Short-wavelength MRT instabilities were observed on the individual vaporized wires, but it was suggested that mitigation techniques, such as tailored density profiles, could be tested in this geometry with parallel arrays.

Baksht *et al.* [VII-21] proposed the concept of a metallic puff as a plasma neutron source. 1-D MHD simulations of a TiD_2 double shell predicted that 2.5×10^9 neutrons could be produced from the thermal process by a 1-MA generator. Klir *et al.* [VI-72] took a different approach with cable guns. In experiments on GIT-12 (3 MA in 700 ns), they arranged 48 guns that injected a carbon+hydrogen (C+H) plasma at a radius of 17.5 cm. The mass loading of this annulus was only ~5 μg/cm. Inside of this annulus was a double-shell D_2 puff at 1.5 and 4-cm radii. The maximum yield of this configuration produced 2.9×10^{12} neutrons (beam–target), an order of magnitude greater than they had achieved on the same generator described in the previous section with a D_2 load using a triple nozzle of an 8-cm outer radius [VI-70]. This is an impressive achievement that required the proper timing between the nozzle, the plasma guns, and the pulsed power. In regard to Fig. VI-17, the progression of GIT-12 shots moved the neutron yields from the lower trend line to the upper one: from short-pulse double shell, to long-pulse double shell, to long-pulse triple shell (not a center jet), and finally to a triple shell including the very large 35-cm-OD cable guns. The proposed trend lines from [I-20] suggest that the beam–target interaction for neutron production became more efficient as the outer load diameter increased. Klir *et al.* [VI-73] showed that the neutron yield increased by an order of magnitude as the effective voltage of (VI-9) increased by a factor of five. The largest values of V_{eff} were achieved on the D_2 puffs with the outer plasma guns. One further point of interest from these experiments in [VI-72] was the observation of 38-MeV protons moving along the axis from stacked CR-39 detectors and up to 22-MeV neutrons from nTOF detectors. Particles of such high energy were not observed in the D_2 gas puffs discussed in the previous section and greatly exceed energy gain from the inferred voltage across the pinch, also supporting the authors claim that the neutrons were nonthermal in origin.

VIII. Present Work and Future Directions

Ar K-Shell Source Development: Much of the motivation that drove the research into gas- puff Z-pinches since Shiloh *et al.*'s originating paper [II-1] has been the development of a robust Ar K-shell source. This progress was highlighted in Section VI-A. With the consistent achievement of >300 kJ yield above 3 keV on the ZR generator at SNL, we can consider the Ar K-shell source as a mature capability on high-current (~15 MA) generators. As mentioned at the end of Section VI-A and listed at the bottom of Table II, these shots used the AASC 8-cm-OD double nozzle with r_N = 1–2/3–4 cm with a total mass loading of 1000 μg/cm over a 2.5-cm length and an inner:outer shell mass ratio of 1.6:1. This source is clearly in the I^2 regime of Fig. VI-1, and RMHD simulations indicate that a 30% conversion efficiency of $E_{j\times b}$ to K-shell radiation is the best that can be expected for Ar [III-18]. There remains interest in understanding the structure of the stagnated plasma [VI-11], [VI-24]

and potential improvements of the yield using a center jet [VIII-1].

Kr K-Shell Source Development: The achievement K-shell radiation from Kr at the level of tens of kilojoules remains a challenge for the largest current generator ZR with an inferred maximum load current of ~15 MA. From fundamental atomic physics considerations, the challenge arises from the large energy per ion ($E_{\min}$) needed for Kr to produce a strong K-shell emitter. From (III-55), this energy is ~500 keV/ion for Kr, which is more than 12.5 times that needed for Ar. The robust shots with Ar on ZR reached $\eta^*(\mathrm{Ar}) > 7$ according to the bottom rows in Table II, i.e., the energy coupled to the load per ion is more than seven times $E_{\min}(\mathrm{Ar})$. For the same nozzle configuration and mass loading, $\eta^*(\mathrm{Kr})$ would be <1. To increase η^* and remain matched to the generator, the load radius must be increased and the load mass decreased such that $M_o r_o^2$ is conserved, according to Fig. III-4. The first large-radius shot with Kr was a double-shell configuration using the AASC 12-cm-OD nozzle shown in Fig. IV-5, but with neither a recess nor a central jet. It produced ~2 kJ yield [VIII-2]. The load mass was ~670 μg/cm over a 2.5-cm length with an inner:outer shell mass ratio of 2.5:1. Based on GORGON simulations of the nozzle outflow and implosion, Jennings *et al.* [VIII-3] concluded that increasing the aperture of the inner nozzle would enhance the yield by forming a density profile with an increasing density ramp toward the axis, like that shown in the inset of Fig. V-4. The trend of the experiments agreed with this prediction, giving an ~5-kJ yield for the ramped profile. Ampleford *et al.*'s report [VIII-4] on X-ray sources covering 1–20 keV on the ZR generator presents a spectrum for this 5-kJ yield. Both the 2- and 5-kJ experimental yields were a factor of ~3 less than the simulated predictions, and [VIII-3] attributed that to using too large a load current as input to the simulation. Agreement with the data was obtained upon lowering the peak load current from ~18 to~15 MA. Jennings [VIII-2] further suggested that adding a central jet to the ramped profile would improve the yield. The central peak in the density would then be in conformity to Fig. V-5. In the experiment, the load mass was the same as the double-shell configuration but with an added 7% in the jet. The Kr K-shell yield increased to ~8 kJ and the simulations with a 15-MA peak load current matched the data. These yields are all in the I^4 scaling regime. Based on [III-10] and [III-14], the coupled energy needed to reach the break point current is ~100 times larger for Kr than for Ar. Fig. VI-1 shows that the break point current for Ar is ~5 MA, so ~50 MA would be needed to reach the I^2 scaling for Kr.

There may still be room for improvement in the Kr yield with the existing ZR generator. Section VI-A noted that the L-3 Pulse Sciences 12-cm-OD triple nozzle achieved significant Ar K-shell yield on the Double-EAGLE, Saturn, and Decade Quad generators with a central jet comprising 20% of the total mass [IV-39]. If the central jet in the Kr load were increased to 20%, the density profile of the triple nozzle would look like the jet-inner-outer profile of [IV-38, Fig. VI-5].

Optimized Initial Conditions: For a better understanding of the scaling of high-Z_A gas puffs with current and atomic number, there are theoretical and experimental efforts that can be pursued. Being able to compute the factor η^* for Kr would be useful for determining the optimum mass and density distribution for maximum K-shell emission. To do this, the highly complex M-and L-shell atomic physics must be delineated [VI-27]. The primary limitation on the modeling approach to optimization in high-current generators (>6 MA) is the present lack of knowledge of the actual load current (I_{load}), as discussed at the end of Section III-E. Current losses in the magnetically insulated transmission line and the final feed to the load are not well understood and this directly impacts source development since I_{load} is the primary physics controlling the pinch dynamics. Measured currents upstream of the load, as well as the radiation properties, can be used to constrain the load current for particular configurations [III-19], [VI-35], [VIII-3]. But such solutions are dependent upon the particular RMHD simulation code employed, and thus do not provide a unique solution that can be used for other load configuration. Thus, in order to rely on predictive simulations, the challenge for experimentalists is a measurement technique for I_{load}, or equivalently the magnetic field in the load region outside of the pinch, in high-current (>6 MA) generators.

To find empirically the optimum gas-puff density distribution for a given generator, it would be useful to systematically vary the gas-puff radius, as well as the mass for a fixed radius, all the while keeping the product $M_o r^2$ constant and matched to ensure that the maximum generator current (and energy) is accessed. Snowplow stabilization, achieved from distributed mass distributions (as discussed in Section V-E), can be employed to reduce or eliminate consideration of the MRT instability from analysis of the results. The major limitation on this empirical approach is the cost of multiple shots on high-current (>6 MA) generators.

Initial Conditions and Preionization: Figs. III-3 and III-4 show that matching the load to the generator is dependent upon the initial mass distribution. In multidimensional simulations, it has been found that $\rho(r, z, t = 0)$ and the location of the gas breakdown can dramatically change the MRT development and the synthetic images with which to compare data [VI-46]. Predicting the mass distribution from a gas-puff nozzle assembly is a daunting but laudable task, but it can be measured fairly accurately. Such measured results should be incorporated as initial conditions in MHD simulations (e.g., to predict zippering correctly). Relying on breakdown to set the initial conditions for the implosion can lead to uncertainties in modeling and analysis, especially for large-diameter nozzles. However, preionization techniques do produce a reproducible initial plasma distribution that can be measured. Knowing the axial and radial distribution of electrons produced by a preionization process should be quite valuable for analysis, modeling, and simulation purposes, whether the generator current is 1 or 15 MA.

Stagnation Physics: One outstanding physics issue for both wire arrays and gas puffs is the origin of the large effective ion temperatures as determined from emission linewidths during assembly on axis as discussed in Section VI-C. High spectral resolution, time-resolved X-ray spectroscopy is needed to observe the phenomena [VI-36], [IV-68]. Unconventional

physical processes such as ion viscous heating [I-13], magnetic bubbles [VI-43], or 3-D turbulence have been proposed as possible explanations. The more pedestrian explanation of Doppler shifts due to steep velocity gradients near the axis match many, but not all, of the features observed from Ne implosions on the 500-kA generator at WIS [VI-46]. But there remains a discrepancy between the simulations and experimental estimates for the ion thermal temperature near the beginning of the stagnation. Furthermore, the Doppler shift analysis based on simulations for Ar stagnations on the high-current ZR generator shows that $T_i^{\text{eff}} \sim 20$ keV, while the data are much larger, ~50 keV [VIII-5]. There may be different physical mechanisms at play depending on the current level.

Magnetic Fields: Azimuthal magnetic fields B_φ in the plasma due to I_{load} are, of course, central to the compression of a Z-pinch. Measurements of the magnetic field during the early implosion phase of a pinch were reported over 15 years ago (Section V-A). Recently, Rosenzweig *et al.* [VIII-6] reported magnetic field measurements through the stagnation phase of a pinch. They developed a spectroscopic setup to simultaneously measure the left and right circularly polarized emission from an oxygen pinch on the WIS generator. The polarization spectroscopy allowed them to distinguish the Zeeman splitting even in the presence of Doppler and Stark broadening. The time-resolved Zeeman splitting from two different oxygen ionization stages provided information on the spatial structure of the azimuthal magnetic field from 26 ns before peak power to 1 ns afterward. The remarkable result of this first measurement for B_φ during stagnation is that the plasma–vacuum interface has a far larger radius throughout this phase than do RMHD simulations. This behavior is difficult to understand and, if substantiated with further experiments, implies that there is fundamental physics missing from the conventional modeling work.

In addition to work on the azimuthal magnetic fields, there is also ongoing research in WIS on axial magnetic flux compression by gas puffs. Mikitchuk *et al.* [VIII-7] present visible images of an Ar pinch clearly showing the mitigation of MRT instabilities (Section V-E) with increasing amplitude of the embedded axial field. It is also of interest to note that the filamentary structures seen in the visible images appear in the azimuthal direction with $B_z = 0$, have a helical character at an intermediate magnitude for the initial embedded field (2 kG), and become predominantly axially directed for a large embedded field (4 kG). The change in direction of the filaments, from the case with no axial field to that with an axial field, is similar to what is observed in the magnetized liner inertial fusion (MagLIF) experiments on the ZR generator [VIII-8]. In the MagLIF shots, the filaments arise from a solid liner and are seen with radiography. Ryutov and Dorf [VIII-9] theoretically studied the evolution of helical perturbations of a thin shell liner during implosion in the presence of azimuthal and axial magnetic fields. It is not clear if these features have a similar origin for liners and gas puffs, nor is it known if the filaments on the MagLIF liner become more axial at a high level of the embedded axial field. The helical $m = 1$ kink instability appears to be primarily responsible for the disruption of the pinch after stagnation, whether in the presence of an ambient axial magnetic field, as in [VIII-7], or in its absence, as noted in Section VI-A from Fig. VI-4(d).

Beams: Recently, there has been interest in using electron beams to produce Kα radiation as a means of creating energetic radiation of >10 keV. The published work has been with Mo wires, producing ~18-keV photons [VIII-10]. On ZR [VIII-11], the decrease in the Kα radiation yield with increasing Z_A (Cu, Kr, Mo, and Ag) is much less than the decrease in the thermal K-shell yield. Gas puffs offer some alternative load designs to investigate electron beam-driven radiation sources. We recall the puff-on-wire reports in Section VII [VII-10], [VII-11]. As opposed to the avoidance of the MRT instability in thermal sources, the production of e-beam-driven radiation may be enhanced through the control of the instabilities to disrupt the imploding plasma just prior to stagnation.

Neutron Plasma Sources: The largest neutron yield (Y_n) from a D_2 gas puff was 3.7×10^{13} on the Z generator (i.e., ZR before refurbishment) [VI-76]. Measurements of the emission isotropy with nTOF detectors were consistent with a thermonuclear origin, but not conclusive. Fully kinetic PIC simulations [VI-79] indicate that at the ~15-MA current level, half the neutrons are thermonuclear in origin and half are from beam–target interactions. To date, there have been no reported follow-up D_2 gas-puff shots on ZR. Double-shell hybrid load designs with a heavy gas in the outer shell imploding onto D_2 have been theoretically proposed to give enhanced yields. Because of cooling, the outer shell in the modeling has a higher density than the swept-up deuterium layer. During implosion, the noble gas-D_2 interface should be stable against MRT until the deuterium starts to decelerate the heavy gas. An example of this configuration is the Xe-on-DT staged Z-pinch of [VII-7] that finds a 1-D computed gain of 42 from the stored energy to the energy in neutrons. The 1-D simulations in [VIII-12] matched the existing neutron yields of pure D_2 loads [VI-76] and then predicted a factor of ~10 increase in Y_n for Ar-on-D_2 loads. A practical advantage of the hybrid D_2 gas-puff design using a high Z_A in the outer shell is that it may be less prone than a pure D_2 puff to expand into the transmission lines of the generator. Gas in these vacuum regions may lead to current losses and can alter the pinch dynamics as the actual outer radius r_o is unknown.

A successful experiment with another hybrid D_2 load used a C+H plasma in a large-radius shell on a D_2 single or double puff [VI-72]. Y_n increased by an order of magnitude compared with a triple-shell load (with three distinct shells, not an inner jet) on the same GIT-12 generator.

This hybrid D_2 load design appears promising for the ZR generator, but the simulated yield improvement has recently been found to be dependent upon the axial variation of the density profile for the two shells [VIII-13]. With smooth profiles, as in the ballistic model [III-17], 2-D simulations of an Ar outer shell provides a twofold increase in Y_n compared with D_2 in the outer shell, but for a measured density profile, the Ar was found to break through the deuterium shell during implosion and thereby attained only a 30% improvement.

Deuterium gas puffs on low-current (<2 MA) generators are believed to produce fusion by beam–target interactions.

Much recent work has been reported by Klir and collaborators as described in Section VI-E, and several phenomena from their results deserve further investigation. The parameter $I_{\text{stag}}/\sqrt{(M_o/\ell)}$ was used to explain the observed peak in Y_n of Fig. VI-18. An integral part of the observation was the observed fact that low-mass loads produced higher energies for the emitted neutrons. The production of protons and neutrons with tens of MeV of energy, far exceeding the measured effective voltage on the load in D_2 gas puffs, remains a theoretical challenge. PIC simulations, as done in [VI-81] for DPFs, could be used to understand how the acceleration mechanisms are sensitive to the D_2 mass loading. Klir *et al*. [VI-72] pointed out that simultaneous measurements of the fast ions and neutrons may be useful for understanding the acceleration mechanism and the beam–target production of neutrons in D_2 gas puff pinches. Based on the radial observed neutron spectra, Klir *et al*. [VI-73] suggest that the fast neutrons are not formed by a monoenergetic beam of deuterons, but rather arise from a distribution of deuterons with a suprathermal tail decreasing as a power law in energy.

Finally, the square of above parameter $I_{\text{stag}}/\sqrt{(M_o/\ell)}$ for neutron yield is similar to the parameter used to optimize K-shell yield (III-58). It is yet to be determined if the optimum value of 225 kA$(\mu$g/cm$)^{-1/2}$ is the same for D_2 gas puffs on other generators, including up to ∼15 MA on ZR, where likely thermonuclear fusion plays a more significant role than in low-current generators.

Metallic Gas Puffs: The most interesting new development in gas puffs are the loads formed of metallic plasma, as in Fig. VII-1. Traditional gas puffs are limited to the naturally occurring gases. The large change in Z_A, particularly between Ar, Kr, and Xe, means that source development requires ever larger currents to achieve K-shell excitation. Plasma guns arranged in an annular array allow one to produce a preionized, axially symmetric shell of material between Ar and Kr. One could design loads of double arrays and central jets, or mix metallic and natural gas puffs. We point out one application of these novel gas-puff loads. The recombination radiation to H- and He-like ions produces a continuum of K-shell photons of energy (E_γ) that extends above the K-shell line emission and with a spectrum $\exp(-E_\gamma/T_e)$. In principle, for the proper load conditions, this continuum may provide a significant yield above 10 keV. For instance, Coleman *et al.* [VI-6] found 5.2 kJ above 10 keV for an Ar double-shell load on Z (Section VI-A). But Velikovich *et al*. [VI-19] showed that optimizing the free-bound continuum in this photon regime would be better done with stainless steel because the Ar emission peaks at too low an electron temperature and because the recombination radiation scales with Z_A^5. To achieve a Z-pinch of high T_e in a metal between Ar and Kr, one needs a low-mass load of a large radius. Such conditions may not be readily achievable, given the limitation of individual wire diameters and a double-shell design to mitigate MRT disruption. Instead, a double array of plasma guns could be used to form the low mass, large-radius load with a structured density profile. Theoretical investigations and modeling would be useful as there would be a significant investment in fabricating and testing the metallic plasma injector.

TABLE III
ALPHABETICAL LIST OF ACRONYMS USED IN THE TEXT

A-K	anode-cathode
AASC	Alameda Applied Sciences Corporation
BFM	ballistic flow model
CCD	charged-coupled device
CRE	collisional radiative equilibrium
DNA	Defense Nuclear Agency
DOE/NNSA	Department of Energy/National Nuclear Security Agency
DPF	Dense Plasma Focus
DTRA	Defense Threat Reduction Agency
FWHM	full width half maximum
HCEI	High Current Electronics Institute
K-shell	hydrogen- and helium like ions
L-3 ATI	L-3 Applied Technologies Incorporated
LANL	Los Alamos National Laboratory
LIF	laser induced fluorescence
LLNL	Lawrence Livermore National Laboratory
LTE	Local Thermodynamic Equilibrium
LWA	laser wavefront analyzer
MagLIF	magnetized liner inertial fusion
MA	Mega - Ampere
MHD	magnetohydrodynamics
MLI	Maxwell Laboratories Incorporated
MPI	Maxwell Physics International
MRT	magnetic Rayleigh - Taylor
NRL	Naval Research Laboratory
nTOF	neutron time-of-flight
OD	outer diameter
OTS	on-the-spot
PCD	photoconductive device
PI	Physics International
PIC	particle-in-cell
PLIF	planar laser - induced fluorescence
POS	plasma opening switch
PRS	plasma radiation source
RMHD	radiation magnetohydrodynamics
RT	Rayleigh - Taylor
SNL	Sandia National Laboratories
TCRE	tabular collisional radiative equilibrium
TPSD	Titan Corporation/Pulsed Sciences Division
UCI	University of California at Irvine
UV	ultraviolet
WIS	Weizmann Institute of Science

A Final Note: Advancement in gas puffs and hybrid designs for the immediate future will be most effectively performed on low-current generators (1–6 MA), such as at universities or moderate-sized laboratories. For example, results from the small double-shell nozzle with a central hole for diagnostic access, designed in a collaboration between WIS and Cornell University, were presented in Sections VI-D and VII. Such environments allow rapid changes in load design, unusual or novel load configurations, multiple shots per day, diagnostic access, and all with lower costs. Many of the research topics and physics issues highlighted in this section originated on ∼1-MA generators, including: 1) effective ion temperatures; 2) measurement of magnetic fields; 3) puff-on-wire for electron beams; 4) MeV neutrons and ions; and 5) metallic gas puffs. Diagnostic techniques, load designs, and physics understanding can translate upward to higher current accelerators—just as the initial work on gas puffs by Fisher *et al*. [II-1], [II-2], [II-3], [II-4] did from the late 1970s.

APPENDIX

For ease in crossreferencing, Table III presents a list of acronyms and their meanings used throughout this paper and

TABLE IV
LIST OF IMPORTANT SYMBOLS USED IN THE TEXT

Symbol	Meaning	Equation/Fig.
B_φ	azimuthal component of the magnetic induction	(III-15)
B_z	axial component of the magnetic induction	(V-3)
B_{zo}	initial axial component of the imposed magnetic induction	(V-3)
E_{jxb}	"J cross B" energy coupled to the pinch through the Lorentz force	(III-10)
E_{load}	energy coupled to the load region from the generator	(III-30)
E_{vac}	magnetic energy in vacuum region between r_o and r_p	(III-31)
E_{kin}	kinetic energy of imploding pinch	(III-33)
E_{min}(K-shell)	minimum energy per ion needed to radiatiate from the K-shell	(III-55)
I_{pk}	peak load current	(III-34)
I_g	scale for generator current	(III-38)
ℓ	A-K gap length	Fig. III-1
L_g	fixed generator impedance	(III-17)
L_{load}	load inductance	(III-19)
L	change of load inductance	(III-38)
M_o	total mass of gas puff	(III-37)
N_o	line integrated neutral density from interferometry	(IV-1)
N_e	line integrated electron density from interferometry	(IV-5)
Q_{ie}	ion-electron thermal equilibration term	(III-7)
R_g	fixed generator impedance	(III-17)
R_{load}	load resistance	(III-22)
R_{bub}	enhanced load resistance due with magnetic bubbles	(VI-4)
r_o	initial outer radius of the cylindrical gas puff	Fig. III-1
r_p	radius of imploding pinch	(III-25)
t_{imp}	implosion time	Fig. III-2
t_g	temporal scale in generator drive voltage	(III-35)
T_i	ion thermal temperature	below (III-6)
T_e	electron thermal temperature	below (III-6)
T_i^{eff}	effective ion temperature from emission line width	(VI-3)
u_p	velocity of imploding pinch	(III-27)
u_f	final velocity of pinch	(III-34)
V_g	generator drive voltage	(III-17)
V_{go}	voltage sale in generator drive voltage	(III-35)
V_{load}	load voltage, measured at r_o	(III-18)
V_{eff}	effective load voltage from inductance and current measurements	(VI-9)
Y_K	K-shell radiation energy or yield	below (III-61)
Y_n	neutron number yield	Section VI-E
$\overline{Z}$	average charge state	below (III-7)
Z_A	atomic number	(III-52)
$_e$	electron thermal energy	(III-8)
$_i$	ion thermal energy	(III-7)
^{x}	excitation + ionization internal energy	(III-8)
$_{jxb}(\ _{kin})$	non-dimensional "J cross B" (kinetic) energy	(III-39)
	laser wavelength	(IV-1)
$_{mfp}$	mean free path	(IV-3)
$_{RT}$	wavelength of Rayleigh-Taylor unstable mode	(V-1)
	radiation cooling (heating) rate	(III-8)
$_{res}$	resistivity	(III-4)
	ratio of kinetic energy per ion to E_{min}	(III-56)
*	ratio of coupled energy per ion to E_{min}	(III-57)
	viscosity stress tensor	(III-7)
ρ_o	initial gas density distribution	(III-28)

Table IV contains a list of important mathematical symbols, with a short description and the equation or figure where they are first used.

ACKNOWLEDGMENT

This review would not have been possible without the input to and reading of various sections by many colleagues. In particular, the authors would like to thank J. Apruzese, B. Weber, S. Velikovich, W. Thornhill, D. Mosher, and S. Jackson of NRL; J. Levine and N. Qi of L-3 ATI; P. Coleman, M. Krishnan, and J. Thompson of AASC; E. Kroupp and Y. Maron of WIS; C. Jennings, B. Jones, D. Ampleford, A. Harvey-Thompson, and C. Coverdale of SNL; C. Deeney of National Security Technologies; and A. Fisher of Technion, Israeli Institute of Technology. Finally, the authors would also like to thank the two reviewers

for their time in reading this long manuscript and their many helpful suggestions.

REFERENCES

[I-1] Y. Li *et al.*, "Influence of insulating coating on aluminum wire explosions," *Phys. Plasmas*, vol. 21, no. 10, pp. 102513-1–102513-7, Oct. 2014.

[I-2] J. Sethian, "The quest for a z-pinch based fusion energy source—A historical perspective," in *4th International Conference on Dense Z-Pinches, AIP Conference Proceedings*, vol. 409, N. Pereira, J. Davis, and P. Pulsifer, Eds. Woodbury, NY, USA: American Institute of Physics, 1997, pp. 3-10.

[I-3] D. J. Ampleford *et al.*, "Opacity and gradients in aluminum wire array z-pinch implosions on the Z pulsed power facility," *Phys. Plasmas*, vol. 21, no. 3, pp. 031201-1–031201-8, Mar. 2014.

[I-4] A. S. Safronova *et al.*, "Radiation from mixed multi-planar wire arrays," *Phys. Plasmas*, vol. 21, no. 3, pp. 031205-1–031205-7-10, Mar. 2014.

[I-5] D. B. Sinars *et al.*, "Measurements of magneto-Rayleigh–Taylor instability growth during the implosion of initially solid al tubes driven by the 20-MA, 100-ns Z facility," *Phys. Rev. Lett.*, vol. 105, no. 18, pp. 185001-1–185001-4, Oct. 2010.

[I-6] G. A. Rochau *et al.*, "High performance capsule implosions driven by the Z-pinch dynamic hohlraum," *Plasma Phys. Control. Fusion*, vol. 49, no. 12B, pp. B591–B600, 2007.

[I-7] K. N. Mitrofanov *et al.*, "Specific features of the structure of the Z-pinch emitting region formed during the implosion of a foam-wire load at the ANGARA-5-1 facility," *Plasma Phys. Rep.*, vol. 39, no. 1, pp. 62–85, Jan. 2013.

[I-8] S. A. Slutz and R. A. Vesey, "High-gain magnetized inertial fusion," *Phys. Rev. Lett.*, vol. 108, no. 2, pp. 025003-1–025003-5, Jan. 2012.

[I-9] M. G. Haines, "Dense plasma in Z-pinches and the plasma focus," *Philos. Trans. Roy. Soc. London A, Math. Phys. Eng. Sci.*, vol. 300, no. 1456, pp. 649–663, Apr. 1981.

[I-10] A. E. Dangor, "High density Z-pinches," *Plasma Phys. Controlled Nucl. Fusion*, vol. 28, no. 12B, pp. 1931–1942, 1986.

[I-11] N. R. Pereira and J. Davis, "X rays from z-pinches on relativistic electron-beam generators," *J. Appl. Phys.*, vol. 64, no. 3, pp. R1–R27, Aug. 1988.

[I-12] D. D. Ryutov, M. S. Derzon, and M. K. Matzen, "The physics of fast Z pinches," *Rev. Modern Phys.*, vol. 72, no. 1, pp. 167–223, Jan. 2000.

[I-13] M. G. Haines, "A review of the dense Z-pinch," *Plasma Phys. Controlled Fusion*, vol. 53, no. 9, pp. 093001-1–093001-168, Sep. 2011.

[I-14] M. A. Liberman, J. S. De Groot, A. Toor, and R. B. Spielman, *Physics of High-Density Z-Pinch Plasmas*. New York, NY, USA: Springer-Verlag, 1999.

[I-15] R. B. Spielman and J. S. De Groot, "Z pinches—A historical view," *Laser Particle Beams*, vol. 19, no. 4, pp. 509–525, 2001.

[I-16] P. L. Coleman *et al.*, "A review of recent z-pinch research at Maxwell Physics International," *Laser Particle Beams*, vol. 19, no. 3, pp. 409–441, 2001.

[I-17] C. A. Coverdale *et al.*, "Scaling of K-shell emission from Z-pinches: Z to ZR," *IEEE Trans. Plasma Sci.*, vol. 35, no. 3, pp. 582–591, Jun. 2007.

[I-18] M. E. Cuneo *et al.*, "Magnetically driven implosions for inertial confinement fusion at Sandia National Laboratories," *IEEE Trans. Plasma Sci.*, vol. 40, no. 12, pp. 3222–3245, Dec. 2012.

[I-19] J. L. Giuliani *et al.*, "Plasma pinch research on university pulsed-power generators in the United States," *IEEE Trans. Plasma Sci.*, vol. 40, no. 12, pp. 3246–3264, Dec. 2012.

[I-20] M. Krishnan, "The dense plasma focus: A versatile dense pinch for diverse applications," *IEEE Trans. Plasma Sci.*, vol. 40, no. 12, pp. 3189–3221, Dec. 2012.

[I-21] D. Osin *et al.*, "Evolution of MHD instabilities in plasma imploding under magnetic field," *IEEE Trans. Plasma Sci.*, vol. 39, no. 1, pp. 2392–2393, Nov. 2011.

[II-1] J. Shiloh, A. Fisher, and N. Rostoker, "Z pinch of a gas jet," *Phys. Rev. Lett.*, vol. 40, no. 8, pp. 515–518, Feb. 1978.

[II-2] P. G. Burkhalter, J. Shiloh, A. Fisher, and R. D. Cowan, "X-ray spectra from a gas-puff z-pinch device," *J. Appl. Phys.*, vol. 50, no. 7, pp. 4532–4540, Jul. 1979.

[II-3] J. Bailey, Y. Ettinger, A. Fisher, and N. Rostoker, "Gas-puff Z pinches with D_2 and D_2-Ar mixtures," *Appl. Phys. Lett.*, vol. 40, no. 6, pp. 460–462, Mar. 1982.

[II-4] T.-F. Chang, A. Fisher, and A. Van Drie, "X-ray results from a modified nozzle and double gas puff z pinch," *J. Appl. Phys.*, vol. 69, no. 6, pp. 3447–3450, Mar. 1991.

[II-5] C. Stallings, K. Childers, I. Roth, and R. Schneider, "Imploding argon plasma experiments," *Appl. Phys. Lett.*, vol. 35, no. 7, pp. 524–526, Oct. 1979.

[II-6] C. Deeney, C. A. Coverdale, and M. R. Douglas, "A review of long-implosion-time z pinches as efficient and high-power radiation sources," *Laser Particle Beams*, vol. 19, no. 3, pp. 497–506, 2001.

[II-7] P. Sincerny, S. Wong, and V. Buck, "Pulsed compression with an imploding gas puff," in *Proc. 5th Pulsed Power Conf.*, Arlington, VA, USA, 1985, pp. 701–703.

[II-8] R. B. Baksht, A. V. Luchinskii, and A. V. Fedunin, "Soft X-ray source using a cascaded liner," *Soviet Phys. Tech. Phys.*, vol. 37, no. 11, pp. 1118–1120, Nov. 1992.

[II-9] W. Clark, R. Richardson, J. Brannon, M. Wilkinson, and J. Katzenstein, "The dynamics of imploding argon plasmas," *J. Appl. Phys.*, vol. 53, no. 8, pp. 5552–5556, Aug. 1982.

[II-10] J. Katzenstein, "Optimum coupling of imploding loads to pulse generators," *J. Appl. Phys.*, vol. 52, no. 2, pp. 676–680, Feb. 1981.

[II-11] R. E. Marrs *et al.*, "Time and space resolved vacuum-ultraviolet spectroscopy of an argon gas-puff Z pinch," *Appl. Phys. Lett.*, vol. 42, no. 11, pp. 946–948, Jun. 1983.

[II-12] J. D. Perez, L. F. Chase, R. E. McDonald, L. Tannenwald, and B. A. Watson, "Subkilovolt X-ray radiation from an argon plasma," *J. Appl. Phys.*, vol. 52, no. 2, pp. 670–675, Feb. 1981.

[II-13] R. E. Stewart, D. D. Dietrich, and R. J. Fortner, "Soft-X-ray spectra of krypton XXIV–XXVII in gas puff *Z*-pinch plasmas," *J. Opt. Soc. Amer. B*, vol. 4, no. 3, pp. 396–404, Mar. 1987.

[II-14] R. E. Stewart, D. D. Dietrich, P. O. Egan, R. J. Fortner, and R. J. Dukart, "Spectroscopic studies of an argon plasma produced in a relativistic electron beam gas puff Z pinch," *J. Appl. Phys.*, vol. 61, no. 1, pp. 126–130, Jan. 1987.

[II-15] D. R. Kania and L. A. Jones, "Observation of an electron beam in an annular gas-puff Z-pinch plasma device," *Phys. Rev. Lett.*, vol. 53, no. 2, pp. 166–170, Jul. 1984.

[II-16] B. A. Hammel and L. A. Jones, "Effects of the internally produced nonthermal electrons on the temperature diagnostics of a hollow gas shell *Z* pinch," *Appl. Phys. Lett.*, vol. 44, no. 7, pp. 667–669, Apr. 1984.

[II-17] J. D. Hares, R. E. Marrs, and R. J. Fortner, "An absolute measure of heating by suprathermal electrons in a gas puff Z-pinch," *J. Phys. D, Appl. Phys.*, vol. 18, no. 4, pp. 627–631, 1985.

[II-18] P. Choi, A. E. Dangor, C. Deeney, and C. D. Challis, "Temporal development of hard and soft X-ray emission from a gas-puff *Z* pinch," *Rev. Sci. Instrum.*, vol. 57, no. 8, pp. 2162–2164, Aug. 1986.

[II-19] P. J. Turchi and W. L. Baker, "Generation of high-energy plasmas by electromagnetic implosion," *J. Appl. Phys.*, vol. 44, no. 11, pp. 4936–4945, Nov. 1973.

[II-20] S. J. Stephanakis *et al.*, "Effect of pulse sharpening on imploding neon Z-pinch plasmas," *Appl. Phys. Lett.*, vol. 48, no. 13, pp. 829–831, Mar. 1986.

[II-21] D. Duston, J. Davis, and C. Agritellis, "Radiative properties of puffed-gas mixtures," *J. Appl. Phys.*, vol. 57, no. 3, pp. 785–793, Feb. 1985.

[II-22] J. P. Apruzese and J. Davis, "Radiative properties of puffed-gas mixtures: The case of optically thick plasmas composed of two elements with similar atomic numbers," *J. Appl. Phys.*, vol. 57, no. 9, pp. 4349–4353, May 1985.

[II-23] R. B. Spielman, M. K. Matzen, M. A. Palmer, P. B. Rand, T. W. Hussey, and D. H. McDaniel, "Z-pinch implosions onto extremely low-density foam cylinders," *Appl. Phys. Lett.*, vol. 47, no. 3, pp. 229–231, Aug. 1985.

[II-24] J. S. Pearlman and J. C. Riordan, "X-ray lithography using a pulsed plasma source," *J. Vac. Sci. Technol.*, vol. 19, no. 4, pp. 1190–1193, Nov./Dec. 1981.

[II-25] J. Bailey, Y. Ettinger, A. Fisher, and R. Feder, "Evaluation of the gas puff z pinch as an X-ray lithography and microscopy source," *Appl. Phys. Lett.*, vol. 40, no. 1, pp. 33–35, Jan. 1982.

[II-26] J. S. Pearlman and J. C. Riordan, "Bright discharge plasma sources for X-ray lithography," *Proc. SPIE*, vol. 537, pp. 102–107, Jun. 1985.

[II-27] I. Okada, Y. Saitoh, S. Itabashi, and H. Yoshihara, "A plasma X-ray source for X-ray lithography," *J. Vac. Sci. Technol. B*, vol. 4, no. 1, pp. 243–247, Jan./Feb. 1986.

[III-1] S. I. Braginskii, "Transport processes in a plasma," in *Reviews of Plasma Physics*, vol. 1, M. A. Leontovich, Ed. New York, NY, USA: Consultants Bureau, 1965, pp. 205–311.

[III-2] W. M. Manheimer, "Energy input into a gas enclosed Z-pinch," *Phys. Fluids*, vol. 17, no. 9, pp. 1767–1770, Sep. 1974.

[III-3] J. D. Jackson, *Classical Electrodynamics*. Hoboken, NJ, USA: Wiley, 1999.

[III-4] E. M. Waisman, M. E. Cuneo, R. W. Lemke, D. B. Sinars, and W. A. Stygar, "Lower bounds for the kinetic energy and resistance of wire array Z pinches on the Z pulsed-power accelerator," *Phys. Plasmas*, vol. 15, no. 4, pp. 042702-1–042702-13, Apr. 2008.

[III-5] O. A. Anderson, W. R. Baker, S. A. Colgate, J. Ise, and R. U. Pyle, "Neutron production in linear deuterium pinches," *Phys. Rev.*, vol. 110, no. 6, pp. 1375–1387, Jun. 1958.

[III-6] D. Potter, "The formation of high-density z-pinches," *Nucl. Fusion*, vol. 18, no. 6, pp. 813–823, 1978.

[III-7] T. Miyamoto, "Analysis of high-density Z-pinches by a snowplow energy equation," *Nucl. Fusion*, vol. 24, no. 3, pp. 337–348, 1984.

[III-8] K. G. Whitney, J. W. Thornhill, J. P. Apruzese, and J. Davis, "Basic considerations for scaling Z-pinch X-ray emission with atomic number," *J. Appl. Phys.*, vol. 67, no. 4, pp. 1725–1735, Feb. 1990.

[III-9] K. G. Whitney *et al.*, "Optimization of K-shell emission in aluminum z-pinch implosions: Theory versus experiment," *Phys. Rev. E, Statist. Phys., Plasmas, Fluids, Rel. Interdiscipl. Topics*, vol. 50, no. 3, pp. 2166–2174, Sep. 1994.

[III-10] J. W. Thornhill, K. G. Whitney, J. Davis, and J. P. Apruzese, "Investigation of K-shell emission from moderate-Z, low-η (-velocity), Z-pinch implosions," *J. Appl. Phys.*, vol. 80, no. 2, pp. 710–718, Jul. 1996.

[III-11] C. Deeney *et al.*, "Radius and current scaling of argon K-shell radiation," *J. Appl. Phys.*, vol. 75, no. 6, pp. 2781–2788, Mar. 1994.

[III-12] J. Huba. *NRL Plasma Formulary*. [Online]. Available: http://www.nrl.navy.mil/ppd/content/nrl-plasma-formulary, accessed 2015.

[III-13] J. W. Thornhill, K. G. Whitney, C. Deeney, and P. D. LePell, "Phenomenological modeling of turbulence in Z-pinch implosions," *Phys. Plasmas*, vol. 1, no. 2, pp. 321–330, Feb. 1994.

[III-14] D. Mosher, N. Qi, and M. Krishnan, "A two-level model for K-shell radiation scaling of the imploding Z-pinch plasma radiation source," *IEEE Trans. Plasma Sci.*, vol. 26, no. 3, pp. 1052–1061, Jun. 1998.

[III-15] D. Mosher, M. Krishnan, N. Qi, P. L. Coleman, E. M. Waisman, and H. Sze, "Current scaling of optimum K-shell X-ray yield and load mass applied to argon gas-puff Z-pinches," in *Proc. 28th IEEE Int. Conf. Plasma Sci.*, Las Vegas, NV, USA, Jun. 2001, pp. 277–280.

[III-16] R. J. Commisso *et al.*, "Results of radius scaling experiments and analysis of neon K-shell radiation data from an inductively driven Z-pinch," *IEEE Trans. Plasma Sci.*, vol. 26, no. 4, pp. 1068–1085, Aug. 1998.

[III-17] D. Mosher *et al.*, "Measurement and analysis of gas-puff density distributions for plasma radiation source z pinches," *Laser Particle Beams*, vol. 19, no. 4, pp. 579–595, 2001.

[III-18] J. W. Thornhill *et al.*, "Assessing the ZR machine's potential for producing multi-keV X-ray yields in K-shell line and free-bound continuum radiation," *IEEE Trans. Plasma Sci.*, vol. 34, no. 5, pp. 2377–2391, Oct. 2006.

[III-19] C. A. Jennings *et al.*, "Circuit model for driving three-dimensional resistive MHD wire array Z-pinch calculations," *IEEE Trans. Plasma Sci.*, vol. 38, no. 4, pp. 529–539, Apr. 2010.

[IV-1] E. Nolting *et al.*, "Cold X-ray simulation technology development at Phoenix," in *Proc. IEEE Radiat. Effects Data Workshop (NSREC)*, Madison, WI, USA, Jul. 1995, pp. 93–98.

[IV-2] B. V. Weber and S. F. Fulghum, "A high sensitivity two-color interferometer for pulsed power plasmas," *Rev. Sci. Instrum.*, vol. 68, no. 2, pp. 1227–1232, 1997.

[IV-3] B. V. Weber, G. G. Peterson, S. J. Stephanakis, R. J. Commisso, and A. Fisher, "Measurement of gas distributions from a PRS nozzle," in *4th International Conference on Dense Z-Pinches, AIP Conference Proceedings*, vol. 409, N. Pereira, J. Davis, and P. Pulsifer, Eds. Woodbury, NY, USA: American Institute of Physics, 1997, pp. 459-462.

[IV-4] J. Kriesel, R. Prohaska, and A. Fisher, "Simple, fast, puff valve," *Rev. Sci. Instrum.*, vol. 62, no. 10, pp. 2372–2374, 1991.

[IV-5] B. Novak and S. Pekarek, "A fast acting all-metal gas valve for plasma research," *Rev. Sci. Instrum.*, vol. 41, no. 3, pp. 369–373, 1970.

[IV-6] M. Krishnan *et al.*, "Electromagnetically driven, fast opening and closing gas jet valve," *Phys. Rev. Special Topics-Accel. Beams*, vol. 14, no. 3, pp. 033502-1–033502-10, 2011.

[IV-7] M. Krishnan *et al.*, "Architecture, implementation, and testing of a multiple-shell gas injection system for high current implosions on the Z accelerator," *Rev. Sci. Instrum.*, vol. 84, no. 6, pp. 063504-1–063504-19, 2013.

[IV-8] A. Fisher, F. Mako, and J. Shiloh, "Fast valve for gas injection into vacuum," *Rev. Sci. Instrum.*, vol. 49, no. 6, pp. 872–873, 1978.

[IV-9] S. Wong, P. Smiley, T. Sheridan, J. Levine, and V. Buck, "Balanced puff valve for imploding gas-puff experiments," *Rev. Sci. Instrum.*, vol. 57, no. 8, pp. 1684–1686, 1986.

[IV-10] J. Marshall, "Acceleration of plasma into vacuum," in *Proc. 2nd United Nat. Int. Conf. Peaceful Uses Atomic Energy*, vol. 31. Sep. 1958, pp. 341–347.

[IV-11] I. S. Shpigel, "Quick-operating electrodynamic vacuum valve," *Instrum. Exp. Tech.*, vol. 1, p. 156, Jan. 1959.

[IV-12] B. Gorowitz, K. Moses, and P. Gloersen, "Magnetically driven fast-acting valve for gas injection into high vacuum," *Rev. Sci. Instrum.*, vol. 31, no. 2, pp. 146–148, 1960.

[IV-13] D. M. Wetstone, "Fast-acting gas valve," *Rev. Sci. Instrum.*, vol. 32, no. 11, pp. 1209–1211, 1961.

[IV-14] R. S. Lowder and F. C. Hoh, "Fast gas valve for plasma research," *Rev. Sci. Instrum.*, vol. 33, no. 11, pp. 1236–1238, 1962.

[IV-15] G. Kuswa, C. Stallings, and A. Stamm, "Improved fast opening gas puff valve," *Rev. Sci. Instrum.*, vol. 41, no. 9, pp. 1362–1363, 1970.

[IV-16] S. Morimoto and K. Kuriki, "Modified poppet valve for quasisteady gas injection into vacuum," *Rev. Sci. Instrum.*, vol. 44, no. 9, pp. 1182–1185, 1973.

[IV-17] C. J. Keyser, M. Dembinski, and P. K. John, "Fast pulsed gas valve," *Rev. Sci. Instrum.*, vol. 51, no. 4, pp. 425–426, 1980.

[IV-18] W. R. Gentry and C. F. Giese, "Ten-microsecond pulsed molecular beam source and a fast ionization detector," *Rev. Sci. Instrum.*, vol. 49, no. 5, pp. 595–600, May 1978.

[IV-19] I. Henins and J. Marshall, "A pulsed gas valve for fast timeable high pressure operation," *Rev. Sci. Instrum.*, vol. 40, no. 7, pp. 875–878, 1969.

[IV-20] D. A. Freiwald, "A fast opening valve for gas injection," *Rev. Sci. Instrum.*, vol. 41, no. 12, pp. 1906–1907, 1970.

[IV-21] M. Badaye, R. Stemprok, and R. P. Gupta, "An improved gas puff design for a Z-pinch X-ray source," *Rev. Sci. Instrum.*, vol. 61, no. 5, pp. 1457–1459, May 1990.

[IV-22] G. G. Peterson and B. V. Weber, "Gas distribution measurements from a PRS nozzle," presented at the Int. Conf. Plasma Sci., Madison, WI, USA, Jun. 1995, p. 207.

[IV-23] J. S. Levine *et al.*, "Long implosion time (240 ns) Z-pinch experiments with a large diameter (12 cm) double-shell nozzle," *Phys. Plasmas*, vol. 11, no. 5, pp. 2054–2059, May 2004.

[IV-24] R. C. Hazelton. (2005). *Heterodyne Interferometer for Triggering Gas-Puff PRSs*. [Online]. Available: http://www.dtic.mil/docs/citations/ADA435380

[IV-25] D. G. Phipps *et al.*, "Results of heterodyne interferometric system for real time trigger of a gas-puff Z-pinch," *IEEE Trans. Plasma Sci.*, to be published.

[IV-26] D. Mosher, "Plasma radiation source implosion limits due to azimuthal asymmetries," in *Proc. 10th Int. Conf. High Power Particle Beams*, San Diego, CA, USA, Jun. 1994, pp. 159–162.

[IV-27] C. H. Stallings and D. H. Martin, "Supersonic annular nozzle as a differential barrier," *Rev. Sci. Instrum.*, vol. 35, no. 8, pp. 1011–1013, 1964.

[IV-28] R. S. Smith, W. O. Doggett, I. Roth, and C. Stallings, "Supersonic gas shell for puff pinch experiments," *Appl. Phys. Lett.*, vol. 41, no. 6, pp. 572–573, Sep. 1982.

[IV-29] G. Mehlman, P. G. Burkhalter, S. J. Stephanakis, F. C. Young, and D. J. Nagel, "Quantitative X-ray spectroscopy of neon Z-pinch plasmas," *J. Appl. Phys.*, vol. 60, no. 10, pp. 3427–3432, Nov. 1986.

[IV-30] H. Sze *et al.*, "Initial results for an argon Z pinch using a double-shell gas puff," *Phys. Plasmas*, vol. 7, no. 10, pp. 4223–4226, Oct. 2000.

[IV-31] P. Coleman, J. Thompson, M. Krishnan, and B. L. Bures, "An alternative concept for the structure of an X-ray emitting Z-pinch," *IEEE Trans. Plasma Sci.*, vol. 38, no. 4, pp. 626–630, Apr. 2010.

[IV-32] R. B. Baksht *et al.*, "Rayleigh–Taylor instability and K-radiation yield in the implosion of the gas-puffs," *Plasma Phys. Rep.*, vol. 21, no. 11, pp. 907–912, 1995.

[IV-33] P. Coleman, J. Rauch, W. Rix, J. Thompson, and R. Wilson, "Recent ACE 4 Z-pinch experiments: Long implosion time argon loads, uniform fill versus annular shell distributions and the Rayleigh–Taylor instability problem," in *4th International Conference on Dense Z-Pinches, AIP Conference Proceedings*, vol. 409, N. Pereira, J. Davis, and P. Pulsifer, Eds. Woodbury, NY, USA: American Institute of Physics, 1997, pp. 119–123.

[IV-34] D. Mosher *et al.*, "Radius scaling of X-radiation from gas-puff implosions on an inductive driver," in *4th International Conference on Dense Z-Pinches, AIP Conference Proceedings*, vol. 409, N. Pereira, J. Davis, and P. Pulsifer, Eds. Woodbury, NY, USA: American Institute of Physics, 1997, pp. 135–140.

[IV-35] Y. Song *et al.*, "Valve and nozzle design for injecting a shell-on-shell gas puff load into a z pinch," *Rev. Sci. Instrum.*, vol. 71, no. 8, pp. 3080–3084, Aug. 2000.

[IV-36] H. Sze *et al.*, "Efficient argon K-shell radiation from a Z pinch at currents >15 MA," *Phys. Plasmas*, vol. 8, no. 7, pp. 3135–3138, Jul. 2001.

[IV-37] R. B. Baksht, A. V. Fedunin, A. Chuvatin, C. Rouaie, B. Etlicher, and S. Semushin, "Electromagnet valve for a multilayer-puff nozzle," *Instrum. Experim. Techn.*, vol. 41, no. 4, pp. 536–538, 1998.

[IV-38] H. Sze *et al.*, "Efficient radiation production in long implosions of structured gas-puff Z pinch loads from large initial radius," *Phys. Rev. Lett.*, vol. 95, pp. 105001-1–105001-4, Sep. 2005.

[IV-39] J. S. Levine *et al.*, "Implosion dynamics and radiative characteristics of a high yield structured gas puff load," *Phys. Plasmas*, vol. 13, no. 8, pp. 082702-1–082702-11, 2006.

[IV-40] S. L. Jackson *et al.*, "A comparison of planar, laser-induced fluorescence, and high-sensitivity interferometry techniques for gas-puff nozzle density measurements," *Rev. Sci. Instrum.*, vol. 79, no. 10, pp. 10E717-1–10E717-4, 2008.

[IV-41] A. Y. Labetsky *et al.*, "Study of the current-sheath formation during the implosion of multishell gas puffs," *Plasma Phys. Rep.*, vol. 34, no. 3, pp. 228–238, Mar. 2008.

[IV-42] J. S. Levine *et al.*, "Long-implosion plasma radiation sources using 'solid-fill' nozzles," *Phys. Plasmas*, vol. 8, no. 2, pp. 533–541, Feb. 2001.

[IV-43] A. V. Shishlov *et al.*, "Long time implosion experiments with double gas puffs," *Phys. Plasmas*, vol. 7, no. 4, pp. 1252–1262, Apr. 2000.

[IV-44] R. S. Smith, III, and W. O. Doggett, "High sensitivity or streak mode interferometer for pulsed plasma diagnostics," *Rev. Sci. Instrum.*, vol. 56, no. 3, pp. 355–358, Mar. 1985.

[IV-45] J.-N. Barnier, J.-M. Chevalier, B. D. Dubroca, and J. Rouch, "Gas puff nozzle characterization using interferometric methods and numerical simulation," *IEEE Trans. Plasma Sci.*, vol. 26, no. 4, pp. 1094–1100, Aug. 1998.

[IV-46] S. Katsuki, K. Murayama, T. Nishi, I. V. Lisitsyn, and H. Akiyama, "Influence of gas density distribution on the pinch process in gas-puff Z-pinch scheme," in *12th IEEE Int. Pulsed Power Conf., Dig. Tech. Papers*, Monterey, CA, USA, Jun. 1999, pp. 1067–1070.

[IV-47] B. Weber, private communication, Sep. 2014.

[IV-48] B. V. Weber, S. J. Stephanakis, and B. Moosman, "Differential phase shift interferometer for measuring axisymmetric gas distributions for high-power Z-pinch research," *Rev. Sci. Instrum.*, vol. 70, no. 1, pp. 687–690, Jan. 1999.

[IV-49] P. L. Coleman *et al.*, "Development and use of a two-dimensional interferometer to measure mass flow from a multi-shell Z-pinch gas puff," *Rev. Sci. Instrum.*, vol. 83, no. 8, pp. 083116-1–083116-10, 2012.

[IV-50] B. H. Failor, S. Chantrenne, P. L. Coleman, J. S. Levine, Y. Song, and H. M. Sze, "Proof-of-principle laser-induced fluorescence measurements of gas distributions from supersonic nozzles," *Rev. Sci. Instrum.*, vol. 74, no. 2, pp. 1070–1076, Feb. 2003.

[IV-51] N. Qi, B. H. Failor, J. Banister, J. S. Levine, H. M. Sze, and D. Lojewski, "Two-dimensional gas density and velocity distributions of a 12-cm-diameter, triple-nozzle argon Z-pinch load," *IEEE Trans. Plasma Sci.*, vol. 33, no. 2, pp. 752–762, Apr. 2005.

[IV-52] R. J. Commisso *et al.*, "Energetics of a long-implosion-time, 12-cm-diameter argon-gas-puff Z pinch at 6.5 MA," in *Proc. 16th IEEE Pulsed Power Conf.*, Albuquerque, NM, USA, Jun. 2007, pp. 1773–1779.

[IV-53] R. J. Commisso *et al.*, "Overview of 12-cm-diameter, argon gas-puff experiments and analyses with implosion times > 200 ns and 3- to 6-MA peak currents," in *7th International Conference on Dense-Z Pinches, AIP Conference Proceedings*, vol. 1088, D. A. Hammer and R. B. Kusse, Eds. Melville, NY, USA: American Institute of Physics, 2009, pp. 233–238.

[IV-54] N. Qi, B. H. Failor, J. S. Levine, J. Goyer, H. Sze, and A. Verma, "Magnetic field diffusion and enhanced resistivity in 12-cm-diameter 200-ns 3.5-MA Z-pinch implosions," *IEEE Trans. Plasma Sci.*, vol. 38, no. 4, pp. 545–553, Apr. 2010.

[IV-55] H. Sze *et al.*, "Magnetic Rayleigh–Taylor instability mitigation and efficient radiation production in gas puff Z-pinch implosions," *Phys. Plasmas*, vol. 14, no. 5, pp. 056307-1–056307-8, 2007.

[IV-56] N. Qi *et al.*, "Magnetic Rayleigh–Taylor instability mitigation in large-diameter gas puff Z-pinch implosions," *Phys. Plasmas*, vol. 15, no. 2, pp. 022703-1–022703-9, 2008.

[IV-57] O. F. Hagena and W. Obert, "Cluster formation in expanding supersonic jets: Effect of pressure, temperature, nozzle size, and test gas," *J. Chem. Phys.*, vol. 56, no. 5, pp. 1793–1802, Mar. 1972.

[IV-58] V. P. Krainov and M. B. Smirnov, "Cluster beams in the super-intense femtosecond laser pulse," *Phys. Rep.*, vol. 370, no. 3, pp. 237–331, 2002.

[IV-59] T. Ditmire, T. Donnelly, A. M. Rubenchik, R. W. Falcone, and M. D. Perry, "Interaction of intense laser pulses with atomic clusters," *Phys. Rev. A*, vol. 53, no. 5, pp. 3379–3401, May 1996.

[IV-60] D. Mosher, R. J. Commisso, and B. V. Weber, "Effects of radial-density and current profiles on PRSs dynamic mass and imploded energy," in *12th IEEE Int. Pulsed Power Conf., Dig. Tech. Papers*, Monterey, CA, USA, Jun. 1999, pp. 1078–1081.

[IV-61] J. O. Hirschfelder, C. F. Curtiss, and R. B. Bird, *Molecular Theory of Gases and Liquids*. New York, NY, USA: Wiley, 1954.

[IV-62] V. V. Vikhrev and S. I. Braginskii, "Dynamics of the Z pinch," in *Reviews of Plasma Physics*, vol. 10, M. A. Leontovich, Ed. New York, NY, USA: Consultants Bureau, 1986, pp. 425–517.

[IV-63] R. S. Smith, III, and W. O. Doggett, "Experimental characterization of a puff-gas z-pinch plasma prior to implosion," *Appl. Phys. Lett.*, vol. 46, no. 12, pp. 1128–1130, Jun. 1985.

[IV-64] R. B. Baksht, A. G. Russkikh, and A. V. Fedyunin, "Preionization of the gas shell of an Ar line," *Tech. Phys.*, vol. 40, no. 12, pp. 1224–1229, Dec. 1995.

[IV-65] E. Ruden, H. U. Rahman, A. Fisher, and N. Rostoker, "Stability enhancement of a low initial density hollow gas-puff z pinch by e^- beam preionization," *J. Appl. Phys.*, vol. 61, no. 4, pp. 1311–1316, Feb. 1987.

[IV-66] D. Osin, "Ion dynamics in hot and dense plasmas under intense magnetic fields," Ph.D. dissertation, Weizmann Inst. Sci., Rehovot, Israel, 2008.

[IV-67] E. Kroupp, private communication, Oct. 2014.

[IV-68] E. Kroupp *et al.*, "Ion temperature and hydrodynamic-energy measurements in a Z-pinch plasma at stagnation," *Phys. Rev. Lett.*, vol. 107, no. 10, pp. 105001-1–105001-5, Sep. 2011.

[IV-69] R. B. Baksht, A. G. Russkikh, and A. A. Chagin, "Study of the effect of preionization on current sharing between sheaths of a double-cascade gas puff," *Plasma Phys. Rep.*, vol. 23, no. 3, pp. 175–182, 1997.

[IV-70] A. G. Russkikh, R. B. Baksht, A. Yu. Labetsky, and A. V. Shishlov, "Influence of preionization on dynamics of a gas puff implosion," in *4th International Conference on Dense Z-Pinches, AIP Conference Proceedings*, vol. 409, N. Pereira, J. Davis, and P. Pulsifer, Eds. Woodbury, NY, USA: American Institute of Physics, 1997, pp. 307–310.

[IV-71] A. G. Rousskikh, R. B. Baksht, A. Y. Labetsky, A. S. Shishlov, and A. V. Fedyunin, "Effect of preionization on the implosion dynamics of single and double argon gas puffs," *Plasma Phys. Rep.*, vol. 25, no. 7, pp. 527–529, 1999.

[IV-72] B. V. Weber, D. D. Hinshelwood, and R. J. Commisso, "Interferometry of flashboard and cable-gun plasma opening switches on Hawk," *IEEE Trans. Plasma Sci.*, vol. 25, no. 2, pp. 189–195, Apr. 1997.

[IV-73] J. R. Woodworth and P. F. McKay, "Surface discharges as intense photon sources in the extreme ultraviolet," *J. Appl. Phys.*, vol. 58, no. 9, pp. 3364–3367, Nov. 1985.

[IV-74] B. V. Weber *et al.*, "Gas pre-ionization system for DECADE module 2 PRS experiments," in *Proc. 12th Int. Conf. High-Power Particle Beams*, Haifa, Israel, Jun. 1998, pp. 342–345.

[IV-75] B. Moosman, B. V. Weber, S. J. Stephanakis, R. J. Commisso, and A. Fisher, "Measurements of gas preionization for plasma radiation sources," *Rev. Sci. Instrum.*, vol. 70, no. 1, pp. 672–676, Jan. 1999.

[IV-76] J. Levine *et al.*, "Long-implosion plasma radiation source development," in *Proc. 12th Int. Conf. High-Power Particle Beams*, Haifa, Israel, Jun. 1998, pp. 95–101.

[IV-77] J. Levine, private communication, Sep. 2014.

[IV-78] P. Coleman, private communication, Sep. 2014.

[IV-79] J. Thompson, private communication, Sep. 2014.

[V-1] M. E. Foord, Y. Maron, G. Davara, L. Gregorian, and A. Fisher, "Particle velocity distributions and ionization processes in a gas-puff Z pinch," *Phys. Rev. Lett.*, vol. 72, no. 24, pp. 3827–3830, Jun. 1994.

[V-2] L. Gregorian, V. A. Bernshtam, E. Kroupp, G. Davara, and Y. Maron, "Use of emission-line intensities for a self-consistent determination of the particle densities in a transient plasma," *Phys. Rev. E*, vol. 67, no. 1, pp. 016404-1–016404-6, 2003.

[V-3] L. Gregorian *et al.*, "Electron density and ionization dynamics in an imploding z-pinch plasma," *Phys. Plasmas*, vol. 12, no. 9, pp. 092704-1–092704-8, 2005.

[V-4] L. Gregorian *et al.*, "Electron-temperature and energy-flow history in an imploding plasma," *Phys. Rev. E*, vol. 71, no. 5, pp. 056402-1–056402-11, 2005.

[V-5] G. Davara, L. Gregorian, E. Kroupp, and Y. Maron, "Spectroscopic determination of the magnetic-field distribution in an imploding plasma," *Phys. Plasmas*, vol. 5, no. 4, pp. 1068–1075, Apr. 1998.

[V-6] S. Tessarin *et al.*, "Beyond Zeeman spectroscopy: Magnetic-field diagnostics with Stark-dominated line shapes," *Phys. Plasmas*, vol. 18, no. 9, pp. 093301-1–093301-9, Sep. 2011.

[V-7] N. Qi *et al.*, "Z pinch imploding plasma density profile measurements using a two-frame laser shearing interferometer," *IEEE Trans. Plasma Sci.*, vol. 30, no. 1, pp. 227–238, Feb. 2002.

[V-8] N. Qi *et al.*, "Laser wavefront analyzer for imploding plasma density and current profile measurements," *Rev. Sci. Instrum.*, vol. 75, no. 10, pp. 3442–3445, Oct. 2004.

[V-9] J. W. Schumer *et al.*, "Two-dimensional MHD simulations of a neon Z pinch on Hawk," *IEEE Trans. Plasma Sci.*, vol. 30, no. 2, pp. 488–497, Apr. 2002.

[V-10] T. W. Hussey, M. K. Matzen, and N. F. Roderick, "Large-scale-length nonuniformities in gas puff implosions," *J. Appl. Phys.*, vol. 59, no. 8, pp. 2677–2684, Apr. 1986.

[V-11] W. W. Hsing and J. L. Porter, "Measurements of axial nonuniformities in gas-puff implosions," *Appl. Phys. Lett.*, vol. 50, no. 22, pp. 1572–1574, Jun. 1987.

[V-12] C. Deeney, P. D. LePell, F. L. Cochran, M. C. Coulter, K. G. Whitney, and J. Davis, "Argon gas puff implosion experiments and two-dimensional modeling," *Phys. Fluids B, Plasma Phys.*, vol. 5, no. 3, pp. 992–1001, Mar. 1993.

[V-13] B. B. Kadomtsev, "Hydromagnetic stability of a plasma," in *Reviews of Plasma Physics*, vol. 2, M. A. Leontovich, Ed. New York, NY, USA: Consultants Bureau, 1966, pp. 153–199.

[V-14] F. L. Cochran, J. Davis, and A. L. Velikovich, "Stability and radiative performance of structured Z-pinch loads imploded on high-current pulsed power generators," *Phys. Plasmas*, vol. 2, no. 7, pp. 2765–2772, Jul. 1995.

[V-15] T. W. Hussey, N. F. Roderick, and D. A. Kloc, "Scaling of (MHD) instabilities in imploding plasma liners," *J. Appl. Phys.*, vol. 51, no. 3, pp. 1452–1463, Mar. 1980.

[V-16] N. F. Roderick and T. W. Hussey, "Magnetic diffusion smoothing with application to the hydromagnetic Rayleigh–Taylor instability," *J. Appl. Phys.*, vol. 59, no. 2, pp. 662–665, Jan. 1986.

[V-17] M. R. Douglas, C. Deeney, and N. F. Roderick, "Computational investigation of single mode vs multimode Rayleigh–Taylor seeding in Z-pinch implosions," *Phys. Plasmas*, vol. 5, no. 12, pp. 4183–4198, Dec. 1998.

[V-18] M. R. Douglas, C. Deeney, and N. F. Roderick, "The effect of load thickness on the performance of high velocity, annular Z-pinch implosions," *Phys. Plasmas*, vol. 8, no. 1, pp. 238–248, 2001.

[V-19] T. W. Hussey, N. F. Roderick, U. Shumlak, R. B. Spielman, and C. Deeney, "A heuristic model for the nonlinear Rayleigh–Taylor instability in fast Z pinches," *Phys. Plasmas*, vol. 2, no. 6, pp. 2055–2062, Jun. 1995.

[V-20] J. W. Thornhill *et al.*, "One- and two-dimensional modeling of argon K-shell emission from gas-puff Z-pinch plasmas," *Phys. Plasmas*, vol. 14, no. 6, pp. 063301-1–063301-14, 2007.

[V-21] M. R. Douglas, J. S. De Groot, and R. B. Spielman, "The magneto-Rayleigh–Taylor instability in dynamic z pinches," *Laser Particle Beams*, vol. 19, no. 4, pp. 527–540, Dec. 2001.

[V-22] R. E. Reinovsky *et al.*, "Inductive store pulse compression system for driving high speed plasma implosions," *IEEE Trans. Plasma Sci.*, vol. 10, no. 2, pp. 73–81, Jun. 1982.

[V-23] G. Cooperstein and P. Ottinger, "Guest editorial fast opening vacuum switches for high-power inductive energy storage," *IEEE Trans. Plasma Sci.*, vol. 15, no. 6, pp. 629–643, Dec. 1987.

[V-24] S. P. Bugaev *et al.*, "A terawatt pulse-power generator with a microsecond plasma-opening switch," *IEEE Trans. Plasma Sci.*, vol. 18, no. 1, pp. 115–118, Feb. 1990.

[V-25] B. M. Koval'chuk and G. A. Mesyats, "Superpower pulsed systems with plasma opening switches," in *Proc. 8th Int. Conf. High-Power Particle Beams (Beams)*, Novosibirsk, Russia, Jul. 1991, pp. 92–103.

[V-26] B. V. Weber *et al.*, "Investigation of plasma opening switch conduction and opening mechanisms," *IEEE Trans. Plasma Sci.*, vol. 19, no. 5, pp. 757–766, Oct. 1991.

[V-27] W. Rix, D. Parks, J. Shannon, J. Thompson, and E. Waisman, "Operation and empirical modeling of the plasma opening switch," *IEEE Trans. Plasma Sci.*, vol. 19, no. 2, pp. 400–407, Apr. 1991.

[V-28] W. Rix, P. Coleman, J. R. Thompson, D. Husovsky, P. Melcher, and R. J. Commisso, "Scaling microsecond-conduction-time plasma opening switch operation from 2 to 5 MA," *IEEE Trans. Plasma Sci.*, vol. 25, no. 2, pp. 169–175, Apr. 1997.

[V-29] R. J. Commisso, P. J. Goodrich, J. M. Grossmann, D. D. Hinshelwood, P. F. Ottinger, and B. V. Weber, "Characterization of a microsecond-conduction-time plasma opening switch," *Phys. Fluids B, Plasma Phys.*, vol. 4, no. 7, pp. 2368–2376, Jul. 1992.

[V-30] R. J. Commisso *et al.*, "Pawn, an inductive storage pulsed power generator for high power applications," in *Proc. 7th IEEE Pulsed Power Conf.*, Monterey, CA, USA, Jun. 1989, pp. 272–274.

[V-31] N. Shimomura, H. Akiyama, and S. Maeda, "Compact pulsed power generator using an inductive energy storage system with two-staged opening switches," *IEEE Trans. Plasma. Sci.*, vol. 19, no. 6, pp. 1220–1227, Dec. 1991.

[V-32] C. Maisonnier, J. G. Linhart, and C. Gourlan, "Rapid transfer of magnetic energy by means of exploding foils," *Rev. Sci. Instrum.*, vol. 37, no. 10, pp. 1380–1384, Oct. 1966.

[V-33] R. Stringfield *et al.*, "Plasma erosion switches with imploding plasma loads on a multiterawatt pulsed power generator," *J. Appl. Phys.*, vol. 52, no. 3, pp. 1278–1284, Mar. 1981.

[V-34] R. Stringfield, P. Sincerny, S.-L. Wong, G. James, T. Peters, and C. Gilman, "Continuing studies of plasma erosion switches for power conditioning on multiterawatt pulsed power accelerators," *IEEE Trans. Plasma Sci.*, vol. 11, no. 3, pp. 200–205, Sep. 1983.

[V-35] W. Rix *et al.*, "Final design and initial pulsed power results for the Decade Quad plasma radiation source machine configurations," in *IEEE Pulsed Power Plasma Sci. Conf., Dig. Tech. Papers*, Las Vegas, NV, USA, Jun. 2001, pp. 573–576.

[V-36] R. Davis *et al.*, "Recent progress in DoD's program to develop Ar K-shell X-ray radiation sources," in *14th IEEE Int. Pulsed Power Conf., Dig. Tech. Papers*, Dallas, TX, USA, Jun. 2001, pp. 37–41.

[V-37] C. Deeney *et al.*, "Neon gas puff implosions on a high-current microsecond generator with and without a plasma opening switch," *J. Appl. Phys.*, vol. 72, no. 4, pp. 1297–1305, Aug. 1997.

[V-38] K. D. Ware, D. E. Bell, R. L. Gullickson, and I. Vitkovitsky, "Evolving approaches to pulsed X-ray sources," *IEEE Trans. Plasma Sci.*, vol. 30, no. 5, pp. 1733–1741, Oct. 2002.

[V-39] M. R. Douglas, C. Deeney, and N. F. Roderick, "Effect of sheath curvature on Rayleigh–Taylor mitigation in high-velocity uniform-fill, Z-pinch implosions," *Phys. Rev. Lett.*, vol. 78, no. 24, pp. 4577–4580, Jun. 1997.

[V-40] S. M. Gol'berg and A. L. Velikovich, "Suppression of Rayleigh–Taylor instability by the snowplow mechanism," *Phys. Fluids B, Plasma Phys.*, vol. 5, no. 4, pp. 1164–1172, Apr. 1993.

[V-41] N. F. Roderick, R. E. Peterkin, Jr., T. W. Hussey, R. B. Spielman, M. R. Douglas, and C. Deeney, "Hydromagnetic Rayleigh–Taylor instability in high-velocity gas-puff implosions," *Phys. Plasmas*, vol. 5, no. 5, pp. 1477–1484, May 1998.

[V-42] A. L. Velikovich, F. L. Cochran, and J. Davis, "Suppression of Rayleigh–Taylor instability in Z-pinch loads with tailored density profiles," *Phys. Rev. Lett.*, vol. 77, no. 5, pp. 853–856, Jul. 1996.

[V-43] A. L. Velikovich, F. L. Cochran, J. Davis, and Y. K. Chong, "Stabilized radiative Z-pinch loads with tailored density profiles," *Phys. Plasmas*, vol. 5, no. 9, pp. 3377–3388, Sep. 1998.

[V-44] J. H. Hammer *et al.*, "Two-dimensional radiation-magnetohydrodynamic simulations of SATURN imploding Z pinches," *Phys. Plasmas*, vol. 3, no. 5, pp. 2063–2069, May 1996.

[VI-1] R. B. Spielman *et al.*, "Z-pinch experiments on Saturn at 30 TW," in *2nd International Conference on Dense Z-Pinches, AIP Conference Proceedings*, vol. 195, N. Pereira, J. Davis, and N. Rostoker, Eds. New York, NY, USA: American Institute of Physics, 1989, pp. 3–16.

[VI-2] J. P. Apruzese *et al.*, "Properties of the best Ar K-shell radiators: Two decades of data analysis from seven Z-pinch drivers," in *7th International Conference on Dense-Z Pinches, AIP Conference Proceedings*, vol. 1088, D. A. Hammer and R. B. Kusse, Eds. Melville, NY, USA: American Institute of Physics, 2009, pp. 239–242.

[VI-3] R. B. Baksht *et al.*, "On stabilization of gas puff implosion: Experiment and simulation," *IEEE Trans. Plasma Sci.*, vol. 26, no. 4, pp. 1259–1266, Aug. 1998.

[VI-4] J. P. Apruzese, private communication, Jun. 2014.

[VI-5] T. W. L. Sanford *et al.*, "Uniform fill improves K-shell power relative to annular fill for argon gas puffs on Saturn," in *Proc. IEEE Int. Conf. Plasmas Sci.*, Boston, MA, USA, Jun. 1996, p. 251.

[VI-6] P. L. Coleman *et al.*, "Measurement of the ∼0.1. to > 10-keV energy distribution for an argon Z-pinch at the 15-MA level," *IEEE Trans. Plasma Sci.*, vol. 35, no. 1, pp. 31–42, Feb. 2007.

[VI-7] J. S. Levine *et al.*, "Z-pinch experiments on decade quad using a double shell gas puff," in *5th International Conference on Dense Z-Pinches, AIP Conference Proceedings*, vol. 651, J. Davis, C. Deeney, and N. Pereira, Eds. Melville, NY, USA: American Institute of Physics, 2002, pp. 109–112.

[VI-8] F. C. Young *et al.*, "Measurement and analysis of continuum radiation from a large-diameter long implosion time argon gas puff Z-pinch at 6 MA," *IEEE Trans. Plasma Sci.*, vol. 34, no. 5, pp. 2312–2324, Oct. 2006.

[VI-9] F. Zucchini *et al.*, "First argon gas puff experiments with 500 ns implosion time on the Sphinx driver," in *7th International Conference on Dense-Z Pinches, AIP Conference Proceedings*, vol. 1088, D. A. Hammer and R. B. Kusse, Eds. Melville, NY, USA: American Institute of Physics, 2009, pp. 247–250.

[VI-10] B. Jones *et al.*, "A renewed capability for gas puff science on Sandia's Z machine," *IEEE Trans. Plasma Sci.*, vol. 42, no. 5, pp. 1145–1152, May 2014.

[VI-11] B. Jones *et al.*, "The effect of gradients at stagnation on K-shell X-ray line emission in high-current Ar gas-puff implosions," *Phys. Plasmas*, vol. 22, no. 2, pp. 020706-1–020706-5, Feb. 2015.

[VI-12] D. Mihalas, *Stellar Atmospheres*. San Francisco, CA, USA: Freeman, 1970.

[VI-13] J. P. Apruzese and J. L. Giuliani, "Radiation transport in Z-pinches," *IEEE Trans. Plasma Sci.*, vol. 43, no. 8, pp. 2454–2462, Aug. 2015.

[VI-14] J. P. Apruzese, "Direct solution of the equation of transfer using frequency- and angle-averaged photon-escape probabilities for spherical and cylindrical geometries," *J. Quant. Spectrosc. Radiat. Transf.*, vol. 25, no. 5, pp. 419–425, 1981.

[VI-15] J. P. Apruzese, "An analytic Voigt profile escape probability approximation," *J. Quant. Spectrosc. Radiat. Transf.*, vol. 34, no. 5, pp. 447–452, 1985.

[VI-16] J. P. Apruzese and P. C. Kepple, "Calculation of the line emission from cylindrical krypton plasmas using a 162-level, 511-line detailed configuration atomic model," *J. Quant. Spectrosc. Radiat. Transf.*, vol. 44, nos. 5–6, pp. 529–540, 1990.

[VI-17] V. V. Sobolev, "The diffusion of L_α radiation in nebulae and stellar envelopes," *Soviet Astron.*, vol. 1, pp. 678–689, Oct. 1957.

[VI-18] R. W. Clark, J. Davis, J. P. Apruzese, and J. L. Giuliani, Jr., "A probabilistic model for continuum transport in dense, optically thick plasmas," *J. Quant. Spectrosc. Radiat. Transf.*, vol. 53, no. 3, pp. 307–320, 1995.

[VI-19] A. L. Velikovich, J. P. Apruzese, J. Davis, and J. W. Thornhill, "Theory of high-energy-photon K-shell recombination continuum radiation from Z-pinch plasmas," *IEEE Trans. Plasma Sci.*, vol. 38, no. 4, pp. 618–625, Apr. 2010.

[VI-20] M. C. Coulter, K. G. Whitney, and J. W. Thornhill, "A new procedure for analyzing X-ray spectra from laboratory plasma," *J. Quant. Spectrosc. Radiat. Transf.*, vol. 44, nos. 5–6, pp. 443–456, 1990.

[VI-21] J. P. Apruzese, K. G. Whitney, J. Davis, and P. C. Kepple, "K-shell line ratios and powers for diagnosing cylindrical plasmas of neon, aluminum, argon, and titanium," *J. Quant. Spectrosc. Radiat. Transf.*, vol. 57, no. 1, pp. 41–61, 1997.

[VI-22] B. H. Failor *et al.*, "Axially resolved z-pinch density, electron temperature, and K-shell emitting mass estimates from charge-coupled device based diagnostics," *Rev. Sci. Instrum.*, vol. 72, no. 1, pp. 1232–1235, Jan. 2001.

[VI-23] J. P. Apruzese, J. L. Giuliani, J. W. Thornhill, C. A. Coverdale, B. Jones, and D. J. Ampleford, "Analysis of spatially resolved Z-pinch spectra to investigate the nature of 'bright spots,'" *Phys. Plasmas*, vol. 20, no. 2, pp. 022707-1–022707-10, 2013.

[VI-24] J. P. Apruzese *et al.*, "Diagnostic constraints on the amount of cold mass in imploded argon pinches on Z," in *9th International Conference on Dense Z-Pinches, AIP Conference Proceedings*, vol. 1639, D. Sinars and S. Bott-Suzuki, Eds. Melville, NY, USA: American Institute of Physics, 2014, pp. 39–42.

[VI-25] R. W. Clark, J. Davis, and F. L. Cochran, "Dynamics of imploding neon gas-puff plasmas," *Phys. Fluids*, vol. 29, no. 6, pp. 1971–1978, Jun. 1986.

[VI-26] R. W. Clark and J. Davis, "Imploding neon puff-gas plasmas. I," *Phys. Fluids B*, vol. 2, no. 7, pp. 1698–1705, Jul. 1990.

[VI-27] J. Davis, J. L. Giuliani, Jr., and M. Mulbrandon, "Influence of L-shell dynamics on K-shell yields for imploding krypton Z-pinch plasmas," *Phys. Plasmas*, vol. 2, no. 5, pp. 1766–1774, May 1995.

[VI-28] J. L. Giuliani *et al.*, "Numerical simulations of PRS yields for a pulsed power decade class generator," *J. Radiat. Effects*, vol. 12, no. 3, pp. 41–50, Sep. 1994.

[VI-29] J. Davis, R. Clark, M. Blaha, and J. L. Giuliani, Jr., "Atomic physics and non-LTE effects," *Laser Particle Beams*, vol. 19, no. 4, pp. 557–577, 2001.

[VI-30] A. S. Chuvatin, L. I. Rudakov, A. L. Velikovich, J. Davis, and V. I. Oreshkin, "Heating of on-axis plasma heating for keV X-ray production with Z-pinches," *IEEE Trans. Plasma Sci.*, vol. 33, no. 2, pp. 739–751, Apr. 2005.

[VI-31] M. Busquet, "Radiation-dependent ionization model for laser-created plasmas," *Phys. Fluids B*, vol. 5, no. 11, pp. 4191–4205, 1993.

[VI-32] J. W. Thornhill *et al.*, "An efficient tabulated collisional radiative equilibrium radiation transport model suitable for multidimensional hydrodynamics calculations," *Phys. Plasmas*, vol. 8, no. 7, pp. 3480–3489, Jul. 2001.

[VI-33] R. E. Peterkin, Jr., M. H. Frese, and C. R. Sovinec, "Transport of magnetic flux in an arbitrary coordinate ALE code," *J. Comput. Phys.*, vol. 140, no. 1, pp. 148–171, 1998.

[VI-34] J. W. Thornhill *et al.*, "Two-dimensional radiation MHD modeling assessment of designs for argon gas puff distributions for future experiments on the refurbished Z machine," *High Energy Density Phys.*, vol. 8, no. 3, pp. 197–208, 2012.

[VI-35] J. W. Thornhill *et al.*, "2-D RMHD modeling assessment of current flow, plasma conditions, and doppler effects in recent Z argon experiments," *IEEE Trans. Plasma Sci.*, vol. 43, no. 8, pp. 2480–2491, Aug. 2015.

[VI-36] K. L. Wong *et al.*, "Spectroscopic characterization of an argon-neon Z-pinch plasma at stagnation," *Phys. Rev. Lett.*, vol. 80, no. 11, pp. 2334–2337, Mar. 1998.

[VI-37] E. Kroupp *et al.*, "Ion-kinetic-energy measurements and energy balance in a Z-pinch plasma at stagnation," *Phys. Rev. Lett.*, vol. 98, no. 11, pp. 115001-1–115001-4, Mar. 2007.

[VI-38] T. W. L. Sanford *et al.*, "Dynamics of a high-power aluminum-wire array Z-pinch implosion," *Phys. Plasmas*, vol. 4, no. 6, pp. 2188–2203, Jun. 1997.

[VI-39] M. G. Haines, P. D. LePell, C. A. Coverdale, B. Jones, C. Deeney, and J. P. Apruzese, "Ion viscous heating in a magnetohydrodynamically unstable Z pinch at over 2×10^9 Kelvin," *Phys. Rev. Lett.*, vol. 96, no. 7, pp. 075003-1–075003-4, Feb. 2006.

[VI-40] Y. Fan *et al.*, "Spatially-resolved spectroscopic diagnosing of aluminum wire array Z-pinch plasmas on QiangGuang-I facility," *Chin. Phys. B*, vol. 19, no. 7, pp. 075204-1–075204-5, 2010.

[VI-41] R. H. Lovberg, R. A. Riley, and J. S. Shlachter, "Instability heating of the HDZP," in *3rd International Conference on Dense Z-Pinches, AIP Conference Proceedings*, vol. 299, M. Haines and A. Knight, Eds. Woodbury, NY, USA: American Institute of Physics, 1994, pp. 59–68.

[VI-42] L. I. Rudakov and R. N. Sudan, "MHD turbulence in radiating intense Z-pinches," *Phys. Rep.*, vol. 283, nos. 1–4, pp. 253–263, 1997.

[VI-43] A. L. Velikovich, J. Davis, J. W. Thornhill, J. L. Giuliani, Jr., L. I. Rudakov, and C. Deeney, "Model of enhanced energy deposition in a Z-pinch plasma," *Phys. Plasmas*, vol. 7, no. 8, pp. 3265–3277, Aug. 2000.

[VI-44] L. I. Rudakov, A. L. Velikovich, J. Davis, J. W. Thornhill, J. L. Giuliani, Jr., and C. Deeney, "Buoyant magnetic flux tubes enhance radiation in Z pinches," *Phys. Rev. Lett.*, vol. 84, no. 15, pp. 3326–3329, Apr. 2000.

[VI-45] M. G. Haines, "Viscous heating at stagnation in Z pinches," in *7th International Conference on Dense-Z Pinches, AIP Conference Proceedings*, vol. 1088, D. A. Hammer and R. B. Kusse, Eds. Melville, NY, USA: American Institute of Physics, 2009, pp. 57–60.

[VI-46] J. L. Giuliani *et al.*, "Effective versus ion thermal temperatures in the Weizmann Ne Z-pinch: Modeling and stagnation physics," *Phys. Plasmas*, vol. 21, no. 3, pp. 031209-1–031209-8, 2014.

[VI-47] Y. Maron *et al.*, "Pressure and energy balance of stagnating plasmas in z-pinch experiments: Implications to current flow at stagnation," *Phys. Rev. Lett.*, vol. 111, no. 3, pp. 035001-1–035001-5, Jul. 2013.

[VI-48] H. R. Strauss, "Stagnation of a gas puff Z pinch," *Phys. Plasmas*, vol. 19, no. 3, pp. 032705-1–032705-7, 2012.

[VI-49] A. Y. Labetsky, R. B. Baksht, V. I. Oreshkin, A. G. Rousskikh, and A. V. Shishlov, "An experimental study of the effect of Rayleigh–Taylor instabilities on the energy deposition into the plasma of a Z pinch," *IEEE Trans. Plasma Sci.*, vol. 30, no. 2, pp. 524–531, Apr. 2002.

[VI-50] D. P. Murphy *et al.*, "Time-resolved voltage measurements of Z-pinch radiation sources with a vacuum voltmeter," *Rev. Sci. Instrum.*, vol. 79, no. 10, pp. 10E306-1–10E306-3, 2008.

[VI-51] B. Jones *et al.*, "Doppler measurement of implosion velocity in fast Z-pinch X-ray sources," *Phys. Rev. E*, vol. 84, no. 5, pp. 056408-1–056408-9, Nov. 2011.

[VI-52] F. S. Felber, M. A. Liberman, and A. L. Velikovich, "Methods for producing ultrahigh magnetic fields," *Appl. Phys. Lett.*, vol. 46, no. 11, pp. 1042–1044, Jun. 1985.

[VI-53] F. J. Wessel, F. S. Felber, N. C. Wild, H. U. Rahman, A. Fisher, and E. Ruden, "Generation of high magnetic fields using a gas-puff Z pinch," *Appl. Phys. Lett.*, vol. 48, no. 17, pp. 1119–1121, Apr. 1986.

[VI-54] F. J. Wessel, N. C. Wild, A. Fisher, H. U. Rahman, A. Ron, and F. S. Felber, "Faraday rotation in a multimode optical fiber in a fast rise-time, high magnetic field," *Rev. Sci. Instrum.*, vol. 57, no. 9, pp. 2246–2249, Sep. 1986.

[VI-55] F. S. Felber *et al.*, "Ultrahigh magnetic fields produced in a gas-puff Z pinch," *J. Appl. Phys.*, vol. 64, no. 8, pp. 3831–3844, Oct. 1988.

[VI-56] F. S. Felber *et al.*, "Compression of ultrahigh magnetic fields in a gas-puff Z pinch," *Phys. Fluids*, vol. 31, no. 7, pp. 2053–2056, Jul. 1988.

[VI-57] A. I. Bykov, M. I. Dolotenko, N. P. Kolokolchikov, V. D. Selemir, and O. M. Tatsenko, "VNIIEF achievements on ultra-high magnetic fields generation," *Phys. B, Condens. Matter*, vols. 294–295, pp. 574–578, Jan. 2001.

[VI-58] J. P. Knauer *et al.*, "Compressing magnetic fields with high-energy lasers," *Phys. Plasmas*, vol. 17, no. 5, pp. 056318-1–056318-8, May 2010.

[VI-59] P. F. Schmit *et al.*, "Understanding fuel magnetization and mix using secondary nuclear reactions in magneto-inertial fusion," *Phys. Rev. Lett.*, vol. 113, no. 15, pp. 155004-1–155004-6, Oct. 2014.

[VI-60] S. A. Chaikovsky *et al.*, "The K-shell radiation of a double gas puff z-pinch with an axial magnetic field," *Laser Particle Beams*, vol. 21, no. 2, pp. 255–264, 2003.

[VI-61] A. V. Shishlov *et al.*, "Formation of tight plasma pinches and generation of high-power soft X-ray radiation pulses in fast Z-pinch implosions," *Laser Phys.*, vol. 16, no. 1, pp. 183–193, 2006.

[VI-62] S. A. Sorokin, "Gas-puff liner implosion in the configuration with helical current return rods," *Plasma Phys. Rep.*, vol. 39, no. 2, pp. 139–143, 2013.

[VI-63] P.-A. Gourdain *et al.*, "Initial magnetic field compression studies using gas-puff Z-pinches and thin liners on COBRA," *Nucl. Fusion*, vol. 53, no. 8, pp. 083006-1–083006-10, 2013.

[VI-64] J. B. Greenly, M. Martin, I. Blesener, D. Chalenski, P. Knapp, and R. McBride, "The role of flux advection in the development of the ablation streams and precursors of wire array Z-pinches," in *7th International Conference on Dense-Z Pinches, AIP Conference Proceedings*, vol. 1088, D. A. Hammer and R. B. Kusse, Eds. Melville, NY, USA: American Institute of Physics, 2009, pp. 53–56.

[VI-65] B. L. Bures and M. Krishnan, "An alternative scaling model for neutron production in Z-pinch devices," *Phys. Plasmas*, vol. 19, no. 11, pp. 112702-1–112702-8, Nov. 2012.

[VI-66] D. Klir *et al.*, "Neutron energy distribution function reconstructed from time-of-flight signals in deuterium gas-puff Z-pinch," *IEEE Trans. Plasma Sci.*, vol. 37, no. 3, pp. 425–432, Mar. 2009.

[VI-67] D. Klir *et al.*, "Efficient production of 100 keV deuterons in deuterium gas puff Z-pinches at 2 MA current," *Plasma Phys. Controlled Fusion*, vol. 52, no. 6, pp. 065013-1–065013-17, 2010.

[VI-68] V. P. Smirnov, "Fast liners for inertial fusion," *Plasma Phys. Controlled Fusion*, vol. 33, no. 13, pp. 1697–1714, 1991.

[VI-69] D. Klir *et al.*, "Deuterium gas puff Z-pinch at currents of 2 to 3 mega-ampere," *Phys. Plasmas*, vol. 19, no. 3, pp. 032706-1–032706-11, 2012.

[VI-70] D. Klir *et al.*, "Characterization of neutron emission from mega-ampere deuterium gas puff Z-pinch at microsecond implosion times," *Plasma Phys. Controlled Fusion*, vol. 55, no. 8, pp. 085012-1–085012-11, 2013.

[VI-71] D. Klir *et al.*, "Search for drive parameter of neutron-optimized Z-pinches and dense plasma foci," *IEEE Trans. Plasma Sci.*, vol. 41, no. 11, pp. 3129–3134, Nov. 2013.

[VI-72] D. Klir *et al.*, "Efficient neutron production from a novel configuration of deuterium gas-puff Z-pinch," *Phys. Rev. Lett.*, vol. 112, no. 9, pp. 095001-1–095001-5, Mar. 2014.

[VI-73] D. Klir *et al.*, "Efficient generation of fast neutrons by magnetized deuterons in an optimized deuterium gas-puff z-pinch," *Plasma Phys. Controlled Fusion*, vol. 57, no. 4, pp. 044005-1–044005-11, Mar. 2015.

[VI-74] R. B. Spielman *et al.*, "D-D fusion experiments using fast Z pinches," Nat. Tech. Inf. Service, Springfield, VA, USA, Tech. Rep. SAND-98-0705, 1998.

[VI-75] C. A. Coverdale *et al.*, "Neutron production and implosion characteristics of a deuterium gas-puff Z pinch," *Phys. Plasmas*, vol. 14, no. 2, pp. 022706-1–022706-7, 2007.

[VI-76] C. A. Coverdale *et al.*, "Deuterium gas-puff Z-pinch implosions on the Z accelerator," *Phys. Plasmas*, vol. 14, no. 5, pp. 056309-1–056309-7, 2007.

[VI-77] A. L. Velikovich *et al.*, "Z-pinch plasma neutron sources," *Phys. Plasmas*, vol. 14, no. 2, pp. 022701-1–022701-16, 2007.

[VI-78] D. R. Welch, D. V. Rose, R. E. Clark, C. B. Mostrom, W. A. Stygar, and R. J. Leeper, "Fully kinetic particle-in-cell simulations of a deuterium gas puff z pinch," *Phys. Rev. Lett.*, vol. 103, no. 25, pp. 255002-1–255002-4, Dec. 2009.

[VI-79] D. R. Welch *et al.*, "Kinetic simulation of thermonuclear-neutron production by a 10^7-A deuterium Z pinch," *Phys. Plasmas*, vol. 17, no. 7, pp. 072702-1–072702-11, 2010.

[VI-80] G. H. McCall, "Calculation of neutron yield from a dense Z pinch," *Phys. Rev. Lett.*, vol. 62, no. 17, pp. 1986–1988, Apr. 1989.

[VI-81] A. Schmidt, V. Tang, and D. Welch, "Fully kinetic simulations of dense plasma focus Z-pinch devices," *Phys. Rev. Lett.*, vol. 109, no. 20, pp. 205003-1–205003-4, Nov. 2012.

[VI-82] D. R. Welch *et al.*, "Kinetic simulations of a deuterium-tritium Z pinch with >1016 neutron yield," *Phys. Plasmas*, vol. 18, no. 5, pp. 056303-1–056303-7, 2011.

[VII-1] J. S. Levine, B. H. Failor, H. M. Sze, and D. Bell, "Mixed gas Z pinch experiments using a shell-on-shell nozzle on double-EAGLE," *IEEE Trans. Plasma Sci.*, vol. 30, no. 2, pp. 512–516, Apr. 2002.

[VII-2] A. V. Shishlov *et al.*, "Experimental study of an argon-hydrogen Z pinch plasma radiation source," *IEEE Trans. Plasma Sci.*, vol. 30, no. 2, pp. 498–511, Apr. 2002.

[VII-3] A. Weingarten, R. Arad, Y. Maron, and A. Fruchtman, "Ion separation due to magnetic field penetration into a multispecies plasma," *Phys. Rev. Lett.*, vol. 87, no. 11, pp. 115004-1–115004-4, Sep. 2001.

[VII-4] N. Qi *et al.*, "Study of gas-puff Z-pinches on COBRA," *Phys. Plasmas*, vol. 21, no. 11, pp. 112702-1-112702-15, Nov. 2014.

[VII-5] P. H. Ney, H. U. Rahman, F. J. Wessel, and N. Rostoker, "Staged Z pinch for controlled fusion," *Phys. Plasmas*, vol. 8, no. 2, pp. 616–624, Feb. 2001.

[VII-6] H. U. Rahman, P. H. Ney, N. Rostoker, A. Van Drie, and F. J. Wessel, "Control of the Rayleigh–Taylor instability in a staged Z pinch," *Phys. Plasmas*, vol. 11, no. 12, pp. 5595–5604, Dec. 2004.

[VII-7] H. U. Rahman, F. J. Wessel, N. Rostoker, and P. H. Ney, "High yield fusion in a staged Z-pinch," *J. Plasma Phys.*, vol. 75, no. 6, pp. 749–768, 2009.

[VII-8] H. U. Rahman, F. J. Wessel, and N. Rostoker, "Staged Z pinch," *Phys. Rev. Lett.*, vol. 74, no. 5, pp. 714–717, Jan. 1995.

[VII-9] H. U. Rahman, P. H. Ney, F. J. Wessel, and N. Rostoker, "Staged pinch for controlled thermonuclear fusion," *J. Plasma Phys.*, vol. 58, no. 2, pp. 367–379, 1997.

[VII-10] F. J. Wessel *et al.*, "Enhanced plasma radiation source: Tandem-puff, pinch-on-wire plasma," *J. Appl. Phys.*, vol. 81, no. 8, pp. 3410–3415, Apr. 1997.

[VII-11] A. Chuvatin, P. Choi, and B. Etlicher, "Formation of a composite pinch," *Phys. Rev. Lett.*, vol. 76, no. 13, pp. 2282–2285, Mar. 1996.

[VII-12] A. V. Branitskii *et al.*, "Penetration of azimuthal magnetic flux to the interior of an unstable liner," *Plasma Phys. Rep.*, vol. 22, no. 4, pp. 277–287, 1996.

[VII-13] R. B. Baksht, A. Y. Labetskii, S. V. Loginov, V. I. Oreshkin, A. V. Fedyunin, and A. V. Shishlov, "Z-pinch of a multiwire liner surrounded by an outer gas sheath," *Plasma Phys. Rep.*, vol. 23, no. 2, pp. 119–125, 1997.

[VII-14] A. V. Shishlov *et al.*, "Gas-puff-on-wire-array Z-pinch experiments on the GIT-12 generator at microsecond implosion times," *IEEE Trans. Plasma Sci.*, vol. 35, no. 3, pp. 592–600, Jun. 2007.

[VII-15] A. G. Rousskikh, A. S. Zhigalin, V. I. Oreshkin, S. A. Chaikovsky, N. A. Labetskaya, and R. B. Baksht, "Use of vacuum arc plasma guns for a metal puff Z-pinch system," *Phys. Plasmas*, vol. 18, no. 9, pp. 092707-1–092707-7, 2011.

[VII-16] A. G. Rousskikh, R. B. Baksht, A. S. Zhigalin, V. I. Oreshkin, S. A. Chaikovsky, and N. A. Labetskaya, "Multichannel vacuum arc discharge used for Z-pinch formation," *Plasma Phys. Rep.*, vol. 38, no. 8, pp. 595–607, 2012.

[VII-17] R. B. Baksht, A. G. Rousskikh, A. S. Zhigalin, and V. I. Oreshkin, "Metal double-puff Z-pinch," *IEEE Trans. Plasma Sci.*, vol. 41, no. 1, pp. 182–186, Jan. 2013.

[VII-18] V. L. Kantsyrev *et al.*, "Radiation properties and implosion dynamics of planar and cylindrical wire arrays, asymmetric and symmetric, uniform and combined X-pinches on the UNR 1-Ma Zebra generator," *IEEE Trans. Plasma Sci.*, vol. 34, no. 2, pp. 194–212, Apr. 2006.

[VII-19] A. G. Rousskikh *et al.*, "Study of the stability of Z-pinch implosions with different initial density profiles," *Phys. Plasmas*, vol. 21, no. 5, pp. 052701-1–052701-7, 2014.

[VII-20] A. J. Harvey-Thompson *et al.*, "Suppression of the ablation phase in wire array Z pinches using a tailored current prepulse," *Phys. Rev. Lett.*, vol. 106, no. 20, pp. 205002-1–205002-4, May 2011.

[VII-21] R. B. Baksht, V. I. Oreshkin, and A. G. Rousskikh, "On the possibility of neutron generation in an imploding TiD_2 puff Z pinch," *Phys. Plasmas*, vol. 20, no. 8, pp. 082701-1–082701-4, 2013.

[VIII-1] A. J. Harvey-Thompson *et al.*, "The effect of adding a center jet to argon gas puff implosions at the Z facility," in *Proc. IEEE 41st Int. Conf. Plasmas Sci.*, Washington, DC, USA, May 2014, p. 1.

[VIII-2] C. A. Jennings, "Computational modeling of Kr gas puffs on Z," *Bull. Amer. Phys. Soc.*, vol. 59, no. 15, p. 287, Oct. 2014.

[VIII-3] C. A. Jennings *et al.*, "Computational modeling of Kr gas puffs on Z," *Bull. Amer. Phys. Soc.*, vol. 58, no. 16, p. 286, Nov. 2013.

[VIII-4] D. J. Ampleford *et al.*, "Contrasting physics in wire array z pinch sources of 1–20 keV emission on the Z facility," *Phys. Plasmas*, vol. 21, no. 5, pp. 056708-1–056708-10, May 2014.

[VIII-5] J. L. Giuliani *et al.*, "Two dimensional modeling of effective ion temperatures in recent ZR argon experiments," in *9th International Conference on Dense Z-Pinches, AIP Conference Proceedings*, vol. 1639, D. Sinars and S. Bott-Suzuki, Eds. Melville, NY, USA: American Institute of Physics, 2014, pp. 31–34.

[VIII-6] G. Rosenzweig, E. Kroupp, A. Starobinets, A. Fisher, and Y. Maron, "Measurements of the time-resolved spatial magnetic field distribution and structure of a Z-pinch plasma throughout the stagnation process," *Bull. Amer. Phys. Soc.*, vol. 59, no. 15, p. 37, Oct. 2014.

[VIII-7] D. Mikitchuk *et al.*, "Mitigation of instabilities in a Z-pinch plasma by a preembedded axial magnetic field," *IEEE Trans. Plasma Sci.*, vol. 42, no. 10, pp. 2524–2525, Oct. 2014.

[VIII-8] T. J. Awe *et al.*, "Modified helix-like instability structure on imploding z-pinch liners that are pre-imposed with a uniform axial magnetic field," *Phys. Plasmas*, vol. 21, no. 5, pp. 056303-1–056303-8, May 2014.

[VIII-9] D. D. Ryutov and M. A. Dorf, "Evolution of helical perturbations in a thin-shell model of an imploding liner," *Phys. Plasmas*, vol. 21, no. 11, pp. 112704-1–112704-17, Nov. 2014.

[VIII-10] S. B. Hansen *et al.*, "Signatures of hot electrons and fluorescence in Mo Kα emission on Z," *Phys. Plasmas*, vol. 21, no. 3, pp. 031202-1–031202-5, Mar. 2014.

[VIII-11] D. Ampleford, private communication, Dec. 2014.

[VIII-12] A. L. Velikovich *et al.*, "Fusion neutron production in deuterium and DT Z-pinch implosions with seeded axial magnetic field at multi-MA current," *Bull. Amer. Phys. Soc.*, vol. 55, no. 15, p. 94, Nov. 2010.

[VIII-13] Y. K. Chong, A. L. Velikovich, J. W. Thornhill, J. L. Giuliani, P. Knapp, and C. Jennings, "D-on-D and Ar-on-D gas puff Z-pinch simulations on ZR for neutron source," in *Proc. IEEE Int. Conf. Plasmas Sci.*, Washington, DC, USA, Jun. 2014, p. 1.

John L. Giuliani (M'91) received the B.S. degree in physics from Georgetown University, Washington, DC, USA, in 1972, and the Ph.D. degree in theoretical astrophysics from Yale University, New Haven, CT, USA, in 1980.

He was involved in research on the interstellar medium with the Institute for Advanced Study and Princeton University, Princeton, NJ, USA, for several years. Since 1983, he has been with the Naval Research Laboratory (NRL), Washington, where he is currently the Head of the Radiation Hydrodynamics Branch with the Plasma Physics Division. He has been involved in high altitude nuclear effects, laser target interactions, strongly coupled plasmas, Z-pinches, arc torches, inductive processing, plasma lighting, and laser gas kinetics with NRL. His current research interests include high energy density physics, in particular, non-LTE radiation sources.

Dr. Giuliani is currently a member of the IEEE Plasma Science and Applications Committee. Since 2008, he has been an Associate Editor of *Physics of Plasmas*.

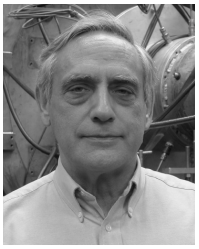

Robert J. Commisso (M'84–F'09) was born in Queens, NY, USA. He received the B.S. degree in physics from the University of Massachusetts at Lowell, Lowell, MA, USA, in 1968, and the Ph.D. degree in physics from the University of Maryland, College Park, MD, USA, in 1976.

He studied plasma physics with the University of Maryland. From 1976 to 1980, he was a Staff Member with the Los Alamos National Laboratory, Los Alamos, NM, USA, where he was involved in controlled fusion research. In 1980, he joined JAYCOR as a Senior Research Scientist, developing novel opening switch concepts with the Naval Research Laboratory (NRL), Washington, DC, USA. He joined NRL as the Head of the Pulsed Power Staff with the Plasma Technology Branch in 1983. He is currently the Head of Strategies and Programs with the Pulsed Power Physics Branch, and a Co-Principal Investigator for DTRA pulsed power and radiation source development. He serves as a Technical Advisor to DTRA. His current research interests include production of high-power electron and ion beams for nuclear weapon effects simulation, detection of fissile material, and flash radiography, high-atomic-number Z-pinches for the production of intense X-rays, plasma opening switches, and the development and application of advanced pulsed power systems.

Dr. Commisso served as an Associated Editor of the IEEE TRANSACTIONS ON PLASMA SCIENCE from 2000 to 2006, and a Senior Editor in charged particle beams and sources from 2006 to 2011. He was the Chair of the IEEE International Conference on Plasma Science in 2004.